

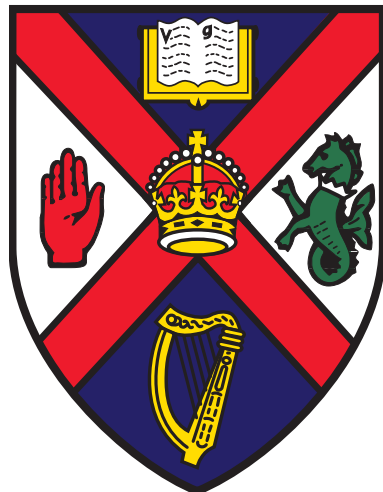
Dissociative ionisation of the hydrogen molecular ion by intense laser fields

a thesis presented upon application for
admission to the degree of

Doctor of Philosophy

in the Atomistic Simulation Centre
by

Alejandro de la Calle
MSci (Hons.)



School of Mathematics and Physics
Queen's University Belfast
Belfast, Northern Ireland
July 2017

Dissociative ionisation of the hydrogen molecular ion by intense laser fields

Abstract

The hydrogen molecular ion represents the simplest molecule in which correlations between electronic and ionic motion can be studied quantum mechanically. Understanding the interplay between electronic and ionic motion is fundamental in a wide range of areas such as the design of electronic devices, probes and sensors, and in the areas of condensed matter and plasma physics, medicine and biochemistry. Of particular importance is the interaction with attosecond laser pulses since this opens up the possibility of steering electron dynamics in order to control chemical reactions. Studying the interaction between the hydrogen molecular ion and ultrashort VUV pulses therefore provides important insights into how these pulses interact with more complex molecules.

This thesis is dedicated to the description of the interaction of the H_2^+ exposed to intense ultra-short laser pulses through the development of two massively parallel codes that efficiently solves the time-dependent Schrödinger equation (TDSE) in full dimensionality using a non-Born-Oppenheimer Hamiltonian that treats electronic and nuclear motion on an equal footing. The codes treat the electronic coordinate in cylindrical coordinates in 2D and in Cartesian coordinates in 3D. This allows us to describe parallel and arbitrary orientations between the molecular axis and the z -axis respectively.

In addition, a parallel library for calculating the photoelectron spectra using three different methods has also been developed. The methods implemented in the library are the time dependent surface flux method (t-SURFF), the sampling point method and the Fourier transform of the spatial wavefunction into momentum space. The library has been written to be as portable as possible and can be interfaced straightforwardly with other codes that are used for modelling laser-matter interactions, such as the codes developed in this thesis, together with other codes that solve the Kohn-Sham equations of the time-dependent density functional theory (TDDFT).

Contents

Introduction	3
1 Overview of strong-field physics and strong laser-matter interaction small molecules	4
1.1 The development of laser technology	6
1.1.1 Laser amplification	7
1.1.2 Free-Electron Lasers (FEL)	10
1.2 Strong-field physics	11
1.2.1 Tunnelling ionisation	11
1.2.2 Over-the-barrier ionisation	13
1.2.3 Multi-photon ionisation	13
1.2.4 Above Threshold Ionisation (ATI)	15
1.2.5 High-Harmonic Generation (HHG)	17
1.2.6 Attosecond pulses	19
1.3 Molecular studies in attosecond science	22
1.3.1 Theoretical approaches in ultrafast molecular dynamics	27
1.4 Summary	28
2 Theoretical treatment of the laser-driven H ₂ ⁺	30
2.1 Overview of the system	31
2.2 Semiclassical treatment of the laser-molecule system	31
2.3 Hamiltonian for the laser-molecule system	32
2.4 Lagrangian formalism	33
2.5 Scaled curvilinear coordinates	34
2.5.1 Scaled Cartesian coordinates	36
2.5.2 Scaled cylindrical coordinates	37
2.5.3 Implementation of scaled curvilinear coordinates	38
2.6 Classical description of the laser pulse	42
2.7 Gauge invariance	46
2.8 Summary	48
3 Numerical implementation of the laser-driven H ₂ ⁺ model: The THeREMIN and RHYthMIC codes	49
3.1 Finite-difference grid technique	50
3.1.1 Calculation of the Coulomb potential in Cartesian coordinates	50
3.2 Time propagation	52

3.3	Absorbing boundaries	54
3.4	Parallelisation of the codes	55
3.5	Summary	56
4	Role of the vibrational states in high harmonic generation and strong-field ionisation and dissociation of H_2^+	59
4.1	Static properties of H_2^+	60
4.2	Dissociative ionisation of H_2^+ by VUV laser pulses	62
4.2.1	Dissociative ionisation from the $1s\sigma_g(\nu = 0)$ state	62
4.2.2	Dissociative ionisation from the $1s\sigma_g(\nu = 2)$ state	73
4.2.3	Interplay between vibrational states	78
4.3	Dissociative ionisation and high harmonic generation of H_2^+ by IR laser pulses	83
4.3.1	Vibrational state dependence on HHG	90
4.4	Summary	98
5	Calculation of photoelectron spectrum: The POpSiCLE library	101
5.1	Fourier method	102
5.1.1	Joint electron-nuclear spectra for the hydrogen molecular ion	104
5.2	The sampling point method	107
5.3	The surface flux method (t-SURFF)	109
5.4	Numerical implementation of the library	115
5.4.1	Implementation of the Fourier method	115
5.4.2	Interpolation of the wavefunction onto spherical surfaces	118
5.4.3	Implementation of the t-SURFF method	121
5.4.4	Implementation of the sampling point method	122
5.5	Efficiency of the interpolation routines	123
5.6	Summary	125
6	Photoelectron spectra of H_2^+ by intense laser pulses	127
6.1	Comparison between different PES approaches	128
6.1.1	Fourier method results	129
6.1.2	Sampling point and t-SURFF results	135
6.2	Comparison of PES approaches in 3D	142
6.3	Photoelectron spectra in strong IR fields	148
6.4	Summary	159
	Conclusions and future work	167
	Appendices	168
A	Bessel functions and spherical harmonics	169
A.1	Bessel functions	169
A.2	Spherical harmonics	171
A.2.1	Spherical harmonics decomposition	172

B Multi-dimensional cubic interpolation	174
C Calculation of the cross section	176
References	194

List of Figures

1.1	The horse in motion. "Sallie Gardner," owned by Leland Stanford; running at a 1:40 gait over the Palo Alto track, 19th June 1878. Eadweard Muybridge. Library of Congress Prints and Photographs Division [8]	5
1.2	(a) Cutting the card quickly (1964) [6] and (b) Bullet through apple (1964) [7]. Images from Edgerton Digital Collections: 'Doc' Edgerton, Visionary Engineer: http://edgerton-digital-collections.org/ . Copyright 2010 MIT. Courtesy of MIT Museum.	5
1.3	Diagram showing the evolution of laser focused intensity over the years since the invention of lasers. The dashed line correspond to the actual predictions about the next future. Adapted from Mourou <i>et al.</i> [28].	7
1.4	Diagram showing the evolution of laser pulse durations over the years since the invention of lasers. Adapted from Corkum and Krausz [29].	8
1.5	Diagram of the chirp pulse amplification technique. An initial ultrashort pulse, in the upper left corner of the figure, is positively chirped when passing through a dispersive medium (stretcher), elongating in time the duration of the pulse. After that, when the peak intensity of the pulse has decreased by several orders of magnitude, the pulse is safely amplified by passing through a gain medium. Finally, the pulse is compressed in time when passing through a dispersive medium (compressors), which negatively chirps the pulse. The resulting pulse is a high-energy, ultrashort laser pulse. Figure reproduced from Wikipedia [35], and adapted from Ref. [36]	9
1.6	Schematic representation showing the evolution of an atomic wavepacket in a potential interacting with an intense laser field. The intensity of the laser field is increased from (a) in the absence of electric field the atomic wavepacket remains in the bound state, to (b) the tunnelling ionisation regime, to (c) the over-the-barrier ionisation regime.	11
1.7	Schematic diagram of (a) a 3-photon MPI process, and (b) a (2+1) REMPI process, where $ g\rangle$ denotes the ground state, $ e\rangle$ an excited state and $ c\rangle$ the continuum.	14

1.8	Diagram of the energy levels shift caused by the AC-stark effect, where $ g\rangle$ denotes the ground state, $ e\rangle$ an excited state and $ c\rangle$ the continuum. Only the high lying levels, that are weakly bound to the core, are shifted by the electric field by an energy equal the ponderomotive energy of the laser field, U_p . In this case, the state $ e\rangle$ also experiences a change in energy, suppressing the resonance with this state.	15
1.9	Schematic diagram of an ATI process, where $ g\rangle$ denotes the ground state and $ c\rangle$ the continuum. In the diagram only 3 photons are required for ionisation, but 5 photons were absorbed.	15
1.10	ATI spectrum of the hydrogen atom after interaction with a 10-cycle laser pulse having a wavelength of $\lambda = 800$ nm (corresponding a photon energy of $\omega_L = 0.058$ Ha), and a peak intensity of $I = 10^{10}$ W/cm ² . At this laser intensity, the ponderomotive energy is $U_p = 5.97$ eV. The spectra presents a low energy region, which extends up to an energy equal to $2U_p$, followed by a plateau, which extends up to $10U_p$	16
1.11	HHG spectrum of the hydrogen atom exposed to a 10-cycle laser pulse having a wavelength of $\lambda = 800$ nm (a photon energy of $\omega_L = 0.058$ Ha), and a peak intensity of $I = 2 \times 10^{14}$ W/cm ² . The ponderomotive energy is $U_p = 11.9$ eV. The peaks in the spectrum are placed at odd multiples of the frequency of the driving laser field. The spectrum is formed by a low energy region, composed by low order harmonics with an exponentially decreasing intensity. The low energy region extends up to a frequency equal the ionisation potential, I_p , and it constitutes the perturbative part of the spectrum. Following this region is the plateau region, in which harmonics presents similar intensities. The plateau ends at the cut-off frequency, which corresponds to a frequency of $3.17U_p + I_p$, where U_p is the ponderomotive energy of the laser field.	18
1.12	Representation of the three-step model for classical HHG. The electric field (red line), induces tunnel ionisation of the electron through the atom potential. The same field accelerates the electron, and then drives it back to the parent ion. When the electron recombines with the atom, a high energy photon is produced.	18
1.13	(a) HHG spectrum obtained after interaction of the hydrogen atom with a 10-cycle IR laser pulse, having a wavelength of 800 nm and a peak intensity of $I = 2 \times 10^{14}$ W/cm ² . (b) Train of four VUV laser pulses with a duration of 320 as at FWHM. The attosecond pulses have been obtained from the inverse Fourier transform of the HHG spectrum in (a), after filtering the high energy harmonics, from harmonic 31 th to 39 th with a rectangular window.	20
1.14	(a) HHG spectrum obtained after interaction of the hydrogen atom with a 6-cycle IR laser pulse, having a wavelength of 800 nm and a peak intensity of $I = 2 \times 10^{14}$ W/cm ² . (b) Isolated VUV laser pulse with a duration of 320 as at FWHM. The single-attosecond pulse have been obtained from the inverse Fourier transform of the HHG spectrum in (a), after filtering the high energy region of the spectrum, from harmonic 25 th to 37 th with a rectangular window.	21

1.15 Diagram of the potential energy curves for the H_2 and H_2^+ showing two different mechanisms leading electron localisation in the experiment reported in Reference [88]. In the mechanism 1, showed in (a), electron localisation is caused by the coupling of the $1s\sigma_g$ and $2p\sigma_u$ potential energy curves of the H_2^+ under the influence of the IR laser field. In the mechanism 2, presented in (b), the localisation is due to a coupling between the autoionising state Q_1 and the $1s\sigma_g$ and $2p\sigma_u$ electronic degrees of freedom. The figures have been adapted from Ref. [112].	26
2.1 Schematic setup for the hydrogen molecular ion, H_2^+ . The internuclear axis is aligned along the z axis. Each of the two H^+ ions is separated at a distance $R/2$ from the centre of mass, O . The electron position vector is denoted by \mathbf{r} , and \mathbf{r}_1 and \mathbf{r}_2 are the relative electron position vectors with respect to each ion.	31
2.2 Illustration of a finite difference grid in cylindrical coordinates using the curvilinear scalings defined in Section 2.5. (a) grid with the global scaling corresponding to Eq. (2.67) is shown while in (b) a grid with the global scaling defined in Eq. (2.73) is shown. We note that for both grids the underlying mesh always has a constant grid spacing.	41
2.3 Vector potentials with temporal profiles for (a) \sin^2 shape and (b) trapezoidal shape. Both frames corresponds to laser pulses with a wavelength of $\lambda = 800$ nm, and an intensity of $I = 10 \times 10^{14} \text{ W/cm}^2$. In frame (a) the pulses has 8 cycles, whereas in frame (b) the pulse has in total 20 cycles, ramped-on and ramped-off over 3 cycles.	45
3.1 Diagram of the communication scheme for a 2D finite-difference grid. The lines represent the processor boundaries and the squares represents the local points. The dots denote the halo points for a given processors, where the red and blue dots are the halo points in the x^1 and x^2 direction respectively.	57
3.2 Scaling results for the THeREMIN and RHYthMIC codes. The plots correspond to the time that a calculation takes depending on the total number of processors. On the tests we have kept the number of grid points per core constant. The points in (a) corresponds to number of cores 888, 1824, 259, while in (b) corresponds to number of 1134, 3402 and 18522. Perfect scaling will result in horizontal lines.	57
4.1 (a) Diagram of the potential energy curves for the H_2^+ molecule as a function of the internuclear distance R . The solid curves are calculated using a close-coupling method (courtesy of Alicia Palacios), while the lines with dots and triangles are obtained using THeREMIN. (b) Detail of the $1s\sigma_g$ state, in which the first lowest vibrational energy levels are shown. Our potential energy curves were calculated with THeREMIN at fixed internuclear distances using a grid spacing of $\Delta\rho = 0.1$ and $\Delta z = 0.05$. The vibrational eigenenergies, labelled with the quantum number ν , were calculated with THeREMIN using grid spacings of $\Delta R = 0.05$, $\Delta\rho = 0.1$ and $\Delta z = 0.05$	61

4.2	The four lowest potential energy surfaces for H_2^+ together with the Coulomb explosion limit. The arrows represent the photon energy associated with a laser wavelength of 105.3 nm. This wavelength is tuned to bridge the energy gap between the $1s\sigma_g$ state and the $2p\sigma_u$ dissociating state.	63
4.3	Probability density plots $P(R, z)$ of H_2^+ at particular instants during its interaction with a 3-cycle VUV laser pulse, having a wavelength of $\lambda = 105.3 \text{ nm}$ (photon energy of $\omega_L = 0.43 \text{ Ha}$) and a peak intensity of $I = 8.4 \times 10^{12} \text{ W/cm}^2$. Each frame corresponds to (a) $t = 0 \text{ fs}$, (b) $t = 1.45 \text{ fs}$, (c) $t = 6.02 \text{ fs}$, (d) $t = 10.02 \text{ fs}$, (e) $t = 12.04 \text{ fs}$, (f) $t = 14.34 \text{ fs}$, (g) $t = 15.25 \text{ fs}$ (h) $t = 16.04 \text{ fs}$, (i) $t = 22.12 \text{ fs}$. The electric field is shown at the top of each frame, where the position of the dot represent the specific time of the calculation.	65
4.4	Probability density plots $P(\rho, z)$ of H_2^+ at particular instants during its interaction with a 3-cycle VUV laser pulse, having a wavelength of $\lambda = 105.3 \text{ nm}$ (photon energy of $\omega_L = 0.43 \text{ Ha}$) and a peak intensity of $I = 8.4 \times 10^{12} \text{ W/cm}^2$. Each frame corresponds to (a) $t = 0 \text{ fs}$, (b) $t = 1.45 \text{ fs}$, (c) $t = 6.02 \text{ fs}$, (d) $t = 10.02 \text{ fs}$, (e) $t = 12.04 \text{ fs}$, (f) $t = 14.34 \text{ fs}$, (g) $t = 15.25 \text{ fs}$ (h) $t = 16.04 \text{ fs}$, (i) $t = 22.12 \text{ fs}$. The electric field is shown at the top of each frame, where the position of the dot represent the specific time of the calculation.	66
4.5	Probability density plots of H_2^+ (starting from the $\nu = 0$ vibrational state) over time during its interaction with a 3-cycle VUV laser pulse having a wavelength $\lambda = 105.3 \text{ nm}$ (photon energy $\omega_L = 0.43 \text{ Hartrees}$) and a peak intensity of $I = 8.4 \times 10^{12} \text{ W/cm}^2$. In (a) we present the density $P(z, t)$ while in (b) we present $P(R, t)$. The electric field used in the calculation is shown at the top of the figure, where the position of the red circle represents the specific time of the calculation. In (b) the dashed lines represents the classical trajectories of the nuclear wavepackets along the $2p\sigma_u$ potential energy curves of the molecule.	68
4.6	Probability density plots of H_2^+ (starting from the $\nu = 0$ vibrational state) over time during its interaction with a 3-cycle VUV laser pulse having a wavelength $\lambda = 105.3 \text{ nm}$ (photon energy $\omega_L = 0.43 \text{ Hartrees}$) and a peak intensity of $I = 8.4 \times 10^{12} \text{ W/cm}^2$. In both plots we present the density $P(R, t)$. The dashed lines represents the classical trajectories of the nuclear wavepackets along (a) the $3d\sigma_g$ and (b) $3s\sigma_u$ potential energy curves of the molecule. The electric field used in the calculation is shown at the top of the figure, where the position of the red circle represents the specific time of the calculation.	69
4.7	Electric field (a) and spectrum (b) of a 3-cycle and a 28-cycle VUV laser pulses, both having a wavelength of $\lambda = 105.3 \text{ nm}$ and a peak intensity of $I = 8.4 \times 10^{12} \text{ W/cm}^2$. The 3-cycle has approximately a duration of 1 fs, while the 28-cycle pulse has a duration of 9.8 fs. The photon energy for both pulses is 0.43 Ha (11.7 eV) and the bandwidth is 0.288 Ha (7.848 eV) and 0.031 Ha (0.841 eV) for the 3 cycle and the 28-cycle pulse respectively.	71

4.8	Probability density plots of H_2^+ (starting from the $\nu = 0$ vibrational state) over time during its interaction with a 28-cycle VUV laser pulse having a wavelength $\lambda = 105.3$ nm (photon energy $\omega_L = 0.43$ Ha) and a peak intensity of $I = 8.4 \times 10^{12}$ W/cm ² . In (a) we present the density $P(z, t)$ while in (b) we present $P(R, t)$. The electric field used in the calculation is shown at the top of the figure, where the position of the red circle represents the specific time of the calculation. In (b) the dashed lines represents the classical trajectories of the nuclear wavepackets along some of the potential energy curves of the molecule.	72
4.9	Time evolution of the population of the six lowest vibrational states of the H_2^+ molecule exposed to a 3-cycle VUV laser pulse, whose photon energy is $\omega_L = 0.43$ Ha and intensity $I = 8.4 \times 10^{12}$ W/cm ² . The initial state corresponds to the ground vibrational state, denote by $\nu = 0$.	73
4.10	Probability density plots $P(R, z)$ of H_2^+ initially in the $\nu = 2$ vibrational state, at particular instants during its interaction with a 3-cycle VUV laser pulse, having a wavelength of $\lambda = 110.3$ nm (photon energy of $\omega_L = 0.43$ Ha) and a peak intensity of $I = 8.4 \times 10^{12}$ W/cm ² . Each frame corresponds to (a) $t = 0$ fs, (b) $t = 1.45$ fs, (c) $t = 10.02$ fs, (d) $t = 14.34$ fs. The electric field is shown at the top of each frame, where the position of the dot represent the specific time of the calculation.	74
4.11	Probability density plots $P(\rho, z)$ of H_2^+ initially in the $\nu = 2$ vibrational state, at particular instants during its interaction with a 10-cycle VUV laser pulse, having a wavelength of $\lambda = 780$ nm (photon energy of $\omega_L = 0.058$ Ha) and a peak intensity of $I = 2 \times 10^{14}$ W/cm ² . Each frame corresponds to (a) $t = 0$ fs, (b) $t = 1.45$ fs, (c) $t = 10.02$ fs, (d) $t = 14.34$ fs. The electric field is shown at the top of each frame, where the position of the dot represent the specific time of the calculation.	75
4.12	Diagrammatic representation of the four lowest eigenstates of the quantum harmonic oscillator. The solid line represents the quadratic potential, while the dashed line represents the $1s\sigma_g$ potential energy curve of the H_2^+ .	77
4.13	Probability density plots of H_2^+ (starting from the $\nu = 2$ vibrational state) over time during its interaction with a three-cycle VUV laser pulse having a wavelength $\lambda = 110.3$ nm (photon energy $\omega_L = 0.43$ Hartrees) and a peak intensity of $I = 8.4 \times 10^{12}$ W/cm ² . The initial state of the molecule is the third vibrational state ($\nu = 2$) in the $1s\sigma_g$ potential energy surface. In (a) we present the density $P(z, t)$ while in (b) we present $P(R, t)$. The electric field used in the calculation is shown at the top of the figure, where the position of the red circle represents the specific time of the calculation. In (b) the dashed lines represents the classical trajectories of the nuclear wavepackets along some of the potential energy curves of the molecule.	79

4.14 Time evolution of the population of the six lowest vibrational states of the H_2^+ molecule exposed to a 3-cycle VUV laser pulse, whose photon energy is $\omega = 0.43$ Hartrees and intensity $I = 8.4 \times 10^{12} \text{ W/cm}^2$. The initial state corresponds to the third vibrational state, denote by $\nu = 2$.	80
4.15 R vs. r diagram showing how we split coordinate space in distinct regions associated with ionisation and dissociation, where R is the internuclear coordinate and r represents the electronic coordinate and it holds the equality $r^2 = \rho^2 + z^2$. The different parts of the coordinate space are: the bound, ionisation, dissociation and dissociative ionisation regions, where the bound region is delimited by R_0 and $r_0 = \sqrt{\rho_0^2 + z_0^2}$, and the width of the dissociative ionisation region is $R_D \leq \sqrt{(z \pm R/2)^2 + \rho^2}$. Wavepacket residing in these regions allow us to calculate the ionisation and dissociation yields after the interaction with the laser pulse.	82
4.16 Ionisation (a) and dissociation (b) yields of the H_2^+ after interaction with a 3-cycle VUV laser pulse having a wavelength $\lambda = 105.3 \text{ nm}$ (corresponding to a photon energy of $\omega_L = 0.43 \text{ Ha}$) and a peak intensity of $I = 8.4 \times 10^{12} \text{ W/cm}^2$. Each line in the plots represent a calculation starting from one particular level of the ten lowest vibrational states ($\nu = 0, \dots, 9$) in the $1s\sigma_g$ potential energy surface, where each yield have been multiplied by its corresponding Franck-Condon factor. The dashed lines correspond to yields that have been scaled by a factor of 10 for clarity. The inset in each plot represents the first ten Franck-Condon factors of table 4.3. Ionisation (c) and dissociation (d) yields for the linear combination of the first ten vibrational states (FC) and the incoherent sum (IS). The yields denoted by FC have been scaled for clarity. The electric field used in the calculation is shown at the top of each plot.	83
4.17 Probability density plots $P(R, z)$ of H_2^+ at particular instants during its interaction with a 10-cycle IR laser pulse, having a wavelength of $\lambda = 780 \text{ nm}$ (photon energy of $\omega_L = 0.058 \text{ Ha}$) and a peak intensity of $I = 2 \times 10^{14} \text{ W/cm}^2$. Each frame, which is a zoom in on z , corresponds to (a) $t = 0 \text{ fs}$, (b) $t = 9.82 \text{ fs}$, (c) $t = 10.41 \text{ fs}$, (d) $t = 11.43 \text{ fs}$, (e) $t = 12.11 \text{ fs}$, (f) $t = 13.80 \text{ fs}$, (g) $t = 15.15 \text{ fs}$, (h) $t = 26.92 \text{ fs}$, (i) $t = 39.03 \text{ fs}$. The electric field is shown at the top of each frame, where the position of the dot represent the specific time of the calculation.	85
4.18 Probability density plots $P(\rho, z)$ of H_2^+ at particular instants during its interaction with a 10-cycle IR laser pulse, having a wavelength of $\lambda = 780 \text{ nm}$ (photon energy of $\omega_L = 0.058 \text{ Ha}$) and a peak intensity of $I = 2 \times 10^{14} \text{ W/cm}^2$. Each frame corresponds to (a) $t = 0 \text{ fs}$, (b) $t = 9.82 \text{ fs}$, (c) $t = 10.41 \text{ fs}$, (d) $t = 11.43 \text{ fs}$, (e) $t = 12.11 \text{ fs}$, (f) $t = 13.80 \text{ fs}$, (g) $t = 15.15 \text{ fs}$, (h) $t = 26.92 \text{ fs}$, (i) $t = 39.03 \text{ fs}$. The electric field is shown at the top of each frame, where the position of the dot represent the specific time of the calculation.	86

4.19 Time evolution of the H_2^+ wavefunction (a): $P(z, t)$, and (b): $P(R, t)$, after the interaction with a 10-cycle IR laser pulse, having a wavelength of $\lambda = 780$ nm (photon energy of $\omega_L = 0.058$ Ha) and a peak intensity of $I = 2 \times 10^{14}$ W/cm ² . The initial molecular state is the lowest vibrational state, $\nu = 0$, of the $1s\sigma_g$ ground state of the H_2^+ . In both frames the rest of the coordinates have been integrated over.	88
4.20 (a) and (c) Ionisation and (b) and (d) dissociation yields for the first eight vibrational states of the H_2^+ interacting with a 10-cycle IR laser pulse having a wavelength of $\lambda = 780$ nm (photon energy of $\omega_L = 0.057$ Ha) and a peak intensity of $I = 2 \times 10^{14}$ W/cm ² . The upper frame in each plot shows the temporal profile of the electric field of the laser pulse. In (a) and (c), a zoom of the ionisation yield for $\nu = 7$ and the electric field is shown in the inset plot. In (b) the dashed lines correspond to the yields for the $\nu = 4$ and $\nu = 5$ states. In the lower frames, (c) and (d) the yields have been multiplied by their correspondent Franck-Condon factors, shown in the inset of Figure 4.20d.	89
4.21 Time-dependent population of the H_2^+ driven by 780 nm IR pulse (10 cycles, 2×10^{14} W/cm ²). In each frame the initial state is a different vibrational state, and each line represents a contribution coming from a different vibrational state. However in this figure all the vibrational states in each frame has been multiplied by a Franck-Condon factor, corresponding to the initial vibrational state. The upper frames represents the temporal profile of the laser pulse.	91
4.22 Final vibrational state populations of the H_2^+ after interaction with an 780 nm IR laser pulse (10 cycles, 2×10^{14} W/cm ²). In each frame the initial state is a different vibrational state, and each bar presents the final population of each vibrational states. However in this figure all the vibrational states in each frame has been multiplied by a Franck-Condon factor, corresponding to the initial vibrational state.	92
4.23 High-Harmonic spectra of H_2^+ driven by 780 nm IR pulse (10 cycles, 2×10^{14} W/cm ²). Each frame corresponds to a different initial state set to one vibrational state from $\nu = 0, 7$. The black vertical grid lines marks the odd harmonics, and the red vertical lines represent the ionisation threshold I_p (left line) and the cut-off limit, $3.17U_p + I_p$ (right line).	94
4.24 High-Harmonic spectra of fixed-nuclei H_2^+ driven by 780 nm IR pulse (10 cycles, 2×10^{14} W/cm ²). Each frame shows the spectra at a particular internuclear distance, increasing R from the upper to the lower part of the figure. The black vertical lines represent the ionisation threshold I_p (left line) and the cut-off limit, $3.17U_p + I_p$ (right line).	96

4.25 Density plots showing the time-frequency analysis on the HHG of H_2^+ interacting with a 10-cycle laser pulse, having a wavelength $\lambda = 780$ nm and a peak intensity of $I = 2 \times 10^{14}$ W/cm ² . In each frame the upper part presents the temporal profile of the electric field of the pulse, while the left side presents the corresponding HHG spectra. For clarity, the horizontal lines marks the even harmonic orders.	97
4.26 Zoom of the time-frequency analysis for the initial vibrational state $\nu = 4$ of the H_2^+ interacting with a 10-cycle laser pulse having a wavelength of $\lambda = 780$ nm and a peak intensity of $I = 2 \times 10^{14}$ W/cm ² (shown in Figure 4.25e), between 10.5 and 17 fs. The upper frame corresponds to the electric field, while the left frame shows the corresponding to the high-harmonic generation spectra. . . .	98
5.1 Diagram of the separation in different regions of the H_2^+ coordinate space interacting with an external laser pulse. The four regions are: Bound (B), Dissociation (D), Ionisation (I) and Dissociative ionisation (DI), and their boundaries are represented by dashed lines at $r = r_b$ and $R = R_b$	105
5.2 Schematic diagram showing how the FFT of a wavefunction parallelised on a 2D grid can be carried out. See text for a complete description.	117
5.3 Schematic diagram showing how the Fourier-Bessel transform of a wavefunction parallelised on a 2D grid can be carried out. See text for a complete description.	117
5.4 Scheme of a cylindrical grid decomposed over processor elements. In this case we can see that the surface only passes through some of these processors. . . .	119
6.1 Snapshots of the wavefunction at the end of the evolution for ionisation of H_2^+ by VUV pulses. The laser polarisation is parallel to the internuclear axis. The laser pulses parameters are shown in table 6.1, and corresponds to: (a) 9-cycle, $\lambda = 33.3$ nm (photon energy $\omega_L = 1.37$ Ha), (b) 13-cycle, $\lambda = 23.05$ nm (photon energy $\omega_L = 1.98$ Ha), (c) 17-cycle, $\lambda = 17.63$ nm (photon energy $\omega_L = 2.58$ Ha) and (d) 21-cycle, $\lambda = 14.27$ nm (photon energy $\omega_L = 3.19$ Ha). All laser pulses have a peak intensity of 8.4×10^{12} W/cm ² and a total duration of 1 fs.	131
6.2 Masking function used to remove the eigenstates from the wavefunction, defined in Eq. (6.1). The function takes the value zero within the inner region and the value within the outer region. The value of the function changes smoothly from zero at r_0 to one at r_1 using a Gaussian function. In this case, the limits of the inner and outer region are $r_0 = 10 a_0$ and $r_1 = 25 a_0$	132

- 6.3 Momentum distribution of the ionised electrons for single-photon ionisation with laser polarisation parallel to the internuclear axis from the $1s\sigma_g$ state of the fixed-nuclei H_2^+ , calculated with the Fourier method. Pulse parameters for each calculation can be found in table 6.1, and corresponds to: (a) 9-cycle, $\lambda = 33.3$ nm (photon energy $\omega_L = 1.37$ Ha), (b) 13-cycle, $\lambda = 23.05$ nm (photon energy $\omega_L = 1.98$ Ha), (c) 17-cycle, $\lambda = 17.63$ nm (photon energy $\omega_L = 2.58$ Ha) and (d) 21-cycle, $\lambda = 14.27$ nm (photon energy $\omega_L = 3.19$ Ha). All laser pulses have a peak intensity of $8.4 \times 10^{12} \text{ W/cm}^2$ and a total duration of 1 fs. In each plot, a white semicircle with radius $k_e = \sqrt{k_\rho^2 + k_z^2}$, the electron momentum, is given. 133
- 6.4 Photoelectron spectra in a logarithmic scale for photoionisation of H_2^+ after interaction with a 13 cycle laser pulse having wavelength $\lambda = 23.05$ nm and peak intensity $1.0 \times 10^{13} \text{ W/cm}^2$. The PES was calculated with the Fourier method, using the grid parameters of set (I) and propagating the wavefunction 10 cycles after the end of the pulse. The first two ATI peak are visible at 0.875 and 2.852 Hartrees respectively. 134
- 6.5 Comparison between photoelectron spectra calculated with the Fourier method for photoionisation of H_2^+ using different time steps for the TDSE evolution. The molecule was exposed to a 13 cycle laser pulse having wavelength $\lambda = 23.05$ nm and peak intensity $1.0 \times 10^{13} \text{ W/cm}^2$ 134
- 6.6 Photoelectron spectra for photoionisation of H_2^+ calculated using the Fourier method. The solid lines correspond the PES were extracted after propagating 20, 40, 45 and 60 optical cycles after the end of a 17 cycle laser pulse having wavelength $\lambda = 17.63$ nm and peak intensity $1.0 \times 10^{13} \text{ W/cm}^2$, from a calculation using the full Coulomb potential. The lines with dots and triangles correspond to the PES were extracted from a calculation using the truncated Coulomb potential, where the TDSE was evolved 10 cycles after the end of the pulse. The Coulomb potential was truncated at radius $r = 20 a_0$ (dots) and $r = 40 a_0$ (triangles). The grid parameters for all the calculations were those of set (I). 135
- 6.7 Electron probability density $|\Psi(r_b, \theta = \pi/2)|^2$ crossing surfaces with different surface radii ($r_b = 20, 50, 80, 100 a_0$) after photo-ionisation of H_2^+ by a 13 cycle laser having a wavelength $\lambda = 23$ nm and a peak intensity $1.0 \times 10^{13} \text{ W/cm}^2$. Also shown is the electric field of the laser pulse. 136
- 6.8 Photoelectron spectra of H_2^+ exposed to a 13-cycle laser pulse, having a wavelength of $\lambda = 23.05$ nm and a peak intensity of $I = 10^{13} \text{ W/cm}^2$. The solid lines correspond to the PES obtained using a truncated Coulomb potential, while the dashed lines correspond to the PES obtained using the full potential. The grid parameters used in the calculations with a surface radius at $r_b = 20 a_0$ are those of set (III), while calculations with $r_b = 50 a_0$ used those of set (IV). In the plot, the line corresponding to truncation at $r_b = 50 a_0$ is completely superimposed to the line corresponding to truncation at $r_b = 20 a_0$ 137

6.9	Photoelectron spectra for photoionisation of H_2^+ after interaction with a 13 cycle laser pulse having wavelength $\lambda = 23.05 \text{ nm}$ and peak intensity $1.0 \times 10^{13} \text{ W/cm}^2$. Results were calculated in THeREMIN by the three methods implemented in POpSiCLE: the Fourier method, the sampling point method and the t-SURFF method. For the sampling point and t-SURFF method we made use of the grid parameters of set (III), while for the Fourier method calculation we used grid parameters of set (I). For the surface calculations (sampling point and t-SURFF method), the surface radius was $r_b = 20 a_0$. For the Fourier method we propagated the wavefunction 10 cycles after the end of the pulse. For all the methods the Coulomb potential is truncated at $r = 20 a_0$	137
6.10	PES calculated with the sampling point method, using set of grid parameters number (III) with a surface radius $r_b = 20 a_0$, for different propagation times after the pulse. The blue line represents the PES calculated after propagation for 1.54 fs (20 laser cycles) more after the pulse, whereas the green line represents the PES calculated after propagation of, in addition to the 20 cycles, 10 fs more after the pulse. (11,54 fs added in total after the pulse). The last 10 fs were added padding with zeros at the end of the surface values over time. . .	138
6.11	Photo-electron spectra of single-photon ionisation of H_2^+ after interaction with pulse 2 of table 6.1. (a): PES calculated with the sampling point method. (b): PES calculated with the t-SURFF method. In both plots the PES have been calculated placing the surface at radius $r_b = 20, 50, 80 a_0$, and the grid parameters used were those of sets (III), (IV) and (V) respectively. In (a), the results for $r_b = 50 a_0$ and $r_b = 80 a_0$ have been scaled by a factor given in the legend.	139
6.12	Polar plots showing the angularly resolved photoelectron distributions of fixed-nuclei H_2^+ after interaction with a 13 cycle laser pulse having wavelength $\lambda = 23.05 \text{ nm}$ and peak intensity $1.0 \times 10^{13} \text{ W/cm}^2$. Results were calculated in 2D using THeREMIN using: (a) the Fourier method, (b) the sampling point method and (c) the t-SURFF method. The sampling point results have been scaled by a factor of 2×10^3	141
6.13	Total cross section for single-photon ionisation of H_2^+ from the Σ_g ground state in the presence of four linearly polarised laser pulses. All the pulses have a total duration of 1 fs, and an intensity of $I = 10^{13} \text{ W/cm}^2$. In the upper frame we compare with the results of Hou [123], obtained with LOPT.	142
6.14	Snapshots of the wavefunction at the end of simulation after photoionisation by a 13-cycle laser pulse of $\lambda = 23 \text{ nm}$ of wavelength and an intensity of $I = 10^{13} \text{ W/cm}^2$. The three frames correspond to (a) $P(x, z)$ (b) $P(x, y)$ and (c) $P(y, z)$ which are been obtained by integrating the 3D density over one coordinate. . .	145
6.15	2D photo-electron momentum distributions after ionisation of H_2^+ from the $1s\sigma_g$ ground state after interaction with a 13-cycle laser pulse of $\lambda = 23 \text{ nm}$ of wavelength and $I = 10^{13} \text{ W/cm}^2$, obtained with the Fourier method using set (I). The frames correspond to (a) $P(k_x, k_z)$ (b) $P(k_x, k_y)$ and (c) $P(k_y, k_z)$ which have been obtained by integrating over one coordinate.	146

6.16	Photoelectron spectra for photoionisation of H_2^+ after interaction with a 13 cycle laser pulse having wavelength $\lambda = 23.05 \text{ nm}$ and peak intensity $1.0 \times 10^{13} \text{ W/cm}^2$. Results were calculated in RHYthMIC (3D) by the three methods implemented in POpSiCLE: the Fourier method, the sampling point method and the t-SURFF method	146
6.17	Photoelectron spectra for photoionisation of H_2^+ after interaction with a 13 cycle laser pulse having wavelength $\lambda = 23.05 \text{ nm}$ and peak intensity $1.0 \times 10^{13} \text{ W/cm}^2$. Results were calculated using the t-SURFF method in 3D with RHYthMIC, except for the line corresponding to set III, which was calculated in 2D with THeREMIN. FD denotes the order of the finite-difference rule employed.	147
6.18	(a): Photoelectron spectra of photoionisation of fixed-nuclei H_2^+ with different internuclear distances, from $R = 2 a_0$ to $R = 10 a_0$, after interaction with a 10 cycle laser pulse having a wavelength of $\lambda = 780 \text{ nm}$ and a peak intensity of $I = 2 \times 10^{14} \text{ W/cm}^2$. In (b), we have sorted out vertically the PES for each internuclear distance in order to compare between them.	149
6.19	Photoelectron spectra for photoionisation of H_2^+ after interaction with a 10-cycle laser pulse having a wavelength of $\lambda = 780 \text{ nm}$ and a peak intensity of $I = 2 \times 10^{14} \text{ W/cm}^2$. On this figure we show the PES for internuclear distances of $R = 2 a_0$, $R = 3 a_0$ and $R = 4 a_0$. The solid black lines correspond to the $2U_p$ and $10U_p$ energy limits.	150
6.20	Photoelectron spectra for photoionisation of H_2^+ after interaction with a 10-cycle laser pulse having a wavelength of $\lambda = 780 \text{ nm}$ and a peak intensity of $I = 2 \times 10^{14} \text{ W/cm}^2$. On this figure we show the PES for internuclear distances of $R = 5 a_0$, $R = 6 a_0$ and $R = 7 a_0$. The solid black lines correspond to the $2U_p$ and $10U_p$ energy limits.	151
6.21	Photoelectron spectra for photoionisation of H_2^+ after interaction with a 10 cycle laser pulse having a wavelength of $\lambda = 780 \text{ nm}$ and a peak intensity of $I = 2 \times 10^{14} \text{ W/cm}^2$. On this figure we show the PES for internuclear distances of $R = 8 a_0$, $R = 9 a_0$ and $R = 10 a_0$. The solid black lines correspond to the $2U_p$ and $10U_p$ energy limits.	152
6.22	Angularly resolved photoelectron spectra for photoionisation of H_2^+ after interaction with a 10 cycle laser pulse having a wavelength of $\lambda = 780 \text{ nm}$ and a peak intensity of $I = 2 \times 10^{14} \text{ W/cm}^2$. On this figure we show PAD for internuclear distances of $R = 2 a_0$, $R = 3 a_0$ and $R = 4 a_0$. The left hand side shows a general view of the PAD up to $10U_p$, whereas in the right panels we show a zoom in up to $2U_p$ of the left hand side.	154
6.23	The same as in Figure 6.22. On this figure we show PAD for internuclear distances of $R = 5 a_0$, $R = 6 a_0$ and $R = 7 a_0$ Bohr. The left hand side shows a general view of the PAD up to $10U_p$, whereas in the right panels we show a zoom in up to $2U_p$ of the left hand side.	155

6.24	The same as in Figure 6.22 and Figure 6.23. On this figure we show PAD for internuclear distances of $R = 8 a_0$, $R = 9 a_0$ and $R = 10 a_0$ Bohr. The left hand side shows a region of the PAD up to 130 eV, whereas in the right panels we show a zoom in of the left hand side panels within a region of 40 eV.	156
6.25	Angularly resolved PES for photoionisation of fixed-nuclei H_2^+ at $R = 2 a_0$, exposed to 3-cycle 780 nm laser pulse at $I = 2 \times 10^{14} \text{ W/cm}^2$. The lower panel on the left hand side corresponds to a pulse with CEP = 0, whereas the lower panel on the right hand side corresponds to a pulse with CEP = $-\pi/2$. In the upper panels the corresponding temporal profile of the electric field are shown.	157
6.26	Angularly resolved PES for photoionisation of fixed-nuclei H_2^+ at $R = 6 a_0$, exposed to 10-cycle 780 nm laser pulse at $I = 2 \times 10^{14} \text{ W/cm}^2$. The horizontal white lines represent the expected two-centre interference energy minima predicted by Eq. (6.14) for the case of $\theta = 0^\circ$, where the electrons are ejected along the molecular axis.	159
6.27	PES for a particular electron emission of H_2^+ after interaction with a 10-cycle laser pulse having a wavelength of $\lambda = 780 \text{ nm}$, and a peak intensity of $I = 2 \times 10^{14} \text{ W/cm}^2$. The plots corresponds to: (a) $\theta = 0^\circ$, (b) $\theta = 30.30^\circ$, (c) $\theta = 59.20^\circ$, where θ is the angle of electron emission with respect to the molecular axis. The solid lines indicate the $2U_p$ and the $10U_p$ thresholds respectively. The energy minima for each emission angle are represented by dashed lines, and can be found in table 6.8.	160
6.28	PES for a particular electron emission of H_2^+ after interaction with a 10-cycle laser pulse having a wavelength of $\lambda = 780 \text{ nm}$, and a peak intensity of $I = 2 \times 10^{14} \text{ W/cm}^2$. The plots corresponds to $\theta = 90^\circ$, where θ is the angle of electron emission with respect to the molecular axis. The solid lines indicate the $2U_p$ and the $10U_p$ thresholds respectively. The energy minima for this emission angle are represented by dashed lines, and can be found in table 6.8.	161
B.1	Unit rectangle on a 2D regular mesh. We must know at the four corners, in the figure labelled p_1 , p_2 , p_3 and p_4 , the values of the function, and its first and cross-derivatives.	174

List of Tables

3.1	Tables containing the data employed in the scaling results shown above. Table (a) corresponds to the THeREMIN results, while table (b) corresponds to the RHYthMIC results.	58
4.1	Vibrational energy states of the H_2^+ molecule. The first and second columns correspond with calculations using THeREMIN, while the third and fourth columns correspond to previous results. In Present (1) the grid parameters employed are $\Delta\rho = 0.1$, $\Delta z = 0.20$ and $\Delta R = 0.20$ (coarse grid), while in Present (2) the grid parameters are $\Delta\rho = 0.1$, $\Delta z = 0.05$, $\Delta R = 0.05$ (fine grid). Previous (1) column correspond to the results available in Niederhausen et al. [155], while column Previous (2) contain the results found in Hilico et al. [235]	62
4.2	Grid parameters employed in the calculation of the response of H_2^+ exposed to a 3 cycle VUV laser pulse, having a wavelength of $\lambda = 105.3$ nm and a peak intensity of $I = 8.4 \times 10^{12}$ W/cm ²	63
4.3	Franck-Condon factors $q_{0,\nu}$ for transitions between the vibrational ground state of the H_2 in the $1s\sigma_g$ potential energy surface and the ν $1s\sigma_g$ state of the 10 lowest vibrational states, $\phi_\nu(r)$, of the H_2^+ in the $1s\sigma_g$ potential energy surface.	80
4.4	Grid parameters used in the calculation of H_2^+ interacting with an intense IR laser pulse, whose wavelength is $\lambda = 780$ nm (photon energy of $\omega_L = 0.058$ Hartrees) and a peak intensity of $I = 2 \times 10^{14}$ W/cm ²	84
5.1	Grid parameters used for testing the interpolation routines in 2D (employing THeREMIN).	124
5.2	Timings for 2D interpolation using both methods: Shepard's method and bicubic interpolation. The 3d state of the hydrogen atom on a surface at radius $r = 20 a_0$ is interpolated from a 2D grid in cylindrical coordinates, whose grid parameters are given in table 5.1, to spherical coordinates. The timings shown in this table have been averaged over 10 runs. The maximum error for each interpolation method is also shown.	124
5.3	Grid parameters used for testing the interpolation routines in 3D (employing RHYthMIC).	125

5.4	Timings for 3D interpolation using both methods: Shepard's method and tricubic interpolation. The 3d state of the hydrogen atom on a surface at radius $r = 4.5 a_0$ is interpolated from a 3D grid in Cartesian coordinates, whose grid parameters are given in table 5.3. The timings shown in this table have been averaged over 10 runs. The maximum error between the trial function and the interpolated one is given. In addition, we also present the maximum interpolation error at the same radius when using the 2D interpolating routines.	125
6.1	Laser pulse parameters for each of the 4 pulses employed in our calculations of photoelectron spectra in H_2^+ . All pulses have a duration of 1 fs, a peak intensity of $I = 10^{13} \text{ W/cm}^2$ and a temporal profile described by a \sin^2 function. In the table, ω_L represents the photon energy, λ the wavelength, and T the period.	128
6.2	Grid parameters employed for calculating the PES in 2D using THeREMIN. Six sets of grid parameters were considered. In set (I) the Fourier method is used, which requires a large grid extent. In sets (II), (III), (IV), (V) and (VI) the surface methods (sampling point and t-SURFF methods) were used, in which during the time evolution we record a single surface file. The surface radius and the mesh extent for each set is given in atomic units.	129
6.3	Timings for the calculation of the TDSE using THeREMIN (2D) for the Fourier method (upper part) and for the surface methods (middle and lower part). The grid parameters of each evolution are given in table 6.2.	142
6.4	Comparison of five lowest eigenvalues of the fixed-nuclei H_2^+ , using different grid spacings calculated in 3D using the RHYthMIC code. The grid spacings and finite-difference (FD) rules are: Fine 1: We use a fine grid with grid spacings $\Delta x = \Delta y = \Delta z = 0.2$ and a 5-point FD rule; Fine 2: We use again a fine grid of grid spacings $\Delta x = \Delta y = \Delta z = 0.2$ and a 9-point FD rule; Coarse 1: We use grid spacings $\Delta x = \Delta y = 0.4$ and $\Delta z = 0.2$, and a 5-point FD rule; Coarse 2: Again we use grid spacings $\Delta x = \Delta y = 0.4$ and $\Delta z = 0.2$, and a 9-point FD rule.	143
6.5	Grid parameters employed for calculating the PES in 3D using RHYthMIC. Four calculations were considered. In set (I) the Fourier method is used, which requires a large grid extent. In sets (II), (III) and (IV) the surface methods (sampling point and t-SURFF methods) were used, in which during the time evolution we record a single surface file. The surface radius employed in these sets is $r_b = 20 a_0$. The mesh extent for each set is given in atomic units.	144
6.6	Timings for the time-evolution of the TDSE using RHYthMIC (3D) for the Fourier method (upper part) and for the surface methods (middle and lower part). The grid parameters of each evolution are given in table 6.5.	147
6.7	Grid parameters employed for calculating the photoelectron spectra of H_2^+ after interacting with an intense, infrared 10-cycle laser pulse having $\lambda = 780$ nm and an intensity of $I = 2 \times 10^{14} \text{ W/cm}^2$. The PES is calculated in 2D using THeREMIN where we employ the t-SURFF method. The surface radius and the mesh extent for each set is given in atomic units.	148

6.8 Energies for the two-centre interference minima calculated from Eq. (6.14) for different electrons emission directions. θ corresponds to angle between the molecular axis and the electron momentum vector. The molecule has a fixed internuclear of $R = 6$ Bohr.	158
---	-----

This thesis is dedicated to the memory of my father,
José Alejandro de la Calle Martín.

Jumping from failure to failure, with undiminished enthusiasm, is the big secret to success.

Savas Dimonopoulos, seen in Particle Fever.

What the book offers is not a neutral analysis but an engaged and extremely 'partial' one—for truth is partial, accessible only when one takes sides, and is no less universal for this reason.

Slavoj Zizek, First as a tragedy, then as farce.

*Ahora que
el futuro está por decidir
activamos mecanismos de control
diseñados por dioses,
extraordinarios trucos del tiempo y del espacio.
Buscamos y buscamos sin parar,
y se oculta la verdad.
Seguimos intentando descifrar
la trama absurda de la realidad.*

Los planetas, Sol y sombra.

Acknowledgments

Many people have contributed to this thesis, directly or indirectly. First of all, I would like to thank my supervisor Dr. Daniel Dundas for being the lighthouse of this work, a researcher I have learnt from loads of things (computational patience and numerical toughness among them), a great support in difficult times, and a person who now I can call friend. Thanks Dan. Then I have to thank my second supervisor Prof. Dr. Hugo van der Hart, again a scientist who learn scientific and computational excellence from, for having given me the opportunity to work at Queen's and be part of the ITN CORINF. Also I am very grateful to the members of the Atomistic Centre and Prof. Dr. Jorge Kohanoff for having welcomed in his group when suddenly I needed one. I felt like an outsider to finally feel really part of that group, even when my molecules are a way smaller than theirs! I have a lot of fun with the Atomistic crew and specially the inhabitants of the room 01.005 in the David Bates building. Abigail Wardlow, Ryan McMillan, there will be always tea time! And my mate Brian Cunningham, a true Irish friend. I do not want to forget to mention all the Belfast gang (Alfred, Chiara, Oier, Onintze, Marta, Joan, Urko, Edu, Andrea, Eudald, Heiko and Claudia), for all the pints and discussions, rock & roll and fun (mostly the fun) over my Belfast years.

Several people within Queen's must also be thanked. Dr. Jonathan Parker for invaluable help with codes and algorithms, Dr. Jack Wragg to be always available for a cheerful conversation, to Dr. Gabriele de Chiara (and Federica), for their friendship and for sharing the same passion for good food, and, of course, to Dr. Héctor Rey, my PhD mate. Our time spent together in offices, courses, conferences and parties afterwards can not be left out of our PhD's.

I would like to thank my scientific visits. Firstly Prof. Dr. Armin Scrinzi for the short but delightful visit to LMU at Munich, where only in one week I could learn the basics of ECS. Secondly, to Fernando Martin and his group at UAM in Madrid. A special mention goes for Dr. Alicia Palacios, because their kindness, patience and encouragement to me (a complete unknown) during this thesis are still greatly appreciated. At the moment I do not know if she is a good scientist and better person or the other way around.

I do not want to forget the extraordinary people from the ALF group at USAL in Salamanca. They warmly gave me shelter at the very last stage of my PhD, when writing

was a struggle, and now Luis and Julio have made possible for me to come back for a while to this group, which I have always considered a home. The fellowship and passion for physics that you can breathe here is contagious.

Last but not least, I would like to take this opportunity to thank my mother for her love, and to Pili, who is my best half. She has been a relentless source of support, encouragement, kindness and love among many other things. We can say that we went two to Ireland and then we came back three, now that little Carmela is with us. Finally, I would like to express my infinite gratitude to my father. This thesis is entirely dedicated to him and his memory.

Introduction

The hydrogen molecular ion represents the simplest molecule in which correlations between electrons and ions can be studied quantum mechanically. Understanding the interplay between electronic and ionic motion is fundamental in a wide range of areas such as the design of electronic devices, probes and sensors, and in the areas of condensed matter and plasma physics, medicine and biochemistry. Of particular importance is the interaction with attosecond laser pulses, since this opens up the possibility of steering electron dynamics in order to control chemical reactions. Studying the interaction between the hydrogen molecular ion and ultrashort VUV pulses therefore provides important insights into how these pulses interact with more complex molecules.

This thesis is dedicated to the description of the interaction of the H_2^+ exposed to intense ultra-short laser pulses through the development of massively parallel codes that efficiently solve the time-dependent Schrödinger equation (TDSE) in full dimensionality using a non-Born-Oppenheimer treatment. Thus, electronic and ionic degrees of freedom are described on an equal footing, allowing nuclear vibration effects to be described. Two codes have been developed: the first code, THeREMIN (vibraTing HydRogEn Molecular IoN) solves the TDSE in cylindrical coordinates for H_2^+ irradiated with a linearly polarised laser pulse with the polarisation direction parallel to the internuclear axis. The second code, RHYthMIC (vibRating HYdrogen Molecular Ion in Cartesians) implements the solution of the TDSE in Cartesian coordinates, allowing arbitrarily orientations between the laser polarisation direction and the internuclear axis. The codes treat electron dynamics in 2D (THeREMIN) and 3D (RHYthMIC), while nuclear dynamics are treated in 1D. Both codes are written to exploit massively parallel supercomputers. In addition, a parallel library for calculating photoelectron spectra using three different methods has also been developed. The methods implemented in the library are the Fourier transform of the spatial wavefunction into momentum space, the sampling point method and the time dependent surface flux (t-SURFF) method. The library has been written to be as portable as possible and can be interfaced straightforwardly with other codes that are used for modelling laser-matter interactions, such as the codes developed in this thesis, or other codes that solve the Kohn-Sham equations of time dependent density functional theory (TDDFT).

This thesis is arranged as follows. In Chapter 1 an overview of the progress of laser technology over the last several decades is given, allowing the development of intense ultrashort

laser pulses. Also included in this chapter, the fundamental processes in strong field physics are presented, and recent experiments and theoretical approaches on ultrafast molecular science, such as ultrafast charge migration, are described at the end of the chapter. In Chapter 2 we introduce the theoretical treatment for describing the H_2^+ when irradiated with intense laser pulses. A Lagrangian formalism and the use of generalised curvilinear coordinates are emphasised. Chapter 3 then gives the details of the numerical implementation of our laser-driven H_2^+ model, which accurately describes electronic and ionic degrees of freedom quantum mechanically. The implementation uses finite-difference grid techniques, where the Taylor series and Arnoldi methods are both employed for efficient time propagation of the wavefunction. The parallelisation scheme is described at the end of the chapter.

Chapter 4 is dedicated to the study of the role of the different vibrational states in strong-field ionisation, dissociation and high harmonic generation of H_2^+ exposed to intense laser fields. First we discuss the accuracy of our numerical implementation by solving the time-independent Schrödinger equation for the hydrogen molecular ion. The lowest vibrational energies obtained are then compared with available results in the literature. Results for dissociative ionisation of H_2^+ by VUV and IR laser pulses, starting from different vibrational states are then presented. We focus on the visual analysis of the resulting wavefunction after the interaction with the laser pulse and show how we can extract information about ionisation and dissociation by dividing configuration space into distinct regions. In the case of H_2^+ interacting with an IR laser pulse, high harmonic spectra and a time-frequency analysis are also presented, where the study of the contributions from different vibrational states is emphasised.

Chapter 5 and 6 are dedicated to the calculation of the photoelectron spectra of the H_2^+ resulting from the interaction with VUV and IR laser pulses. In Chapter 5 we present three methods to extract scattering information from the solution of the time-dependent Schrödinger equation, namely the Fourier method, the sampling point method and the t-SURFF method. Details on the numerical implementation of the methods are given, focusing on their use in massively parallel supercomputers. We also show how to efficiently calculate the interpolation of the wavefunction onto spherical surfaces required for the sampling point and the t-SURFF methods in order to minimise the additional overhead during time propagation of the wavefunction. In Chapter 6 photoelectron spectra of fixed-nuclei H_2^+ obtained with the methods introduced in Chapter 5 are presented. We explore the dependence that different parameters have on the PES by irradiating H_2^+ with a VUV laser pulse in 2D and 3D calculations. The influence of long range potentials on the resulting PES is particularly relevant in our study, where we show how the accuracy of the spectra can be increased by truncating the Coulomb potential. Angularly resolved photoelectron spectrum for H_2^+ exposed to intense IR laser pulses for a range of internuclear distances are finally presented. In particular, two-centre interferences in the PES are discussed at the end of the chapter.

In this thesis we make a special emphasis on the visualisation of the molecular wavefunction. To this end, a CD-ROM containing animations of the time-dependent wavefunction is

provided. All the animations are in MPEG-4 format, and further details can be found in the text itself.

Throughout this thesis atomic units will be used, unless otherwise states.

The enormous energy of the twentieth century, enough to drive the planet into a new orbit around a happier star, was being expended to maintain this immense motionless pause.

J. G. Ballard, Crash

1

Overview of strong-field physics and strong laser-matter interaction small molecules

After spectacular progress over the last decade, attoscience is now a well-established field in its own right. A wide variety of laser sources are readily available in national facilities (using free-electron lasers) or as table-top devices (using Ti:Sa laser technology). These sources can easily produce ultra-short laser pulses with durations in the femtosecond ($1 \text{ fs} = 10^{-15} \text{ s}$) and attosecond ($1 \text{ as} = 10^{-18} \text{ s}$) regimes. The availability of ultrafast pulses is crucial to study electron dynamics in matter. If we consider that the period of an electron in the ground state of the hydrogen atom is approximately 150 attoseconds (using Bohr's semiclassical model of the atom), this indicates that in order to time-resolve electronic processes in atoms and molecules we require shorter duration light sources to capture the dynamics.

This is precisely the principle of photography and cinema: by using fast mechanical shutter speeds it is possible to obtain still images of an object from recording the light reflected from it. If the shutter speed is not fast enough to resolve the moving object, the image will appear blurred. The introduction of spark photography, developed in the 19th century by Töpler during his pioneering work on recording sound waves in the millisecond domain [1], opened the way to ultrafast photography. In the 1870's, Eadweard Muybridge, answered what at that time was an open question: during a gallop, do horses lift all four hooves off the ground? The event is too fast to be observed with the human eye, so Muybridge prepared several cameras to capture a series of still images at different instants during the gallop [2]. The resulting sequence of frames is shown in figure 1.1, where it can be seen that the horse does indeed lift all four hooves off the ground. A major advance in fast photography was made by Harold Egerton in the 1930's, who used stroboscopic light to capture phenomena too fast for mechan-

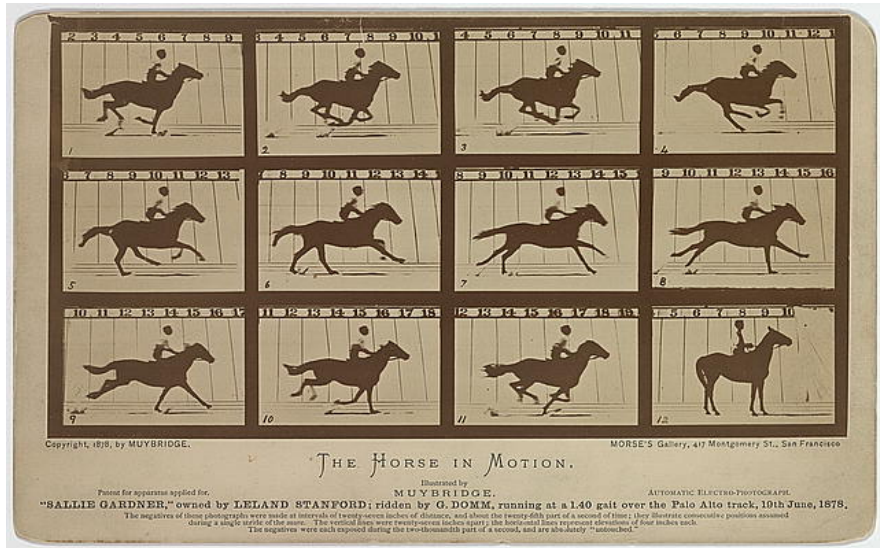


Figure 1.1: The horse in motion. "Sallie Gardner," owned by Leland Stanford; running at a 1:40 gait over the Palo Alto track, 19th June 1878. Eadweard Muybridge. Library of Congress Prints and Photographs Division [8]

ical shutters. With this technique, Edgerton was able to photograph events on the microsecond timescale [3, 4], such as the splash of a milk drop [5], a bullet cutting a playing card [6], or the famous bullet through apple [7], as shown in figure 1.2. The work of Edgerton showed that in order to time-resolve fast processes, shorter light flashes are needed.

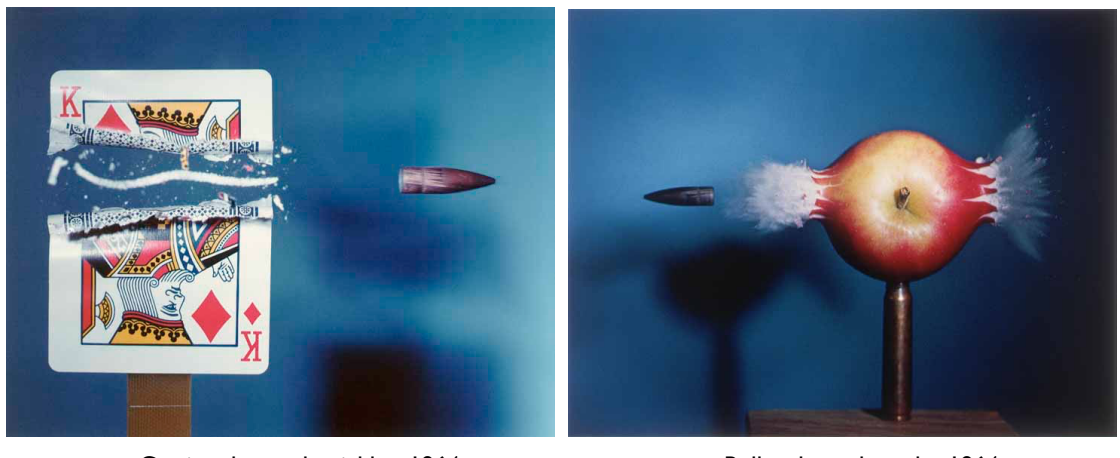


Figure 1.2: (a) Cutting the card quickly (1964) [6] and (b) Bullet through apple (1964) [7].

Images from Edgerton Digital Collections: 'Doc' Edgerton, Visionary Engineer: <http://edgerton-digital-collections.org/>. Copyright 2010 MIT. Courtesy of MIT Museum.

With the invention of the laser, the study of ultrafast phenomena entered a new era. In the 1980's, the development of lasers capable of delivering pulses in the femtosecond regime paved the way for a new branch of chemistry called femtochemistry. With femtosecond laser pulses it is possible to resolve ionic dynamics in molecules, thus helping to understand how chemical reactions occur. Examples of femtochemistry include studies on the dynamics of

bond dissociation [9], charge transfer in molecular reactions [10], and bond exchange in dissociative reactions [11]. These works were recognised with the Nobel prize in chemistry for Ahmed H. Zewail in 1999 [9].

Currently, attoscience is extending the study of dynamics in matter from ionic dynamics to electron dynamics. This has involved the development of a range of techniques such as self-induced electron diffraction [12–14] and high harmonic spectroscopy [15, 16]. It is clear that after being dedicated to the study of one- and two-electron systems, attoscience now faces new challenges in extending and developing techniques to explore multi-electron dynamics in complex atoms and molecules. Attoscience can deepen our understanding of chemical processes and the conversion between light and energy. Some of the goals that are achievable include bioenergetics, efficiency improvements in solar cells [17, 18], cancer treatments, and the study of DNA damage after irradiation [19, 20]. In order to study ultrafast correlated electron-ion dynamics, the hydrogen molecular ion, the most simple molecule in nature, serves as a basic platform to understand more complex many-body dynamics.

The goal of this chapter is to present an introduction to strong field phenomena, focusing in attosecond science applied to molecules. The chapter is divided in three sections, arranged as follows. Section 1.1 gives a brief review of the development of lasers in the last sixty years. In Section 1.2 the fundamental concepts of Strong-Field Physics are presented. Finally, in Section 1.3 we discuss the advances in attosecond chemistry, with a comment on the correlated electron-ion dynamics in H_2^+ irradiated by ultrafast laser pulses.

1.1 The development of laser technology

The word laser (Light Amplification by Stimulated Emission of Radiation) was coined in 1959 by Gordon Gould [21, 22]. A few years later, Charles Townes and Arthur Schawlow built the first maser (Microwave amplification by stimulated emission of Radiation) [23] while Nikolai Basov and Alexander Prokhorov proposed a maser based on the ammonia molecule [24, 25]. Actually, Townes and Schalow at that time preferred the term “optical maser”, understanding that the maser was the basic device [21].

The first laser was build by Theodor Maiman in 1960 [26]. It was a Ruby laser, with an active medium made of corundum (an oxide of aluminium) containing chromium impurities, and it could emit visible light at wavelengths between 693 and 700 nm (corresponding to the deep red part of the spectrum). Population inversion was achieved by electric discharge from a flash lamp that pumped a ruby rod placed between two mirrors with high reflectivity, creating a Fabry-Pérot cavity. Ruby fluorescence produces light, causing stimulated emission. The key aspect of stimulated emission is that the resulting light has the same characteristics (frequency, direction, polarisation and phase) of the incident one, obtaining amplified radiation that preserves coherence in space and time. Characteristics like monochromaticity and directionality make the laser very different from the rest of light sources (the sun, light bulbs, fluorescence lamps, etc).

Two of the main challenges since the invention of the laser were to produce shorter duration pulses and to produce higher intensities. these two aspects have developed simultaneously.

1.1.1 Laser amplification

Since the invention of the laser there have been three milestones in amplification, which are related with the decreasing duration of pulses: Q-switching, mode-locking and chirped-pulse amplification (CPA) [27]. In Figure 1.3 we can see the evolution of laser intensity over the last 50 years, while in figure 1.4 we can observe the analogous evolution of laser pulse durations.

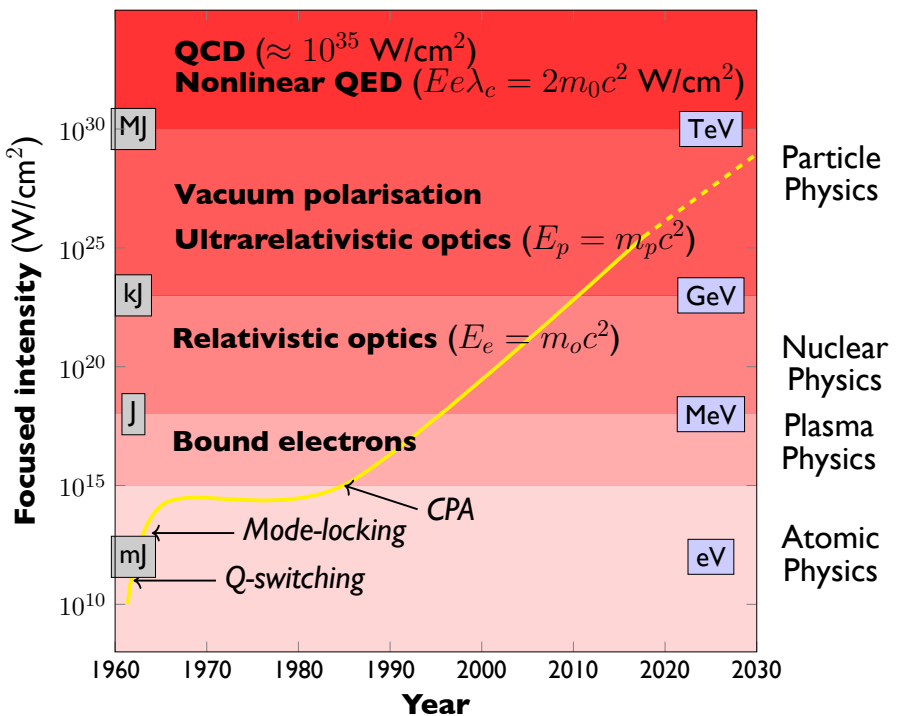


Figure 1.3: Diagram showing the evolution of laser focused intensity over the years since the invention of lasers. The dashed line correspond to the actual predictions about the next future. Adapted from Mourou *et al.* [28].

The first major milestone was the Q-switched oscillator. In Q-switching, Q refers to the resonator quality factor. The idea is to produce amplification by introducing a modulator absorber inside the resonant cavity [30, 31]. When the absorber is switched on, the cavity has high losses (Q is low). Because the pump continues at constant power at all times, the atoms in the cavity accumulate population inversion. When the absorber is switched off, cavity losses decrease (Q is high), and the energy from the large population inversion accumulated is released, generating a short pulse of nanosecond duration and with a power of about one Megawatt.

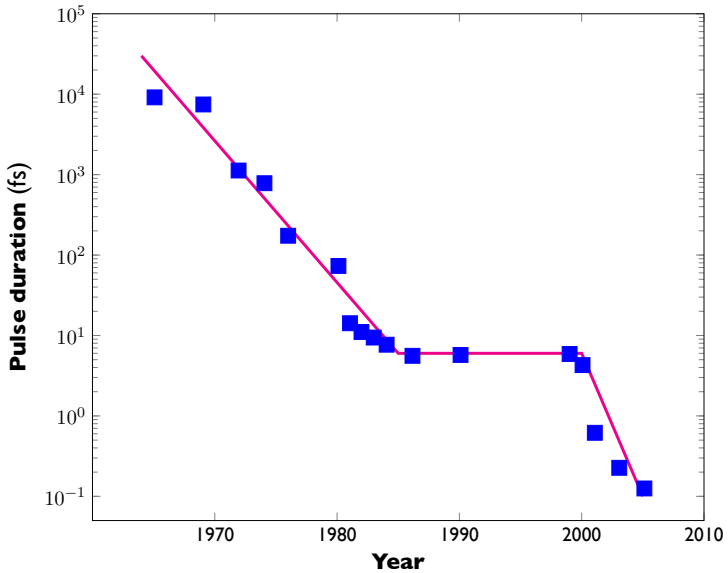


Figure 1.4: Diagram showing the evolution of laser pulse durations over the years since the invention of lasers. Adapted from Corkum and Krausz [29].

A few years after the introduction of Q-switching, attention turned to mode-locking techniques. In mode-locking, amplification is achieved by inducing a coupling between the different modes of a laser and by locking the phases [30, 31]. Consider the longitudinal modes of a Fabry-Pérot cavity. The light oscillates inside the cavity at frequencies that are separated by the intermodal spacing $\nu_F = c/2d$, where c is the speed of light and d is the length of the cavity. Then, by an external mechanism, the phases of the different components are locked. The modes behave like the components of a Fourier series of a periodic function in time, with period $T = 1/\nu_F$, generating a pulse train. The locking between modes can be obtained by passive mode-locking or active mode-locking, by introducing a passive modulator (a switch), or an active modulator. With this technique it is possible to achieve pulses in the femtosecond domain.

In order to achieve high laser intensities, energies of the order of several millijoules (or even several joules) are required. Basically the route to inject more energy is to add an amplification stage after the oscillator. The amplifier has an active medium and delivers laser pulses when it is pumped by the oscillator to cause stimulated emission.

An important characteristic of the amplification medium is the saturation fluence, which is the maximum energy per unit surface that can be extracted from the active medium [32]. The media usually employed in amplification include gases, dyes and solid state media [27]. Gases and dyes have large cross-sections that saturate easily, reaching fluences of about 1 mJ. Solid states media, such as Ti:Sapphire (760 nm), Nd:Glass (1053 nm) and Nd:YAG (1064 nm) are capable of deliver pulses with fluences of 1 J/cm^2 . However, with such large energies it is easy to exceed the damage threshold of the medium, which is an intrinsic property of the material. One route to work under the damage threshold is to enlarge the transversal section of the medium, i.e. building expensive amplification crystals with large diameters (up to the

metre length scale) [33].

The other route, feasible in table-top setups, is not to stretch the pulse in space (transversally), but in time. This is the key idea of Chirped-Pulse Amplification (CPA) technique, proposed by Strickland and Mourou [34].

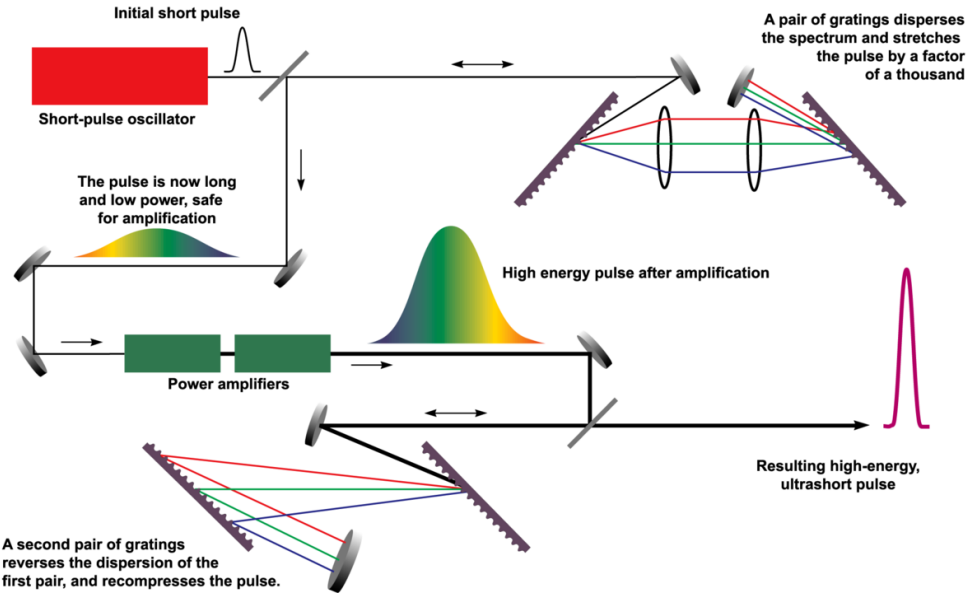


Figure 1.5: Diagram of the chirp pulse amplification technique. An initial ultrashort pulse, in the upper left corner of the figure, is positively chirped when passing through a dispersive medium (stretcher), elongating in time the duration of the pulse. After that, when the peak intensity of the pulse has decreased by several orders of magnitude, the pulse is safely amplified by passing through a gain medium. Finally, the pulse is compressed in time when passing through a dispersive medium (compressors), which negatively chirps the pulse. The resulting pulse is a high-energy, ultrashort laser pulse. Figure reproduced from Wikipedia [35], and adapted from Ref. [36]

Figure 1.5 illustrates the CPA technique, where a short duration laser pulse is stretch in time using a dispersive device, such a pair of diffraction gratings [34] or dispersive mirrors [37]. The dispersive system introduces a chirp in the pulse, making the low frequencies travel a shorter optical path than the higher frequencies. After that, the chirped pulse is reduced in intensity (usually lower than the GW/cm^2) and can be amplified when it passes through the active medium. Later, the pulse is compressed by another dispersive system which unchirps the pulse with the inverse process that took place in the first stage, when the pulse was stretched. The intensity of the output pulse can easily reach $10^{18} \text{ W}/\text{cm}^2$ [27].

It has been demonstrated that with CPA and Optical Parametric CPA (OPCPA) techniques it is possible to produce pulses with intensities in the range $10^{15} - 10^{22} \text{ W}/\text{cm}^2$ [28]. Further improvements on pulse compression, such thin film compression and the λ^3 regime are required to inject an energy of the order of kilojoules to pulses of only 10 fs of duration [28], allowing peak intensities of $10^{25} \text{ W}/\text{cm}^2$ [38]. At the moment, the first exawatt-class (10^{18} W) laser is under construction in ELI (European Light Infrastructure,), where it will be possible

to produce sub-attosecond pulses with these enormous intensities. This new class of laser will pave the way to explore different areas of physics in the time domain. These areas include nuclear physics, particle physics, and even non-linear Quantum Electrodynamics (QED) by reaching the Schwinger limit (10^{29} W/cm²), where the electromagnetic field becomes non-linear and production of electron-positron pairs from the vacuum can arise [28].

1.1.2 Free-Electron Lasers (FEL)

Free-electron lasers (FEL's) are another open route to achieve coherent radiation from a wide range of photon energies at high intensities. Free-electron lasers produce coherent radiation from the acceleration of a relativistic electron beam that is injected into a periodically alternating magnetic field, called an undulator. Population inversion is achieved from the alternating positive and negative acceleration that the electron beam experiences when passing through the undulator, and the coherence is given by the phase between the electron beam and the emitted electromagnetic wave. Hence, the main difference with respect to conventional lasers in that radiative transitions in FEL's do not come from transitions between bound states of an atom or molecule but from the acceleration of charged particles. Therefore, the central frequency of the pulse can be controlled by modifying the group velocity of the electron bunch. This characteristic allows FELs to be highly tunable, covering a wide range of photon energies, even reaching the water window at high intensity and brightness (this is crucial for investigating biological samples) [39].

The first two FEL's were built in the 1970s by Madley and co-workers [40–42]. They were able to amplify radiation from a CO₂ laser at wavelengths of 10.6 μm and 3.4 μm, using 24 MeV and 43 MeV electron beams respectively, delivered from the linac accelerator, at Stanford. Current FELs focus on producing x-rays (x-ray FEL), where the amplification comes from the self-amplified spontaneous emission (SASE) effect. The first SASE x-ray FEL was proposed by Pellegrini in 1992, using the linear accelerator at the SLAC National laboratory [42]. This project produced the LCLS (Linear Coherent Light Source), where it was possible to produce laser pulses at a wavelength of 1.5 Å with a peak power of tens of GW and time durations in the range 1-100 fs [43]. Although the pulses are spatially coherent, much work is required to improve the longitudinal coherence of the beam to get nearly transform limited pulses. Three other soft x-ray FELs are in operation: FLASH at DESY (Deutsches Elektronen Synchrotron) and the recently inaugurated XFEL (the European x-ray Free-Electron Laser,) in Hamburg (Germany) and Fermi at the Sincrotrone Trieste in Italy. In addition, several x-ray FEL's are currently under construction: SACLAC (Spring-8 Angstrom Compact free electron LASer) in Hyogo (Japan), PAL-XFEL (Pohang Laboratory Accelerator) in Pohang (Korea), SwissFEL in Würenlingen (Switzerland).

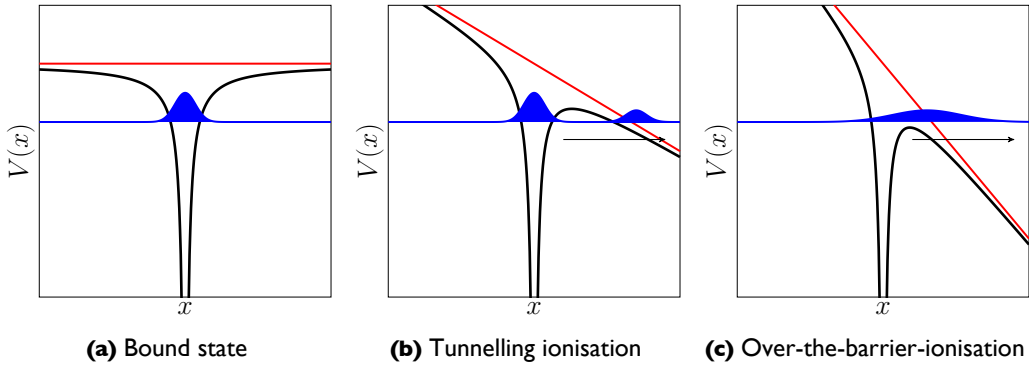


Figure 1.6: Schematic representation showing the evolution of an atomic wavepacket in a potential interacting with an intense laser field. The intensity of the laser field is increased from (a) in the absence of electric field the atomic wavepacket remains in the bound state, to (b) the tunnelling ionisation regime, to (c) the over-the-barrier-ionisation regime.

1.2 Strong-field physics

Whenever an electromagnetic field interacts with an atom or molecule, electrons can be excited and also ionised. It is said that the interaction is nonlinear when more than one photon is absorbed by the system. This situation can be expressed as $N\hbar\omega_L < I_p$, where N is the number of photons absorbed, ω_L is the frequency of the incident radiation and I_p is the ionisation potential of the quantum system, and implies that the photon energy is lower than the energy required to pull out an electron. Multiphoton processes were first discussed by Maria Göppert-Mayer in 1931 when studying two-photon absorption [44]. The uncertainty principle allows multiphoton transitions from an initial to a final state passing through multiple virtual states, if the relation $\Delta E \Delta t \geq \hbar$ is fulfilled, where Δt is the time over which that the transition takes place and ΔE is the energy difference between states. After the invention of Q-switching, the first experiments on ionisation of air (with an ionisation potential around 10 eV) using a Ruby laser (whose photon energy is around 2 eV) at intensities around 10^{13} W/cm^2 showed an ionisation rate that depends exponentially on the intensity and not a power law as predicted by perturbation theory [45], indicating the breakdown of perturbation theory.

Usually strong field physics refers to a variety of phenomena that arise in laser-matter interactions at laser intensities around 10^{14} W/cm^2 , where it is known that perturbation theory breaks down. In the following we review some of the processes that occur in fundamental strong field physics. More detailed discussions on the field can be found in references [32, 46, 47].

1.2.1 Tunnelling ionisation

The soviet physicist L.V. Keldysh proposed a rather different mechanism for ionisation, named tunnel ionisation [48]. Assuming that the frequency of the laser field ω is low enough so it can be considered to be a dc field, then at sufficiently high laser intensities the potential barrier formed by the Coulomb potential and the dipole interaction can be distorted so that the prob-

ability of a bound electron tunnelling through the barrier is significant: see figure 1.6. Indeed, if the laser intensity increases further, the barrier is distorted so much that it lies below the energy of the bound state, and so the electron wavepacket is free to escape. This results in either over-the-barrier ionisation (OTBI) or barrier suppression ionisation (BSI).

The tunnelling time, the time taken by the electron to tunnel through the barrier, can be estimated if we consider the bound electron initially at $x_0 = 0$ with a bound energy ϵ_0 [49]. The distorted potential barrier intersects the energy level of the electron when $\epsilon_0 = -E_0 x$, where E_0 is the amplitude of the electric field. Hence, the distance at which the electron exits the barrier is

$$x_0 = \frac{|\epsilon_0|}{E_0}. \quad (1.1)$$

If we assume constant velocity while the electron escapes the potential barrier, $v_0 = \sqrt{2m\epsilon_0}$, where m is the electron's mass, the tunnelling time is

$$\tau_t = \frac{x_0}{v_0} = \frac{1}{E_0} \sqrt{\frac{I_p}{2m}}. \quad (1.2)$$

where we have used $I_p = |\epsilon_0|$, I_p being the ionisation potential.

After ionisation, the influence of the Coulomb potential, and also the magnetic field is neglected, and we consider the ejected electron wavepacket governed only by the electric field

$$E(t) = E_0 \sin(\omega_L t) \quad (1.3)$$

where ω_L is the frequency of the laser field and E_0 is the amplitude of the laser field. In this situation, from classical mechanics, the drift velocity of the electron in the electric field

$$v = \frac{E_0}{m\omega_L} (\cos \omega_L t_0 - \cos \omega_L t) \quad (1.4)$$

where m is the mass of the electron and t_0 is the time at which the electron was ionised. Thus, the electron's cycle-average kinetic energy

$$U_p = \langle \frac{1}{2}mv^2 \rangle = \frac{e^2 E^2}{4m\omega_L^2} \quad (1.5)$$

is usually called the ponderomotive energy, and it is one of the fundamental quantities in strong field physics.

Moreover, it can be shown that the transition in the ionisation rate from a power law to a exponential law is given by the Keldysh adiabaticity parameter, which is the ratio between the laser frequency ω_L , and the tunnelling frequency $\omega_t = 2\pi/\tau_t$

$$\gamma = \frac{\omega_L}{\omega_t} = \sqrt{\frac{I_p}{2U_p}}. \quad (1.6)$$

In the limit of low laser frequencies and high intensities, when tunnelling ionisation dominates, the Keldysh parameter satisfies $\gamma \ll 1$. The ionisation rate, given by

$$W_t \propto \exp\left(-\frac{2\gamma}{3\omega_L}\right), \quad (1.7)$$

is similar to the tunnelling formula [48].

Eq. (1.6) also suggest tunnelling ionisation is most probable when the electric field is a maximum, therefore ionisation occurs near the peaks of the electric field, twice per optical cycle. We can also express the Keldysh parameter as a function of the tunnelling time and the period of a laser cycle, T , i.e.

$$\gamma \approx 4\pi \frac{|\tau_t|}{T}. \quad (1.8)$$

Eq. (1.8) indicates that the lower the laser frequency the larger the probability of an electron escaping because the barrier is distorted for longer, giving the electron more time to tunnel through.

1.2.2 Over-the-barrier ionisation

At intensities higher than 10^{14} W/cm^2 the ionisation mechanism reaches the over-the-barrier regime, where the barrier is distorted so far by the electric field that the electron is no longer bound and it is free to escape. However, counter-intuitively, in this regime ionisation can be suppressed by two different mechanism: dynamic stabilisation and adiabatic stabilisation.

- In dynamic stabilisation, a quantum destructive interference in the ionisation probability is caused by close-lying bound states. Indeed, numerical simulations [50] showed that if bound states with the same parity are spaced less than the laser bandwidth apart, a destructive interference in the ionisation probability amplitude can be created at intensities around 10^{14} W/cm^2 . This effect has been observed in Rydberg atoms [51, 52].
- In addition, stabilisation can be achieved at very high intensities (10^{17} W/cm^2) and high frequencies, where the oscillating electron quiver motion is faster than the electron motion within the atomic potential. In this scenario, the coupling between the electron and the nucleus becomes weak, because the electron wavepacket can not adiabatically adjust with the laser field, a mechanism called adiabatic stabilisation [53]. This effect has been observed for high-lying Rydberg states [54], requiring ultra-intense laser pulses with a ramp-on of less than one cycle.

1.2.3 Multi-photon ionisation

If we now consider weak, high-frequency laser fields, the ponderomotive energy is smaller than the ionisation potential. This regime corresponds to a Keldysh parameter $\gamma \gg 1$, where multiphoton ionisation (MPI) dominates.

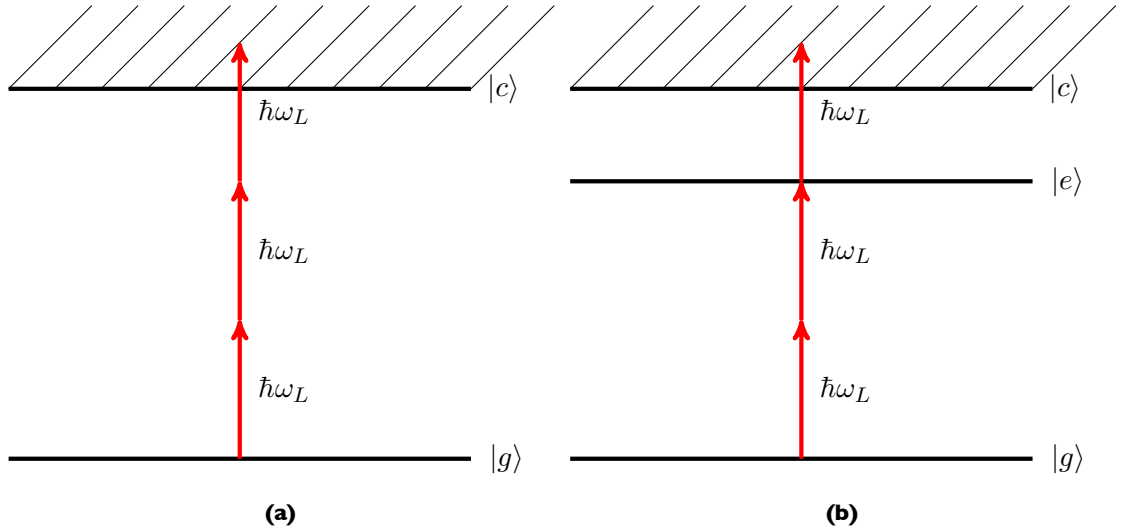


Figure 1.7: Schematic diagram of (a) a 3-photon MPI process, and (b) a (2+1) REMPI process, where $|g\rangle$ denotes the ground state, $|e\rangle$ an excited state and $|c\rangle$ the continuum.

In the multiphoton ionisation regime the photon energy of the laser field is smaller than the ionisation potential of the system. Thus, ionisation occurs after one or more electrons absorb several photons from the field so

$$n\omega_L \geq I_p \quad (1.9)$$

where n is the minimum number of photons required for the inequality to hold. This process is illustrated in figure 1.7a, where three photons are required for ionisation. Voronov and Delone observed a six-photon ionisation process when irradiated xenon atoms, whose ionisation potential is 12.27 eV with a Q-switched Rubi laser, whose photon energy is 2.34 eV [55]. In the MPI regime, lowest order perturbation theory (LOPT) can be used to obtain an ionisation rate which follows a power law [56]

$$W_{\text{MPI}}^{(n)} = \sigma_n I_0^n \quad (1.10)$$

where σ_n is the generalised n -photon cross-section and I_0 is the peak intensity of the laser field, given by

$$I_0 = \frac{c}{8\pi} |E_0|^2 \quad (1.11)$$

with c the speed of light.

The number of photons required for ionisation can be modified at very high laser intensities, because the electric field can shift the energy levels of an atom. This effect is known as the ac-Stark shift. In particular, the energy of weakly bound states, i.e. Rydberg states, are shifted by approximately the ponderomotive energy of the laser field, increasing the ionisation potential of the atom, as is shown in figure 1.8.

Furthermore, when the photon energy is such that there is a resonance with an excited state, the ionisation process is said to be resonantly enhanced, and resonantly enhanced mul-

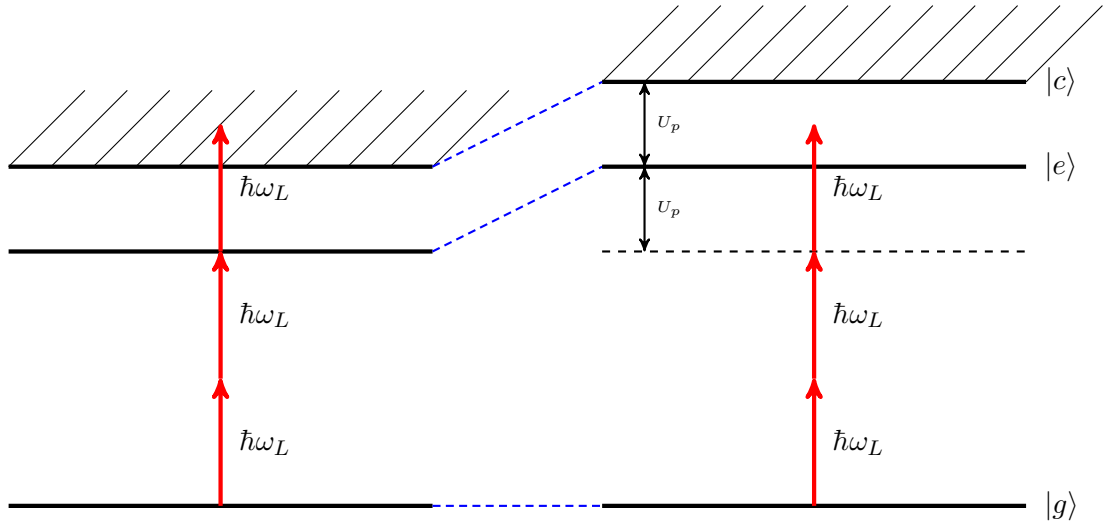


Figure 1.8: Diagram of the energy levels shift caused by the AC-stark effect, where $|g\rangle$ denotes the ground state, $|e\rangle$ an excited state and $|c\rangle$ the continuum. Only the high lying levels, that are weakly bound to the core, are shifted by the electric field by an energy equal the ponderomotive energy of the laser field, U_p . In this case, the state $|e\rangle$ also experiences a change in energy, suppressing the resonance with this state.

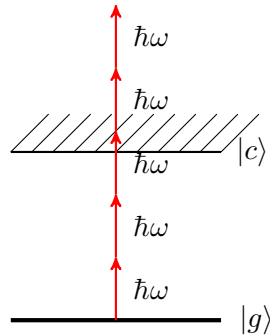


Figure 1.9: Schematic diagram of an ATI process, where $|g\rangle$ denotes the ground state and $|c\rangle$ the continuum. In the diagram only 3 photons are required for ionisation, but 5 photons were absorbed.

triphoton ionisation (REMPI) occurs [57], as shown in figure 1.7b. If n photons are required to ionise the system and m photons to excite the intermediate resonant state, the REMPI process is labelled as a $(m + p)$ process, where $p = n - m$. REMPI can also be affected by high intensities, when the ac-Stark shifts plays a role in modifying the energy levels of an atom. This can result in intermediate excited states that are no longer resonant at the photon energy of the incident radiation [58], as is shown in figure 1.8.

1.2.4 Above Threshold Ionisation (ATI)

After multiphoton ionisation, one can think in a situation in which the atom absorbs more than the minimum number of photons required for ionisation. This is precisely the case of above threshold ionisation (ATI), a name given by Karule [59]. This process was first studied in ionisation of xenon by Agostini et al. [60], when the photoelectron energy of electrons was measured instead of the kinetic energy released of ions. The photon energy of the incident laser field was such that only absorption of six photons is required to achieve ionisation.

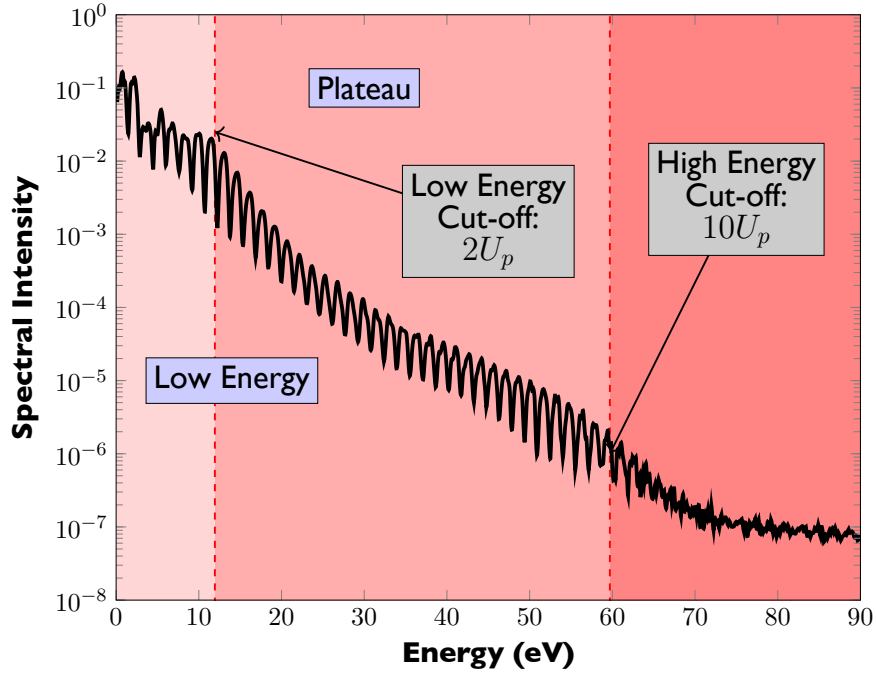


Figure 1.10: ATI spectrum of the hydrogen atom after interaction with a 10-cycle laser pulse having a wavelength of $\lambda = 800$ nm (corresponding a photon energy of $\omega_L = 0.058$ Ha), and a peak intensity of $I = 10^{10}$ W/cm². At this laser intensity, the ponderomotive energy is $U_p = 5.97$ eV. The spectra presents a low energy region, which extends up to an energy equal to $2U_p$, followed by a plateau, which extends up to $10U_p$.

However, a peak in the spectra corresponding to absorption of one more photon was found.

In figure 1.9, we illustrate the case the ionisation of five photons, where only three photons are required for ionisation. Indeed, as the laser intensity increases, more photons are absorbed from the field. For low intensities, perturbation theory still applies and the ionisation rate can be generalised as [56, 61]

$$W_{n+s} \propto I^{n+s} \quad (1.12)$$

where n is the number of photons needed to ionise the atom, and s the excess number of absorbed photons.

Although ATI spectra were initially interpreted using perturbation theory, soon after the first non-perturbative studies began to appear [62, 63], followed by the Simpleman's theory [64], which gives an intuitive picture of strong field ionisation in terms of classical mechanics and tunnelling ionisation. In particular, ATI spectrum can be interpreted using Simpleman's theory [65, 66] as follows: the spectrum presents a region of low energy electrons with a first cut-off at an energy of $2U_p$, followed by a plateau that extends from an energy of $2U_p$ to an energy of $10U_p$. The $2U_p$ cut-off energy can be explained classically by integrating Newton's equation for a charged particle in an electric field

$$\frac{d^2x}{dt^2} = E_0 \sin \omega_L t, \quad (1.13)$$

where x is the position of the electron, $E_0 \sin \omega_L t$ is the electric field of the laser pulse, defined in Eq.(1.3), and we have assumed that the mass and the electric charge of the electron is equal to one. Since the laser field is linearly polarised, we assume the motion of the electron only along the polarisation direction. Assuming that the electron tunnels out with no velocity near to the parent ion, the initial conditions will be $t_0 = 0$, $v = 0$ and $x = 0$, which yields

$$\frac{dx}{dt} = \frac{E_0}{\omega_L} (1 - \cos \omega_L t). \quad (1.14)$$

which is equivalent to Eq. (1.4). From Eq. (1.14), the corresponding electron's kinetic energy

$$K(t) = 2U_p(1 - \cos \omega_L t)^2. \quad (1.15)$$

From Eq. (1.15), electrons released when the laser pulse has zero field, i.e. $\omega_L t_0 = 0$, have a maximum kinetic energy of $2U_p$. Hence, the energy cut-off at $2U_p$ is due to electrons ionised by the field, called direct electrons. The plateau, which extends from $2U_p$ to $10U_p$ is explained if we consider the electrons that scatter back from the core at time $t_1(t_0)$, whose kinetic energy is

$$K(t_0) = 2U_p (2 \cos \omega_L t_1(t_0) - \cos \omega_L t_0)^2. \quad (1.16)$$

Then, the high energy cut-off at $10U_p$ yields from the maximum kinetic energy of backscattered electrons given by Eq. 1.16. A typical ATI spectrum for the hydrogen atom is shown in figure 1.10, where we observe that the spectrum is formed by a series of peaks separated by the photon energy of the laser field.

1.2.5 High-Harmonic Generation (HHG)

High-order harmonic generation (HHG) is intimately related to ATI. By focusing an intense, low-frequency laser pulse into an atomic or molecular target, coherent radiation is emitted at multiples of the laser frequency to very high orders. An example of HHG spectrum is shown in figure 1.11. We observe, a low energy region up to an energy equal to I_p , the ionisation potential, which follows a perturbative law. The low energy region is followed by a plateau of constant spectral amplitude up to an exponential cut-off energy around $3U_p$. This spectrum can be easily explained by classical models (the rescattering model, by Schafer et al. [65], or the widely known three-step model by Corkum [67]) which extend Simpleman's theory to HHG.

Within these classical pictures, the electron is first tunnel ionised by an intense, long wavelength laser pulse, accelerates in the continuum and is then driven back to the atom or molecule by the laser field before finally recombining with the parent ion. This recombination releases a photon with an energy that is equal to the ionisation potential plus the energy gained by the electron in its excursion in the continuum. The picture is summarised in figure 1.12. HHG can therefore be seen as the inverse process of ATI: the electron absorbs many more photons than needed to ionise, but instead of leaving the ion or scattering from it, the electron recombines to its original state, with a probability amplitude that depends on the dipole moment of the

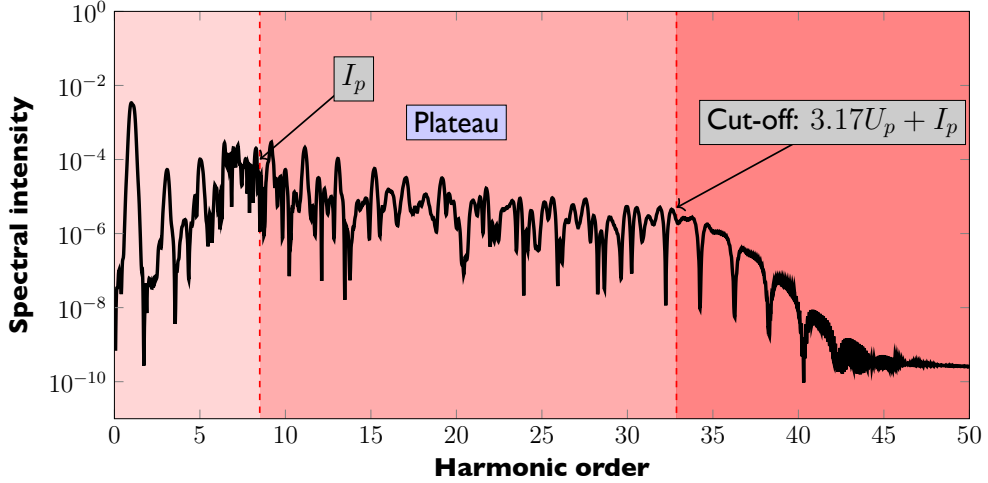


Figure 1.11: HHG spectrum of the hydrogen atom exposed to a 10-cycle laser pulse having a wavelength of $\lambda = 800$ nm (a photon energy of $\omega_L = 0.058$ Ha), and a peak intensity of $I = 2 \times 10^{14}$ W/cm². The ponderomotive energy is $U_p = 11.9$ eV. The peaks in the spectrum are placed at odd multiples of the frequency of the driving laser field. The spectrum is formed by a low energy region, composed by low order harmonics with an exponentially decreasing intensity. The low energy region extends up to a frequency equal the ionisation potential, I_p , and it constitutes the perturbative part of the spectrum. Following this region is the plateau region, in which harmonics presents similar intensities. The plateau ends at the cut-off frequency, which corresponds to a frequency of $3.17U_p + I_p$, where U_p is the ponderomotive energy of the laser field.

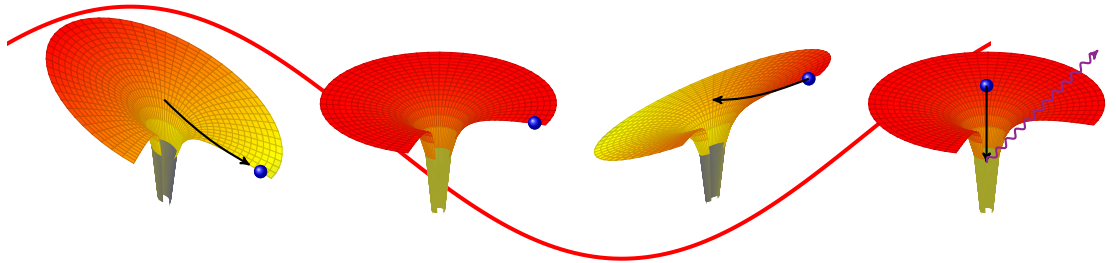


Figure 1.12: Representation of the three-step model for classical HHG. The electric field (red line), induces tunnel ionisation of the electron through the atom potential. The same field accelerates the electron, and then drives it back to the parent ion. When the electron recombines with the atom, a high energy photon is produced.

electron and the hole.

The sharp cut-off of the HHG spectrum at an energy of $3.17U_p$ can be obtained from the classical equation of motion Eq. (1.13) if we consider only those electron trajectories that return to the parent ion, at time $t_1(t_0)$, after tunnel ionisation at time t_0 . Equation. (1.16) yields a maximum return kinetic energy of $3.17U_p$, with an electron excursion time of $0.63T$, where T is the period of the laser pulse. This maximum return electron kinetic energy gives a maximum photon energy

$$\hbar\omega_{\max} = I_p + 3.17U_p \quad (1.17)$$

where U_p is the ponderomotive energy of the electron and I_p is the ionisation potential of the system. We also note that, from solving classical equations of motion, there are two possible trajectories which lead to the same return kinetic energy, named short and long trajectories af-

ter their respective electron excursion time [68]. In addition, in media which posses symmetry inversion, such as rare gases, only odd-order harmonics are generated, since harmonics produce from electrons recombining the ion from opposite directions have the same amplitude but opposite signs. Hence, odd-order harmonics interfere constructively while even-order harmonics interfere destructively [69].

After first experiments in late 80's using krypton-fluoride (with a driving laser wavelength of $\lambda = 248$ nm) [70] and neodymium-glass ($\lambda = 1064$ nm) [71], spectra with harmonic orders greater than the 109th were observed [72]. Since then, it was a continuous effort in extending the cut-off frequency to higher energies, which in a typical HHG experiment can range from tens of eV to 1 keV. Since $U_p \propto \lambda^2 I$, (which is known as the scaling law), and considering the cut-off law, Eq. (1.17), which is proportional of the ponderomotive energy, there are two routes to increase the cut-off frequency: either increasing the wavelength, λ , or increasing the intensity, I , of the incident laser field. However, the scaling law presents several limitations: Firstly, if we increase the intensity at some point the ionisation will reach the over the barrier regime, which does not follow the cut-off law in Eq. (1.17). Secondly, the efficiency in the production of the highest harmonics decrease dramatically with the wavelength [73, 74]. Lastly, phase matching effects plays a crucial role in the propagation and emission of high harmonic radiation.

1.2.6 Attosecond pulses

It was clear from the first experiments that HHG opened a new route to produce high-frequency coherent radiation in the sub-femtosecond domain [67, 75–77]. Indeed, high harmonic generation allows the production of XUV attosecond pulse trains by selecting a few harmonics from the high energy region of the spectrum. Developing an alternative method to produce ultrashort laser pulses in the VUV and even in the X-ray regime is especially interesting, since table-top laser technology based on stimulated emission from crystals has a limited spectral bandwidth, which limits the shortest pulse duration. For instance, Ti:Sa technology is only capable of delivering laser pulses in the femtosecond domain. The first train of attosecond pulses, each one of approximately of 250 attoseconds (as) of duration were observed by filtering five consecutive harmonics from a HHG spectrum in argon [78]. At the same time soft X-ray pulses with duration of 650 as were measured when filtering a few harmonics from the cut-off region [79].

The shortest attosecond pulses can be achieved if the filtered harmonics form a frequency comb with similar intensity and a constant relative phase. Thus, in the Fourier limit, the pulse duration is inversely proportional to the bandwidth of the selected harmonics. However, this optimal situation can not be reached since generated pulses have an intrinsic chirp, called the attochirp, which is due to different recollision times from different electron trajectories. Since lower harmonics are emitted before the higher, radiation emitted from short trajectories have a positive chirp while long trajectories imprint a negative chirp [80, 81].

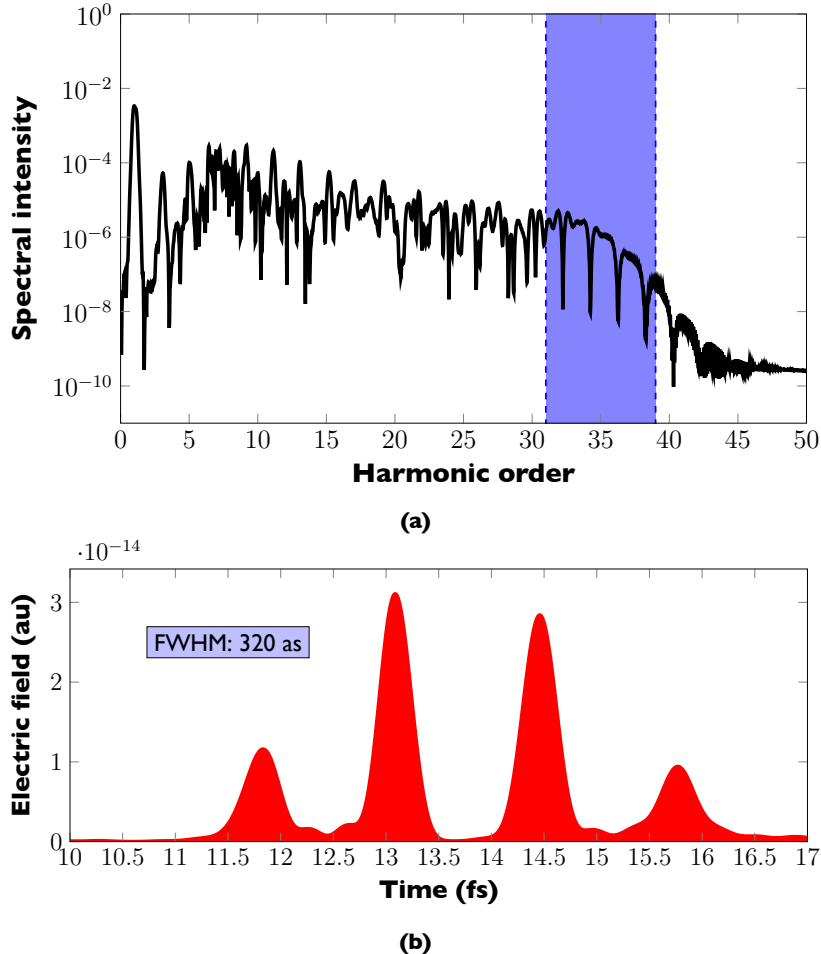


Figure 1.13: (a) HHG spectrum obtained after interaction of the hydrogen atom with a 10-cycle IR laser pulse, having a wavelength of 800 nm and a peak intensity of $I = 2 \times 10^{14} \text{ W/cm}^2$. (b) Train of four VUV laser pulses with a duration of 320 as at FWHM. The attosecond pulses have been obtained from the inverse Fourier transform of the HHG spectrum in (a), after filtering the high energy harmonics, from harmonic 31th to 39th with a rectangular window.

Since the first theoretical calculation of a resulting temporal profile extracted from a superposition of harmonics located in the plateau region [76], it was shown that there is a natural phase-matching between the highest harmonics [82]. This phase-locking arises from the correlation between the Gouy phase (the geometrical phase shift that acquires a Gaussian beam with respect to the focus along the propagation direction), and the change in the phase due to its dependence on the laser intensity distribution. [83]. These works showed the mechanism that allows for the production of coherent high-frequency radiation with sub-femtosecond duration [75]. The first evidence of attosecond dynamics was given in 2001 [78, 79]. Indeed, under optimal phase-matching conditions [84] it is possible to produce harmonics over the 5000th order, broadening the spectrum of laser frequencies from the vacuum ultraviolet to the soft x-ray regime [85].

In Figure 1.13 we present a HHG spectrum produced from hydrogen exposed to a 10-cycle

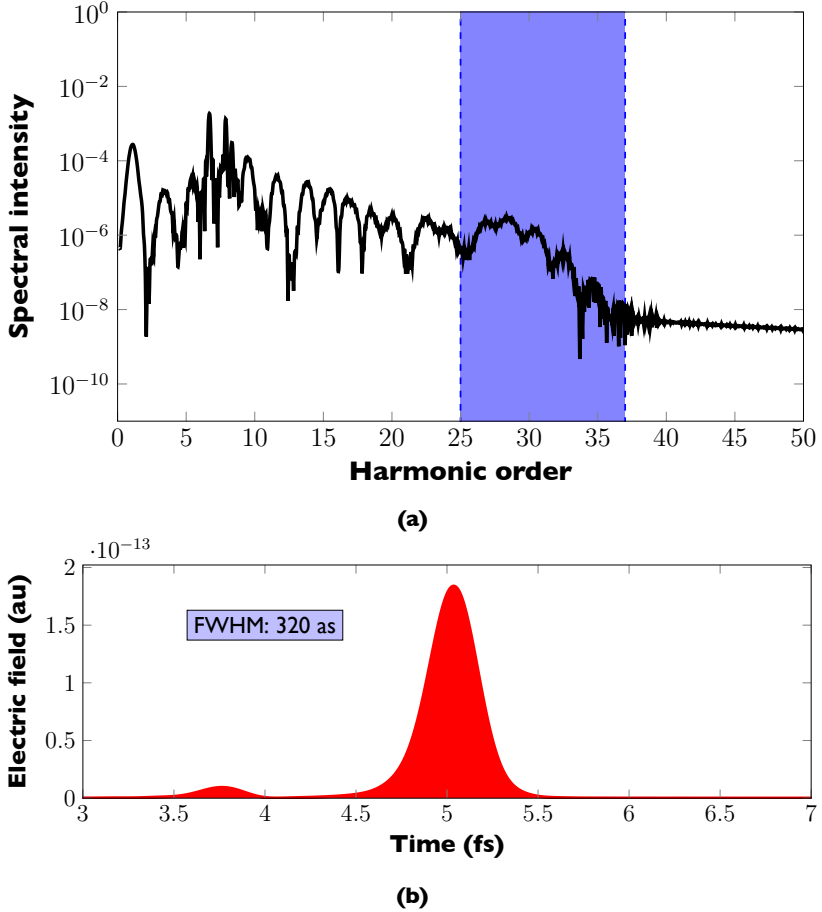


Figure 1.14: (a) HHG spectrum obtained after interaction of the hydrogen atom with a 6-cycle IR laser pulse, having a wavelength of 800 nm and a peak intensity of $I = 2 \times 10^{14} \text{ W/cm}^2$. (b) Isolated VUV laser pulse with a duration of 320 as at FWHM. The single-attosecond pulse have been obtained from the inverse Fourier transform of the HHG spectrum in (a), after filtering the high energy region of the spectrum, from harmonic 25th to 37th with a rectangular window.

laser pulse, having a wavelength of $\lambda = 800 \text{ nm}$ and a peak intensity of $I = 2 \times 10^{14} \text{ W/cm}^2$. VUV attosecond laser pulses can be produced if we filter the spectrum from harmonic 31th to harmonic 39th with a rectangular window, as indicated in Figure 1.13a, and perform an inverse Fourier transform. The resulting train of four pulses with a duration of roughly 320 as at FWHM can be found in Figure 1.13b, where each attosecond pulse is produced each half-cycle of the driving laser field. The presence of sidebands of the pulse is due to the fact that the spectral phase is not constant, and therefore the resulting pulses are not Fourier-limited.

After generating attosecond pulse trains, the next goal was to generate isolated attosecond pulses. One route to obtain an isolated attosecond pulse is to use a few-cycle laser pulse to produce harmonics in a single rescattering event [77, 79]. In Figure 1.14 we present the HHG spectrum obtained from the hydrogen atom interacting with a 6-cycle IR laser pulse, again having a wavelength of $\lambda = 800 \text{ nm}$ and a peak intensity of $I = 2 \times 10^{14} \text{ W/cm}^2$. The rectangular window filters the high energy region of the HHG spectrum, from harmonic 25th to harmonic 37th. The filtered spectral bandwidth contains the radiation produced in a

single rescattering event, at the third cycle of the driving laser field. The bandwidth of the resulting attosecond pulse depends again on the shape of the spectral phase. Other routes to obtain isolated pulses include the polarisation gate technique, in which the polarisation of a few cycle during pulse is modulated to confine a single rescattering event [86–88], and more recent techniques based on controlling electron motion in plasmas [89–91].

1.3 Molecular studies in attosecond science

Since the first train of attosecond pulses was produced in 2001 [78, 79] and the first isolated attosecond pulse were characterised in 2006 [88], a new route to explore and study electronic and nuclear motion on the attosecond timescale was opened. Electrons are related with the optical properties of materials and chemical reactions, because they are responsible for the formation of chemical bonds between atoms. Moreover, ionisation, dissociation, fragmentation, charge transfer and charge migration represents molecular phenomena in which electronic and nuclear dynamics interact on an equal footing. Studying electron-electron and electron-ion correlations are crucial to understanding and controlling molecules at the most fundamental level.

In addition, treating both electronic and ionic degrees of freedom on an equal footing represents a major theoretical and computational challenge. The equation which describes the dynamics of a molecule with M ions and N electrons is the time-dependent Schrödinger equation (TDSE)

$$i\frac{\partial\Psi(\mathbf{R}_1, \dots, \mathbf{R}_M, \mathbf{r}_1, \dots, \mathbf{r}_N, t)}{\partial t} = \mathcal{H}(t)\Psi(\mathbf{R}_1, \dots, \mathbf{R}_M, \mathbf{r}_1, \dots, \mathbf{r}_N, t) \quad (1.18)$$

where \mathbf{r}_i denotes the vector position of the electron i , and \mathbf{R}_j the vector position of the ion j , Ψ is the molecular wavefunction and \mathcal{H} is the Hamiltonian of the system. The molecular Hamiltonian $\mathcal{H}(t)$ can always be written as

$$\mathcal{H} = T_e + T_N + V, \quad (1.19)$$

where T_e corresponds to the electronic kinetic energy, T_N the nuclear kinetic energy, and V the total potential energy of the molecule, which, neglecting spin-dependent interactions, reads

$$V(\mathbf{R}_1, \dots, \mathbf{R}_M, \mathbf{r}_1, \dots, \mathbf{r}_N) = -\sum_{i,j} \frac{Z_j}{|\mathbf{r}_i - \mathbf{R}_j|} + \frac{1}{2} \sum_{i < k} \frac{1}{|\mathbf{r}_i - \mathbf{r}_k|} + \sum_{j < l} \frac{Z_j Z_l}{|\mathbf{R}_i - \mathbf{R}_l|} \quad (1.20)$$

where Z_j is the electric charge on the ion j . We see that the number of degrees of freedom in the wavefunction makes attempts to solve directly Eq. (1.18) prohibitively expensive. Instead of solving the TDSE, a common approximation used to describe molecular dynamics is the Born-Oppenheimer (BO) approximation [92]. The BO approximation considers that electronic and nuclear dynamics occur on different timescales, and so factorises the total molecular

wavefunction into an electronic wavefunction and a nuclear wavefunction

$$\Psi(\mathbf{R}_1, \dots, \mathbf{R}_M, \mathbf{r}_1, \dots, \mathbf{r}_N) = \sum_s \chi_s(\mathbf{R}_1, \dots, \mathbf{R}_M) \phi_s(\mathbf{R}_1, \dots, \mathbf{R}_M, \mathbf{r}_1, \dots, \mathbf{r}_N) \quad (1.21)$$

where Ψ is the total molecular wavefunction, ϕ_s the electronic wavefunction and χ_s the nuclear wavefunction, and s denotes the electronic state. It is possible to split the Hamiltonian (1.19) into electronic and nuclear parts, as

$$\mathcal{H} = \mathcal{H}_e + \mathcal{H}_N \quad (1.22)$$

where the electronic part

$$\mathcal{H}_e = T_e + V. \quad (1.23)$$

Consider the time-independent Schrödinger equation (TISE) for a molecule composed of N electrons and M ions is

$$\mathcal{H}\Psi(\mathbf{R}_1, \dots, \mathbf{R}_M, \mathbf{r}_1, \dots, \mathbf{r}_N) = E\Psi(\mathbf{R}_1, \dots, \mathbf{R}_M, \mathbf{r}_1, \dots, \mathbf{r}_N). \quad (1.24)$$

In the BO approximation, the molecular dynamics is solved in two-steps. We first consider the time-independent Schrödinger equation for electrons

$$H_e \phi_s(R_1, \dots, R_M, \mathbf{r}_1, \dots, \mathbf{r}_N) = E_s(R_1, \dots, R_M) \phi_s(R_1, \dots, R_M, \mathbf{r}_1, \dots, \mathbf{r}_N), \quad (1.25)$$

where $E_s(R_1, \dots, R_M)$ are the electronic eigenenergies for each electronic state s . Eq. (1.25) is known as the electronic wave equation, where the position of each ion \mathbf{R}_j is taken as a parameter. Thus, assuming that the ions are frozen in space, the electronic wave equation is solved for a range of nuclear positions, \mathbf{R}_j . Then, we can write the TISE for the molecule as

$$(T_N + \mathcal{H}_e) \Psi(\mathbf{R}_1, \dots, \mathbf{R}_M, \mathbf{r}_1, \dots, \mathbf{r}_N) = E\Psi(\mathbf{R}_1, \dots, \mathbf{R}_M, \mathbf{r}_1, \dots, \mathbf{r}_N). \quad (1.26)$$

We substitute Eq. (1.21) into Eq. (1.26), and obtain

$$(T_N + \mathcal{H}_e - E) \sum_s \chi_s(\mathbf{R}_1, \dots, \mathbf{R}_M) \phi_s(R_1, \dots, R_M, \mathbf{r}_1, \dots, \mathbf{r}_N) = 0 \quad (1.27)$$

By projecting the basis of electronic wavefunctions $\phi_s(R_1, \dots, R_M, \mathbf{r}_1, \dots, \mathbf{r}_N)$ onto Eq. (1.27), we obtain a system of coupled equations

$$\sum_s \langle \phi_k | T_N + H_e - E | \phi_s \rangle \chi_s(\mathbf{R}_1, \dots, \mathbf{R}_M) = 0 \quad k = 0, 1, 2, \dots, W, \quad (1.28)$$

where W is the total number of electronic states. Using the electronic wave equation, Eq. (1.25), the systems of equations (1.28) can be written as

$$\sum_s \langle \phi_k | T_N | \phi_s \rangle \chi_s(\mathbf{R}_1, \dots, \mathbf{R}_M) + [E_s(R_1, \dots, R_M) - E] \chi_s(\mathbf{R}_1, \dots, \mathbf{R}_M) = 0 \quad k = 0, 1, 2, \dots, W. \quad (1.29)$$

Assuming the adiabatic approximation (the ions move much slower than the electrons), we can neglect the derivatives of the electronic wavefunctions with respect to the nuclear coordinates, which leads to a set of uncoupled equations of the form [93]

$$\sum_k T_N \chi_k(\mathbf{R}_1, \dots, \mathbf{R}_M) + [E_k(R_1, \dots, R_M) - E] \chi_k(\mathbf{R}_1, \dots, \mathbf{R}_M) = 0 \quad k = 0, 1, 2, \dots, W. \quad (1.30)$$

Hence, the nuclear dynamics can be obtain by solving the set of uncoupled equations (1.30), where the energy of the each electronic state, $E_s(R_1, \dots, R_M)$, acts as a potential. This approximation remains valid as long as we can consider that the electronic motion is fast compared to ionic motion, i.e. the electrons see ions as if they are in a fixed configuration.

After being successfully applied in femtochemistry to study chemical reactivity [9, 94], there are efforts to extend the BO adiabatic approximation to the time domain. Among these works we can cite time-dependent potential energy surfaces (TDPES) introduced by Kono [95], the generalised time-dependent Born-Oppenheimer approximation by Cederbaum [96], or even beyond the BO approximation, the exact factorisation of the time-dependent electron-nuclear wavefunction [97]. The goal of these approaches is to conserve the computational benefits and also the intuitive picture that potential energy surfaces provided.

One example of a case in which BO behaviour is assumed is the ultrafast dynamics of an electronic wavefunction due to a coherent superposition of excited electronic states that occurs on a faster timescale than the ionic motion. In this scenario, the ionic dynamics are driven by the ultrafast electronic wavepacket motion rather than potential energy surfaces. Breidbach and Cederbaum proposed the ultrafast response of the electronic wavepacket after sudden ionisation [98]. In the N-methylacetamide molecule, the strong ionisation of the $3\pi_u$ orbital left the molecule in a non-stationary coherent superposition of one-particle orbitals that are eigenstates of the ion. Electronic correlations cause the evolution of the electron density over a timescale of 50 attoseconds. The high energy of the incident laser pulse needed for the sudden ionisation of the molecule makes the ejected electron leave the remaining ion before it had time to re-adapt, justifying the assumption that considers the ions fixed during the ionisation.

Indeed, a coherent superposition of ionic states induced by photoionisation of a molecule by a XUV attosecond pulse evolves on a ultrafast timescale depending on the energy difference between the ionic states and the geometry of the ion [99]. In Ref. [100] the hole created after sudden ionisation travels along the N-methylacetamide molecule within a few femtoseconds, whereas in Ref. [101] hole migration is investigated in glycine, which constitutes the simplest amino-acid in nature. Remacle and Levine, in Ref. [102], consider charge migration in the peptides TrpLeu₃ and TrpAla₃ after removal of the highest occupied molecular orbital (HOMO), which is again a linear combination of orbitals of the cation. In this case the hole found in TrpLeu₃ takes less than 1 fs to travel from one end of the peptide to the other, whereas in the case of TrpAla₃ the migration lasts 10 fs.

All the calculations mentioned are examples on how attosecond science is relevant to the study of charge transfer in large bio-molecules. Although the nuclear motion is considered uncoupled from the electronic motion, it can be expected that the coupling between electrons and ions induced by strong laser fields play a non-trivial role in the relaxation process of the molecules, as the geometry of the ions is decisive in the dynamics of the hole density after ionisation. Particularly, Baker et al. use high harmonic spectroscopy to track the ultrafast rearrangement of protons in molecules following ionisation [16]. They showed that it is possible to time-resolve the dissociation of small molecules by measuring the intrinsic chirp present in the HHG spectrum. Consider each of the short trajectories of the electron after ionisation, that are associated with a different electron kinetic energy at recollision with the parent ion at a particular delay in return time, Δt . The spread in time of the returning electron wavepacket causes a chirp in the harmonic emission [68]. Therefore, by filtering out the contributions of the long trajectories in the harmonic spectrum, it is possible to build a one-to-one mapping between recollision energies (harmonic orders) and returning time delay. With a single laser frequency, measuring the chirp within a series of HHG spectra generated for a range of pump-probe time delays, the internal changes is resolved with attosecond resolution. For instance, consider that the 15th harmonic probes the nuclear wavepacket at a time t , while 30th harmonic probes the nuclear wavepacket at a later time $t + \Delta t$. This technique has been dubbed PACER (Probing attosecond dynamics with chirp encoded recollisions) [16, 103, 104]. With this technique, Baker and co-workers were able to time-resolve the dissociation of H₂⁺ [105]. Since the high harmonic yield from this molecule is reduced as the molecule elongates, the observation of the yield reduction as a function of the harmonic order leads to the determination of internuclear distance as a function of time.

Another example of correlated electron-ion dynamics and attosecond charge control in small molecules are the experiments of Kling et. al. [106, 107] and Sansone et. al. [88, 108]. In the experiment of Kling, after dissociation of D₂ by a few-cycle, carrier envelope phase (CEP) stabilised, IR laser pulse, the angularly-resolved kinetic energy release spectrum of the resulting D and D⁺ fragments is measured. The experiment reveals that it is possible to control the direction of the fragments by changing the CEP of the laser pulse. This is presented in Figure 1.15a, if we first consider the ejected electron from ionisation of D₂ to D₂⁺. Due to the polarisation of the laser field, this electron can further recollide with D₂⁺, exciting the ion from the 2s σ_g state to the 2p σ_u dissociative state. Subsequently, as the molecule dissociates, the laser pulse couples the 2p σ_u with the 2s σ_g state via a three-photon and one-photon resonant transitions at particular internuclear distances, where this coherent superposition of electronic states leads to a beating of the probability density of the electron from being localised in one of the two ions. When the molecule continues to dissociate, the gap between these states becomes small compared to the photon energy so that the laser no longer induce the coupling, trapping the electron in one of the states. This localises the electron to one of the ions, causing an asymmetry in the kinetic energy distribution of the photofragments. Indeed, the asymmetry can be controlled by tuning the CEP of the laser pulse [109–111]. The experiment shows how to control molecular dissociation with few-cycles IR laser pulses, and how nuclear dy-

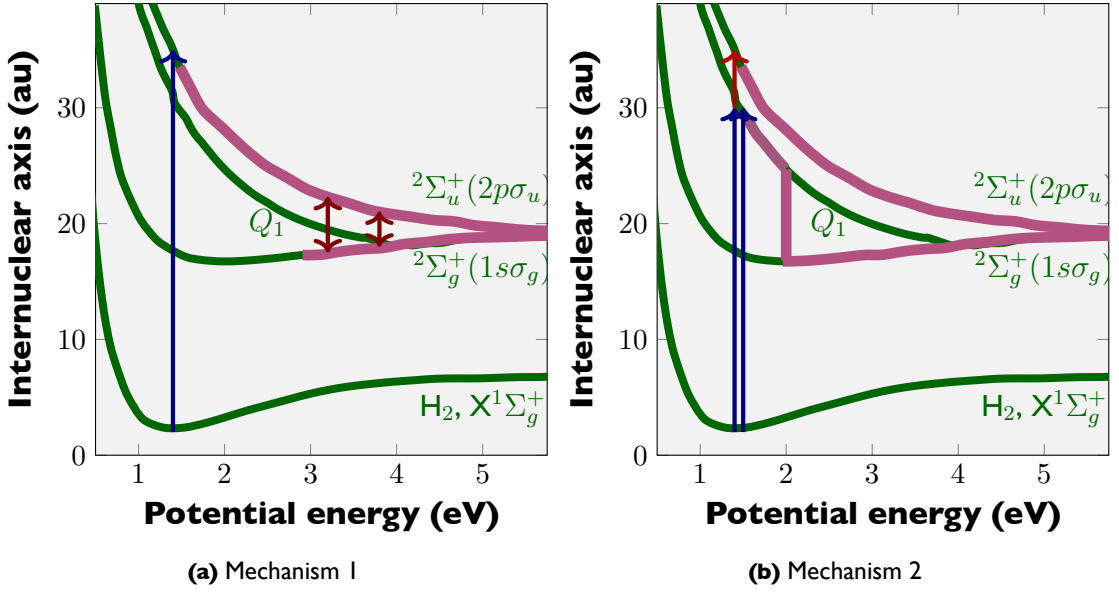


Figure 1.15: Diagram of the potential energy curves for the H_2 and H_2^+ showing two different mechanisms leading electron localisation in the experiment reported in Reference [88]. In the mechanism I, showed in (a), electron localisation is caused by the coupling of the $1s\sigma_g$ and $2p\sigma_u$ potential energy curves of the H_2^+ under the influence of the IR laser field. In the mechanism 2, presented in (b), the localisation is due to a coupling between the autoionising state Q_1 and the $1s\sigma_g$ and $2p\sigma_u$ electronic degrees of freedom. The figures have been adapted from Ref. [112].

namics affect electron dynamics in a chemical reaction.

In the experiment carried out by Sansone et. al. [88], the electron localisation is triggered by a pump-probe scheme, where the pump is a XUV laser pulse that ionises a neutral H_2 molecule, and the probe is an IR laser pulse that is intense enough to resonantly excite the resulting molecular ion from the $1s\sigma_g$ bound state to the $2p\sigma_u$ excited state, showed in Figure 1.15a. This time, the electron localisation can be controlled by changing the time delay between the XUV pulse and the IR pulse. In this case they identify a second mechanism, illustrated in Figure 1.15b, that causes electron localisation: the XUV pulse can not only ionise H_2 but also excite the molecule to a doubly-excited state. This doubly-excited state, is dissociative, and leads to the production of two neutral H atoms. However, the doubly-excited state can also auto-ionise and decay into the $1s\sigma_g$ state, which by the IR pulse will be coupled to the $2p\sigma_u$ state. Finally, both mechanisms lead to electron localisation on one of the two ions. While in the first mechanism the IR pulse couples electronic and nuclear degrees of freedom, in the second mechanism the probe pulse only couples electronic degrees of freedom, causing the bound electron to be preferentially localised to one of the parent ions. These experiments raised the need for developing theoretical tools in order to extend our understanding of electron-ion correlation to larger, more complex molecules, where multielectron dynamics is also involved.

1.3.1 Theoretical approaches in ultrafast molecular dynamics

As it was mentioned earlier, the fundamental equation that describes the dynamics of a molecular system is the time-dependent Schrödinger equation (1.18). However, an approach that treats electronic and ionic degrees of freedom on an equal footing in a fully quantum mechanical treatment is only available for the hydrogen molecule, H_2 , and the hydrogen molecular ion, H_2^+ . There is, a vast literature on strong field phenomena in H_2 and H_2^+ [113, 114]. Most of the previous work on H_2 and H_2^+ have considered the ions fixed in space: using this approximation one-photon cross sections [115–123], ionisation rates in the multiphoton regime [124–132], and one- and two-photon double ionisation cross sections of H_2 [133–142], high harmonic generation for arbitrary orientations between the molecular axis and the laser polarisation [16, 143–148] have all been calculated. However, even in this case, the solution of the TDSE for the H_2 and H_2^+ can be considered a challenge, because of the extraordinary computational effort required.

Usually grid-based computer codes are memory-limited by the number of grid points required for each coordinate (in terms of the mesh extent and the spacing required), or the number of basis functions we need to properly describe the behaviour of the system. These parameters in turn depend on the laser parameters used: the longer the wavelength the larger the extent required, but the shorter the wavelength the smaller the spacing required. This requirement is exacerbated when performing pump-probe simulations in which a short wavelength pulse is used to excite the molecule followed by probing the response by a long wavelength pulse. The reason for the scale of these mesh calculations is that electrons ionised by ultra-intense, ultra-short laser pulses can quickly travel several hundreds of Bohr from the parent ion. If the electron reaches the edge of the mesh and reflects back to the parent ion, this will cause spurious effects in the result. In order to eliminate reflections, absorbing boundaries are introduced near the edges of the mesh. But the problem arises if we want to collect the wavefunction at the end of the simulation, since the absorber destroys all the scattering information once the electronic wavepackets has entered the absorbing region. Several highly accurate numerical methods have been developed to solve the TDSE for H_2^+ and H_2 irradiated by intense laser pulses. These have generally been based on mesh techniques such as finite elements [149], the discrete variable representation (DVR) method [150, 151] and finite differences [152–155].

However, currently there are a range of theoretical approaches and methodologies to tackle interactions of molecules with attosecond laser pulses. The performance and efficiency of theoretical tools relies on their level of approximation, which at the same time depends on the size of the system we want to describe. The complexity of large targets, such as biomolecules, represents a challenge in the description of ultrafast chemical processes. To describe photoionisation in large amino-acids, density functional theory (DFT) [102, 156, 157] and configuration interaction (CI) methods [158] have been used. Usually these methods, as implemented in standard software packages [159–161], consider the ions fixed in space if the molecules involved in sub-fs and few-fs charge rearrangement and fragmentation [162] include heavy ions.

Other researchers have developed mixed quantum-classical techniques in which electrons are treated quantum mechanically while ions are treated classically. In this approach, called non-adiabatic quantum molecular dynamics (NAQMD) [163–165], the electrons dynamics are described using TDDFT [166]. NAQMD has been implemented using basis set methods [163–165, 167], grid methods [161, 168–173].

A difficulty in the treatment of ultrafast molecular problems is the description of electron wavepackets in the continuum after interaction with an attosecond pulse. In many early studies, a sudden ionisation is considered [102, 158, 174, 175], projecting out the molecular ground state against ionic states to obtain the ejected wavepacket distributions. In addition, DFT with a B-spline basis set which describes the electronic continuum can be used to obtain more accurately photoionisation amplitudes [157, 176].

DFT and TDDFT descriptions gives a correct description of laser-matter interactions where single excitations are considered. In contrast, CI methods can handle double excitation, being able to describe inner excitation and ionisation [99, 158, 174, 175]. Another efficient approach that can accurately describe double excitations is the multi-configurational time-dependent Hartree-Fock (MCTDHF) method [177–181]. This method has been successfully applied to small diatomic molecules such as the hydrogen molecule, reproducing photoionisation cross-sections and laser-induced electron dynamics effects [182–184].

Even with the success of CI and MCTDHF methods, considering electron correlations when treating electrons and ions quantum mechanically is a heroic task. One example of the difficulty of a problem that considers both the electronic and nuclear degrees of freedom in full dimensionality is the four body Coulomb break-up of H_2 after multiphoton absorption, which is still unsolved. Approaches capable of describing electron correlations are the time-dependent Feshbach close-coupling (TDFCC) method [185–190], which have been successfully applied to describe a number of experiments in which autoionisation of H_2 was involved [112, 191–193], or the R-Matrix incorporating time (RMT) [194–196] method, a powerful approach to describe multi-electron systems that has been recently applied to the description of H_2^+ [197, 198]. One of the advantages of this approach is that it can be extended for handling two-electron photoionisation problems, as it has been proven in helium [199, 200].

1.4 Summary

In this chapter we have given a brief introduction of strong field physics and attosecond science, especially focused on molecules. In Section 1.1 we have reviewed the progress of laser technology since its invention in the 1960’s, with a special remark on laser amplification: from the Q-switched oscillator to the recent chirp pulse amplification technique, which have allowed a relentless increase of laser intensities, making pulse durations progressively shorter. Closing Section 1.1 a very brief description of free-electron lasers is given. Later, in Section 1.2, we have summarised the fundamental concepts of Strong field physics, namely tunnel ion-

isation, over-the-barrier ionisation, multiphoton ionisation, above threshold ionisation and high harmonic generation. At the end of Section 1.2 a comment on generation of attosecond pulses from HHG is given. Finally, in Section 1.3 an overview on recent development in ultrafast molecular science is given, including novel experiments on ultrafast charge migration on biomolecules, attosecond observation of nuclear dynamics by HHG spectroscopy and attosecond molecular charge control in small molecules. We have ended Section 1.3 summarising the main theoretical tools in ultrafast molecular science.

Nuestra historia es la multiplicidad de formas con que eludimos las trampas infinitas que se alzan a nuestro paso. Rutina y tesón. Recuperación de cadáveres y registro de incidentes. Días idénticos y tranquilos.

Roberto Bolaño, El policía de las ratas.

2

Theoretical treatment of the laser-driven H₂⁺

In the present chapter we introduce the theoretical background needed for the full quantum mechanical treatment of the laser-driven hydrogen molecular ion. The hydrogen molecular ion is the simplest molecule in nature possessing two ionic centres and a single electron. It is the prototypical system for studying electron-ion interactions. In spite of this simplicity, H₂⁺ possesses rich and complex dynamics when exposed to strong, ultra-short laser pulses. Due to the highly non-perturbative behaviour of the laser-molecule interactions, an accurate numerical approach is needed to study the dynamics. Our model aims to solve the problem in its full dimensionality. A few assumptions and approximations are made, which are justified for the laser frequencies and intensities that are generally employed. The resulting problem is then tractable on modern supercomputers.

The chapter is arranged as follows. We give a schematic overview of the H₂⁺ model in Section 2.1. Section 2.2 justifies the use of the semiclassical approximation in the model for treating the interaction between the molecule and the laser field. Section 2.3 introduces the Hamiltonian of the H₂⁺ model, which treats the electron and the nuclear motion in equal footing, while Section 2.4 develops the Lagrangian formalism needed to introduce coordinate scaling techniques for solving the TDSE. These coordinate scalings are described in detail in Section 2.5. Section 2.6 discusses the characteristics of the laser field employed to excite the molecule. In Section 2.7 the gauges commonly used in laser-matter interaction studies are presented and a proof of their invariance is given. Throughout this thesis atomic units will be used, unless otherwise stated.

2.1 Overview of the system

The subject of this thesis has been the investigation of the hydrogen molecular ion exposed to intense laser fields. The molecule is illustrated in Figure 2.1. We consider the molecule aligned as shown with the centre of mass being the origin of coordinates. We denote by \mathbf{r} the position vector of the electron with respect to the centre of mass, and \mathbf{r}_1 and \mathbf{r}_2 the relative electron position with respect to each nucleus. The spacing between the two ions is R and each ion has mass $M = 1$ amu and $Z = 1$.

It is easy to generalise this description of a homonuclear molecule to the case of a heteronuclear molecule, in which each nucleus can have different charges and masses. This is considered later in the chapter.

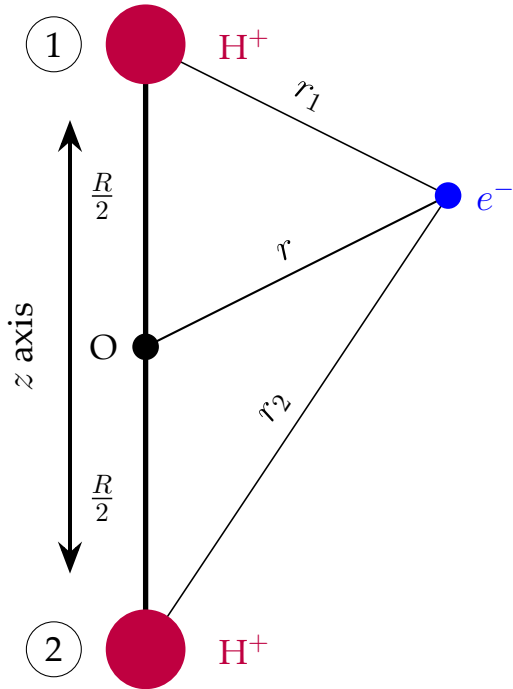


Figure 2.1: Schematic setup for the hydrogen molecular ion, H_2^+ . The internuclear axis is aligned along the z axis. Each of the two H^+ ions is separated at a distance $R/2$ from the centre of mass, O . The electron position vector is denoted by \mathbf{r} , and \mathbf{r}_1 and \mathbf{r}_2 are the relative electron position vectors with respect to each ion.

2.2 Semiclassical treatment of the laser-molecule system

We employ a semiclassical treatment of the system, in which the molecule is treated quantum mechanically while the laser field is treated classically. Such a treatment is historically known as first quantisation. It was the first formalism developed by the founders of quantum mechanics: Schrödinger, Heisenberg and Dirac [201, 202]. Later the formalism was extended to second quantisation [203], in which the electromagnetic field is also quantised. As a historical note, it was firstly applied to the study of spontaneous emission by Dirac [204]. Afterwards, in the works of Jordan, Wigner, Fermi, Heisenberg and Pauli [203], it was shown that particles

can be understood as field quanta, just as photons are the quanta of the electromagnetic field. The second quantisation led the birth of quantum electrodynamics (QED) and quantum field theory (QFT).

In principle, the full quantum treatment given by QED is the most accurate and precise description of laser-matter interactions. However, in the limit of a high density of photons, the electromagnetic field is well described classically using Maxwell's equations. Therefore, in the current context the semiclassical approximation is justified: it is also preferred because of its simplicity. The justification of the semi-classical approximation is as follows. For an arbitrary laser field, the photon density is given by [205]

$$\rho = \frac{I\lambda^3}{\omega_L c}, \quad (2.1)$$

where I is the intensity, λ is the wavelength, ω_L is the frequency and c is the speed of light. Typically, in strong-field physics we deal with laser pulses that have intensities around $I = 10^{14} \text{ W/cm}^2$ and wavelengths in the IR ($\lambda \approx 800 \text{ nm}$), or VUV ($\lambda \approx 248.6 \text{ nm}$). For IR pulse, the photon density is $\rho = 1.2 \times 10^9$, whereas for the VUV pulse it is $\rho = 1.1 \times 10^7$. In both cases $\rho \gg 1$, and so use of the semiclassical approximation is justified.

2.3 Hamiltonian for the laser-molecule system

The fundamental equation in quantum mechanics which governs the dynamics of this molecule is the time-dependent Schrödinger equation (TDSE)

$$i\frac{\partial\Psi(\mathbf{r}, \mathbf{R}, t)}{\partial t} = \mathcal{H}(\mathbf{r}, \mathbf{R}, t)\Psi(\mathbf{r}, \mathbf{R}, t), \quad (2.2)$$

where $\Psi(\mathbf{r}, \mathbf{R}, t)$ is the wavefunction of the molecule, and $\mathcal{H}(\mathbf{r}, \mathbf{R}, t)$ is the time-dependent Hamiltonian operator. The wavefunction of the molecule depends on the electronic position \mathbf{r} , the internuclear vector position \mathbf{R} (see Figure 2.1), and on time.

The Hamiltonian of a charged particle moving in an external potential V , in the presence of an electromagnetic field takes the form [93]:

$$\mathcal{H}(\mathbf{r}, \mathbf{R}, t) = -\frac{1}{2}\left(\mathbf{p} - \frac{q}{c}\mathbf{A}(\mathbf{r}, t)\right)^2 + q\varphi(\mathbf{r}, t) + V(\mathbf{r}, \mathbf{R}, t) \quad (2.3)$$

where the first term in the right hand side is the kinetic energy, \mathbf{p} is the canonical momentum, q is the charge of the particle, c is the speed of light, and finally \mathbf{A} and φ are respectively the vector and scalar potential of the electromagnetic field. We consider the case of a diatomic molecule with only one electron, interacting with an electromagnetic field. Assuming the Coulomb gauge for the electromagnetic field, the scalar potential become zero, $\varphi = 0$ (for more details see Section 2.6). Taking into account the molecular potential, the Hamiltonian

can be written as

$$\mathcal{H}(\mathbf{r}, \mathbf{R}, t) = \frac{1}{2\mu_e} \left(-i\boldsymbol{\nabla}_e + \frac{1}{c}\mathbf{A}(t) \right)^2 - \frac{1}{2\mu_N} \nabla_N^2 - \frac{Z_1}{|\mathbf{r} - 1/2\mathbf{R}|} - \frac{Z_2}{|\mathbf{r} + 1/2\mathbf{R}|} + \frac{Z_1 Z_2}{\mathbf{R}}, \quad (2.4)$$

where μ_e is the reduced electronic mass, defined as

$$\frac{1}{\mu_e} = \frac{1}{m_e} + \frac{1}{M_1 + M_2}, \quad (2.5)$$

and μ_N is the reduced nuclear mass

$$\mu_N = \frac{1}{M_1} + \frac{1}{M_2}. \quad (2.6)$$

In these equations, m_e is the electron mass, M_1 and M_2 are the proton masses, Z_1 and Z_2 are the charge of the protons, and $q = -e = -1$ the charge of the electron. We have used the fundamental quantum relation $\mathbf{p} = -i\boldsymbol{\nabla}$, which quantifies the canonical momentum. In Eq. (2.4) the last four terms describe the kinetic energy of the ions, electron-ion Coulomb potentials and the ion-ion Coulomb potential respectively.

2.4 Lagrangian formalism

In order to accurately and efficiently solve the TDSE for H_2^+ we will use generalised curvilinear coordinates. As we will see later, when these coordinates are employed in conjunction with finite differences methods, we obtain deformed finite difference meshes in which mesh points can be concentrated on specific areas of the grid. This is achieved with a simple underlying Cartesian structure which simplifies communication patterns in parallel calculations. In order to use generalised curvilinear coordinates we must derive the TDSE in these coordinates, while maintaining the Hermiticity of the resulting finite-difference operators. This can be achieved most easily using a Lagrangian formalism [171, 206] which we now describe.

The Lagrangian for a molecule in an external potential can be written as [207]

$$\begin{aligned} \mathcal{L}(\Psi, \dot{\Psi}, t) = & i \int d\mathbf{r} d\mathbf{R} \Psi^* \dot{\Psi} + \frac{1}{2} \int d\mathbf{r} d\mathbf{R} \Psi^* \nabla_e^2 \Psi + \frac{1}{2} \int d\mathbf{r} d\mathbf{R} \Psi^* \nabla_N^2 \Psi \\ & + \int d\mathbf{r} d\mathbf{R} \Psi^* V_C \Psi + \int d\mathbf{r} d\mathbf{R} \Psi^* V_I \Psi, \end{aligned} \quad (2.7)$$

where Ψ is the wavefunction which describes the molecule, ∇_e^2 and ∇_N^2 are the electronic and nuclear Laplacians respectively, V_C is the molecular potential

$$V_C(\mathbf{r}, \mathbf{R}) = -\frac{Z_1}{|\mathbf{r} - 1/2\mathbf{R}|} - \frac{Z_2}{|\mathbf{r} + 1/2\mathbf{R}|} + \frac{Z_1 Z_2}{|\mathbf{R}|}, \quad (2.8)$$

and V_I is the laser-matter interaction potential given by

$$V_I(\mathbf{r}, t) = -\frac{i}{c} \mathbf{A} \cdot \boldsymbol{\nabla}. \quad (2.9)$$

Invoking the principle of least action, a variation of the wavefunction that leaves the action stationary

$$\delta S = \delta \int_{t_1}^{t_2} dt \mathcal{L}(\Psi, \dot{\Psi}, t) = 0 \quad (2.10)$$

leads to the Euler-Lagrange (E-L) equations of motion

$$\frac{\partial \mathcal{L}}{\partial \Psi^*} = \frac{d}{dt} \left(\frac{\partial \mathcal{L}}{\partial \dot{\Psi}^*} \right) \quad (2.11)$$

$$\frac{\partial \mathcal{L}}{\partial \Psi} = \frac{d}{dt} \left(\frac{\partial \mathcal{L}}{\partial \dot{\Psi}} \right). \quad (2.12)$$

Eq. (2.11) is nothing more than the time-dependent Schrödinger equation, and Eq. (2.12) is its complex conjugate. We note that the E-L equations hold in any coordinate system, which allows us to express the TDSE in curvilinear coordinates.

2.5 Scaled curvilinear coordinates

Consider first an orthogonal coordinate system in 4D in which an arbitrary point is described by the coordinates $(\xi^1, \xi^2, \xi^3, \xi^4)$. The position vector is simply

$$\mathbf{r}_M = x^1(\xi^1) \mathbf{i} + x^2(\xi^2) \mathbf{j} + x^3(\xi^3) \mathbf{k} + x^4(\xi^4) \mathbf{l}. \quad (2.13)$$

Consider now a general curvilinear coordinate system in 3D. It is always possible to find a continuous transformation to another coordinate system so that the new coordinates (x^1, x^2, x^3, x^4) can be expressed as

$$x^1 = x^1(\xi^1, \xi^2, \xi^3, \xi^4) \quad (2.14)$$

$$x^2 = x^2(\xi^1, \xi^2, \xi^3, \xi^4) \quad (2.15)$$

$$x^3 = x^3(\xi^1, \xi^2, \xi^3, \xi^4) \quad (2.16)$$

$$x^4 = x^4(\xi^1, \xi^2, \xi^3, \xi^4). \quad (2.17)$$

The above transformation is described by the Jacobian [208]

$$\mathbf{J} = \begin{pmatrix} \frac{\partial x^1}{\partial \xi^1} & \frac{\partial x^1}{\partial \xi^2} & \frac{\partial x^1}{\partial \xi^3} & \frac{\partial x^1}{\partial \xi^4} \\ \frac{\partial x^2}{\partial \xi^1} & \frac{\partial x^2}{\partial \xi^2} & \frac{\partial x^2}{\partial \xi^3} & \frac{\partial x^2}{\partial \xi^4} \\ \frac{\partial x^3}{\partial \xi^1} & \frac{\partial x^3}{\partial \xi^2} & \frac{\partial x^3}{\partial \xi^3} & \frac{\partial x^3}{\partial \xi^4} \\ \frac{\partial x^4}{\partial \xi^1} & \frac{\partial x^4}{\partial \xi^2} & \frac{\partial x^4}{\partial \xi^3} & \frac{\partial x^4}{\partial \xi^4} \end{pmatrix} \quad (2.18)$$

In addition, in our new coordinate system, integrals will transform as

$$\int d\mathbf{x} f(\mathbf{x}) \rightarrow \int d\xi |J| f(\xi), \quad (2.19)$$

where $|J| = \det \mathbf{J}$.

We will now apply such transformations to our Lagrangian defined in Eq. (2.7). The 3D electron position vector in a general curvilinear system is

$$\mathbf{r} = x^1(\xi^1, \xi^2, \xi^3) \mathbf{i} + x^2(\xi^1, \xi^2, \xi^3) \mathbf{j} + x^3(\xi^1, \xi^2, \xi^3) \mathbf{k} \quad (2.20)$$

while the 1D internuclear distance vector is just

$$\mathbf{R} = x^4(\xi^4) \mathbf{l}, \quad (2.21)$$

where $\{x^1, x^2, x^3, x^4\}$ are the Cartesian coordinates [208], and $\{\mathbf{i}, \mathbf{j}, \mathbf{k}, \mathbf{l}\}$ are the unit vectors. We note that the scale factors can be real or complex-valued functions. In this work, we only consider orthogonal coordinates transformations so that non-diagonal terms in the Jacobian, Eq. (2.18), will be zero. The volume element is given by

$$d\mathbf{r}_M = h_1 h_2 h_3 h_4 d\xi^1 d\xi^2 d\xi^3 d\xi^4 = |J| d\xi^1 d\xi^2 d\xi^3 d\xi^4, \quad (2.22)$$

where

$$h_j = \frac{\partial x^j(\xi^j)}{\partial \xi^j} \quad \text{for } j = 1, 2, 3, 4, \quad (2.23)$$

are the scale factors.

We can write now the Lagrangian in these coordinates as

$$\mathcal{L}(\Psi, \dot{\Psi}, t) = i \int d\xi^1 d\xi^2 d\xi^3 d\xi^4 |J| \Psi^* \dot{\Psi} + \frac{1}{2} \int d\xi^1 d\xi^2 d\xi^3 d\xi^4 |J| \Psi^* \nabla_e^2 \Psi + \quad (2.24)$$

$$+ \frac{1}{2} \int d\xi^1 d\xi^2 d\xi^3 d\xi^4 |J| \Psi^* \nabla_N^2 \Psi + \quad (2.25)$$

$$+ \int d\xi^1 d\xi^2 d\xi^3 d\xi^4 |J| \Psi^* V_C \Psi + \int d\xi^1 d\xi^2 d\xi^3 d\xi^4 |J| \Psi^* V_I \Psi \quad (2.26)$$

For an orthogonal coordinate system, the gradient operator takes the form [208]

$$\nabla = \mathbf{i} \frac{1}{h_1} \frac{\partial}{\partial \xi^1} + \mathbf{j} \frac{1}{h_2} \frac{\partial}{\partial \xi^2} + \mathbf{k} \frac{1}{h_3} \frac{\partial}{\partial \xi^3} + \mathbf{l} \frac{1}{h_4} \frac{\partial}{\partial \xi^4}, \quad (2.27)$$

and the Laplacian is given by [208]

$$\nabla^2 = \frac{1}{|J|} \left[\frac{\partial}{\partial \xi^1} \left(\frac{h_2 h_3 h_4}{h_1} \right) \frac{\partial}{\partial \xi^1} + \frac{\partial}{\partial \xi^2} \left(\frac{h_1 h_3 h_4}{h_2} \right) \frac{\partial}{\partial \xi^2} + \frac{\partial}{\partial \xi^3} \left(\frac{h_1 h_2 h_4}{h_3} \right) \frac{\partial}{\partial \xi^3} + \frac{\partial}{\partial \xi^4} \left(\frac{h_1 h_2 h_3}{h_4} \right) \frac{\partial}{\partial \xi^4} \right]. \quad (2.28)$$

Transforming the wavefunction as

$$\Psi(\xi^1, \xi^2, \xi^3, \xi^4) = \frac{\psi(\xi^1, \xi^2, \xi^3, \xi^4)}{\sqrt{|J|}}, \quad (2.29)$$

using this together with Eq. (2.27) and Eq. (2.28) in Eq. (2.24), and using the principle of least

action Eq. (2.10), result in the TDSE

$$i \frac{\partial \psi}{\partial t} = [T_e + T_N + V_C + V_I] \psi. \quad (2.30)$$

In this equation the electronic kinetic energy term is

$$T_e = -\frac{1}{2} \frac{1}{\sqrt{|J|}} \left[\frac{\partial}{\partial \xi^1} \left(\frac{h_2 h_3}{h_1} \right) \frac{\partial}{\partial \xi^1} + \frac{\partial}{\partial \xi^2} \left(\frac{h_1 h_3}{h_2} \right) \frac{\partial}{\partial \xi^2} + \frac{\partial}{\partial \xi^3} \left(\frac{h_1 h_2}{h_3} \right) \frac{\partial}{\partial \xi^3} \right] \frac{1}{\sqrt{|J|}}. \quad (2.31)$$

the nuclear kinetic energy term is

$$T_N = -\frac{1}{2} \frac{1}{\sqrt{h_4}} \left[\frac{\partial}{\partial \xi^4} \left(\frac{1}{h_4} \right) \frac{\partial}{\partial \xi^4} \right] \frac{1}{\sqrt{h_4}}, \quad (2.32)$$

the molecular Coulomb potential term is

$$V_C = -\frac{Z_1}{\sqrt{(x^1)^2 + (x^2)^2 + (x^3 - x^4/2)^2}} - \frac{Z_2}{\sqrt{(x^1)^2 + (x^2)^2 + (x^3 + x^4/2)^2}} + \frac{Z_1 Z_2}{x^4} \quad (2.33)$$

and the laser-molecule interaction term is

$$V_I = -\frac{i}{c} \mathbf{A} \cdot \left[i \frac{1}{\sqrt{h_1}} \frac{\partial}{\partial \xi^1} \frac{1}{\sqrt{h_1}} + j \frac{1}{\sqrt{h_2}} \frac{\partial}{\partial y} \frac{1}{\sqrt{h_2}} + k \frac{1}{\sqrt{h_3}} \frac{\partial}{\partial z} \frac{1}{\sqrt{h_3}} \right]. \quad (2.34)$$

It is convenient for us to express the electron dynamics in the two most common coordinate systems, Cartesian and cylindrical coordinates. In the following subsections we will give the explicit representation of the TDSE in both of these coordinate systems. We point out that if no scaling is introduced, we recover the textbook definitions of the differential operators.

Adaptive curvilinear coordinates have been employed in the past in electronic structure calculations, both in real-space grid methods [152, 154, 161, 172, 209–211] and plane-wave basis set methods [212]. When applied to finite difference methods, these generalised curvilinear coordinates allow a high density of points to be concentrated in regions of special interest.

2.5.1 Scaled Cartesian coordinates

Here we consider orthogonal scaling applied to each coordinate. In Cartesian coordinates, we consider a transformation from standard coordinates. The electron position vector is given by

$$\mathbf{r} = x \mathbf{i} + y \mathbf{j} + z \mathbf{k}, \quad (2.35)$$

where

$$x = x^1(\xi^x) \quad (2.36)$$

$$y = x^2(\xi^y) \quad (2.37)$$

$$z = x^3(\xi^z). \quad (2.38)$$

Thus, the scale factors are

$$h_1 = x'(\xi^x) \quad (2.39)$$

$$h_2 = y'(\xi^y) \quad (2.40)$$

$$h_3 = z'(\xi^z). \quad (2.41)$$

As we only allow the nuclei to vibrate along the internuclear axis, the nuclear coordinate is given by

$$R = x^4(\xi^R) \quad (2.42)$$

and the correspondent scale factor

$$h_4 = R'(\xi^R). \quad (2.43)$$

The Jacobian

$$|J| = h_1 h_2 h_3 h_4 \quad (2.44)$$

In the scaled Cartesian coordinates, the electron kinetic energy term takes the simple form

$$T_e = -\frac{1}{2} \frac{1}{\sqrt{x'}} \frac{\partial}{\partial \xi^x} \left(\frac{1}{x'} \right) \frac{\partial}{\partial \xi^x} \frac{1}{\sqrt{x'}} + \frac{1}{\sqrt{y'}} \frac{\partial}{\partial \xi^y} \left(\frac{1}{y'} \right) \frac{\partial}{\partial \xi^y} \frac{1}{\sqrt{y'}} + \frac{1}{\sqrt{z'}} \frac{\partial}{\partial \xi^z} \left(\frac{1}{z'} \right) \frac{\partial}{\partial \xi^z} \frac{1}{\sqrt{z'}}, \quad (2.45)$$

and the nuclear kinetic energy

$$T_N = -\frac{1}{2} \frac{1}{\sqrt{R'}} \frac{\partial}{\partial \xi^R} \left(\frac{1}{R'} \right) \frac{\partial}{\partial \xi^R} \frac{1}{\sqrt{R'}}. \quad (2.46)$$

The molecular Coulomb potential is

$$\begin{aligned} V_C = & -\frac{Z_1}{\sqrt{(x(\xi^x))^2 + (y(\xi^y))^2 + (z(\xi^z) - R(\xi^R)/2)^2}} \\ & -\frac{Z_2}{\sqrt{(x(\xi^x))^2 + (y(\xi^y))^2 + (z(\xi^z) + R(\xi^R)/2)^2}} + \frac{Z_1 Z_2}{R(\xi^R)} \end{aligned} \quad (2.47)$$

and the laser-molecule interaction term is

$$V_I = -\frac{i}{c} \mathbf{A} \cdot \left[\mathbf{i} \frac{1}{\sqrt{x'}} \frac{\partial}{\partial \xi^x} \frac{1}{\sqrt{x'}} + \mathbf{j} \frac{1}{\sqrt{y'}} \frac{\partial}{\partial \xi^y} \frac{1}{\sqrt{y'}} + \mathbf{k} \frac{1}{\sqrt{z'}} \frac{\partial}{\partial \xi^z} \frac{1}{\sqrt{z'}} \right]. \quad (2.48)$$

2.5.2 Scaled cylindrical coordinates

Now consider a transformation from standard cylindrical coordinates. The electron vector position is given by

$$\mathbf{r} = \rho(\xi^\rho) \cos \varphi \mathbf{i} + \rho(\xi^\rho) \sin \varphi \mathbf{j} + z(\xi^z) \mathbf{k} \quad (2.49)$$

where the angular coordinate is not scaled. The nuclear coordinate is again

$$R = R(\xi^R) \quad (2.50)$$

The scale factors in this case are

$$h_1 = \rho'(\xi^\rho) \quad (2.51)$$

$$h_2 = \rho(\xi^\rho) \quad (2.52)$$

$$h_3 = z'(\xi^z) \quad (2.53)$$

$$h_4 = R'(\xi^R), \quad (2.54)$$

and the determinant of the Jacobian is

$$|J| = \rho\rho'z'R'. \quad (2.55)$$

In these coordinates, the electron kinetic energy is given by

$$T_e = -\frac{1}{2} \frac{1}{\sqrt{\rho\rho'}} \frac{\partial}{\partial\xi^\rho} \left(\frac{\rho'}{\rho} \right) \frac{\partial}{\partial\xi^\rho} \frac{1}{\sqrt{\rho\rho'}} + \frac{1}{\rho'^2} \frac{\partial^2}{\partial\varphi^2} + \frac{1}{\sqrt{z'}} \frac{\partial}{\partial\xi^z} \left(\frac{1}{z'} \right) \frac{\partial}{\partial\xi^z} \frac{1}{\sqrt{z'}}. \quad (2.56)$$

We are interested in using cylindrical coordinates in situations where the laser polarisation axis is parallel to the internuclear axis. In such scenario, the angular momentum L_z is conserved, therefore m is a good quantum number and φ is a cyclic coordinate. If we consider the molecule in its ground state taking $m = 0$, there is no azimuthal dependence in the Hamiltonian, leaving the electron kinetic energy as

$$T_e = -\frac{1}{2} \frac{1}{\sqrt{\rho\rho'}} \frac{\partial}{\partial\xi^\rho} \left(\frac{\rho'}{\rho} \right) \frac{\partial}{\partial\xi^\rho} \frac{1}{\sqrt{\rho\rho'}} + \frac{1}{\sqrt{z'}} \frac{\partial}{\partial\xi^z} \left(\frac{1}{z'} \right) \frac{\partial}{\partial\xi^z} \frac{1}{\sqrt{z'}}. \quad (2.57)$$

In addition, in order to cancel the 2π factor introduced by the integrals over the φ coordinate,

$$\int d\varphi \Psi(\rho, z, R, t) = 2\pi\Psi(\rho, z, R, t) \quad (2.58)$$

we transform the wavefunction as

$$\Psi(\rho, z, R, t) = \frac{\psi(\rho, z, R, t)}{\sqrt{2\pi\rho'\rho z'}}. \quad (2.59)$$

The nuclear kinetic energy takes exactly the same form as in the Cartesian case, Eq. (2.46). The molecular Coulomb potential is

$$V_C = -\frac{Z_1}{\sqrt{\rho^2(\xi^\rho) + \left(z(\xi^z) - \frac{R(\xi^R)}{2}\right)^2}} - \frac{Z_2}{\sqrt{\rho^2(\xi^\rho) + \left(z(\xi^z) + \frac{R(\xi^R)}{2}\right)^2}} + \frac{Z_1 Z_2}{R(\xi^R)} \quad (2.60)$$

and the laser-molecule interaction term is

$$V_I = -\frac{i}{c} \mathbf{A} \cdot \left[\mathbf{i} \frac{1}{\sqrt{\rho'}} \frac{\partial}{\partial\xi^\rho} \frac{1}{\sqrt{\rho'}} + \mathbf{k} \frac{1}{\sqrt{z'}} \frac{\partial}{\partial\xi^z} \frac{1}{\sqrt{z'}} \right]. \quad (2.61)$$

2.5.3 Implementation of scaled curvilinear coordinates

The Laplacian operator in Eq. (2.31), expressed in finite-differences using the central difference approximation to the first derivative terms, will be symmetric. This ensures that the resulting finite difference Hamiltonian is Hermitian and thus time propagation will be unitary. For

convenience we can rewrite Eq. (2.31) in terms of second derivatives, while maintaining the symmetry of the resulting operator. For example, if we only consider the term involving ξ^1 , and using the wavefunction transformation in Eq. (2.29), we can write

$$\left[\frac{1}{\sqrt{|J|}} \frac{\partial}{\partial \xi^1} \frac{1}{h_1} \frac{\partial}{\partial \xi^1} \frac{1}{\sqrt{|J|}} \right] \psi = \frac{1}{2} \left[\frac{1}{h_1^2} \frac{\partial^2}{\partial \xi^{12}} + \frac{\partial^2}{\partial \xi^{12}} \frac{1}{h_1^2} \right] \psi + M\psi \quad (2.62)$$

where h_1 is the corresponding scale factor of the coordinate ξ^1 , and M is a function of ξ^1 and its derivatives.

Considering the case of generalised cylindrical coordinates in Section 2.5.2, we can rewrite the kinetic energy operators as

$$T_\rho = \frac{1}{2} \left[\frac{1}{(g')^2} \frac{\partial^2}{\partial \rho^2} + \frac{\partial^2}{\partial \rho^2} \frac{1}{(g')^2} \right] + \left(\frac{g'''}{2(g')^3} - \frac{7(g'')^2}{4(g')^4} + \frac{1}{4g^2} \right) \quad (2.63)$$

and analogy for the z term

$$T_z = \frac{1}{2} \left[\frac{1}{(z')^2} \frac{\partial^2}{\partial (\xi^2)^2} + \frac{\partial^2}{\partial (\xi^2)^2} \frac{1}{(z')^2} \right] + \left(\frac{z'''}{2(z')^3} - \frac{7(z'')^2}{4(z')^4} \right), \quad (2.64)$$

where the second term in the right hand side of Eq.(2.63) and (2.64) corresponds to the M term of Eq.(2.62). The nuclear kinetic energy term takes the same form as Eq. (2.64).

The advantage of expressing the kinetic energy operator as in Eq. (2.63) and Eq. (2.64) is that it needs to be evaluated at fewer grid points in each coordinate compared with Eq. (2.57). For example, consider evaluating the kinetic energy operator in ρ using a 5-point finite difference rule. Using Eq. (2.57), which is based on first-order derivatives, will require wavefunction values at 7 points. Using Eq. (2.63), however will only require wavefunction values at 5 points. The resulting parallel code of the operator in Eq. (2.57) would require 3 halo points¹ rather than 2 points required by the operators in Eq. (2.63) Eq. (2.64). Thus using Eq. (2.63) and Eq. (2.64) will result in less communication overhead between processors in order to apply this finite difference rule. For details in communication patterns, see Section 3.4.

For the case of generalised cylindrical coordinates, we have used the following global adaptation for the ρ coordinate [21]

$$\rho(\xi^\rho) = \rho \left(\frac{(\xi^\rho)^n}{\beta(\xi^\rho)^n + \alpha^n} \right)^\nu, \quad z(\xi^z), \quad (2.65)$$

where n takes on integer values, ν takes on half-integer values and α and β are real numbers. With this scaling we get a high density of points near the internuclear axis and an equidistant spacing far from the origin. The transition between the two regions is controlled by the pa-

¹Usually grid points belonging to the neighbours's grid domain that are contiguous to the local grid domain are called halo points. Those points are stored locally at the halo of the grid, and exchanged between processors. For more info see Section 3.4

parameter α . Since we only use the cylindrical coordinate in case of parallel orientation between the internuclear axis and the laser polarisation, it is reasonable to use a equally spaced grid in the z coordinate in order to describe properly electrons in continuum states. An illustration of the scalings used in given in Figure 2.2.

In practice we use two set of parameters depending on the wavelength of the laser field:

1. In the first set we take

$$\alpha = 1, \quad \beta = 0, \quad n = 1, \quad \nu = \frac{1}{2} \quad (2.66)$$

which leads the scaling functions to take the form [211]

$$\rho(\xi^\rho) = (\xi^\rho)^{3/2}, \quad h(\xi^z) = \xi^z \quad (2.67)$$

As we can see in Figure 2.2a, with this exponential scaling for the ρ coordinate, the transformed wavefunction in Eq. (2.59) scales as ρ for small values of ρ , near the origin, ensuring accurate evaluation of derivatives in the ρ direction and thus improving the calculation of the eigenvalues of the molecule. This scaling is used in the case of ionisation of the molecule by long laser wavelengths whose polarisation axis is parallel to the internuclear axis, because the dynamics of the ionised electron take place predominantly along the molecular axis.

The kinetic energy operators Eq. (2.63) and Eq. (2.64) take the form

$$T_\rho = \frac{2}{9} \left(\frac{1}{\rho} \frac{\partial^2}{\partial(\xi^\rho)^2} + \frac{\partial^2}{\partial(\xi^\rho)^2} \frac{1}{\rho} \right) + M_\rho \quad (2.68)$$

and

$$T_z = \frac{\partial^2}{\partial(\xi^z)^2}. \quad (2.69)$$

However, from Eq. (2.59) we have $\psi(\rho(\xi^\rho) = 0, z, R, t) = 0$, but

$$\frac{\psi}{\rho} \propto \Psi \neq 0 \quad \text{at} \quad \rho(\xi^\rho) = 0. \quad (2.70)$$

A solution to this problem, used in reference [211] by Kawata and Kono, is to expand this term, which leads to a non-Hermitian operator in Eq. (2.63). In our implementation we obtain the value of $\psi(\rho(\xi^\rho) = 0)$ through interpolation. The value at $\rho(\xi^\rho) = 0$ is just a multiple of $\psi(\delta\xi^\rho)$, such that

$$\psi(\rho(\xi^\rho) = 0) = C\psi(\delta\xi^\rho) \quad (2.71)$$

where is C is a parameter that depends on the grid parameters $\delta\xi^\rho$ and $\delta\xi^z$, and it can be tuned to accurately described the eigenenergies of the system. In practice we use a 3-point central difference approximation for T_ρ , so the fictitious point required by the

rule is taken as $\psi(-\delta\xi^\rho) = \psi(\delta\xi^\rho)$.

2. In the second set the parameters take the value

$$\alpha = 5, \quad \beta = 1, \quad n = 1, \quad \nu = \frac{1}{2} \quad (2.72)$$

which leads to the scaling functions [213]

$$\rho(\xi^\rho) = \xi^\rho \sqrt{\frac{\xi^\rho}{\xi^\rho + 5}}, \quad z(\xi^z) = \xi^z \quad (2.73)$$

With this scaling (Figure 2.2b) in the ρ direction we also ensure high density of grid points in the vicinity of the internuclear axis, and a constant grid spacing for $\rho > \alpha$. The transition between regions has found to be optimal at $\alpha = 5$. These scalings are applied when the molecule is exposed to VUV pulses, since an ionised electron wavepackets can be ejected at any direction.

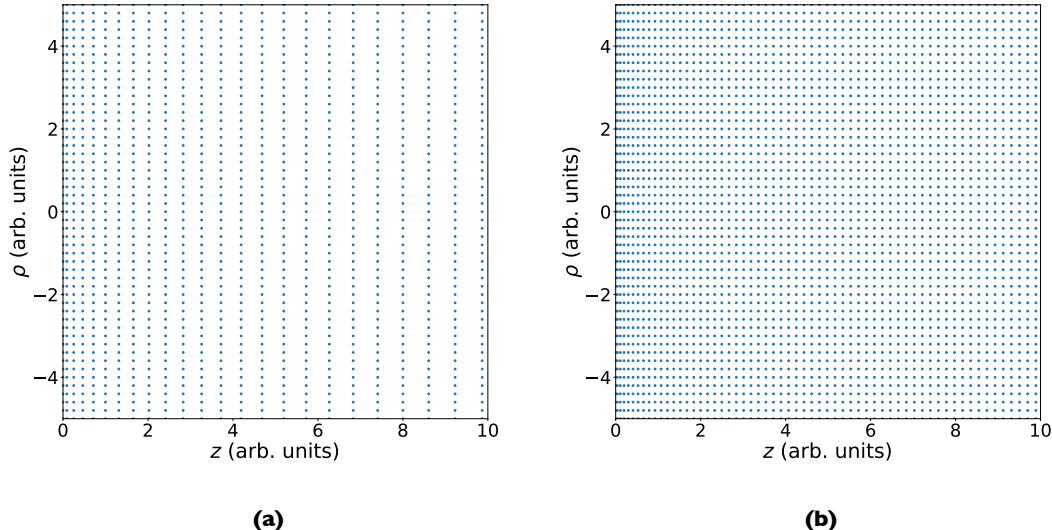


Figure 2.2: Illustration of a finite difference grid in cylindrical coordinates using the curvilinear scalings defined in Section 2.5. (a) grid with the global scaling corresponding to Eq. (2.67) is shown while in (b) a grid with the global scaling defined in Eq. (2.73) is shown. We note that for both grids the underlying mesh always has a constant grid spacing.

2.6 Classical description of the laser pulse

Consider Maxwell's equations (in a vacuum) describing electromagnetic fields

$$\nabla \cdot \mathbf{E} = 0 \quad (2.74)$$

$$\nabla \cdot \mathbf{B} = 0 \quad (2.75)$$

$$\nabla \times \mathbf{B} - \frac{1}{c^2} \frac{\partial \mathbf{E}}{\partial t} = \mathbf{0} \quad (2.76)$$

$$\nabla \times \mathbf{E} + \frac{\partial \mathbf{B}}{\partial t} = \mathbf{0} \quad (2.77)$$

where \mathbf{E} is the electric field and \mathbf{B} the magnetic field [214]. It is useful to express the fields in terms of a vector potential, \mathbf{A} , and a scalar potential, φ . From the equation Maxwell equation representing the absence of free magnetic poles, Eq. (2.75), we can always write the magnetic field as a function of a vector potential

$$\mathbf{B} = \nabla \times \mathbf{A}. \quad (2.78)$$

Next, we can make use of the Maxwell's equation representing Faraday's law, Eq.(2.77), and write:

$$\nabla \times \left(\mathbf{E} + \frac{\partial \mathbf{A}}{\partial t} \right) = \mathbf{0}. \quad (2.79)$$

Eq. (2.79) implies that the quantity inside brackets can be written as the gradient of a scalar function, $-\nabla\phi$. Then, the electric field can be expressed as

$$\mathbf{E}(\mathbf{r}, t) = -\nabla\varphi(\mathbf{r}, t) - \frac{\partial}{\partial t} \mathbf{A}(\mathbf{r}, t) \quad (2.80)$$

With the use of these potentials, we can reduce Maxwell's equations to two inhomogeneous equations

$$\nabla^2\varphi + \frac{\partial}{\partial t} (\nabla \cdot \mathbf{A}) = 0 \quad (2.81)$$

$$\nabla^2 \mathbf{A} - \frac{1}{c^2} \frac{\partial^2 \mathbf{A}}{\partial t^2} - \nabla \left(\nabla \cdot \mathbf{A} + \frac{1}{c^2} \frac{\partial \varphi}{\partial t} \right) = 0 \quad (2.82)$$

The fields \mathbf{E} and \mathbf{B} are invariant under the transformation

$$\mathbf{A} \rightarrow \mathbf{A}' = \mathbf{A} + \nabla\chi \quad (2.83)$$

$$\varphi \rightarrow \varphi' = \varphi - \frac{\partial\chi}{\partial t} \quad (2.84)$$

where $\chi(\mathbf{r}, t)$ is an arbitrary scalar field. These transformations, called gauge transformations, allow us to choose a function $\chi(\mathbf{r}, t)$ such that the fields $\mathbf{A}(\mathbf{r}, t)$ and $\varphi(\mathbf{r}, t)$ satisfy the Lorentz condition

$$\nabla \cdot \mathbf{A} + \frac{1}{c^2} \frac{\partial \varphi}{\partial t} = 0. \quad (2.85)$$

The Lorentz condition uncouples Maxwell's equations into two inhomogeneous differen-

tial equations

$$\nabla^2 \varphi - \frac{1}{c^2} \frac{\partial^2 \varphi}{\partial t^2} = 0 \quad (2.86)$$

$$\nabla^2 \mathbf{A} - \frac{1}{c^2} \frac{\partial^2 \mathbf{A}}{\partial t^2} = \mathbf{0} \quad (2.87)$$

Consider working in the Coulomb gauge (also called the radiation, or the transverse gauge), in which $\nabla \cdot \mathbf{A} = 0$. In this gauge, and when no charges are present, i.e. $\varphi = 0$, Eq. (2.87) becomes a homogeneous differential equation

$$\nabla^2 \mathbf{A} - \frac{1}{c^2} \frac{\partial^2 \mathbf{A}}{\partial t^2} = \mathbf{0} \quad (2.88)$$

Eq. (2.88) is a wave equation with solutions of the form

$$\mathbf{A}(\mathbf{r}, t) = \frac{\mathbf{A}_0}{2} \left[e^{i(\mathbf{k} \cdot \mathbf{r} - \omega_L t + \delta)} + e^{-i(\mathbf{k} \cdot \mathbf{r} - \omega_L t + \delta)} \right], \quad (2.89)$$

where \mathbf{A}_0 is the peak of the vector potential, \mathbf{k} is the propagation vector, ω_L is the frequency of the radiation and δ is the phase of the field. Expanding the term $e^{i\mathbf{k} \cdot \mathbf{r}}$ in a Taylor series gives

$$e^{i\mathbf{k} \cdot \mathbf{r}} = 1 + \mathbf{k} \cdot \mathbf{r} + \frac{1}{2}(\mathbf{k} \cdot \mathbf{r})^2 + \dots \quad (2.90)$$

Consider the case in which the wavelength is much larger than the size of the atom or molecule. The typical atomic radius is $a_0 = 0.1$ nm, and the typical wavelength of an infrared pulse is $\lambda = 800$ nm. Thus, $k = 2\pi/\lambda = 0.0078$ nm $^{-1}$, and so $kr = 7.8 \times 10^{-4} \ll 1$. Therefore, we can truncate Eq. (2.90) at its first term thus eliminating the spatial dependence in the vector potential. This truncation is known as the dipole approximation. In the dipole approximation we understand that across all space the electrons and protons feel the same electric field. Eq. (2.89) now becomes

$$\mathbf{A}(t) = \frac{\mathbf{A}_0}{2} \left[e^{i(\omega_L t + \delta)} + e^{-i(\omega_L t + \delta)} \right] \quad (2.91)$$

i.e. the vector potential only depends on time. The dipole approximation remains valid in a wide range of situations. It breaks down when short wavelengths are considered and also if pulses of sufficient intensity are used. See the discussion in chapter 2, section 2 of Ref. [215].

If the laser field is intense enough, the velocity that an electron can gain in the field is comparable to the speed of light. In the relativistic limit, the dipole approximation no longer holds and the electron dynamics must be described by the Dirac equation. To estimate an electron's velocity, we employ the semi-classical model of strong field-matter interaction [216]. In this model we consider that only one electron can be ionised, and that after ionisation, the dynamics can be described by Newton's equation of motion. We consider that the electron has zero velocity at the point of ionisation, and we assume that the Coulomb potential can be

neglected. In that case, Newton's second law becomes

$$\ddot{x}(t) = -E(t). \quad (2.92)$$

In the dipole approximation, we write the electric field analogously to the vector potential in Eq. (2.91), i.e.

$$E(t) = E_0 \cos(\omega_L t + \delta). \quad (2.93)$$

Integrating Eq. (2.92) gives the velocity as

$$\dot{x}(t) = \frac{E_0}{\omega_L} \left[\sin(\omega_L t_0 + \delta) - \sin(\omega_L t + \delta) \right] \quad (2.94)$$

where E_0 is the peak of the electric field, t_0 is the time when the electron was ionised. Therefore, the maximum velocity that an electron can gain in the field is

$$v_{\max} = \frac{E_0}{\omega_L}. \quad (2.95)$$

For a laser pulse of $\lambda = 800$ nm and $I = 10^{14}$ W/cm² of intensity, the velocity is about $v_{\max} \approx 0.93$ au. Comparing with the speed of light gives

$$\frac{v_{\max}}{c} \approx \frac{0.93}{137} = 0.0068. \quad (2.96)$$

This small ratio justifies the use of the dipole approximation and the non-relativistic Schrödinger equation. Relativistic effects start to play a role for velocities greater than a tenth of the speed of light. For an IR wavelength ($\lambda \approx 800$ nm), the threshold intensity is about $I_c = 2.1 \times 10^{16}$ W/cm², which is much higher than the intensities employed in this work. For more information about dynamics beyond the dipole approximation and relativistic effects in strong field ionisation, see references [217, 218].

Short duration laser pulses are considered in this work, as opposed to the continuous wave fields described by Eq. (2.91). In that case the field is modified by a pulse envelope. Consider a laser pulse linearly polarised along the z direction. The vector potential can be written as

$$\mathbf{A}(t) = A_0 f(t) \cos(\omega_L t + \phi) \hat{\epsilon}_z, \quad (2.97)$$

where ϕ is now called the carrier-envelope phase, and $f(t)$ is the function that describes the temporal envelope of the pulse. We model the envelope as

$$f(t) = \begin{cases} \sin^2\left(\frac{\pi t}{T}\right) & \text{for } 0 \leq t \leq T \\ 0 & \text{otherwise} \end{cases} \quad (2.98)$$

where T is the pulse duration.

An example of this pulse is shown in Figure 2.3a. This is the pulse shape that we considered

in this thesis. One important aspect of this pulse description is that it ensures that both the electric field and the vector potential are zero at $t = 0$ and at the end of the pulse, $t = T$. Such an envelope overcomes problems associated with Gaussian envelopes which satisfy $f(t) = 0$ when $t = \pm\infty$. For longer pulses, the temporal profile is better described by the trapezoidal shape, those function is

$$f(t) = \begin{cases} \frac{1}{2} \left[1 - \cos \frac{\pi(t)}{t_1} \right] & \text{for } 0 \leq t \leq t_1 \\ 1 & \text{for } t_1 \leq t \leq t_2 \\ \frac{1}{2} \left[1 - \cos \frac{\pi(t-T)}{T-t_2} \right] & \text{for } t_2 \leq t \leq T \\ 0 & \text{otherwise} \end{cases} \quad (2.99)$$

where there is a ramp-on that goes from $t = 0$ to $t = t_1$, then there is a flat region, and later the pulse ends with a ramp-off from $t = t_2$ to $t = T$. An example is shown in Figure 2.3b. The ramp-on and ramp-off usually lasts only a few cycles, in order to avoid pre-ionisation before the pulse reaches its peak intensity.

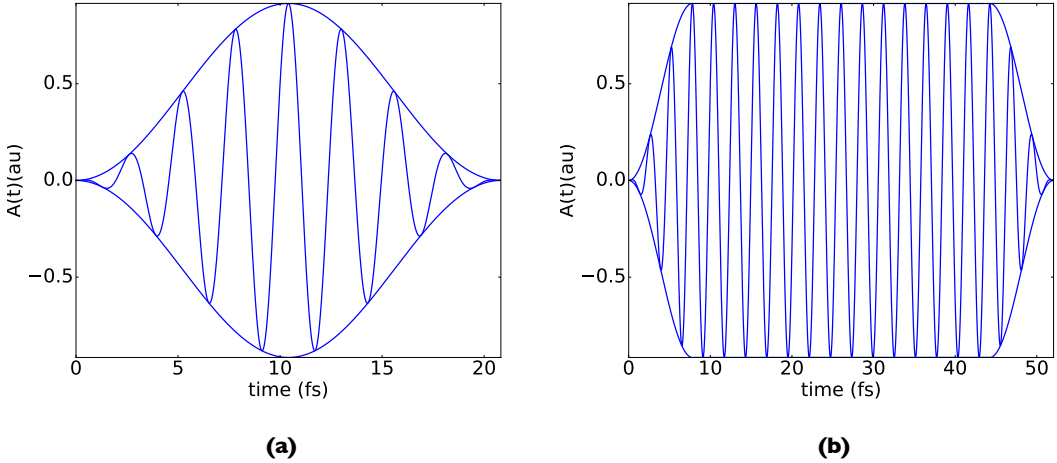


Figure 2.3: Vector potentials with temporal profiles for (a) \sin^2 shape and (b) trapezoidal shape. Both frames corresponds to laser pulses with a wavelength of $\lambda = 800$ nm, and an intensity of $I = 10 \times 10^{14}$ W/cm². In frame (a) the pulses has 8 cycles, whereas in frame (b) the pulse has in total 20 cycles, ramped-on and ramped-off over 3 cycles.

Using Eq. (2.80), the electric field is related with the vector potential by

$$\mathbf{E} = -\frac{1}{c} \frac{\partial \mathbf{A}}{\partial t}. \quad (2.100)$$

Hence, the electric field is just

$$E(t) = E_0 f(t) \sin(\omega_L t + \phi) - \frac{E_0}{\omega_L} \frac{\partial f}{\partial t} \cos(\omega_L t + \phi). \quad (2.101)$$

The above formalism can be extended to consider circularly polarised pulses. Consider a circularly polarised pulse which lies in the $x - z$ plane and propagates in the y direction. The

vector potential can be written as

$$\mathbf{A}_{r/l}(t) = A_0 f(t) [\cos(\omega_L t + \phi) \hat{\epsilon}_x \pm \sin(\omega_L t + \phi) \hat{\epsilon}_z]. \quad (2.102)$$

where positive sign in the brackets correspond to right-handed (*r*) polarisation, whereas the negative sign corresponds to left-handed (*l*) polarisation. The electric field is

$$\mathbf{E}_{r/l}(t) = E_x(t) \hat{\epsilon}_x \pm E_z(t) \hat{\epsilon}_z, \quad (2.103)$$

where

$$E_r(t) = \frac{E_0}{\sqrt{2}} f(t) \sin(\omega_L t + \phi) - \frac{E_0}{\omega_L \sqrt{2}} \frac{\partial f}{\partial t} \cos(\omega_L t + \phi) \quad (2.104)$$

and

$$E_l(t) = -\frac{E_0}{\sqrt{2}} f(t) \cos(\omega_L t + \phi) - \frac{E_0}{\omega_L \sqrt{2}} \frac{\partial f}{\partial t} \sin(\omega_L t + \phi). \quad (2.105)$$

2.7 Gauge invariance

Expanding the Hamiltonian given in Eq. (2.4) we obtain

$$\begin{aligned} \mathcal{H} = & -\frac{1}{2\mu_e} \nabla_e^2 + \frac{1}{\mu_e c^2} \mathbf{A}^2(t) - i \frac{1}{2\mu_e c} \nabla_e \cdot \mathbf{A}(t) - i \frac{1}{2\mu_e c} \mathbf{A}(t) \cdot \nabla_e \\ & - \frac{1}{2\mu_N} \nabla_N^2 - \frac{Z_1}{|\mathbf{r} - \mathbf{R}|} - \frac{Z_2}{|\mathbf{r} + \mathbf{R}|} + \frac{Z_1 Z_2}{\mathbf{R}}. \end{aligned} \quad (2.106)$$

In Section 2.7 we have assumed the Coulomb gauge, $\nabla \cdot \mathbf{A} = 0$, so

$$\nabla \cdot (\mathbf{A}\Psi) = \mathbf{A} \cdot (\nabla\Psi) + (\nabla \cdot \mathbf{A})\Psi = \mathbf{A} \cdot (\nabla\Psi) \quad (2.107)$$

for any wavefunction Ψ . Therefore, ∇ and \mathbf{A} commute. We can now write the Hamiltonian in Eq. (2.106) as

$$\mathcal{H} = -\frac{1}{2\mu_e} \nabla_e^2 + \frac{1}{\mu_e c^2} \mathbf{A}^2(t) - i \frac{1}{\mu_e c} \mathbf{A}(t) \cdot \nabla_e - \frac{1}{2\mu_N} \nabla_N^2 - \frac{Z_1}{|\mathbf{r} - \mathbf{R}|} - \frac{Z_2}{|\mathbf{r} + \mathbf{R}|} + \frac{Z_1 Z_2}{\mathbf{R}}. \quad (2.108)$$

This is the velocity gauge description of the electron-field interaction (also known as minimal coupling gauge). The ponderomotive terms, those which contains $\mathbf{A}^2(t)$, have an average value which is equal to the ponderomotive energy. These terms can be removed from the Hamiltonian with the gauge transformation

$$\Psi(\mathbf{r}, \mathbf{R}, t) \rightarrow \exp \left[\frac{i}{c^2} \int_0^t \mathbf{A}^2(t') dt' \right] \Psi(\mathbf{r}, \mathbf{R}, t) \quad (2.109)$$

as they only introduce a phase in the wavefunction. Applying this transformation to the TDSE, the Hamiltonian now has the form

$$\mathcal{H} = -\frac{1}{2\mu_e}\nabla_e^2 - i\frac{1}{\mu_e c}\mathbf{A}(t)\cdot\boldsymbol{\nabla}_e - \frac{1}{2\mu_N}\nabla_N^2 - \frac{Z_1}{|\mathbf{r} - \mathbf{R}|} - \frac{Z_2}{|\mathbf{r} + \mathbf{R}|} + \frac{Z_1 Z_2}{\mathbf{R}}. \quad (2.110)$$

Another popular form for expressing the Hamiltonian is achieved with the transformation

$$\Psi(\mathbf{r}, \mathbf{R}, t) \rightarrow \exp\left[\frac{i}{c}\mathbf{r}\cdot\mathbf{A}(t)\right]\Psi(\mathbf{r}, \mathbf{R}, t). \quad (2.111)$$

Applying this transformation to the TDSE with the Hamiltonian given by Eq. (2.108) gives

$$\mathcal{H} = -\frac{1}{2\mu_e}\nabla_e^2 - \frac{1}{\mu_e}\mathbf{r}\cdot\mathbf{E}(t) - \frac{1}{2\mu_N}\nabla_N^2 - \frac{Z_1}{|\mathbf{r} - \mathbf{R}|} - \frac{Z_2}{|\mathbf{r} + \mathbf{R}|} + \frac{Z_1 Z_2}{\mathbf{R}}, \quad (2.112)$$

where we have used Eq. (2.100). This Hamiltonian is known as the length gauge description of the electron-field interaction, and was first introduced by Maria Göppert-Meyer [44].

The main difference between the length and velocity gauge is the description of mechanical momentum. In velocity gauge, the canonical momentum will be a slowly varying function. Consider the gauge-invariant mechanical momentum for the electron

$$\mathbf{P}(t) = \frac{d\mathbf{r}}{dt} = i[\mathcal{H}, \mathbf{r}]. \quad (2.113)$$

In the velocity gauge, the mechanical momentum is just

$$\mathbf{P}(t) = \mathbf{p} - \frac{1}{c}\mathbf{A}(t), \quad (2.114)$$

whereas for the length gauge the mechanical momentum coincides with the canonical momentum, i.e. $\mathbf{P}(t) = \mathbf{p}(t)$. For an electron oscillating in the presence of the laser field the amplitude of motion is given by

$$\boldsymbol{\alpha}(t) = \frac{1}{c} \int_0^t dt' \mathbf{A}'(t'). \quad (2.115)$$

$\boldsymbol{\alpha}(t)$ is known as the quiver amplitude of the electron in the field. The momentum of the electron due to the laser field is then

$$\dot{\boldsymbol{\alpha}}(t) = \frac{1}{c}\mathbf{A}(t). \quad (2.116)$$

Hence the momentum of the electron given by the field is separated from the canonical momentum. Therefore, in the velocity gauge, the canonical momentum will be a slowly varying function that can be seen as the mean mechanical momentum averaged over one cycle of the field, whereas in the length gauge the canonical momentum will be a rapidly varying function.

Another frame, not widely used, is the Kramers-Henneberger (KH) gauge, also called the acceleration gauge. This gauge moves the reference frame to that of the oscillating electron. Now the ions potential is time-dependent, and the fast oscillations of the electron in the field

is removed. The transformation for this gauge is given by [219]

$$\Psi(\mathbf{r}, \mathbf{R}, t) \rightarrow \exp \left[-\frac{i}{c} \mathbf{p} \cdot \int_0^t dt' \mathbf{A}(t') \right] \Psi(\mathbf{r}, \mathbf{R}, t). \quad (2.117)$$

The resulting Hamiltonian has the form

$$\mathcal{H} = -\frac{1}{2\mu_e} \nabla_e^2 - \frac{1}{2\mu_N} \nabla_N^2 - \frac{Z_1}{|\mathbf{r} + \boldsymbol{\alpha} - \mathbf{R}|} - \frac{Z_2}{|\mathbf{r} + \boldsymbol{\alpha} + \mathbf{R}|} + \frac{Z_1 Z_2}{\mathbf{R}}. \quad (2.118)$$

where $\boldsymbol{\alpha}$ is the quiver oscillation of the electron in the laser field. It was first used by Henneberger to study multiphoton process with a perturbative treatment at a non-perturbative laser intensities. More recently, it has been used to study atomic stabilisation in laser fields at very high intensities [220, 221].

Throughout this thesis we will be use both velocity and length gauges descriptions.

2.8 Summary

In this chapter we have discuss the theoretical treatment used for the quantum mechanical description of the hydrogen molecular ion exposed to intense laser fields. In particular, for the range of laser frequencies and intensities employed in this work, the semi-classical description of the laser-molecule system is justified, where the laser radiation is simplified assuming the dipole approximation. Moreover, our treatment assumes a non-Born-Oppenheimer description of the molecular Hamiltonian, thus treating quantum-mechanically both electronic and nuclear degrees of freedom. In Section 2.4 the Lagrangian formalism is introduced in order to express the time-dependent Schrödinger equation in generalised curvilinear coordinates. Transformations for scaled cylindrical and Cartesian coordinates systems, that they will be used later in Chapter 3, are introduced to efficiently solve the TDSE. The laser radiation is simplified assuming the dipole approximation. Finally, a brief review on gauge descriptions commonly used in laser-matter interactions and their transformations are given in Section 2.7.

Programming computers to perform simple human tasks is difficult: getting a computerized robot to vacuum a room or empty a dishwasher, even to minimal standards, is a problem that has outstripped the abilities of several generations of researchers in artificial intelligence. By contrast, no special effort is required to program a computer to behave in unpredictable and annoying ways. When it comes to their capacity to screw things up, computers are becoming more human every day. “To err is human. To really screw things up requires a computer.”

Seth Lloyd, Programming the Universe

3

Numerical implementation of the laser-driven H_2^+ model: The THeREMIN and RHYthMIC codes

In this chapter we present computational details of the codes we have developed to implement the solutions of the TDSE using the methods described in Chapter 2. THeREMIN (vibraTing HydRogEn Molecular IoN) and RHYthMIC (vibRating HYdrogen Molecular Ion in Cartesian) are codes which solve the time-dependent Schrödinger equation for H_2^+ interacting with intense ultra-short laser pulses. The codes treat both the electronic and the nuclear motion quantum mechanically. THeREMIN solves the TDSE for H_2^+ in the presence of a linearly polarised laser pulse with the polarisation direction parallel to the molecular axis. The code solves the TDSE using cylindrical coordinates and thus treats the electronic dynamics in 2D. RHYthMIC is an extension of THeREMIN which relaxes the constraints on parallel transitions. It solves the TDSE in Cartesian coordinates, treating the electronic dynamics in 3D. Arbitrary orientations between the molecule and laser can be considered and laser pulses of general polarisation (including circularly polarised pulses) can be described. For the laser frequencies and intensities generally considered in strong field physics and attosecond science, it is reasonable to restrict the nuclear motion along the internuclear axis. Therefore, THeREMIN solves the TDSE in 3D (2D+1D), while RHYthMIC solves it in 4D (3D+1D). The dimensionality of the codes, in addition to the sizes of the grids needed to describe interactions with strong laser pulses, results in large memory requirements. For that reason, both codes are specifically designed at the outset to exploit high performance computing (HPC) facilities. Both codes have been written in modern Fortran 2003, and parallelised using the MPI protocol.

The chapter is arranged as follows: Section 3.1 presents the grid method used for discretising the TDSE and the use of coordinates scalings to adapt the resulting meshes to a particular problem. Section 3.2 introduces the Arnoldi method, used to numerically propagate the TDSE in time. In Section 3.3 the wavefunction splitting methods used to avoid reflections from the edges of the grid are detailed. Finally, Section 3.4 introduces the grid parallelisation strategy employed and gives some code scaling results for both THeREMIN and RHYthMIC.

3.1 Finite-difference grid technique

The numerical treatment chosen to solve the TDSE is the finite-difference method. In finite-differences we discretise a continuous space, x , in a set of n grid points, $\{x_i, i = 1, \dots, n\}$. In most cases the grid points are equidistant with spacing Δx . Functions that live in this space, $f(x)$, take values at each grid point, $f_i \equiv f(x_i)$.

The method is easily extended to several dimensions. In the follow we will introduce the formalism for one dimension. For coordinate x we employ N_x points to cover the range $x_{\min} \leq x \leq x_{\max}$, where the grid spacing is given by

$$\Delta x = \frac{x_{\max} - x_{\min}}{N_x - 1}. \quad (3.1)$$

This results in equally spaced grids. The grid points are labelled by

$$x_j = x_{\min} + (j - 1)\Delta x, \quad j = 1, \dots, N_x. \quad (3.2)$$

Derivatives are approximated by finite difference formulae. In particular central difference rules are used for greatest accuracy and because they result in Hermitian finite difference matrices. The formulae for the derivative of order k of a function $f(x)$ at the grid point x_j can be written as

$$\frac{\partial^k}{\partial x^k} f(x_j) \approx \sum_{\nu=-N_{\text{fd}}}^{N_{\text{fd}}} C_{\nu}^{(k)} f(x_{j+\nu}) \quad (3.3)$$

where the $C_{\nu}^{(k)}$ are the finite difference coefficients for the k^{th} derivative, and the order of the finite difference formula is $2N_{\text{fd}} + 1$. Particular finite difference rules are obtained by approximating $f(x)$ by a Lagrange interpolating polynomial. An efficient algorithm to obtain finite different coefficients at any order can be found in Ref. [222, 223]. These formula are used for the derivative operators appearing in the scaled coordinates in Section 2.5.

3.1.1 Calculation of the Coulomb potential in Cartesian coordinates

From Eq. (2.4), the molecular Coulomb potential is defined as

$$V(\mathbf{r}, \mathbf{R}) = -\frac{Z_1}{|\mathbf{r} - \mathbf{R}/2|} - \frac{Z_2}{|\mathbf{r} + \mathbf{R}/2|} + \frac{Z_1 Z_2}{\mathbf{R}}, \quad (3.4)$$

where Z_1 and Z_2 are the charges of the nuclei, \mathbf{r} denotes the electronic position vector and \mathbf{R} the internuclear position vector. The easiest way to describe this potential on a finite difference grid is to evaluate Eq. (3.4) at each grid point. However, if a grid point coincides with the position of one of the ions, i.e. $|\mathbf{r} \pm \mathbf{R}/2| = 0$, this will result in a singularity on the grid. In order to avoid such singularities while also describing the Coulomb potential accurately we obtain the potential associated at each ion, $V_k(\mathbf{r}, \mathbf{R})$ by solving the corresponding Poisson equation $\nabla^2 V = -4\pi\rho$

$$\nabla^2 V_k(\mathbf{r}, \mathbf{R}) = -4\pi Z_k \delta(\mathbf{r} - \mathbf{R}_k) \quad \text{for } k = 1, 2. \quad (3.5)$$

In this equation $Z_k \delta(\mathbf{r} - \mathbf{R}_k)$ is the volume charge density that describes a point charge located at each ion. To avoid a singularity we approximate the Dirac delta function as a narrow Gaussian, i.e. [171, 210]

$$\delta(\mathbf{r}, \mathbf{R}_k) \approx A_k \exp \left[-\frac{(\mathbf{r} - \mathbf{R}_k)^2}{\gamma_k^2} \right] \quad (3.6)$$

where A_k is a normalisation factor which must satisfy

$$\int d\mathbf{r} A_k \exp \left[-\frac{(\mathbf{r} - \mathbf{R}_k)^2}{\gamma_k^2} \right] = 1, \quad (3.7)$$

and

$$\int d\mathbf{r} \mathbf{r} A_k \exp \left[-\frac{(\mathbf{r} - \mathbf{R}_k)^2}{\gamma_k^2} \right] = \mathbf{R}_k. \quad (3.8)$$

By tuning the width of this Gaussian, γ_k , we can accurately tune to the correct energy states on the grid. The Poisson equation is solved numerically on a finite difference grid using a conjugate gradient method. In order to apply the boundary conditions required for solving the Poisson equation we use a multipole expansion of the charge distribution [224]. Hence, the potential given by each ion is

$$V_k(\mathbf{r} - \mathbf{R}_k) = \frac{\int d\mathbf{r} \rho_k(\mathbf{r}' - \mathbf{R}_k)}{|\mathbf{R}_k|} + \sum_{\mu} p_{\mu} \frac{r_{\mu}}{|\mathbf{R}_k|^3} + \sum_{\mu, \nu} q_{\mu} \frac{3r_{\mu}r_{\nu} - \delta_{\mu, \nu} R_k^2}{|\mathbf{R}_k|^5} \quad \mu, \nu = x, y, z, + \dots \quad (3.9)$$

where $\rho_k(\mathbf{r})$ is the charge density associated with the ion k , $\delta_{\mu, \nu}$ is the Kronecker delta, p_{μ} is the dipole moment

$$p_{\mu} = \int d\mathbf{r} r_{\mu} \rho_k(\mathbf{r} - \mathbf{R}_k), \quad (3.10)$$

and $q_{\mu, \nu}$ is the quadrupole moment

$$q_{\mu, \nu} = \int d\mathbf{r} \frac{1}{2} r_{\mu} r_{\nu} \rho_k(\mathbf{r} - \mathbf{R}_k). \quad (3.11)$$

For more detail on solving the Poisson equation, see Reference [224]. The total Coulomb potential created by both ions is simply

$$V(\mathbf{r}, \mathbf{R}) = \sum_{k=1}^2 V_k(\mathbf{r}, \mathbf{R}_k) \quad (3.12)$$

This approach to obtain the Coulomb potential has been implemented by Modine et. al. [210] and Dundas [171] in the context of electronic structure calculations and multi-electronic molecules.

3.2 Time propagation

We start by writing the solution of the TDSE in Eq. (2.2) as

$$\Psi(t + \Delta t) = \hat{U}(t + \Delta t, t)\Psi(t) \approx \exp^{-i\mathcal{H}\delta t} \Psi(t) \quad (3.13)$$

where

$$\hat{U}(t + \Delta t, t) = \exp(-i\mathcal{H}\Delta t) \quad (3.14)$$

is the time evolution operator. We can obtain this expression for the evolution operator by Taylor expanding $\Psi(t + \Delta t)$. This gives

$$\Psi(t + \Delta t) \approx \Psi(t) + \frac{\partial\Psi(t)}{\partial t}\Delta t + \frac{1}{2!}\frac{\partial^2\Psi(t)}{\partial t^2}(\Delta t)^2 + \frac{1}{3!}\frac{\partial^3\Psi(t)}{\partial t^3}(\Delta t)^3 + \dots \quad (3.15)$$

Now from the TDSE we have $\partial_t\Psi = -i\mathcal{H}\Psi$ and $\partial_t^2\Psi = (-i\mathcal{H})^2 - i(\partial_t\mathcal{H})\Psi$. Neglecting the time derivatives of \mathcal{H} we can write the time-derivatives in Eq. (3.15) in terms of successive applications of the Hamiltonian

$$\frac{\partial^k\Psi(t)}{\partial t^k} = (-iH)^k \Psi(t). \quad (3.16)$$

This approximation is justified since the time derivatives of \mathcal{H} can be approximated as sinusoidal perturbations of the electric field that have an intensity three or four orders of smaller than the intensity of the electric field. Thus Eq. (3.15) can be written as

$$\Psi(t + \Delta t) = \sum_{k=0}^{\infty} \frac{(-i\mathcal{H}(t)\Delta t)^k}{k!} \Psi(t). \quad (3.17)$$

and so

$$U(t + \Delta t, t) = \sum_{k=0}^{\infty} \frac{(-i\mathcal{H}(t)\Delta t)^k}{k!} = \exp(-i\mathcal{H}\Delta t) \quad (3.18)$$

Hence the simplest explicit approximation to this propagator is the n^{th} order Taylor Series

$$U(t + \Delta t, t) = \sum_{k=0}^n \frac{(-i\mathcal{H}(t)\Delta t)^k}{k!}. \quad (3.19)$$

One significant drawback of this propagation is that it is not unitary. We would like to overcome this problem while retaining much of the desirable qualities for applying it. We can achieve this using the Arnoldi propagator. We begin by constructing a set of vectors that span the Krylov subspace K_{n+1}

$$K_{n+1} \equiv \{\Psi, \mathcal{H}\Psi, \mathcal{H}^\epsilon\Psi, \dots, \mathcal{H}^n\Psi\}, \quad (3.20)$$

Gram-Schmidt orthonormalisation is required to obtain the orthonormal set $\{Q_0, Q_1, \dots, Q_n\}$ that span K_{n+1} . These vectors form the $(n + 1)$ columns of the orthonormal matrix Q (where $Q_0 = \Psi/|\Psi|$). This means that Q_k is obtained by calculating $\mathcal{H}Q_{k-1}$ and then orthonormalising this vector with respect to Q_0, \dots, Q_{k-1} . We can write

$$\mathcal{H}Q_k = h_{k+1,k}Q_{k+1} + h_{k,k}Q_k + \dots \quad (3.21)$$

where h_{ij} are the coefficients of the upper-Hessenberg matrix of dimension $(n + 1) \times (n + 1)$. The above equation can be expressed in matrix form as

$$h = Q^\dagger \mathcal{H} Q. \quad (3.22)$$

We point out that h is the Hamiltonian in the Krylov subspace. At this point, we can interpret the Arnoldi method as a orthonormal reduction of the Hamiltonian to a Hessenberg form.

Now, we can approximate \mathcal{H} by

$$\mathcal{H} = QhQ^\dagger \quad (3.23)$$

in Eq. (3.13) using the fact that $(QhQ^\dagger)^m = Qh^mQ^\dagger$, so that

$$e^{-i\hat{\mathcal{H}}\delta t} = Q e^{-ih\delta t} Q^\dagger. \quad (3.24)$$

The exponentiation through direct diagonalisation of h is inexpensive compared to the same operation over \mathcal{H} . Not only is h a tridiagonal matrix (if \mathcal{H} is Hermitian), but is also generally much smaller than the size of the typical Hamiltonian in our calculations.

One of the main benefits of the Arnoldi method is that it gives a more accurate solution of Eq. (3.13) compared to other propagators, allowing the use of larger time-steps obtaining results with the same level of accuracy. This is because if the wavefunction is a linear combination of $n + 1$ eigenvectors of the Hamiltonian \mathcal{H} , these eigenvectors are contained in the Krylov subspace K_{n+1} . Hence the propagator is unitary and the solution is exact up to order $n + 1$. We can mention other advantages, for example

- the computational overhead rises linearly with the order of the propagator,
- the method also provides an efficient way of calculating the eigenstates of the Hamiltonian, and
- the performance of the Arnoldi method scales linearly with the order of the propagator. This feature makes the propagator over twice as efficient compared to other explicit

propagators, such as the Taylor series.

These advantages make the use of the Arnoldi method ideal for massively parallel calculations. Indeed, this method has been widely used in many studies such as the study of the laser-driven helium atom [225, 226], the study of laser-driven H₂⁺ [153, 154] and the study of N₂ and benzene using a mixed quantum-classical approach (the nuclei are described classically and the electrons quantumly through TDDFT) [171, 172].

3.3 Absorbing boundaries

Studying laser-matter interactions involves the description of high-energy electrons ionised by the intense laser field. These electrons can travel far away from the parent system, meaning that large simulation boxes are required to calculate the dynamical response. Since we are limited to finite grid sizes, the use of some type of absorbing boundary is mandatory to avoid reflections of the wavefunction from the edges. Therefore, the absorption will divide our space in two regions: in the absorption region, the outgoing wavefunction will be damped exponentially, whereas in the inner region the evolution of the wavefunction will be unaffected by the absorber. There are three methods usually employed for absorbing boundaries. We will describe each of these considering a wavefunction in one spatial dimension, $\Psi(r)$.

- **Mask function absorption (MFA):** The first and most simple approach is to write a mask function that splits the wavefunction in two parts

$$\Psi(r) = M(r)\Psi(r) + [1 - M(r)]\Psi(r) \quad (3.25)$$

where the first term in the right-hand side represents the bound states, located near the origin, and the second term represents the outgoing ionised wavepackets. This method is usually called the mask function absorption (MFA) [227, 228] or splitting technique. The masking function effectively acts as a potential that, in the limit of larger distances, damped the outgoing flux to zero. The transition between regions must be smooth to avoid artefacts as the wavepacket moves between the two zones.

- **Complex absorbing potential (CAP):** The second approach is called the complex absorbing potential method. It is similar to MFA. In this case, we introduce a complex potential which has a purely imaginary part in the outer region, that acts as an absorber of the electron wavepacket. As in the MFA method, the transition between the inner and outer region must be smooth. The Hermiticity of the Hamiltonian is broken by the use of complex potentials, so the Hamiltonian is no longer unitary. Although this is precisely what we are looking for (i.e. to lose population at the edges of the box), one must be especially careful when we work with non-hermitian Hamiltonians because now eigenfunctions are not square-integrable. A discussion of CAP can be found in [227, 229].
- **Exterior Complex Scaling (ECS):** This is the most sophisticated of the three methods, and it is called Exterior Complex Scaling. It consists of transforming the coordinate

space to the complex plane from a certain scaling radius [230]:

$$r \rightarrow z(r) = \begin{cases} r & \text{if } |r| < r_0 \\ e^{i\theta} (r \pm r_0) \mp r_0 & \text{if } |r| > r_0 \end{cases} \quad (3.26)$$

Assuming this scaling, the outgoing wavepackets can be written as

$$\exp(ipr) \rightarrow \exp(ipr_0) \exp(ip \cos \theta(r - r_0)) \exp(-p \sin \theta(r - r_0)) \quad (3.27)$$

where the last term causes exponentially damping. The method has been optimised for long wavelengths [149], as the problem of absorption of outgoing wavepackets with low frequencies arises in strong field ionisation. The implementation is called infinite-range exterior complex scaling (ir-ECS). It was firstly coded using the finite-elements method (FEM), and now it has been extended to finite-elements methods with the discrete variable representation method (FEM-DVR) and finite difference methods [151].

In our work we use the MFA. We have considered two forms for the mask function, namely

$$M(r) = \begin{cases} 1 & \text{if } |r| < r_A \\ \exp\left[-\left(\frac{|r|-r_A}{\sigma}\right)^2\right] & \text{if } |r| > r_A \end{cases} \quad (3.28)$$

and

$$M(r) = \begin{cases} 1 & \text{if } |r| < r_A \\ 1 - \alpha(|r|-r)^5 & \text{if } |r| > r_A \end{cases} \quad \alpha = \frac{1 - M_f}{(r_{\max} - r_A)^5} \quad (3.29)$$

In these equations r_A is the position at which the absorber starts, r_{\max} is the maximum extent of the grid in that dimension, M_f is the value of the masking function at the edges of the grid, and finally σ controls the slope of the function (3.28). The advantage of the function (3.29) rather than the function (3.28) is that it causes a smooth damping up to the 4th derivative.

Using these definitions of the mask functions in 1D, the total mask function applied to the n -dimensional wavefunction is

$$M(x^i, \dots, x^n) = \prod_{k=1}^n M(x^k) \quad (3.30)$$

where $\{x^1, \dots, x^n\}$ are the electronic coordinates of the particular coordinate system we are using.

3.4 Parallelisation of the codes

Parallelisation of the resulting codes is performed using a technique called regular domain decomposition, in which each processor is responsible for a particular subset of the grid, in that case the full finite-difference grid is split across processors. In the following, to illustrate the parallel scheme, we consider a 2D spatial grid, with coordinates x^1 and x^2 . Along the x^1 direction, N_{loc}^1 local points are stored per processor, so the total number of points in this

direction is $N^1 = N_P^1 N_{\text{loc}}^1$, where N_P^1 is the number of processors in the x^1 direction. The x^2 coordinate is distributed analogously, so the total number of processors involved in the calculation is

$$N_P = N_P^1 N_P^2. \quad (3.31)$$

We can label each processor as

$$P_\rho^i \quad i = 1, 2 \text{ and } \rho = 1, \dots, N_p^i. \quad (3.32)$$

To map a local point x_k^i on processor ρ we write

$$x_\rho^i = -x_{\text{max}}^i + (N_{\text{loc}}^i \times P_\rho^i + k - 1) \times \Delta x^i, \quad k = 1, \dots, N_{\text{loc}}^i. \quad (3.33)$$

In order to calculate the derivatives present in the Laplacian operator and in the laser interaction term we required N_{fd} halo points per dimension. The following communication pattern can be applied: we must only communicate the points that are located at the boundaries of each processor with their neighbours, in a process called boundary swapping. An illustration of this scheme can be seen in figure 3.1, where the squares represents the points that lies in the processor's domain, whereas the dots represents the halo points that the processor needs from their neighbours to calculate the derivatives at the grid points on the edges. In this example we use a 5-point finite-difference rule, so only two halo points are required for communication on each boundary. Swapping only halo points for finite-difference operators with neighbouring processors reduces the communication overhead between processors. In fact, the calculation of the Laplacian operator is the cause of the major communication bottleneck during calculations. Using the parameters presented in table 3.1, we show scaling results for the THeREMIN and RHYthMIC codes in figure 3.2. In these figures, we have kept the number of points per processor constants while increasing the total number of processors involved in the calculations. In a perfect situation in which no communication overhead where present, the plots will represent a flat line at a constant calculation time, because the calculation time would be independent of the number of processors used. Our results shows a scaling which is near constant for both codes. In figure 3.2a the calculation time increases 10%, whereas in figure 3.2b the calculation time only increases 5%. The better scaling found in RHYthMIC is due to the lower workload in THeREMIN compared to RHYthMIC, which causes a larger communication bottleneck. On the contrary, in RHYthMIC the larger calculation time spend by each processor compared to the overhead caused by communication reduces the communication bottleneck.

3.5 Summary

In this chapter we have discussed the numerical implementation our H_2^+ model, which as a result two codes have been written: THeREMIN, implemented in cylindrical coordinates, and RHYthMIC, implemented in Cartesian coordinates. We have presented how the time-

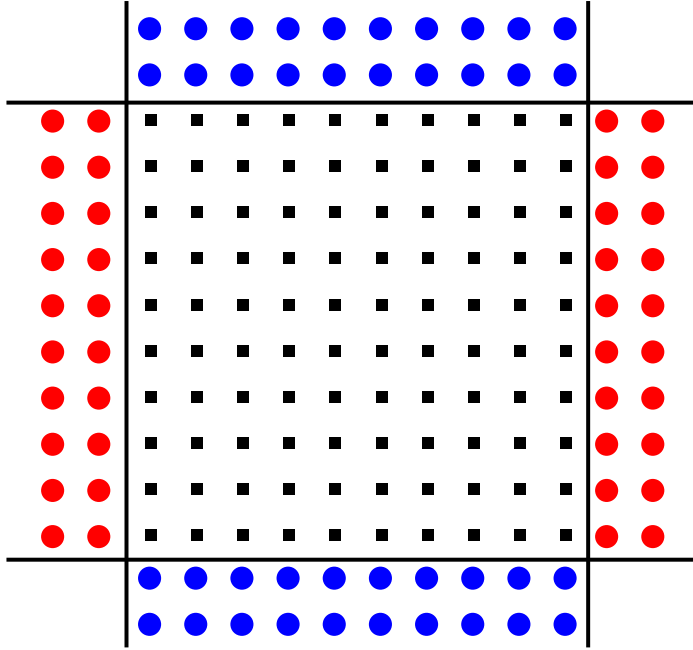


Figure 3.1: Diagram of the communication scheme for a 2D finite-difference grid. The lines represent the processor boundaries and the squares represents the local points. The dots denote the halo points for a given processors, where the red and blue dots are the halo points in the x^1 and x^2 direction respectively.

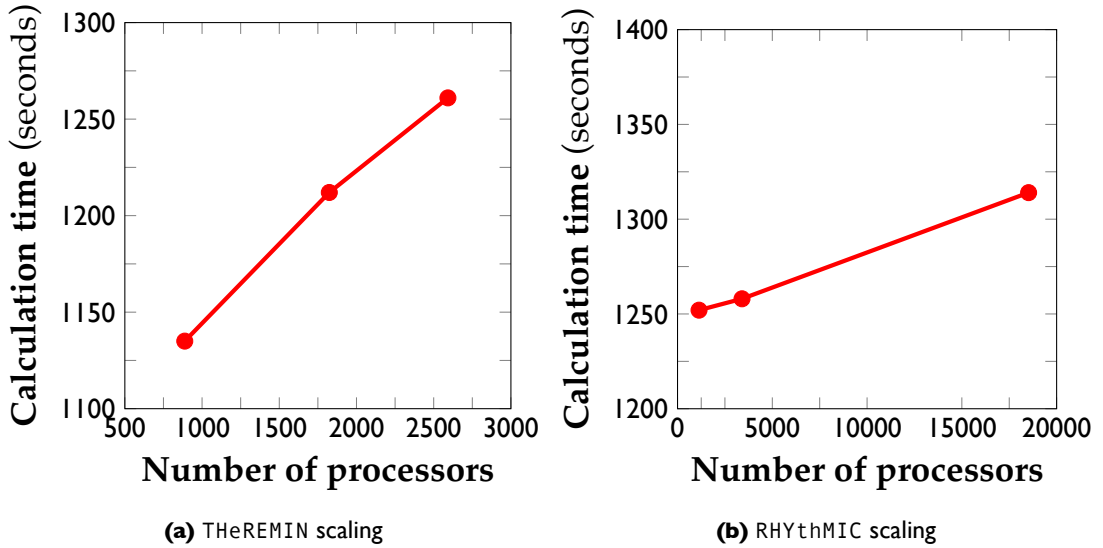


Figure 3.2: Scaling results for the THeREMIN and RHYthMIC codes. The plots correspond to the time that a calculation takes depending on the total number of processors. On the tests we have kept the number of grid points per core constant. The points in (a) corresponds to number of cores 888, 1824, 259, while in (b) corresponds to number of 1134, 3402 and 18522. Perfect scaling will result in horizontal lines.

dependent Schrödinger equation can be efficiently solved by using a finite-difference grid technique. The use of scaled coordinates allow us to accumulate a higher density of points in specific regions in order to improve the accuracy of the calculation. Also, the Coulomb potential in Cartesian coordinates is obtained from the solution of the Poisson equation, since direct evaluation of the Coulomb potential potentially arises a grid discontinuity if one of the grid

Simulation	Number of cores	Grid Extent
1	$P_R = 8$	$0 \leq R \leq 42$
	$P_\rho = 3$	$0 \leq \rho \leq 67$
	$P_z = 37$	$-102 \leq z \leq 102$
2	$P_R = 8$	$0 \leq R \leq 42$
	$P_\rho = 4$	$0 \leq \rho \leq 103$
	$P_z = 57$	$-157 \leq z \leq 157$
3	$P_R = 8$	$0 \leq R \leq 42$
	$P_\rho = 4$	$0 \leq \rho \leq 103$
	$P_z = 81$	$-223 \leq z \leq 223$

(a) THeREMIN parameters

Simulation	Number of cores	Grid Extent
1	$P_R = 2$	$0 \leq R \leq 14$
	$P_x = 9$	$-31 \leq x \leq 31$
	$P_y = 9$	$-31 \leq y \leq 31$
	$P_z = 7$	$-24 \leq z \leq 24$
2	$P_R = 2$	$0 \leq R \leq 14$
	$P_x = 9$	$-31 \leq x \leq 31$
	$P_y = 9$	$-31 \leq y \leq 31$
	$P_z = 21$	$-73 \leq z \leq 73$
3	$P_R = 2$	$0 \leq R \leq 14$
	$P_x = 21$	$-73 \leq x \leq 73$
	$P_y = 21$	$-73 \leq y \leq 73$
	$P_z = 21$	$-73 \leq z \leq 73$

(b) RHYthMIC parameters

Table 3.1: Tables containing the data employed in the scaling results shown above. Table (a) corresponds to the THeREMIN results, while table (b) corresponds to the RHYthMIC results.

points coincides with the position of one of the ions. For time propagating the wavefunction, two different method are discussed: the Taylor series and the Arnoldi method. The Taylor series is a straightforward method based on a expansion in time of the wavefunction, where the terms in the Taylor series can be obtain by applying successively the Hamiltonian on the wavefunction. At the same time, the Arnoldi method is based on the diagonalisation of the Hamiltonian in the Krylov subspace using a Lanczos iteration. The performance of the latter method presents advantages over the Taylor series, which converts the Arnoldi method an ideal propagator for massively parallel calculations. We ended this chapter illustrating how the codes can be parallelised across many processors, and describing a technique required for the calculation of the Laplacian operator called boundary swapping, that allows efficient communication between neighbour processors. Scaling results for the codes is also presented, where we have plotted calculation time against number of processors. For the THeREMIN code calculation time increases 10%, while for the RHYthMIC code calculation time only increases 5%.

4

Role of the vibrational states in high harmonic generation and strong-field ionisation and dissociation of H₂⁺

As we have already seen in the introduction, the interaction of strong laser pulses with atoms and molecules leads to the generation of high harmonic radiation. This highly non-linear phenomena is the source of light pulses of attosecond duration in the XUV regime. The development and advances in this new kind of laser sources have inaugurated a new field in physics: attosecond science.

The attosecond domain is the natural timescale for electronic processes occurring in atoms and molecules. Many fundamental processes such as ionisation, dissociation or dissociative ionisation happen within the sub-femtosecond timescale. If we consider molecules, electron-ion correlations play a crucial role in molecular dissociation, dissociative ionisation and electron localisation. Those mechanisms are the key to understanding more complex molecular processes such as charge migration and chemical reactivity. In order to study these processes in detail, accurate theoretical tools that take into account electron-nuclear correlation are required.

The hydrogen molecular ion represents one of the best platforms to understand the complexity of electron-ion correlations, since it only involves one electron and two protons. Nowadays, it is one of the few systems that allows the quantum-mechanical treatment of electrons and ions on an equal footing and in full dimensionality. With a non-Born-Oppenheimer approach it is possible to study in detail the rich variety of phenomena, such as electron cor-

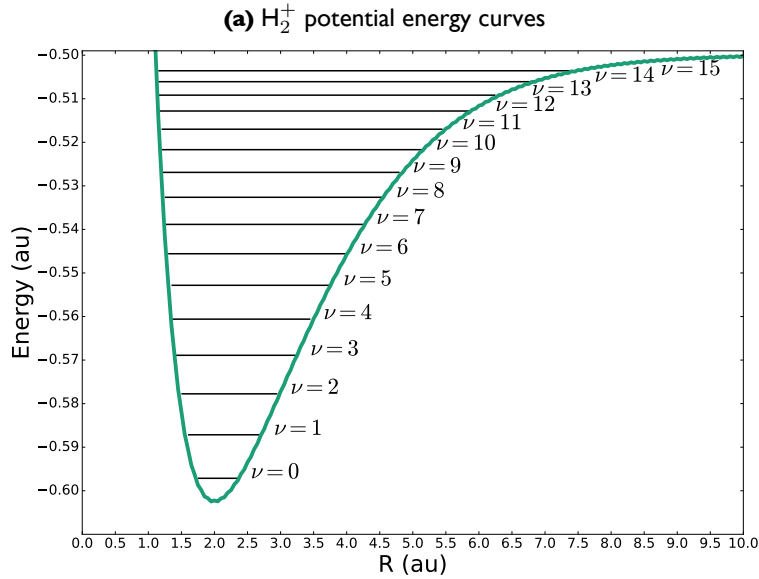
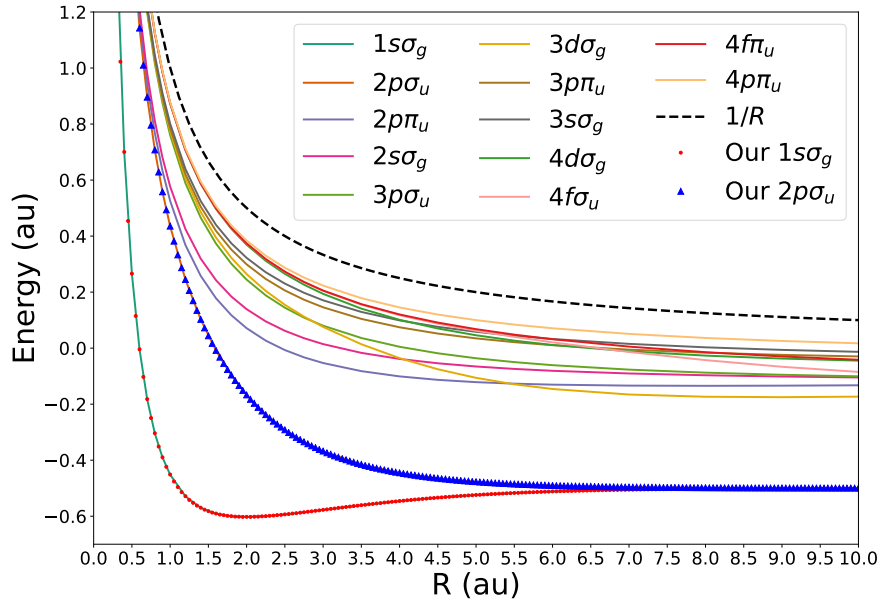
relation [106, 112] that occur in this simple molecule. Due to the huge computational effort required to solve this problem, an implementation of a TDSE solver that is as accurate and efficient as possible is essential. The codes presented in this thesis, THeREMIN and RHYthMIC, were created to achieve these goals.

The chapter is arranged as follows: Section 4.1 we present static properties of H_2^+ , calculated using a static Hamiltonian with THeREMIN. We compare calculated eigenenergies of the molecule with previous results available in the literature. We also discuss the convergence criteria for the grid parameters used in these calculations. In Section 4.2 dissociative ionisation of H_2^+ by short duration VUV laser pulses is studied. The photon energy of the laser pulse is tuned to match the energy gap between the ground σ_g state and the σ_u dissociative state. This scenario has been studied previously using a 1D description of the electron dynamics and a 1D description of the ionic dynamics [231]. In Section 4.3 we study HHG in H_2^+ exposed to intense IR laser pulses. In these calculations we calculate the response starting from different vibrational states.

4.1 Static properties of H_2^+

As we saw in the Chapter 2, to include nuclear vibration the nuclear coordinate, R , is treated as another quantum coordinate rather than a fixed parameter in our calculations. In that case, the resulting molecular wavefunction, $\Psi(\mathbf{r}, R, t)$, is not factorised into an electronic part and a nuclear part, as in the Born-Oppenheimer approximation. Calculating time-independent solutions of the TDSE therefore gives us information about the vibrational states of the molecule.

The non-Born-Oppenheimer eigensolutions for the molecular Hamiltonian are obtained using the Thick-restarted Lanczos (TRLan) method, which is an iterative scheme based on the eigen-decomposition of the Krylov-subspace Hamiltonian [232]. The method is implemented in the library TRLan [233, 234], which calculates the eigenenergies and eigenvectors for a given Hamiltonian. In Figure 4.1a we present the potential energy curves of the H_2^+ molecule. The solid lines are calculated using a close-coupling method (courtesy of Alicia Palacios). In our work to test the accuracy of the eigenstates obtained with THeREMIN we only compare the two lowest electronic states, $1s\sigma_g$ and $2p\sigma_u$ potential energy curves, calculated with THeREMIN, plotted over the corresponding solid lines. We found good agreement between the close-coupling results and our results obtained solving our finite difference Hamiltonian. In the diagram, only states with σ and π symmetry are represented. We note that linearly polarised light aligned parallel to the molecular axis can only excite σ_g/σ_u states ($\Delta M = 0$), whereas linearly polarised light aligned perpendicular to the molecular axis will populate π_g/π_u states ($\Delta M = \pm 1$). Subsequently photon absorptions may reach σ or δ states and so on. We note that, since in THeREMIN only allows laser polarisation to be parallel to the molecular axis, only σ states can be obtained in our calculation. In figure 4.1b we present the fifteen lowest eigenvalues of the molecular Hamiltonian: these correspond to the fifteen lowest vibrational states of the H_2^+ molecule in the σ_g potential energy surface.



(b) H_2^+ potential energy curves. Zoom in showing the lowest vibrational states of the molecule.

Figure 4.1: (a) Diagram of the potential energy curves for the H_2^+ molecule as a function of the internuclear distance R . The solid curves are calculated using a close-coupling method (courtesy of Alicia Palacios), while the lines with dots and triangles are obtained using THeREMIN. (b) Detail of the $1s\sigma_g$ state, in which the first lowest vibrational energy levels are shown. Our potential energy curves were calculated with THeREMIN at fixed internuclear distances using a grid spacing of $\Delta\rho = 0.1$ and $\Delta z = 0.05$. The vibrational eigenenergies, labelled with the quantum number ν , were calculated with THeREMIN using grid spacings of $\Delta R = 0.05$, $\Delta\rho = 0.1$ and $\Delta z = 0.05$.

In order to test the accuracy of the eigenenergies obtained with THeREMIN we have compared against accurate results available in the literature. The ten lowest energies are shown in table 4.1, which have been calculated using both a coarse and a fine grid. The grid parameters

corresponding to each set can be found in the caption of table 4.1. In addition, we compare our results with two sets of previous results, from references [155, 235]. In Previous (1) [155] a finite difference grid is also used, and the eigenenergies are obtained from the diagonalisation of the Hamiltonian using the PETSc [236–238] and SLEPc [239–241] routines. In contrast, in Previous (2) [235] an accurate variational method using a basis set in perimetric coordinates is implemented. The diagonalisation of the Hamiltonian is performed with a Lanczos algorithm [242]. The largest difference between Present (1) and Previous (2) is less than 1%.

State	Present (1)	Present (2)	Previous (1)	Previous (2)
$\nu = 0$	-0.59707	-0.59714	-0.59740	-0.59714
$\nu = 1$	-0.58713	-0.58715	-0.58744	-0.58716
$\nu = 2$	-0.57920	-0.57774	-0.57808	-0.57775
$\nu = 3$	-0.57271	-0.56890	-0.56930	-0.56891
$\nu = 4$	-0.56064	-0.56060	-0.56106	-0.56061
$\nu = 5$	-0.54971	-0.55283	-0.55337	-0.55284
$\nu = 6$	-0.54644	-0.54558	-0.54619	-0.54559
$\nu = 7$	-0.53807	-0.53885	-0.53951	-0.53886
$\nu = 8$	-0.53563	-0.53262	-0.53334	-0.53263
$\nu = 9$	-0.52949	-0.52690	-0.52766	-0.52691

Table 4.1: Vibrational energy states of the H_2^+ molecule. The first and second columns correspond with calculations using THeREMIN, while the third and fourth columns correspond to previous results. In Present (1) the grid parameters employed are $\Delta\rho = 0.1$, $\Delta z = 0.20$ and $\Delta R = 0.20$ (coarse grid), while in Present (2) the grid parameters are $\Delta\rho = 0.1$, $\Delta z = 0.05$, $\Delta R = 0.05$ (fine grid). Previous (1) column correspond to the results available in Niederhausen et al. [155], while column Previous (2) contain the results found in Hilico et al. [235]

4.2 Dissociative ionisation of H_2^+ by VUV laser pulses

In the following section we discuss results for the interaction of H_2^+ with an ultrashort laser pulse in the VUV frequency regime at moderate intensities. We present two sets of results: In the first set of results we consider the molecule is initially in the vibrational ground state ($\nu = 0$) of the $1s\sigma_g$ potential energy curve, and in the second set the molecule is initially in the third vibrational state ($\nu = 2$) of the $1s\sigma_g$ potential energy curve. Both initial states have been previously obtained with TRLan method.

4.2.1 Dissociative ionisation from the $1s\sigma_g(\nu = 0)$ state

We now consider the response of the H_2^+ molecule exposed to a VUV laser pulse whose central frequency is resonant with the energy gap between the $1s\sigma_g(\nu = 0)$ state (which corresponds to the ground state of the molecule) and the $2p\sigma_u$ state (which corresponds with the first excited and first dissociating state of the molecule). A schematic diagram of the molecular transition in terms of potential energy curves are shown in Figure 4.2.

Consider a 3-cycle pulse. The total duration of the pulse is approximately 1 fs, the central frequency is $\omega_L = 0.43$ au (11.23 eV), which corresponds to a wavelength of $\lambda = 105.3$ nm, and with a peak intensity of $I = 8.4 \times 10^{12}$ W/cm². These laser parameters are well within the multiphoton regime, and so we expect multiphoton ionisation to be the dominant ionisation mechanism. In particular for the given photon energy, see Figure 4.2, the one and two-photon ionisation channels are expected to be forbidden since three photons are required to reach the continuum.

The grid parameters used in the calculation are given in table 4.2. For these parameters the size of the resulting wavefunction is 22377600 elements. For the time evolution, we use an 18th order Arnoldi propagator with a time-step $\Delta t = 0.05$ au. The wavefunction is propagated for 60 cycles after the end of the pulse. The resulting calculation was parallelised over 270 cores and the calculation time was 56 minutes.

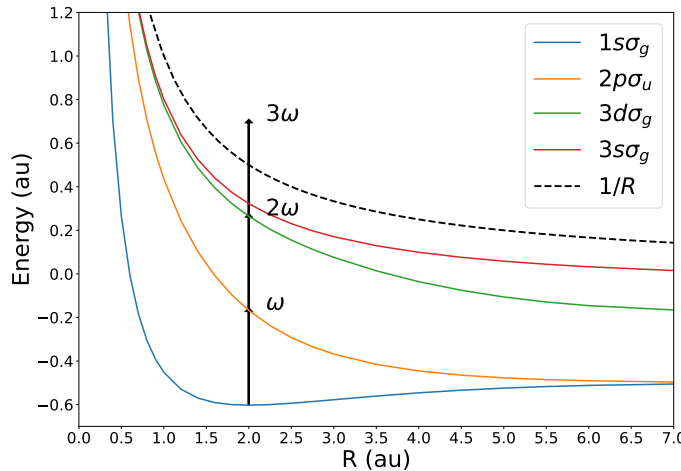


Figure 4.2: The four lowest potential energy surfaces for H_2^+ together with the Coulomb explosion limit. The arrows represent the photon energy associated with a laser wavelength of 105.3 nm. This wavelength is tuned to bridge the energy gap between the $1s\sigma_g$ state and the $2p\sigma_u$ dissociating state.

Coordinate	Points per core	Number of cores	Grid spacing	Mesh extent
R	80	10	0.05	$0 \leq R \leq 40$
ρ	28	3	0.1	$0 \leq \rho \leq 24.3$
z	37	9	0.2	$-32.4 \leq z \leq 32.4$

Table 4.2: Grid parameters employed in the calculation of the response of H_2^+ exposed to a 3 cycle VUV laser pulse, having a wavelength of $\lambda = 105.3$ nm and a peak intensity of $I = 8.4 \times 10^{12}$ W/cm².

Plots of the probability density at various instants during the time evolution are present in Figures 4.3 and 4.4. Also, an animation showing the full evolution of the probability density

can be found in the additional material contained in the CD supplied in this thesis (file labelled movie1.mp4 in the CD). Figure 4.3 presents the density integrated over the ρ coordinate

$$P(R, z, t) = \int d\rho \Psi^*(R, \rho, z, t)\Psi(R, \rho, z, t) \quad (4.1)$$

while Figure 4.4 presents the density integrated over the R coordinate

$$P(\rho, z, t) = \int dR \Psi^*(R, \rho, z, t)\Psi(R, \rho, z, t). \quad (4.2)$$

The former density provides information about the electron dynamics along the laser polarisation direction together with the vibrational motion along R . The latter density presents information about the electron dynamics only, and it is useful for understanding when a 3D description of the electron dynamics is essential.

In Figures 4.3a and 4.4a we present density plots of the ground state wavefunction in the $\nu = 0$ vibrational state. The probability density is centred at the origin of the coordinates in the $\rho - z$ plot, while in the $R - z$ plot is centred at $z = 0$ and $R = 2$, which corresponds to the equilibrium internuclear distance of the H_2^+ . During the interaction with the pulse, the probability density oscillates back and forth along the z axis, i.e. parallel to the laser polarisation direction. This oscillation is visible in the movie. Figures 4.3b and 4.4b presents density plots at the end of the 3-cycle laser pulse. At this point several vibrational states of the molecule have been excited, causing a distortion of the density in the $R - z$ plane. In addition, some wavefunction is ejected out of the molecule along the z axis, a signature of ionisation. Thus we are observing ionisation and vibrational excitation. At this point we expect the molecule to have been excited to the $2p\sigma_u$ state. Therefore if we consider the time-evolution of this excited state over a longer timescale we should see evidence of dissociation.

In the $P(R, z)$ plot, in Figure 4.3c, 5 fs after the end of the pulse, we can distinguish a group of two additional nuclear wavepackets at different internuclear separations. These wavepackets travel out along the lines $z = \pm R/2$ and are thus associated with dissociation. The wavepacket at the largest internuclear separation has the highest density. However, in Figure 4.4c, $P(\rho, z)$ plot, the motion of the nuclear wavepackets is still visible as wavepacket along the z direction.

Figures 4.3d, 4.3e, 4.3f and 4.3g for $P(R, z)$ and Figures 4.4d, 4.4e, 4.4f and 4.4g for $P(\rho, z)$ present the densities at 10 fs, 12 fs, 14 fs and 15 fs respectively. We see a electron wavepacket oscillating between the nuclear centres. This electron transfer is due to a coupling between states with gerade and ungerade symmetry, in particular the coupling between $1s\sigma_g$ and $2p\sigma_u$ states. The linear combination of these two states causes an asymmetry in the electron density that causes electron localisation around one of the nuclei [106, 112]. Finally in Figures 4.3h and 4.3i we clearly see the molecule dissociated with two nuclear wavepackets far out along the

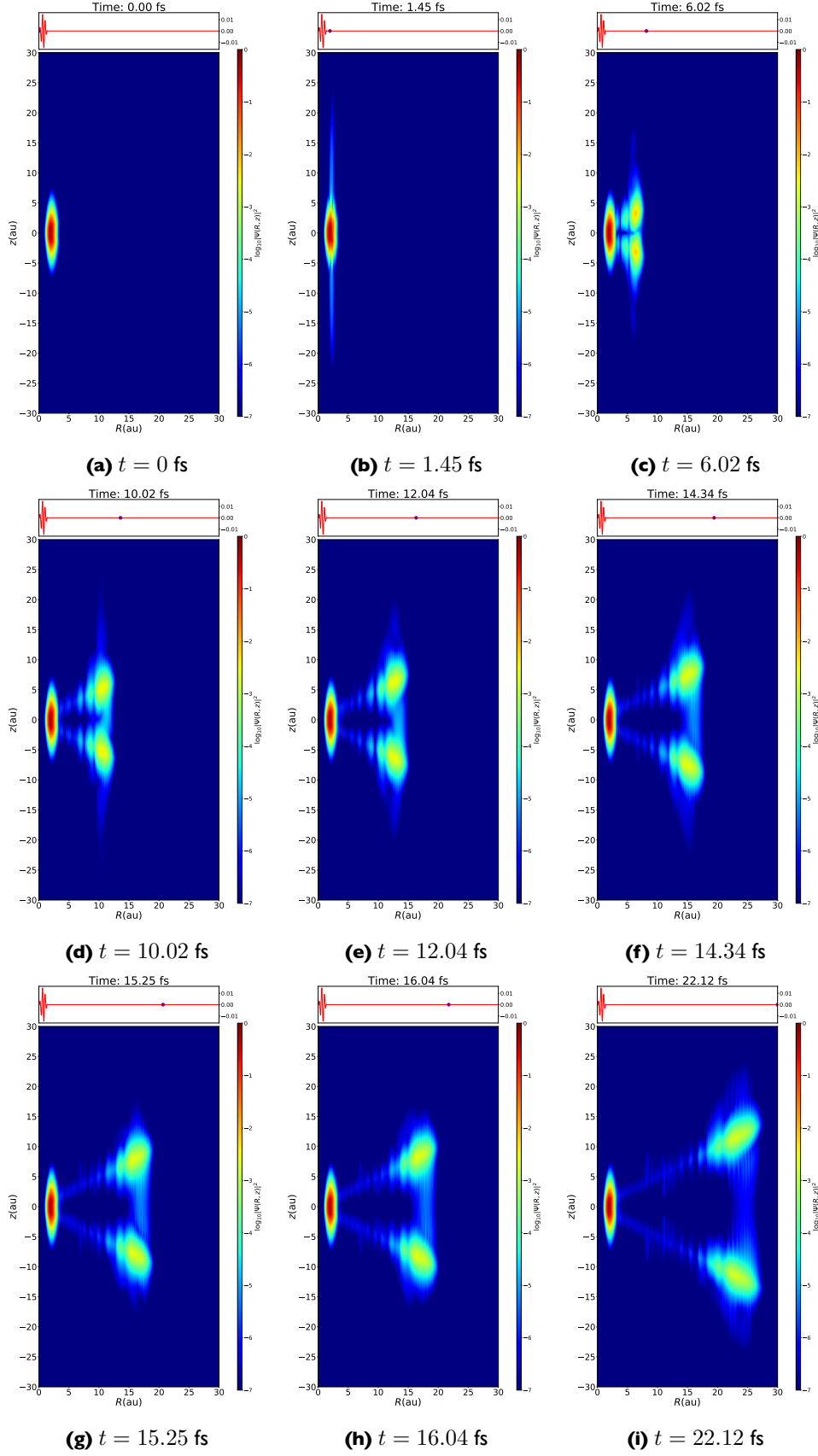


Figure 4.3: Probability density plots $P(R, z)$ of H_2^+ at particular instants during its interaction with a 3-cycle VUV laser pulse, having a wavelength of $\lambda = 105.3 \text{ nm}$ (photon energy of $\omega_L = 0.43 \text{ Ha}$) and a peak intensity of $I = 8.4 \times 10^{12} \text{ W/cm}^2$. Each frame corresponds to (a) $t = 0 \text{ fs}$, (b) $t = 1.45 \text{ fs}$, (c) $t = 6.02 \text{ fs}$, (d) $t = 10.02 \text{ fs}$, (e) $t = 12.04 \text{ fs}$, (f) $t = 14.34 \text{ fs}$, (g) $t = 15.25 \text{ fs}$ (h) $t = 16.04 \text{ fs}$, (i) $t = 22.12 \text{ fs}$. The electric field is shown at the top of each frame, where the position of the dot represent the specific time of the calculation.

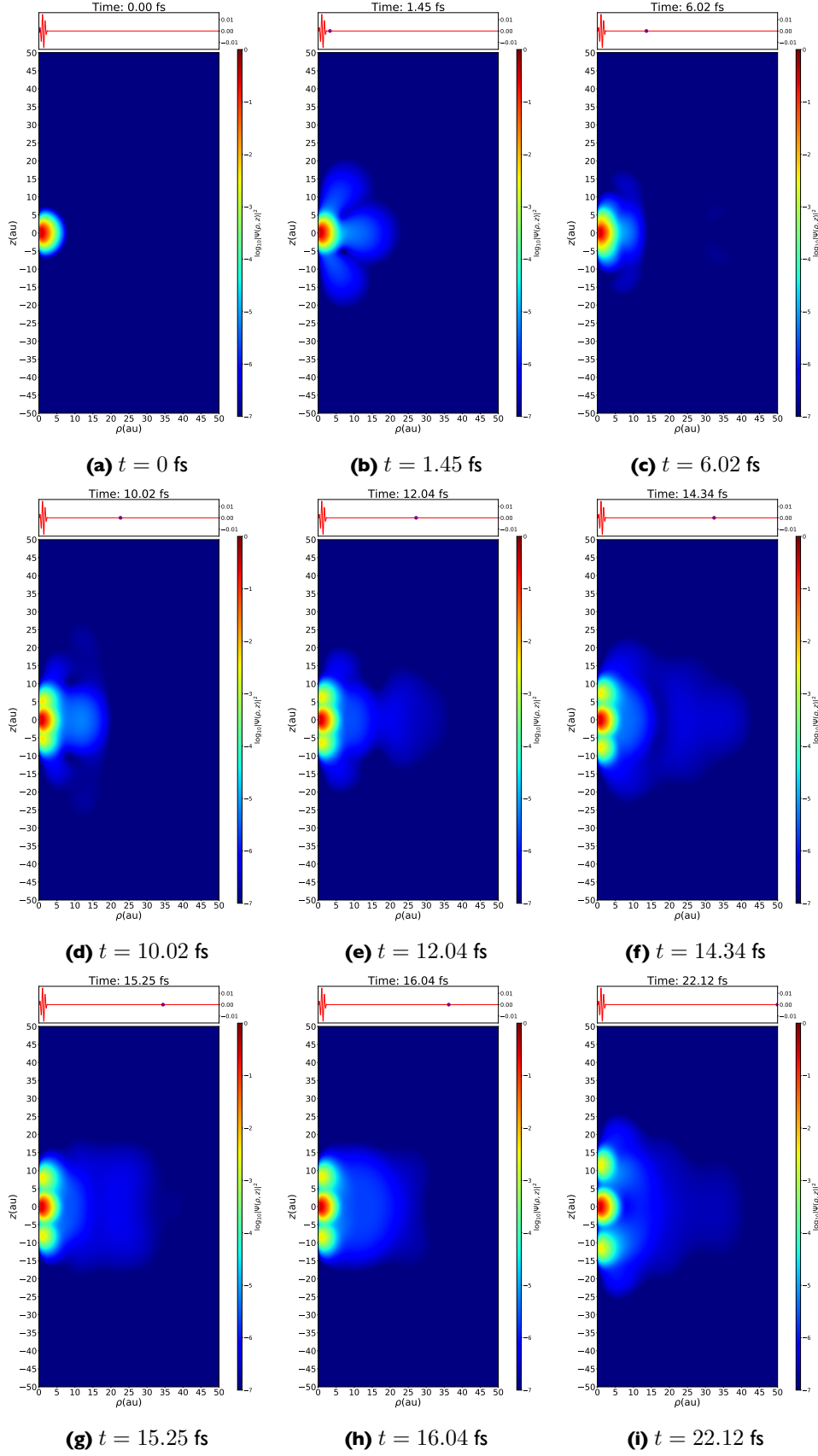


Figure 4.4: Probability density plots $P(\rho, z)$ of H_2^+ at particular instants during its interaction with a 3-cycle VUV laser pulse, having a wavelength of $\lambda = 105.3 \text{ nm}$ (photon energy of $\omega_L = 0.43 \text{ Ha}$) and a peak intensity of $I = 8.4 \times 10^{12} \text{ W/cm}^2$. Each frame corresponds to (a) $t = 0 \text{ fs}$, (b) $t = 1.45 \text{ fs}$, (c) $t = 6.02 \text{ fs}$, (d) $t = 10.02 \text{ fs}$, (e) $t = 12.04 \text{ fs}$, (f) $t = 14.34 \text{ fs}$, (g) $t = 15.25 \text{ fs}$ (h) $t = 16.04 \text{ fs}$, (i) $t = 22.12 \text{ fs}$. The electric field is shown at the top of each frame, where the position of the dot represent the specific time of the calculation.

lines $z = \pm R/2$ for the density $P(R, z)$, while in the $P(\rho, z)$ plots these nuclear wavepackets are separated along the z direction, visible in Figures 4.4h and 4.4i.

Now we integrate the density further. Consider integrating the probability density over all spatial degrees of freedom apart from one. We consider two cases, $P(z, t)$ and $P(R, t)$. Plots of these densities will allow us to follow the behaviour of the system in these coordinates over all times considered. These density plots are shown in Figure 4.5. In Figure 4.5a, we distinguish again between a central thick stripe centred at $z = 0$, which represents the bound states, and two diagonal stripes, one for positive and negative z , both representing dissociating wavepackets. We also see a fast modulation of the density in the z direction which begins before the end of the laser pulse. We associate this modulation with a superposition between bound states of the molecule. The period of the oscillations for the first 4 fs is approximately $\Delta t \approx 0.3507 \text{ fs}$. Using the uncertainty principle

$$\Delta E \approx \frac{2\pi}{\Delta T} \quad (4.3)$$

we obtain an energy difference $\Delta E \approx 0.4317 \text{ Ha}$, which is precisely the energy gap between the $1s\sigma_g$ ground state and the $2p\sigma_u$ excited state of the molecule at $R = 2 a_0$, but also coincides with the energy gap between the $2p\sigma_u$ and the $3d\sigma_g$ states, that are connected by a two-photon transition. At a later time, the period of these oscillations slowly increase. At 22 fs, the period is approximately $\Delta t \approx 0.388 \text{ fs}$, which is coincident with the energy gap between the $2p\sigma_u$ and the $3d\sigma_g$ states at $R = 22 a_0$. This confirms that a two-photon transition took place, and indicates that the superposition between the two states have evolved along the potential energy curves.

In the lower frame, Figure 4.5b we distinguish a horizontal stripe centred at $R = 2 a_0$, which represents the bound states of the molecule, and a diagonal structure composed by three main stripes of different widths, which corresponds to the group of three nuclear wavepackets ejected after the interaction with the laser pulse, between 2 and 4 fs. These diagonal stripes are a clear signature of dissociation, and their slope is the velocity of the nuclear wavepacket; therefore from the slope it is possible to retrieve the energy of the nuclear fragments. We see that the width of the diagonal stripes increases over time, which indicates the spread of the wavepacket over time.

To study the evolution of the nuclear wavepackets more in detail, we calculate the nuclear trajectories using classical equations of motion. In a conservative system, the force can be written as the gradient of a potential [243]

$$F(R) = -\frac{d}{dR}V(R) \quad (4.4)$$

where $F(R)$ is the conservative force, and $V(R)$ is the potential energy. Then, we can substi-

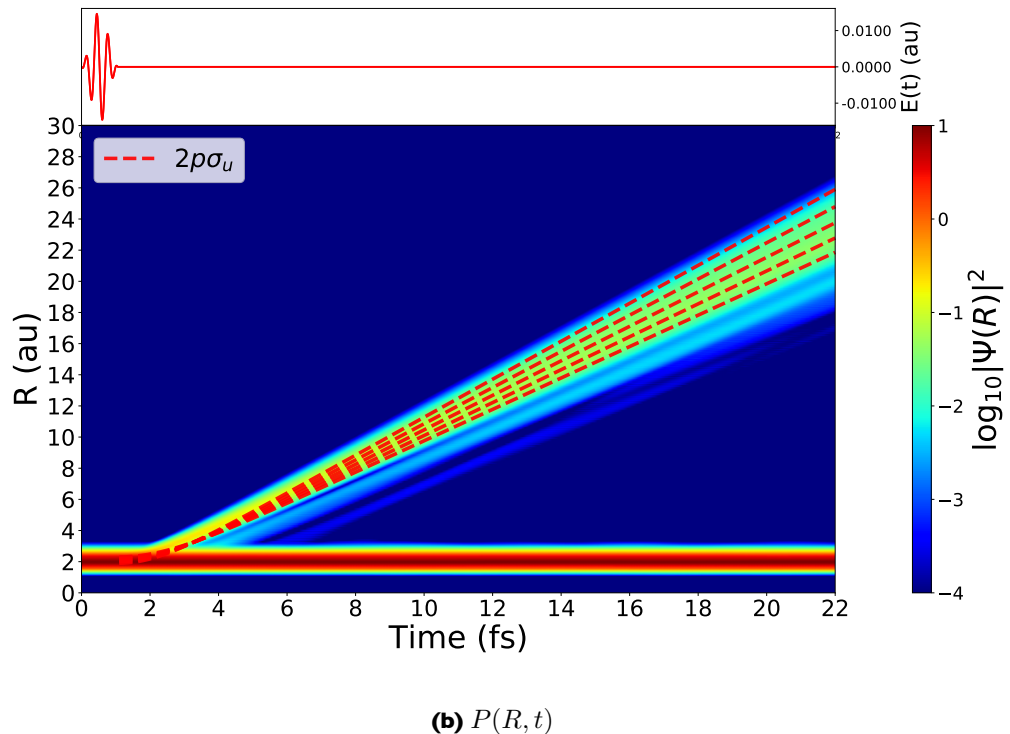
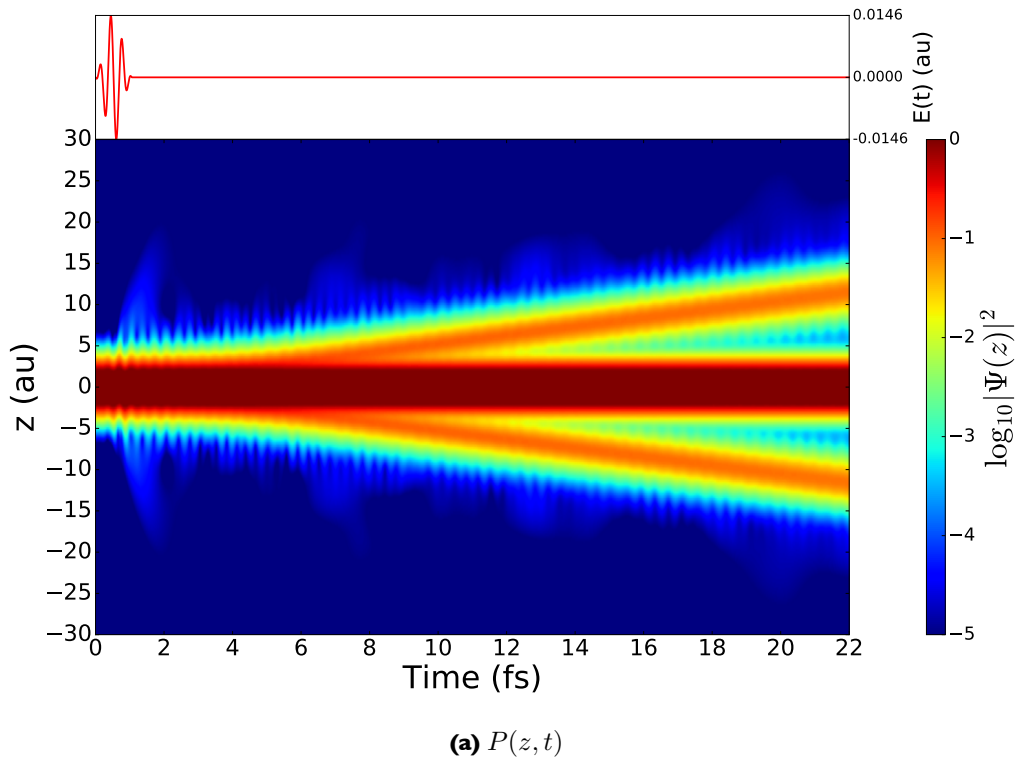
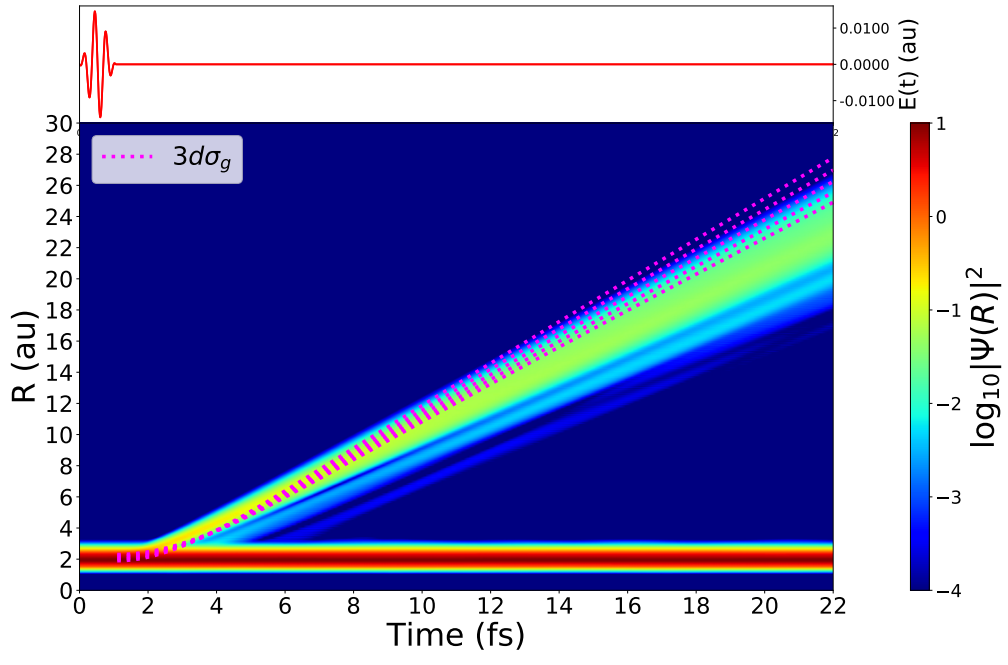
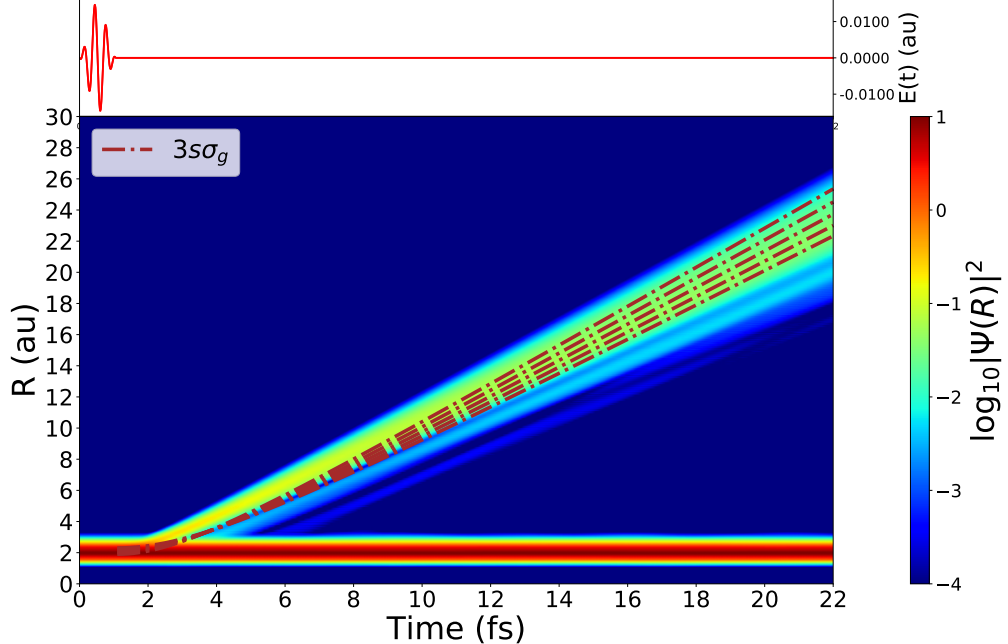


Figure 4.5: Probability density plots of H_2^+ (starting from the $\nu = 0$ vibrational state) over time during its interaction with a 3-cycle VUV laser pulse having a wavelength $\lambda = 105.3$ nm (photon energy $\omega_L = 0.43$ Hartrees) and a peak intensity of $I = 8.4 \times 10^{12} \text{ W/cm}^2$. In (a) we present the density $P(z, t)$ while in (b) we present $P(R, t)$. The electric field used in the calculation is shown at the top of the figure, where the position of the red circle represents the specific time of the calculation. In (b) the dashed lines represent the classical trajectories of the nuclear wavepackets along the $2p\sigma_u$ potential energy curves of the molecule.



(a) $P(z, t)$



(b) $P(R, t)$

Figure 4.6: Probability density plots of H_2^+ (starting from the $\nu = 0$ vibrational state) over time during its interaction with a 3-cycle VUV laser pulse having a wavelength $\lambda = 105.3$ nm (photon energy $\omega_L = 0.43$ Hartrees) and a peak intensity of $I = 8.4 \times 10^{12} \text{ W/cm}^2$. In both plots we present the density $P(R, t)$. The dashed lines represent the classical trajectories of the nuclear wavepackets along (a) the $3d\sigma_g$ and (b) $3s\sigma_u$ potential energy curves of the molecule. The electric field used in the calculation is shown at the top of the figure, where the position of the red circle represents the specific time of the calculation.

tute Eq.(4.4) in Newton's equation of motion to get

$$\frac{d^2R(t)}{dt} = -\frac{1}{\mu_N} \frac{dV(R)}{dR} \quad (4.5)$$

where $R(t)$ is the position of the wavepacket, and μ_M is reduced nuclear mass. In order to calculate the trajectory of the nuclear wavepackets, we transform Eq. (4.5) in a system of coupled first order differential equations,

$$\frac{dv(t)}{dt} = -\frac{1}{\mu_N} \frac{dV(R)}{dR} \quad (4.6)$$

$$\frac{dr(t)}{dt} = v(t) \quad (4.7)$$

In order to numerically obtain the trajectories $R(t)$, instead of solving Eq. (4.5), it is better to solve consistently the equations of motion (4.6) using the Verlet algorithm [244]

$$v(t_{i+1}) = v(t_i) + a(t_i)\Delta t \quad (4.8)$$

$$r(t_{i+1}) = r(t_i) + v(t_{i+1})\Delta t \quad (4.9)$$

where $a(t_i)$ denotes the acceleration, which is equal to the right hand side of Eq. (4.5), $t_{i+1} = t_i + \Delta t$, and Δt is the time step used in the calculation. If look at Figure 4.5, we can assume that the wavepacket motion starts at $t = 0.5$ fs, thus the initial conditions are $a_0 = a(t = 0.5)$, $v_0 = v(t = 0.5) = 0$ (the time is given in fs). For each potential energy curve, we consider a bunch of trajectories whose initial positions cover the spread of the initial nuclear wavepackets over a range of internuclear distances R from $r_0 = r(t = 0.5) = 1.7 a_0$ to $r_0 = r(t = 0.5) = 2.5 a_0$.

In Figures 4.5b and 4.6 we observe the bunch of classical trajectories that corresponds to a nuclear wavepacket travelling along the $2p\sigma_u$, $3d\sigma_g$ and $3s\sigma_g$ potential energy curve of the H_2^+ , that are superimposed to the main diagonal stripe. We observe that, although the slope of the trajectories does not match perfectly with the slope of the diagonal, the trajectories that are in better agreement are the ones corresponding to the $2p\sigma_u$ and the $3s\sigma_g$ states. Thus, the coincidences with these two states are a signature of a one and even two-photon transitions. However, in order to resolve the role of the dissociative states in the ionisation and dissociation of H_2^+ observables as the kinetic energy released (KER) spectra or the correlated electron-nuclear energy spectra are required.

As we can see from Figure 4.2, one-photon transition at the laser frequency $\omega = 0.43$ Hartrees is resonant with the $2p\sigma_u$ state. In addition, the pulse bandwidth is broad enough to cause the two-photon transition to excite not only the $3d\sigma_g$ state, but also the $3s\sigma_g$ state. The use of short laser pulses of only a few femtoseconds allows the excitation of molecular states with $(N - 1)$ -photon transitions when the photon energy is such that N photons are required to reach the ionisation threshold of the molecule [245]. In contrast, for a longer pulse, the band-

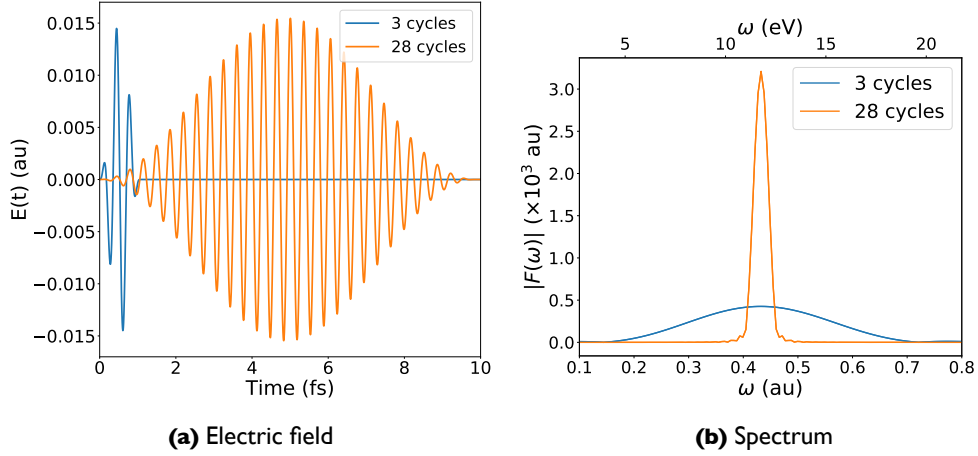


Figure 4.7: Electric field (a) and spectrum (b) of a 3-cycle and a 28-cycle VUV laser pulses, both having a wavelength of $\lambda = 105.3$ nm and a peak intensity of $I = 8.4 \times 10^{12}$ W/cm². The 3-cycle has approximately a duration of 1 fs, while the 28-cycle pulse has a duration of 9.8 fs. The photon energy for both pulses is 0.43 Ha (11.7 eV) and the bandwidth is 0.288 Ha (7.848 eV) and 0.031 Ha (0.841 eV) for the 3 cycle and the 28-cycle pulse respectively.

width would be narrower as the duration of the pulse increases (see Figure 4.7), approaching to the continuous wave limit as the pulse length increases. In that limit, three-photon ionisation dominate over one-photon and two-photon ionisation. However, in this case, the photon energy is always resonant with the first excited state, $2p\sigma_u$. In Figure 4.8, we show the time evolution of the probability densities $P(z, t)$ and $P(R, t)$ after interaction with a 28-cycle laser pulse (the other laser parameters are kept the same). The animation labelled movie2.mp4 in the supplied CD shows the time evolution for this case. This time, ionisation happens on a longer timescale. As it is shown in Figure 4.8a ionisation occurs when the pulse is ramping on, where a single broad nuclear wavepacket escapes the molecule continuously from 3 to 10 fs approximately. During the pulse, we observe the fast oscillations in time in the probability density along z . The oscillations have a period of approximately $\Delta t \approx 0.353$ fs, which corresponds to the period of a transition between the $1s\sigma_g$ and the $2p\sigma_u$ states, with an energy gap of $\Delta E = 0.437$ Ha. The oscillations vanishes after the end of the pulse, as expected for Rabi oscillations. In Figure 4.8b, the classical prediction of the slope for the trajectory of a nuclear wavepacket moving along the $2p\sigma_u$ state is in good agreement with the probability density coming out the molecule.

We can consider which vibrational states have been excited during the interaction with these laser pulses. We do this by projecting the time-dependent wavefunction onto the ground state vibrational eigenstates of the system, i.e.

$$P_\nu(t) = \int d\mathbf{r} d\mathbf{R} \psi_\nu^*(\mathbf{r}, \mathbf{R}) \Psi(\mathbf{r}, \mathbf{R}, t) \quad (4.10)$$

where $\psi_\nu(\mathbf{r}, \mathbf{R})$ are the vibrational eigenstates of the molecule, and $\Psi(\mathbf{r}, \mathbf{R}, t)$ is the time-dependent molecular wavefunction. We remember that, as explained in Section 4.1, the vibrational eigenstates of the system are not factorised between electronic and nuclear coordinates

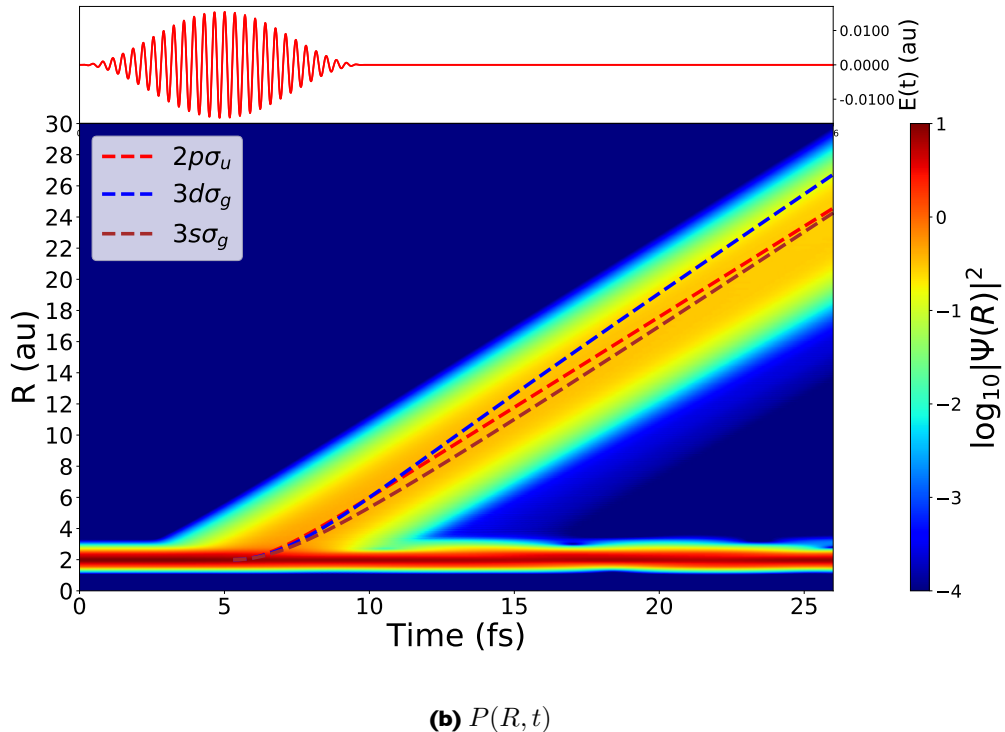
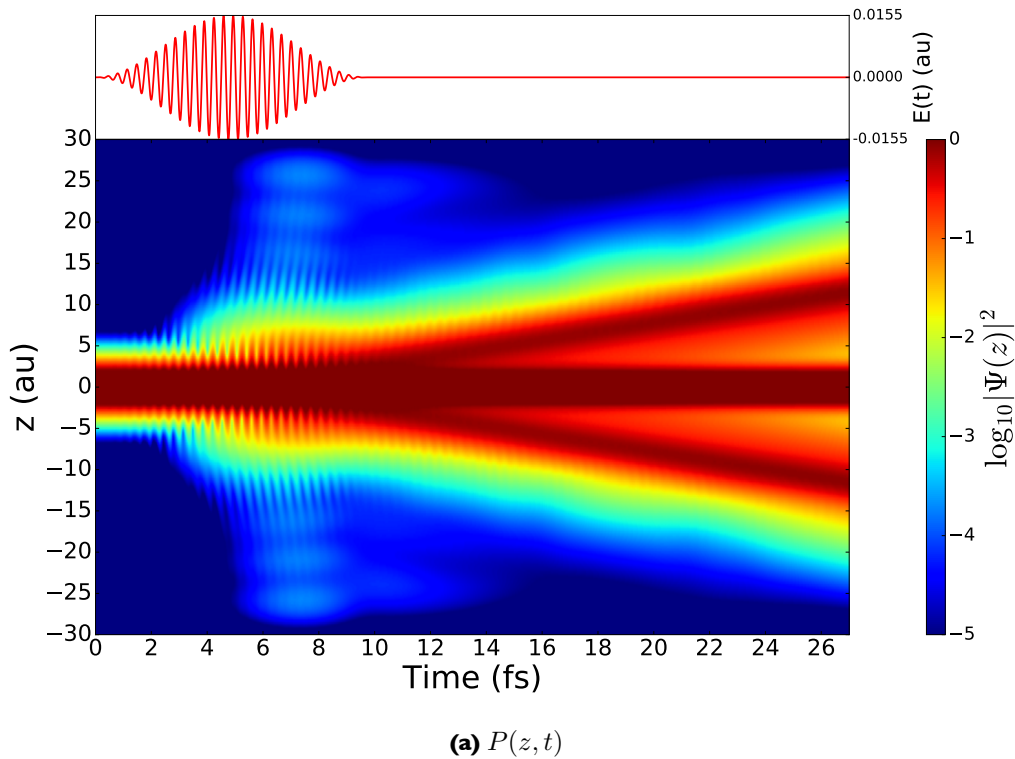


Figure 4.8: Probability density plots of H_2^+ (starting from the $\nu = 0$ vibrational state) over time during its interaction with a 28-cycle VUV laser pulse having a wavelength $\lambda = 105.3$ nm (photon energy $\omega_L = 0.43$ Ha) and a peak intensity of $I = 8.4 \times 10^{12}$ W/cm^2 . In (a) we present the density $P(z, t)$ while in (b) we present $P(R, t)$. The electric field used in the calculation is shown at the top of the figure, where the position of the red circle represents the specific time of the calculation. In (b) the dashed lines represent the classical trajectories of the nuclear wavepackets along some of the potential energy curves of the molecule.

in our non-Born-Oppenheimer treatment and so the eigenstates depend on both the electronic and nuclear coordinates. The evolution of $P_\nu(t)$, $\nu = 0, \dots, 5$ with a 3-cycle laser pulse whose wavelength is $\lambda = 105.3$ nm and an intensity of $I = 8.4 \times 10^{12} \text{ W/cm}^2$, are shown in Figure 4.9. The calculation commences with the total population in the $\nu = 0$ state. During the interaction with the pulse a small fraction of the population is excited to higher vibrational states at each maximum and minima of the electric field. This excitation first populates the $\nu = 1$ state, and then successive states in turn, and it is a signature of the excitation that takes place as ionisation occurs.

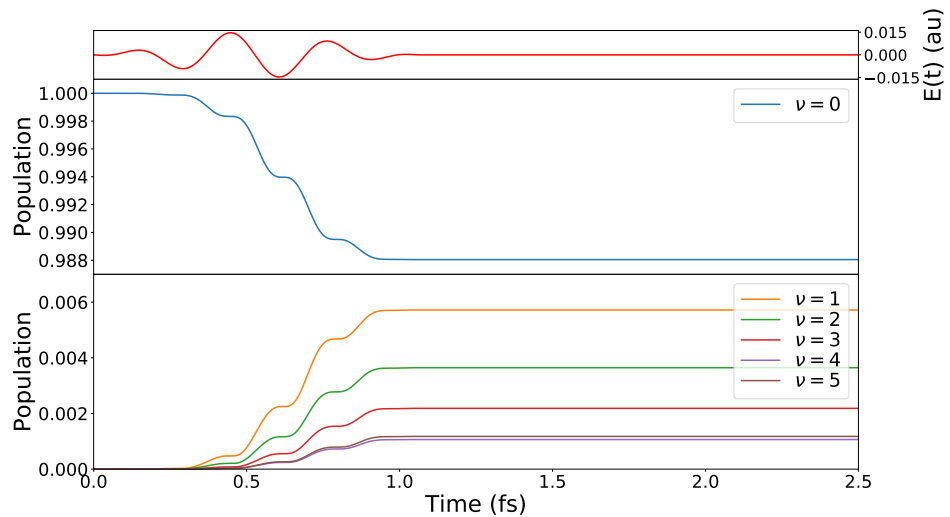


Figure 4.9: Time evolution of the population of the six lowest vibrational states of the H_2^+ molecule exposed to a 3-cycle VUV laser pulse, whose photon energy is $\omega_L = 0.43 \text{ Ha}$ and intensity $I = 8.4 \times 10^{12} \text{ W/cm}^2$. The initial state corresponds to the ground vibrational state, denote by $\nu = 0$.

4.2.2 Dissociative ionisation from the $1s\sigma_g$ ($\nu = 2$) state

Now, we consider the molecule is initially in the $\nu = 2$ vibrational state. We expose again the molecule to a 3-cycle VUV laser pulse, having a wavelength of $\lambda = 110.3$ nm (which corresponds to a photon energy of 0.41 Ha), and a peak intensity of $8.4 \times 10^{12} \text{ W/cm}^2$. The photon energy is chosen to match the energy gap between the third vibrational state ($\nu = 2$) in the $1s\sigma_g$ potential energy curve and the first excited state of the molecule, the $2p\sigma_u$ potential energy curve. The animation showing the time evolution of the probability density plots for this case can be found in the supplied CD, labelled with the name movie3.mp4.

It is visible in the $R - z$ density plots in Figure 4.10 that the initial state has two nodes along the R coordinate. This compares with the single node for the $\nu = 0$ initial state in Figure 4.3a. In order to understand the nodal structure of the initial vibrational state, we can approximate analytically the vibrational states of the H_2^+ by expanding the $1s\sigma_g$ potential energy curve

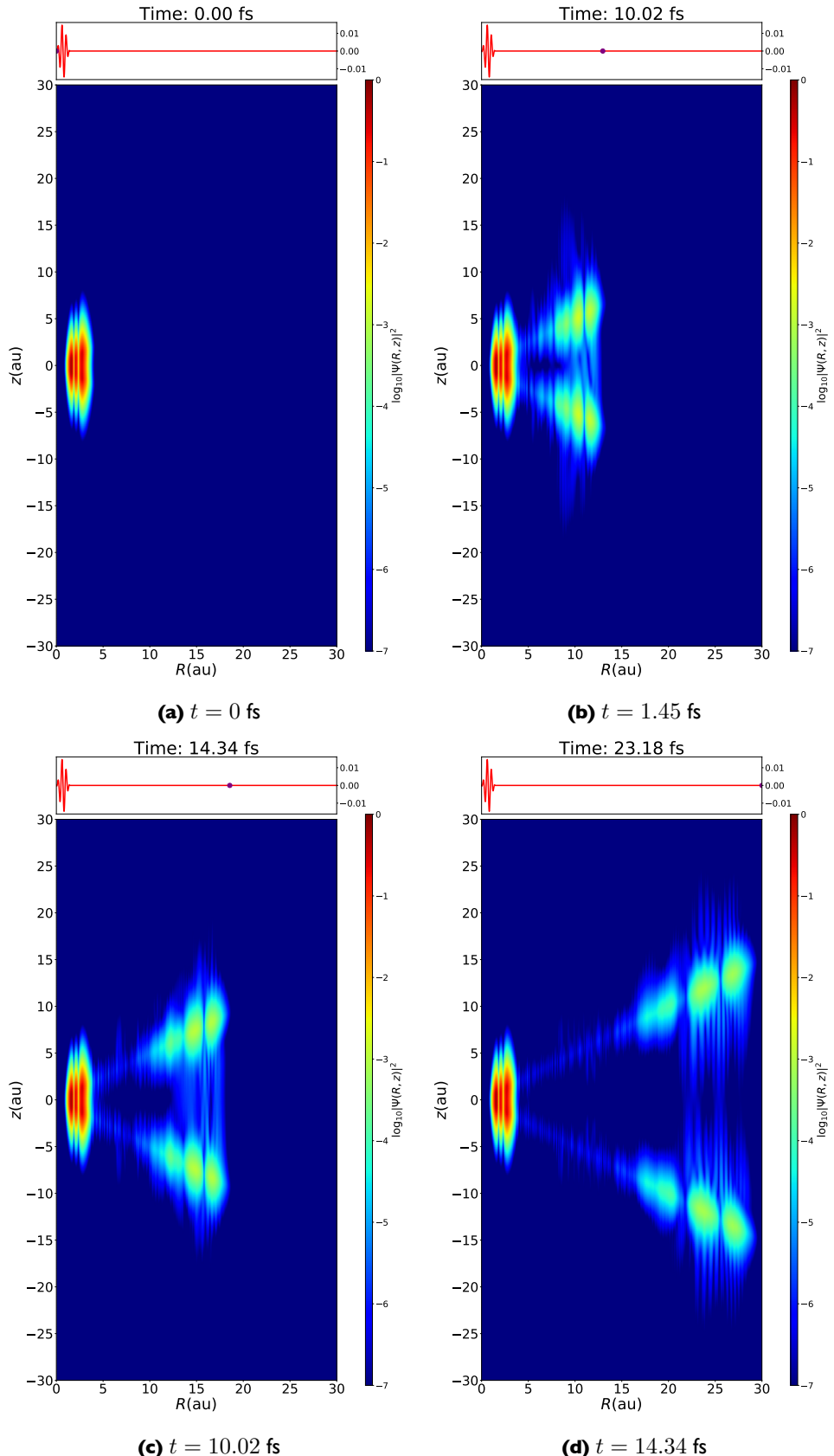


Figure 4.10: Probability density plots $P(R, z)$ of H_2^+ initially in the $\nu = 2$ vibrational state, at particular instants during its interaction with a 3-cycle VUV laser pulse, having a wavelength of $\lambda = 110.3 \text{ nm}$ (photon energy of $\omega_L = 0.43 \text{ Ha}$) and a peak intensity of $I = 8.4 \times 10^{12} \text{ W/cm}^2$. Each frame corresponds to (a) $t = 0 \text{ fs}$, (b) $t = 1.45 \text{ fs}$, (c) $t = 10.02 \text{ fs}$, (d) $t = 14.34 \text{ fs}$. The electric field is shown at the top of each frame, where the position of the dot represent the specific time of the calculation.

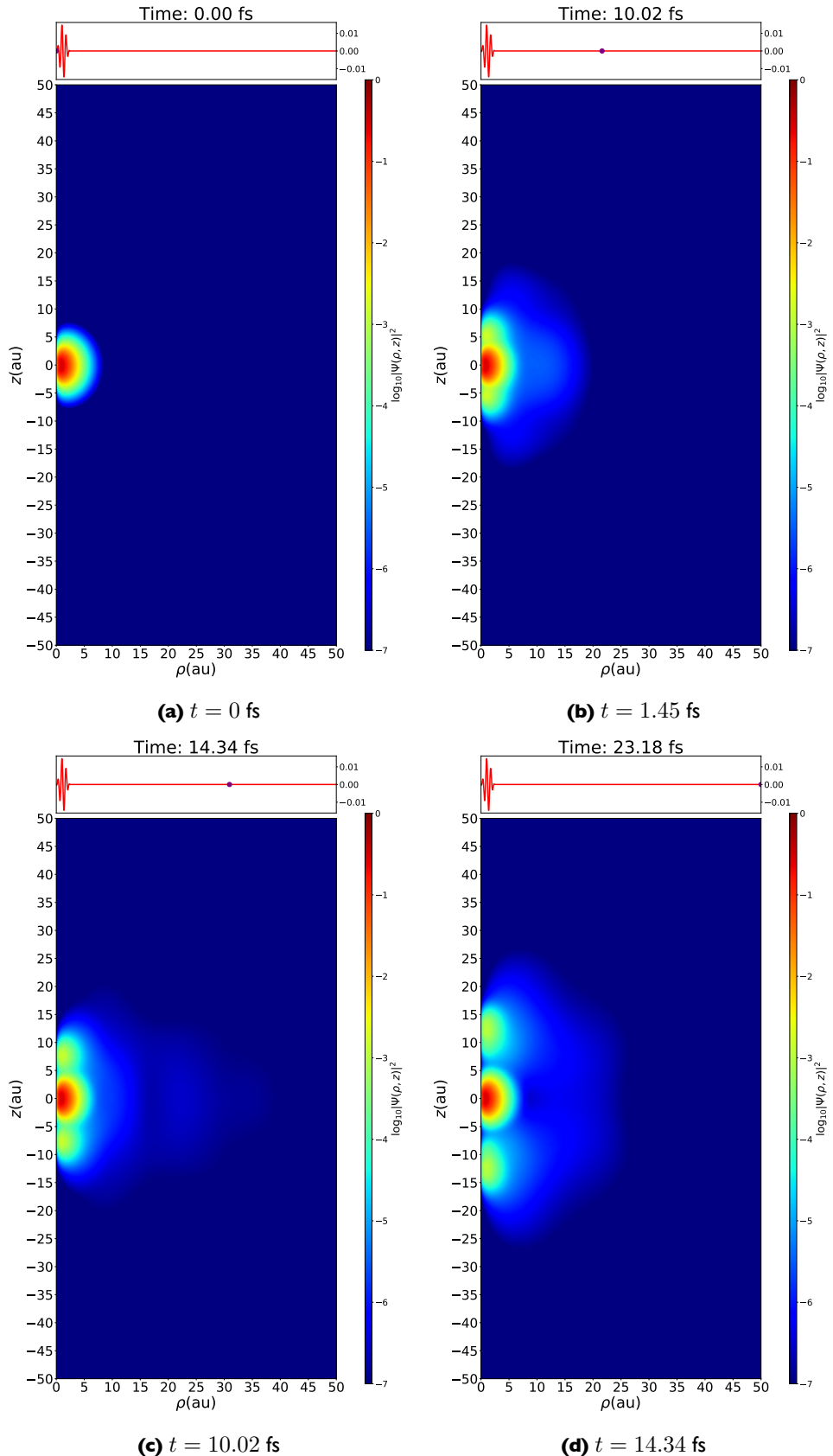


Figure 4.11: Probability density plots $P(\rho, z)$ of H_2^+ initially in the $\nu = 2$ vibrational state, at particular instants during its interaction with a 10-cycle VUV laser pulse, having a wavelength of $\lambda = 780 \text{ nm}$ (photon energy of $\omega_L = 0.058 \text{ Ha}$) and a peak intensity of $I = 2 \times 10^{14} \text{ W/cm}^2$. Each frame corresponds to (a) $t = 0 \text{ fs}$, (b) $t = 1.45 \text{ fs}$, (c) $t = 10.02 \text{ fs}$, (d) $t = 14.34 \text{ fs}$. The electric field is shown at the top of each frame, where the position of the dot represent the specific time of the calculation.

about the minimum at $R_0 = 2 a_0$

$$V_s(R) = V_s(R_0) + (R - R_0) \left(\frac{dV_s(R)}{dR} \right)_{R=R_0} + \frac{1}{2}(R - R_0)^2 \left(\frac{d^2V_s(R)}{dR^2} \right)_{R=R_0} + \dots \quad (4.11)$$

where $V_s(R)$ denotes the $1s\sigma_g$ potential energy curve in function of R . Since $V_s(R)$ has a minimum at $R = R_0$ the second term in the right hand side is zero. If we truncate the expansion (4.11) at the quadratic term, and neglect higher orders, we get

$$V_s(R) = V_s(R_0) + \frac{1}{2}\omega_s(R - R_0)^2 \quad (4.12)$$

where we have defined

$$\omega_s = \left(\frac{d^2V_s(R)}{dR^2} \right)_{R=R_0}. \quad (4.13)$$

The potential in Eq. (4.12) is precisely the potential for the quantum harmonic oscillator [202], where ω_s is the oscillation frequency. The approximation of the potential energy curve $1s\sigma_g$ to Eq. (4.12) is called the parabolic approximation [93]. The solutions of the harmonic oscillator

$$\phi_\nu(R) = C_\nu e^{-\omega_s R^2/2} H_\nu(\beta R) \quad (4.14)$$

where $\beta = \sqrt{\omega_s}$, C_n is a normalisation factor, and $H_\nu(\beta R)$ are the Hermite polynomials

$$H_n(z) = (-1)^n e^{z^2} \frac{d^n}{dz^n} \left(e^{-z^2} \right). \quad (4.15)$$

Moreover, we can approximate the vibrational energy levels by

$$E_{s,\nu} = \omega_s \left(\nu + \frac{1}{2} \right), \quad \nu = 0, 1, 2, \dots \quad (4.16)$$

In Figure 4.12 we show the lowest eigenvalues for the quantum harmonic oscillator. As we can observe, for the $\nu = 2$ state, the wavefunction presents two nodes. The parabolic approximation remains valid for small values of $|R - R_0|$, close to the equilibrium internuclear distance, thus only the lowest vibrational states will be well represented by Eq. (4.14). As we can see in Figure 4.1b, the highest vibrational levels are more closely spaced, and another approximation is needed to achieve a better representation. Indeed, it is possible to write an empirically approximated potential, known as the Morse potential [93], as

$$V_M(R) = D_e \{ \exp[-2\alpha(R - R_0)] - 2 \exp[-\alpha(R - R_0)] \} \quad (4.17)$$

where D_e is the electronic dissociation energy, R_0 the equilibrium distance and α is the 'force constant', similarly to the constant ω_s in Eq. (4.12). For a given diatomic molecule, D_e , R_0 and α are known parameters that can be found in tables. At large distance the potential (4.17) is attractive, and it posses a minimum at the equilibrium distance R_0 . In contrast, it is repulsive at short distances. One of the defects of the approximation is that the potential remains finite

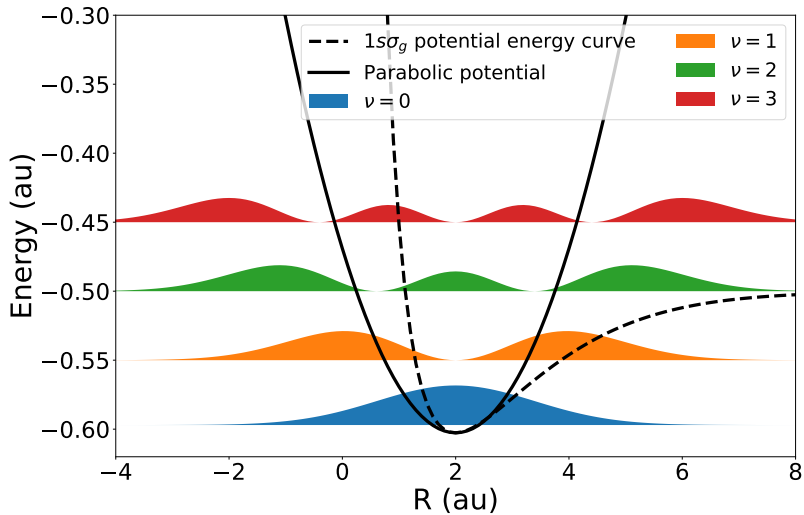


Figure 4.12: Diagrammatic representation of the four lowest eigenstates of the quantum harmonic oscillator. The solid line represents the quadratic potential, while the dashed line represents the $1s\sigma_g$ potential energy curve of the H_2^+ .

at $R = 0$. The potential energy curves $E_s(R)$ can be expressed as

$$E_s(R) = E_s(\infty) + V(R). \quad (4.18)$$

Then, for the Morse potential, the lower vibrational energy levels are given by

$$E_\nu = \hbar\omega_0 \left[\left(\nu + \frac{1}{2} \right) - \beta \left(\nu + \frac{1}{2} \right)^2 \right] \quad (4.19)$$

where the second term in the right hand side is a correction term to the energy levels in Eq. (4.16). $\beta\omega_0$ is usually known as the anharmonicity constant, and is given by

$$\beta\omega_0 = \frac{\hbar\omega_0^2}{4D_e}. \quad (4.20)$$

Hence, the molecular dissociation energy, D_0 is

$$D_0 = D_e - \hbar\omega_0/2. \quad (4.21)$$

At a later time, in Figure 4.10b, we observe that the initial nodal structure is imprinted in the dissociating nuclear wavepacket, and it evolves in Figures 4.10c and 4.10d, spreading along the R coordinate. We note that the wavepacket is initially distributed along different values of R , and therefore when the nuclear wavepacket is promoted to an excited state, the parts of the wavepacket evolve with different velocities along the potential energy curve.

The evolution of the probability $P(\rho, z)$, presented in Figure 4.11 it is similar to the $\nu = 0$ case. In Figure 4.11b, and most in Figures 4.11c and 4.11d the dissociative wavepackets, clearly visible along the z coordinate, have a larger probability than in Figure 4.4, when the molecule

is initially in the $\nu = 0$ vibrational state.

The time evolution of the probability density $P(z, t)$ and $P(R, t)$ are shown in Figure 4.13. The $P(z, t)$ plot is practically identical to Figure 4.5a (the $\nu = 0$ case), where we still observe the oscillations due to superposition of molecular bound states. However, in the $P(R, t)$ plot (Figure 4.13b) the nodal structure is visible. We observe in the main horizontal stripe centred at $R = 2 a_0$, representing the bound state of the molecule, two thin lines of lower density that represents the nodes of the initial vibrational state. Moreover, there are two diagonal stripes that come out the horizontal stripe between $t = 2$ fs and $t = 4$ fs, in contrast to the single diagonal stripe that comes out in Figure 4.5b for the $\nu = 0$ case.

Analogously to Figure 4.9, in Figure 4.14 we present the populations of the lowest six vibrational states during the interaction with the 3-cycle VUV laser pulse of wavelength $\lambda = 110.3$ nm and peak intensity $I = 8.4 \times 10^{12}$ W/cm², where for obtaining the populations we have used again Eq. (4.10). As in the case where the molecule was initially in the $\nu = 0$ state, we observe excitation taking place, first exciting the levels $\nu = 1$ and $\nu = 3$, and then the successive the upper states in turn.

4.2.3 Interplay between vibrational states

We now study the interplay of vibrational states in the strong field ionisation and dissociation of H₂⁺. In the following we consider H₂⁺ produced from the ionisation of the hydrogen molecule, H₂. The initial state of H₂⁺, formed from a linear combination of vibrational states, will have an influence on the subsequent evolution of the molecular ion in strong laser fields. In order to take into contributions from different vibrational states we introduce the Franck-Condon principle [246, 247], which states that the intensity of an electronic transition between vibrational states is given by the overlap of their corresponding wavefunctions. The weight of a particular vibrational state in an electronic transition is given by the Franck-Condon factors, which are defined as the overlap of the initial and final vibrational wavefunctions

$$q_{\nu_i, \nu_f} = \left| \int dr \psi_{\nu_i}(r) \phi_{\nu_f}(r) \right|^2 \quad (4.22)$$

where q_{ν_i, ν_f} is the Franck-Condon factor of the transition, ψ_ν is the initial vibrational wavefunction and $\phi_{\nu f}(r)$ is the final vibrational wavefunction. In this case we consider transitions from the ground state of the H₂ (the vibrational ground state in the $1s\sigma_g$ potential energy surface) to the vibrational states of H₂⁺ (in the $1s\sigma_g$ potential energy surface). The Franck-Condon factors for this transition are detail in table 4.3, which have been taken from Ref. [248].

In order to study how these vibrational states affect the response we will consider ten independent calculations in which H₂⁺ starts from one particular vibrational level, and multiply each particular state with their correspondent Franck-Condon factor. We then calculate the ionisation and dissociation yields.

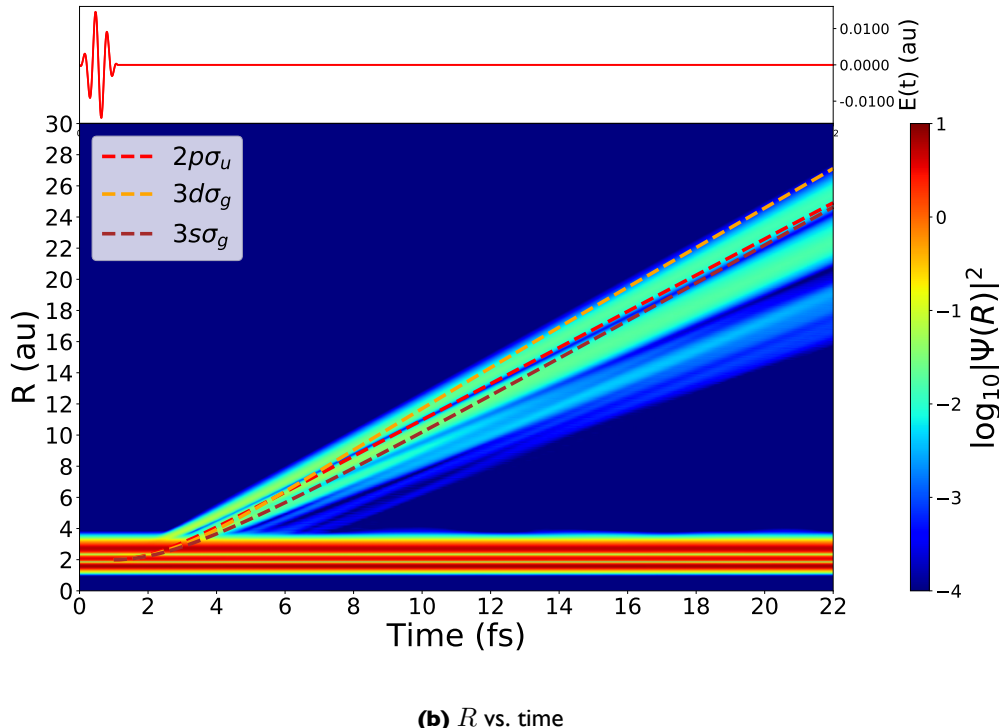
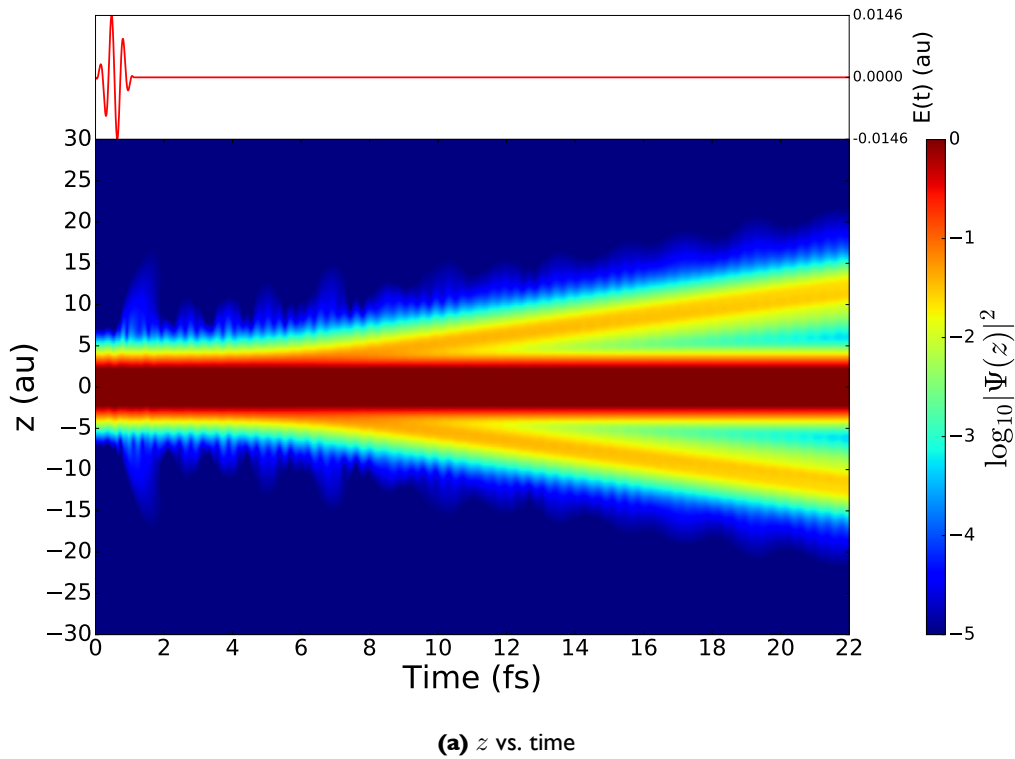


Figure 4.13: Probability density plots of H_2^+ (starting from the $\nu = 2$ vibrational state) over time during its interaction with a three-cycle VUV laser pulse having a wavelength $\lambda = 110.3$ nm (photon energy $\omega_L = 0.43$ Hartrees) and a peak intensity of $I = 8.4 \times 10^{12} \text{ W/cm}^2$. The initial state of the molecule is the third vibrational state ($\nu = 2$) in the $1s\sigma_g$ potential energy surface. In (a) we present the density $P(z, t)$ while in (b) we present $P(R, t)$. The electric field used in the calculation is shown at the top of the figure, where the position of the red circle represents the specific time of the calculation. In (b) the dashed lines represent the classical trajectories of the nuclear wavepackets along some of the potential energy curves of the molecule.

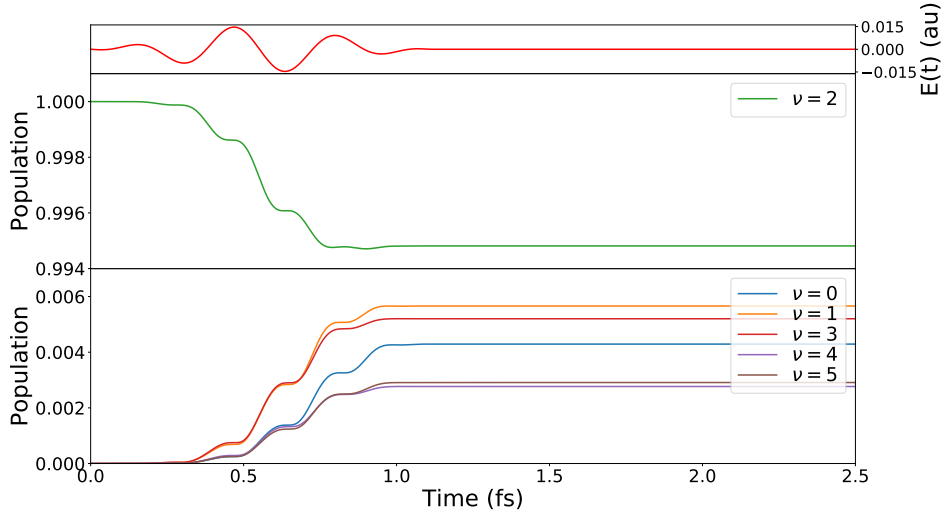


Figure 4.14: Time evolution of the population of the six lowest vibrational states of the H_2^+ molecule exposed to a 3-cycle VUV laser pulse, whose photon energy is $\omega = 0.43$ Hartrees and intensity $I = 8.4 \times 10^{12} \text{ W/cm}^2$. The initial state corresponds to the third vibrational state, denote by $\nu = 2$.

ν	$q_{0,\nu}$	ν	$q_{0,\nu}$
0	0.0911850	5	0.0875530
1	0.1605800	6	0.0619910
2	0.1742600	7	0.0431950
3	0.1521300	8	0.0299210
4	0.1190800	9	0.0207080

Table 4.3: Franck-Condon factors $q_{0,\nu}$ for transitions between the vibrational ground state of the H_2 in the $1s\sigma_g$ potential energy surface and the $\nu 1s\sigma_g$ state of the 10 lowest vibrational states, $\phi_\nu(r)$, of the H_2^+ in the $1s\sigma_g$ potential energy surface.

In order to analyse the resulting wavefunction after the interaction with the laser pulse, the diagram in Figure 4.15 illustrates how different regions of coordinate space are used to define the ionisation and dissociation yields. The regions are split into an ionisation region, whose boundaries are limited by electronic boundary, $r_0 = \sqrt{z_0^2 + \rho_0^2}$, and a dissociation region, whose boundary is limited by the nuclear boundary, R_0 . The dissociative ionisation are contained in two horns, shown in Figure 4.15, whose width is R_D . The upper horn contain the population of the electron escaping with the nuclei located at $z = R/2$, labelled dissociation up in the figure (D_+), or with the nuclei located at $z = -R/2$, labelled as dissociation down (D_-). The dissociative ionisation region corresponds to an area where the electron and the nuclei travel large distances in electronic and nuclear coordinates respectively.

The ionisation yield is calculated integrating over the population of the wavefunction con-

tained within the ionisation region

$$I(t) = \int_{S>S_0} dr d\mathbf{R} \psi^*(\mathbf{r}, \mathbf{R}, t) \psi(\mathbf{r}, \mathbf{R}, t) \quad (4.23)$$

where $S_{\pm} = \sqrt{(z \pm R/2)^2 + \rho_0^2}$ and $S_0 = \sqrt{r_0^2 + R_0^2}$. The ionisation region corresponds to an area of large values of the electronic coordinate and small values of the nuclear coordinate in which the ejected electron is located far from the molecule and the two nuclei still close to each other.

Analogously, the dissociation yield results from integrating over the population contained in the dissociation up / down regions

$$D_{\pm}(t) = \int_{R>R_0, S_{\pm} < R_D} dr d\mathbf{R} \psi^*(\mathbf{r}, \mathbf{R}, t) \psi(\mathbf{r}, \mathbf{R}, t). \quad (4.24)$$

The total dissociation yield is obtained adding the dissociation up and down yields

$$D(t) = D_+(t) + D_-(t). \quad (4.25)$$

The ionisation and dissociation yields, I_{ν} and D_{ν} , calculated using Eqs. (4.23), (4.24) and (4.25) for $\nu = 0, \dots, 9$ taking ν as the initial vibrational state, are shown in Figure 4.16. Each yield is multiplied by the Franck-Condon factor that corresponds to the initial vibrational state, i.e. the yields that corresponds to the initial vibrational state $\nu = 1$ is multiplied by the Franck-Condon factor $q_{0,1}$. Doing so we compare the yields obtained separately from the vibrational states that compose the initial state of the H_2^+ obtained from ionisation of H_2 . As we expect, the dissociation yield is two orders of magnitude larger than the ionisation yields, because the photon energy is resonant with the transition between the ground state ($1s\sigma_g$) and the first excited state ($2p\sigma_u$) of the molecule. Also, the low ionisation yields are due to the fact that several photons are required to reach the ionisation threshold, and the intensity of the laser pulse is not high enough for multiphoton ionisation. For both ionisation and dissociation, the highest yields arise from the $\nu = 2$ and $\nu = 3$ states, which also are the states that have the largest Franck-Condon factors.

In addition, we consider two cases. In the first case we consider the molecule in a superposition of vibrational states, ψ_{FC} , where

$$\psi_{\text{FC}} = \sum_{\nu=0}^9 \sqrt{q_{0,\nu}} \psi_{\nu}. \quad (4.26)$$

In this case ψ_{ν} are the vibrational states of H_2^+ , obtained by diagonalisation of the molecular Hamiltonian, and $q_{0,\nu}$ are the ten Franck-Condon factors from table 4.3. The initial state ψ_{FC} has been normalised at the start of the calculation. The ionisation and dissociation yield are denoted by I_{FC} and D_{FC} . In the second case we calculate the incoherent sum (IS) of the yields

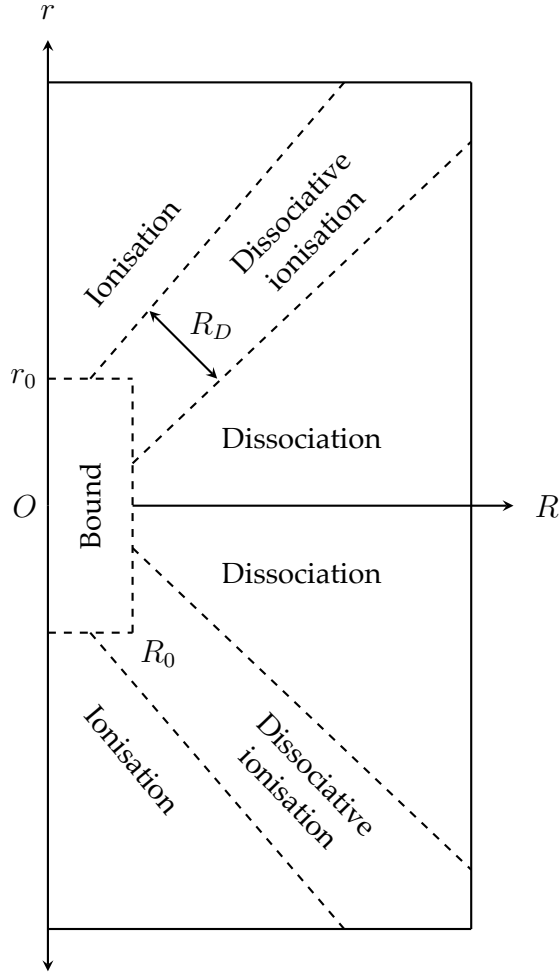


Figure 4.15: R vs. r diagram showing how we split coordinate space in distinct regions associated with ionisation and dissociation, where R is the internuclear coordinate and r represents the electronic coordinate and it holds the equality $r^2 = \rho^2 + z^2$. The different parts of the coordinate space are: the bound, ionisation, dissociation and dissociative ionisation regions, where the bound region is delimited by R_0 and $r_0 = \sqrt{\rho_0^2 + z_0^2}$, and the width of the dissociative ionisation region is $R_D \leq \sqrt{(z \pm R/2)^2 + \rho^2}$. Wavepacket residing in these regions allow us to calculate the ionisation and dissociation yields after the interaction with the laser pulse.

from the ten lowest vibrational states according to

$$O_{IS} = \sum_{\nu=0}^9 q_\nu O_\nu \quad (4.27)$$

where O denotes ionisation (I) or dissociation (D). In Figures 4.16c and 4.16d we compare the incoherent sum yields against the yields obtained from the linear combination of vibrational states, denoted by FC. The difference in yield between the two calculations is due to different normalisation of the initial wavefunctions. For that reason we have scaled by a different factor the FC yield in order to compare the results. In Figure 4.16a, the ionisation yields present a similar evolution, although for the FC calculation the yield presents shaper peaks. In contrast, in Figure 4.16b the yield for the FC calculation starts later than in the IS case. Also, the FC dissociation presents a hump around 9 fs. This suggests that the coherent combination of vibrational states prevent earlier dissociation, and the hump indicates a change in the dissoci-

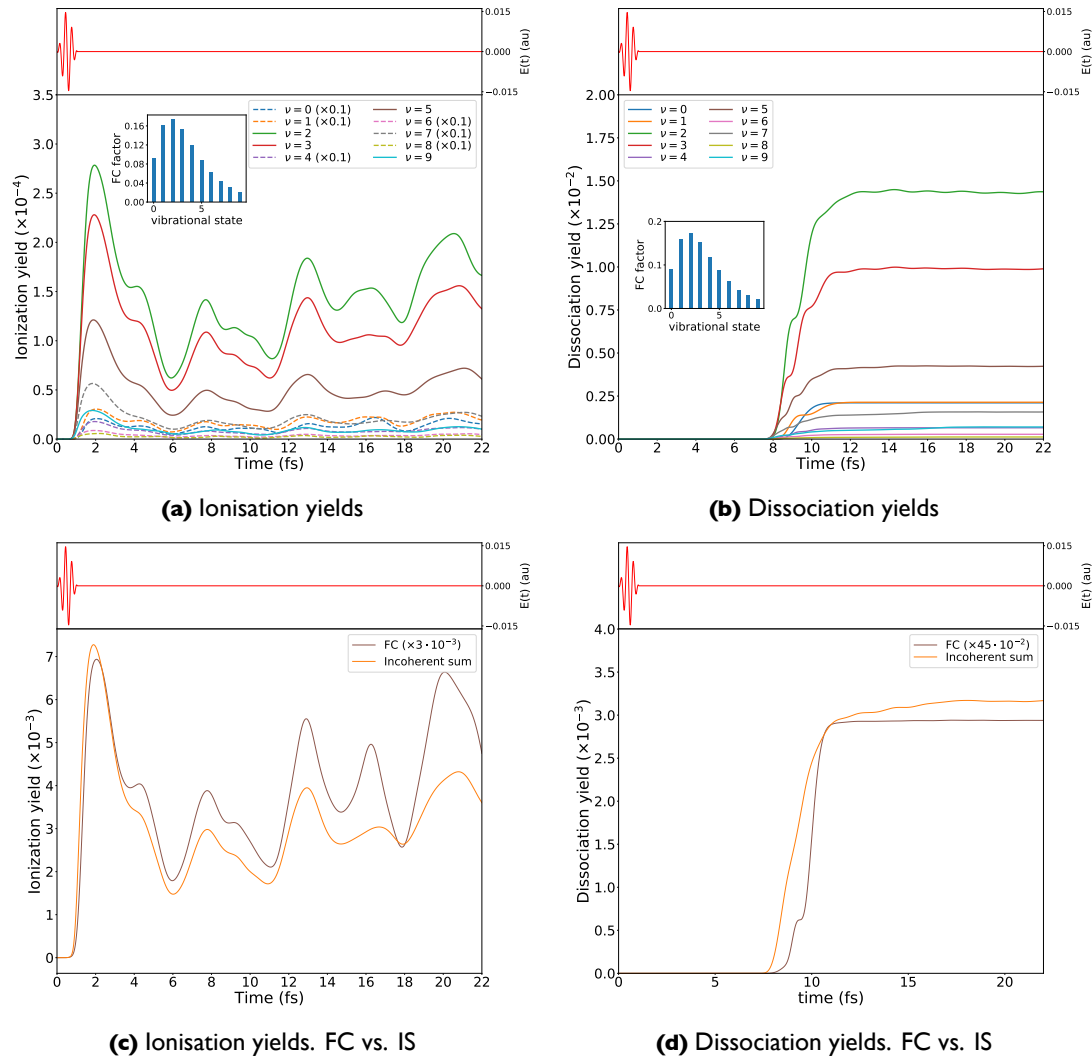


Figure 4.16: Ionisation (a) and dissociation (b) yields of the H_2^+ after interaction with a 3-cycle VUV laser pulse having a wavelength $\lambda = 105.3$ nm (corresponding to a photon energy of $\omega_L = 0.43$ Ha) and a peak intensity of $I = 8.4 \times 10^{12} \text{ W/cm}^2$. Each line in the plots represent a calculation starting from one particular level of the ten lowest vibrational states ($\nu = 0, \dots, 9$) in the $1s\sigma_g$ potential energy surface, where each yield have been multiplied by its corresponding Franck-Condon factor. The dashed lines correspond to yields that have been scaled by a factor of 10 for clarity. The inset in each plot represents the first ten Franck-Condon factors of table 4.3. Ionisation (c) and dissociation (d) yields for the linear combination of the first ten vibrational states (FC) and the incoherent sum (IS). The yields denoted by FC have been scaled for clarity. The electric field used in the calculation is shown at the top of each plot.

ation rate due to an intermediate resonant state.

4.3 Dissociative ionisation and high harmonic generation of H_2^+ by IR laser pulses

In the previous section we considered the interaction of H_2^+ with a VUV laser pulse. In this section we now consider the interaction of the molecule with an intense IR laser pulse. In particular we consider a 10-cycle laser pulse having a wavelength of $\lambda = 780$ nm (corresponding to a photon energy of $\omega_L = 0.058$ Hartrees) with a peak intensity of $I = 2 \times 10^{14} \text{ W/cm}^2$. The total duration of the pulse is approximately 26 fs. The grid parameters used in this calculation

can be found in table 4.4. With these laser parameters, the size of the grid is set to contain the quiver amplitude of the electron, especially along the z coordinate. We remember that the quiver amplitude is related to the electric field and frequencies of the laser pulse via

$$\alpha(t) = \frac{E(t)}{\omega_L^2}, \quad (4.28)$$

where ω_L is the central frequency of the laser pulse. The quiver amplitude for the current laser parameters is $\alpha_0 = E_0/\omega_L^2 = 22.1 a_0$. The grid size must be large enough to allow the motion of the electron wavepacket without reaching the absorbing boundaries.

The size of the resulting Hamiltonian is in this case roughly $125 \text{ M} \times 125 \text{ M}$ elements. For the time evolution, we use again an 18^{th} order Arnoldi propagator with a time step of $\delta t = 0.05$. The resulting calculation was parallelised over 540 cores, and the calculation time was 13 hours and 30 minutes.

Coordinate	Points per core	Number of cores	Grid spacing	Mesh extent
R	67	3	0.1	$0 \leq R \leq 20.1$
ρ	50	4	0.1	$0 \leq \rho \leq 89.4$
z	69	45	0.1	$-155.2 \leq z \leq 155.2$

Table 4.4: Grid parameters used in the calculation of H_2^+ interacting with an intense IR laser pulse, whose wavelength is $\lambda = 780 \text{ nm}$ (photon energy of $\omega_L = 0.058 \text{ Hartrees}$) and a peak intensity of $I = 2 \times 10^{14} \text{ W/cm}^2$.

A series of snapshots of the time evolution of the probability densities, $P(R, z)$ and $P(\rho, z)$, of the wavefunction exposed to an IR laser pulse is presented in Figures 4.17 and 4.18 respectively. An animation of these probability densities is also contained in the supplied CD (the corresponding file is labelled as movie4.mp4). In Figures 4.17a and 4.18a we present the density for H_2^+ in the ground vibrational state ($\nu = 0$) of the $1s\sigma_g$ potential energy curve. In the following frame, Figure 4.17b, during the ramp on of the pulse a small amount of ionisation and dissociation occurs but most of the response is the distortion of the electronic wavepacket in anti-phase to the field, Figure 4.18b. The system is behaving as tightly bound oscillator. The horns suggest that before ionisation, the laser has excited a dissociative state. At a later point, in Figure 4.17c and 4.18c, ionisation has fully commenced and we see a significant fraction of the wavepacket travelling away from the molecule. The ionised electron then accelerates in the electric field and travels far away from the parent ion.

Eventually, a fraction of the ionised wavepacket is driven back to the parent ion when the electric field changes direction, as shown in Figures 4.17d and 4.18d. The electron then recollides with the ion, and two processes can then occur. Firstly, the electron can rescatter from the parent ion; alternatively, it can recombine resulting in the emission of high-order harmonics.

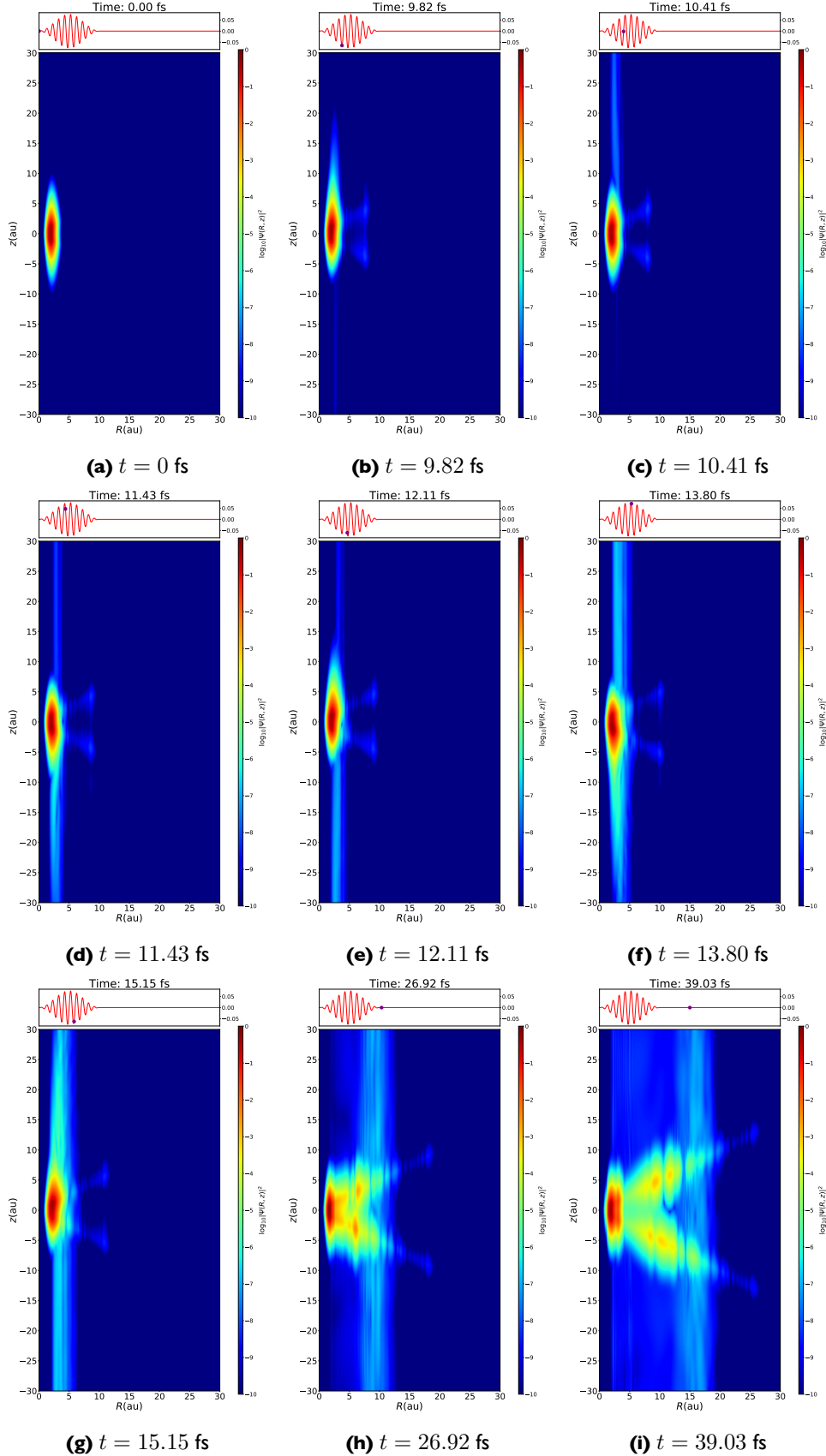


Figure 4.17: Probability density plots $P(R, z)$ of H_2^+ at particular instants during its interaction with a 10-cycle IR laser pulse, having a wavelength of $\lambda = 780 \text{ nm}$ (photon energy of $\omega_L = 0.058 \text{ Ha}$) and a peak intensity of $I = 2 \times 10^{14} \text{ W/cm}^2$. Each frame, which is a zoom in on z , corresponds to (a) $t = 0 \text{ fs}$, (b) $t = 9.82 \text{ fs}$, (c) $t = 10.41 \text{ fs}$, (d) $t = 11.43 \text{ fs}$, (e) $t = 12.11 \text{ fs}$, (f) $t = 13.80 \text{ fs}$, (g) $t = 15.15 \text{ fs}$ (h) $t = 26.92 \text{ fs}$, (i) $t = 39.03 \text{ fs}$. The electric field is shown at the top of each frame, where the position of the dot represent the specific time of the calculation.

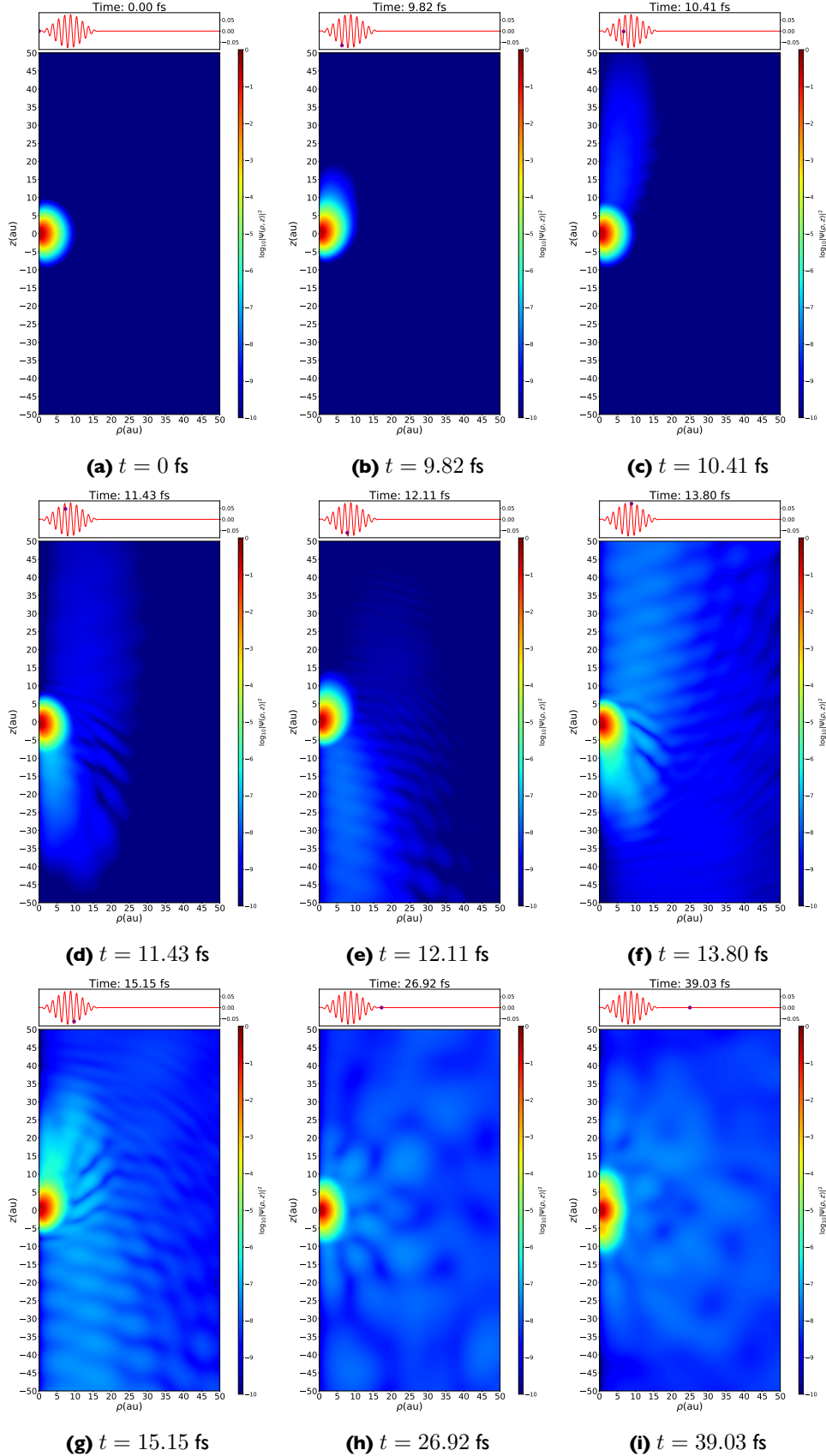


Figure 4.18: Probability density plots $P(\rho, z)$ of H_2^+ at particular instants during its interaction with a 10-cycle IR laser pulse, having a wavelength of $\lambda = 780 \text{ nm}$ (photon energy of $\omega_L = 0.058 \text{ Ha}$) and a peak intensity of $I = 2 \times 10^{14} \text{ W/cm}^2$. Each frame corresponds to (a) $t = 0 \text{ fs}$, (b) $t = 9.82 \text{ fs}$, (c) $t = 10.41 \text{ fs}$, (d) $t = 11.43 \text{ fs}$, (e) $t = 12.11 \text{ fs}$, (f) $t = 13.80 \text{ fs}$, (g) $t = 15.15 \text{ fs}$, (h) $t = 26.92 \text{ fs}$, (i) $t = 39.03 \text{ fs}$. The electric field is shown at the top of each frame, where the position of the dot represent the specific time of the calculation.

In Figures 4.18e, 4.18f and 4.18g we observe the regular nodal structure of the electron wavepacket travelling in the continuum. The nodal structure, an interference pattern that is modulated in the polarisation direction, along the z coordinate, is a signature of plane wave, i.e. an ionised wavepacket.

At the same time, in Figure 4.17f and 4.17g, the molecule is stretched by vibrational excitation during the interaction with the laser pulse (we will consider this later in Figure 4.21) and we observe a large density along the z coordinate, associated with a much larger ionisation yield. This is due to the dependence of the ionisation rate on the internuclear distance of the molecule. Indeed, it is known that the ionisation rate presents maxima at certain internuclear distances caused by charge-resonance states coupled by intense low frequency fields. This effect is known as charge-resonance enhanced ionisation (CREI) [124]. After the end of the laser pulse, in Figures 4.17h and 4.17i, a large fraction of the wavepacket is coming out along the horns in the $z = \pm R/2$ direction, indicating that the molecule is clearly dissociating. Finally, in Figure 4.18i the molecule is left in a resonant bound state. This state, that presents six lobes, decays quickly, as it is shown in Figure 4.18i.

In Figure 4.19 we present plots of the density $P(z, t)$ and $P(R, t)$ throughout the duration of the calculation. In the upper frame (Fig. 4.19a), which corresponds to the plot of density $P(z, t)$, we can observe that ionisation events happen at the maxima of the electric field. Indeed, as Becker and co-workers have pointed out, there are multiple ionisation bursts per half-cycle of the laser pulse [249–251]. In principle, it is expected that ionisation occurs at the peak of the electric field, when the tunnel barrier is lowest and the electron is more likely to escape through the barrier. However, in diatomic molecules, multiple bursts are due to the attosecond transient localisation of the electron at one of the ions. Also in Figure 4.19a, we can distinguish the electron quantum trajectories. Most of these trajectories escape with only a fraction returning to the molecule to produce high harmonic radiation. In the lower frame (Fig. 4.19b), which can be seen as the nuclear probability density, $P(R, t)$, dissociation commences around 14 fs as a jet-like structure, with the slope of the jets associated with the kinetic energy release of the fragments. The ejected nuclear wavepacket splits in two around 28 fs. The width of the main stripe of density centred at the internuclear distance of equilibrium, $R = 2 a_0$ widens and narrows between 14 and 22 fs. This indicates vibrational motion with stretching and compression of the molecule.

We now investigate the role of vibrational states in the response of the molecule. As before, we calculate the ionisation and dissociation yields defined in Eq. (4.23), (4.24) and (4.25) for the eight lowest vibrational states. These are presented in Figure 4.20. Only eight states, and not ten as for the VUV results, are included due to the larger grid spacing used here ($\Delta R = 0.1$ as opposed to $\Delta R = 0.05$ for the VUV results). The smaller grid spacing would give a more accurate representation of the higher vibrational states. However, this would come at a higher

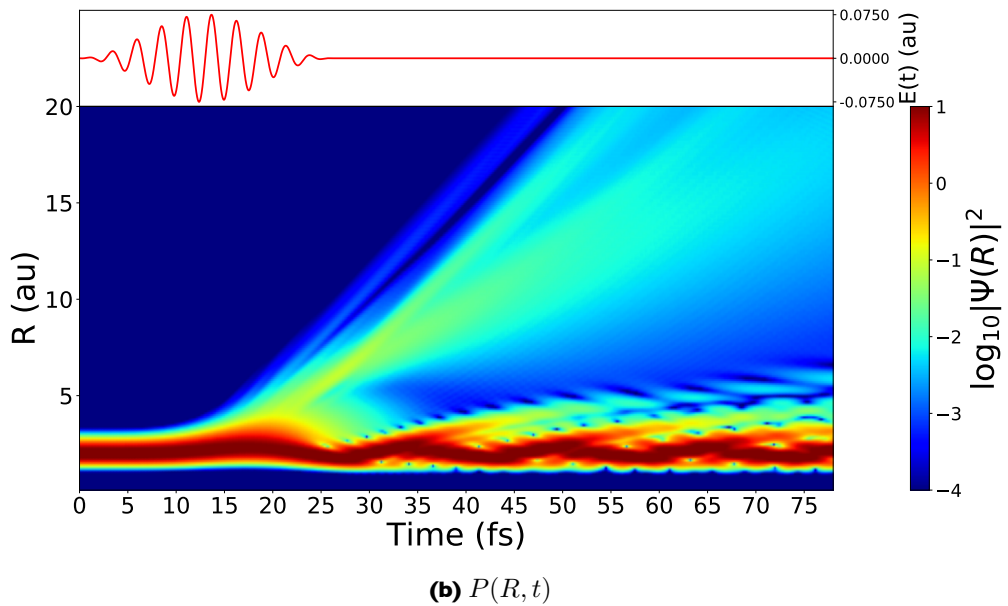
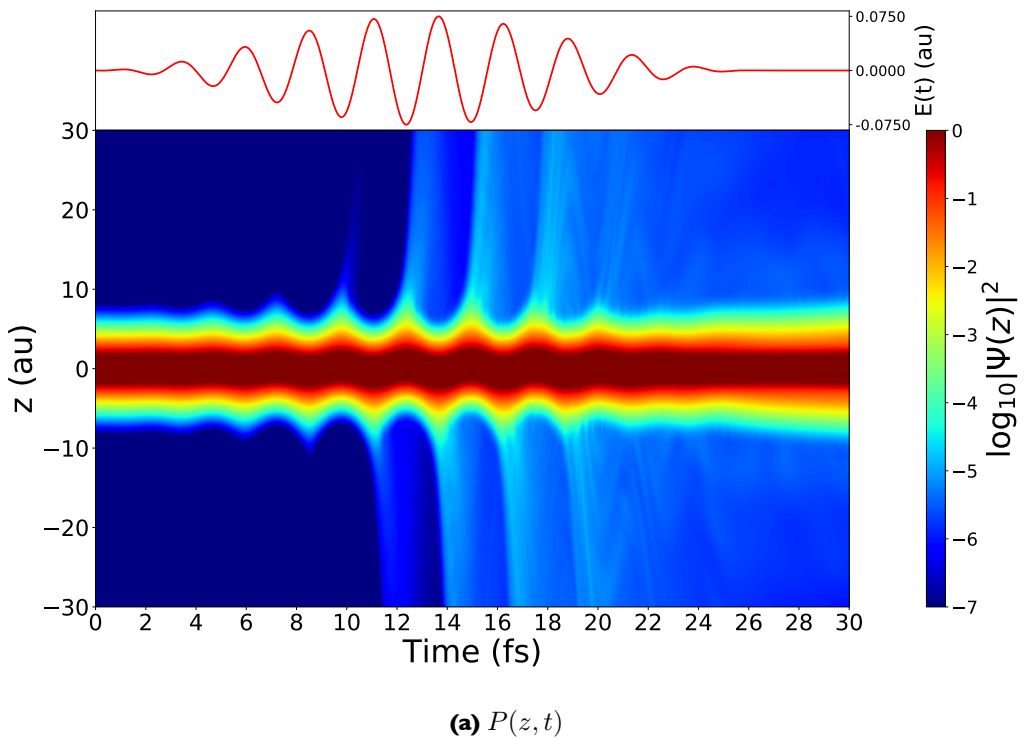


Figure 4.19: Time evolution of the H_2^+ wavefunction (a): $P(z, t)$, and (b): $P(R, t)$, after the interaction with a 10-cycle IR laser pulse, having a wavelength of $\lambda = 780 \text{ nm}$ (photon energy of $\omega_L = 0.058 \text{ Ha}$) and a peak intensity of $I = 2 \times 10^{14} \text{ W/cm}^2$. The initial molecular state is the lowest vibrational state, $\nu = 0$, of the $1s\sigma_g$ ground state of the H_2^+ . In both frames the rest of the coordinates have been integrated over.

computational cost. For the ionisation yields shown in Figure 4.20a, we see that the ionisation yield increases for higher vibrational states. This yield is modulated in time by the electric field and, as expected, the yield increases as the field passes through maxima. Indeed, the

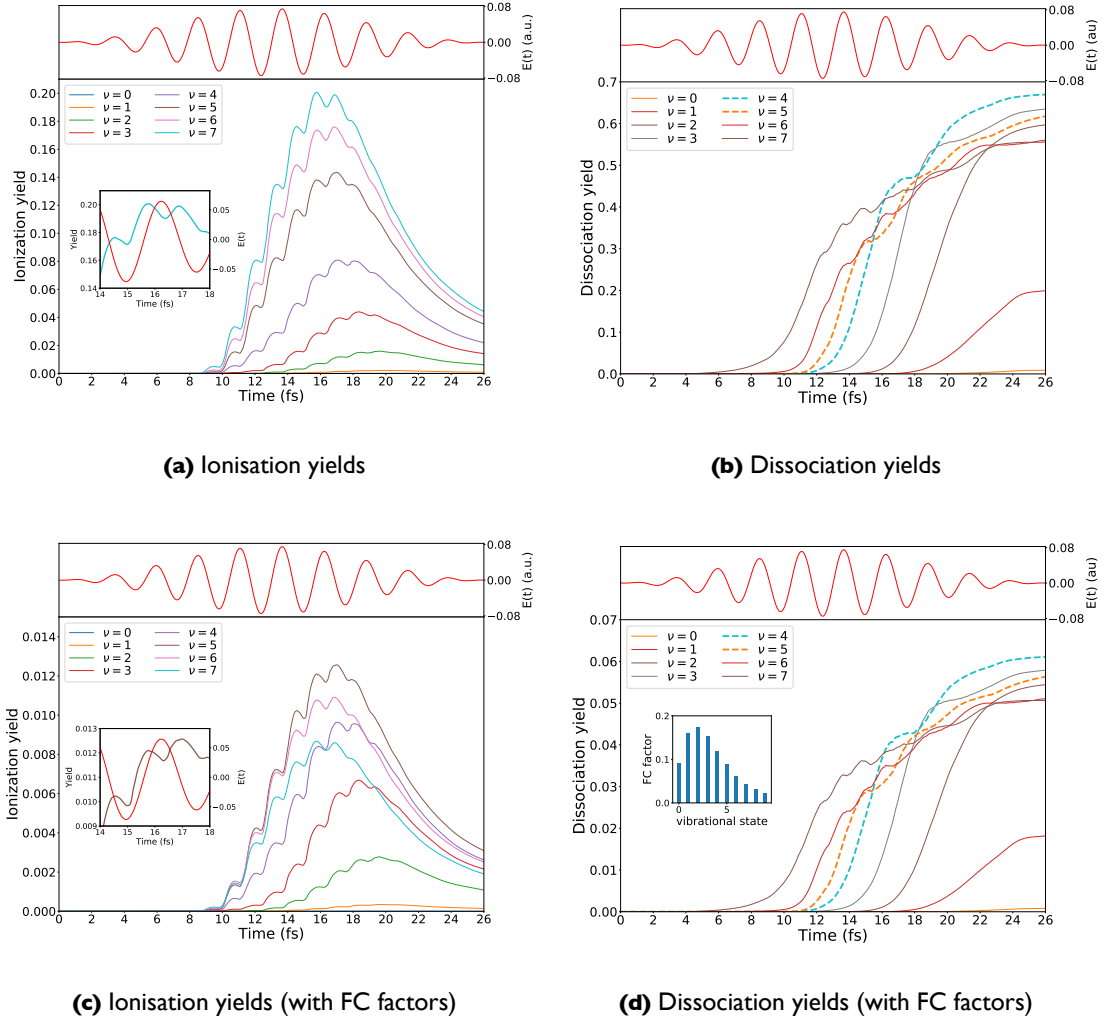


Figure 4.20: (a) and (c) Ionisation and (b) and (d) dissociation yields for the first eight vibrational states of the H_2^+ interacting with a 10-cycle IR laser pulse having a wavelength of $\lambda = 780 \text{ nm}$ (photon energy of $\omega_L = 0.057 \text{ Ha}$) and a peak intensity of $I = 2 \times 10^{14} \text{ W/cm}^2$. The upper frame in each plot shows the temporal profile of the electric field of the laser pulse. In (a) and (c), a zoom of the ionisation yield for $\nu = 7$ and the electric field is shown in the inset plot. In (b) the dashed lines correspond to the yields for the $\nu = 4$ and $\nu = 5$ states. In the lower frames, (c) and (d) the yields have been multiplied by their correspondent Franck-Condon factors, shown in the inset of Figure 4.20d.

humps on the ionisation yields that coincides with each maxima of the electric field are a signature of the already mentioned multiple ionisation bursts [249]. The inset plot of Figure 4.20a presents the ionisation yield for $\nu = 7$ zoomed in over one cycle of the pulse. We observe that the yield has two maxima and a minima within half cycle of the pulse, and the minima coincides with the peak of the laser field. This suggest that there are two ionisation burst per half cycle, and not one burst as expected, when the tunnel barrier is lowest at the peak of the electric field. If we want to have a better description of the ionisation yields resulting from H_2^+ in an initial state produced from ionisation of H_2 , we must multiply each ionisation yield by its corresponding Franck-Condon factor. The result is shown in Figure 4.20c, where we observe that although the structure of the yields have not changed, the relative magnitude between yields have changed, leading to final state that is a different combination of vibrational

states. The dissociation yields are shown in Figure 4.20b. In this case, yields corresponds to starting in vibrational states $\nu = 3$ and $\nu = 4$ have one and two humps respectively, indicating the dissociation slows at several points and suggesting that several intermediate and final states are involved in the dissociation. In contrast, the yields for $\nu = 0$ and $\nu = 1$ do not posses hump-like structures, indicating that for these states there is not an intermediate state that contributes to the dissociation. Figure 4.20d, where the dissociation yields have been multiplied by the Franck-Condon factors, is similar to Figure 4.20b and there is no difference between yields, except for the overall magnitude. The hump structure in yields $\nu = 4$ and $\nu = 5$ is still present. We note that while ionisation commences at the same time for all the initial states considered, dissociation commences at different times for different initial states: the higher the initial vibrational state, the sooner that dissociation starts.

To better understand the contribution of different vibrational states in a given calculation, we consider the molecule starting from a particular vibrational state and then calculate the population transfer to other vibrational states during the interaction using Eq. (4.10). Each yield has been multiplied by the Franck-Condon factor corresponding to the initial vibrational state. The results are shown in Figure 4.21. For reference, the upper panels correspond to the temporal profile of the electric field of the laser pulse.

In all frames of Figure 4.21 we see that, from the initial state, the excitation first populates the closest states in energy, and then successive states in turn. For instance, consider the frame corresponding to the initial state $\nu = 1$, where the contiguous states $\nu = 0$ and $\nu = 2$ are first to be excited, followed by the excitation of $\nu = 3$ and $\nu = 4$, and so on. In addition, the decay time of the initial state becomes shorter for higher vibrational states. Moreover, the peaks in the populations are due to Rabi oscillations, indicating a coherent exchange of energy between the laser field and the different vibrational levels. These oscillations vanishes at the end of the pulse. The amplitude of the Rabi oscillations are smaller with higher initial vibrational states. Since high vibrational states have large ionisation rates, ionisation causes more population loss from these states, resulting in shorter lifetimes and smaller Rabi oscillations. Another interesting feature, evident in Figure 4.21, is that, depending on the initial vibrational state, the final state is composed of different coherent superpositions of the vibrational states, as we can see in Figure 4.22. This can be crucial in understanding pump-probe studies in which the pump pulse can prepare the molecule to different excited states.

4.3.1 Vibrational state dependence on HHG

From the previous results we know that ionisation and recollisions occur at these long wavelengths and that different vibrational states play a role as well. Since high harmonic generation occurs we can ask how these vibrational states can influence HHG.

It is expected that the vibrational states will have an impact on high harmonic generation.

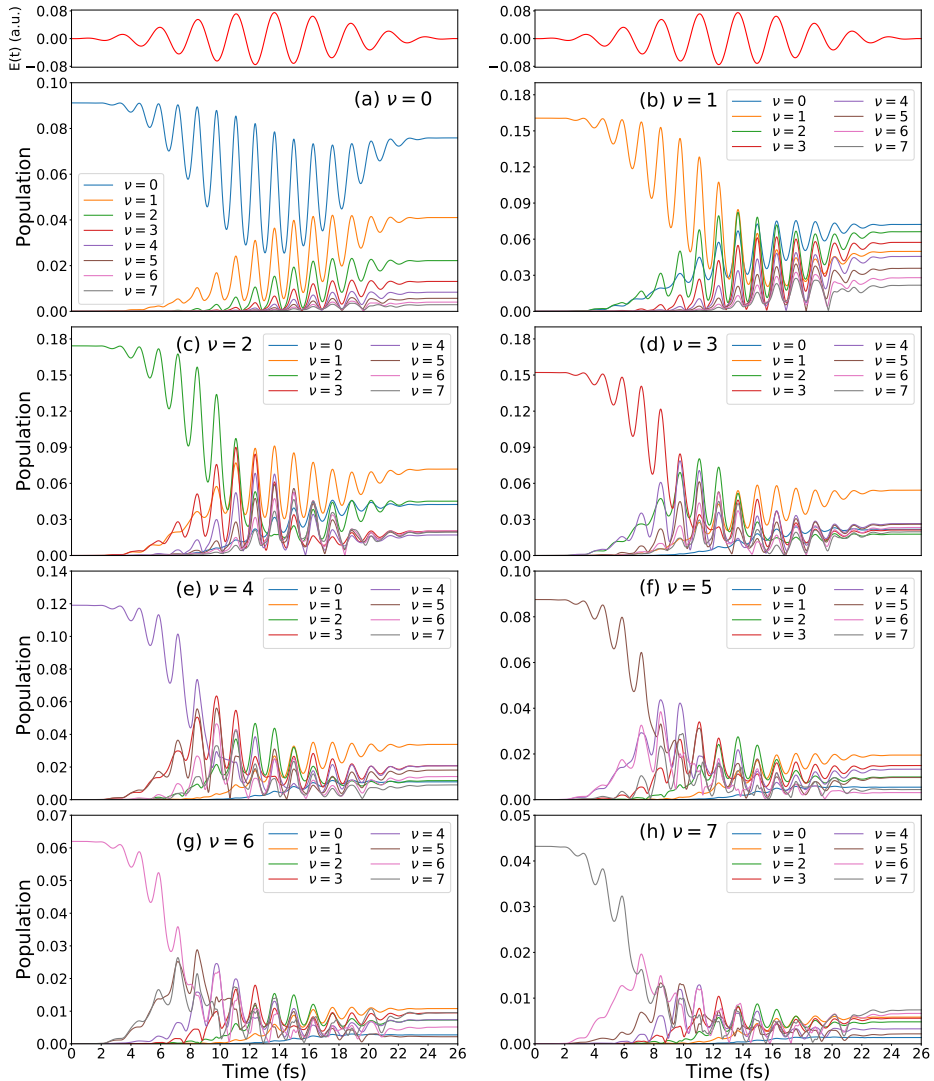


Figure 4.21: Time-dependent population of the H_2^+ driven by 780 nm IR pulse (10 cycles, 2×10^{14} W/cm²). In each frame the initial state is a different vibrational state, and each line represents a contribution coming from a different vibrational state. However in this figure all the vibrational states in each frame has been multiplied by a Franck-Condon factor, corresponding to the initial vibrational state. The upper frames represents the temporal profile of the laser pulse.

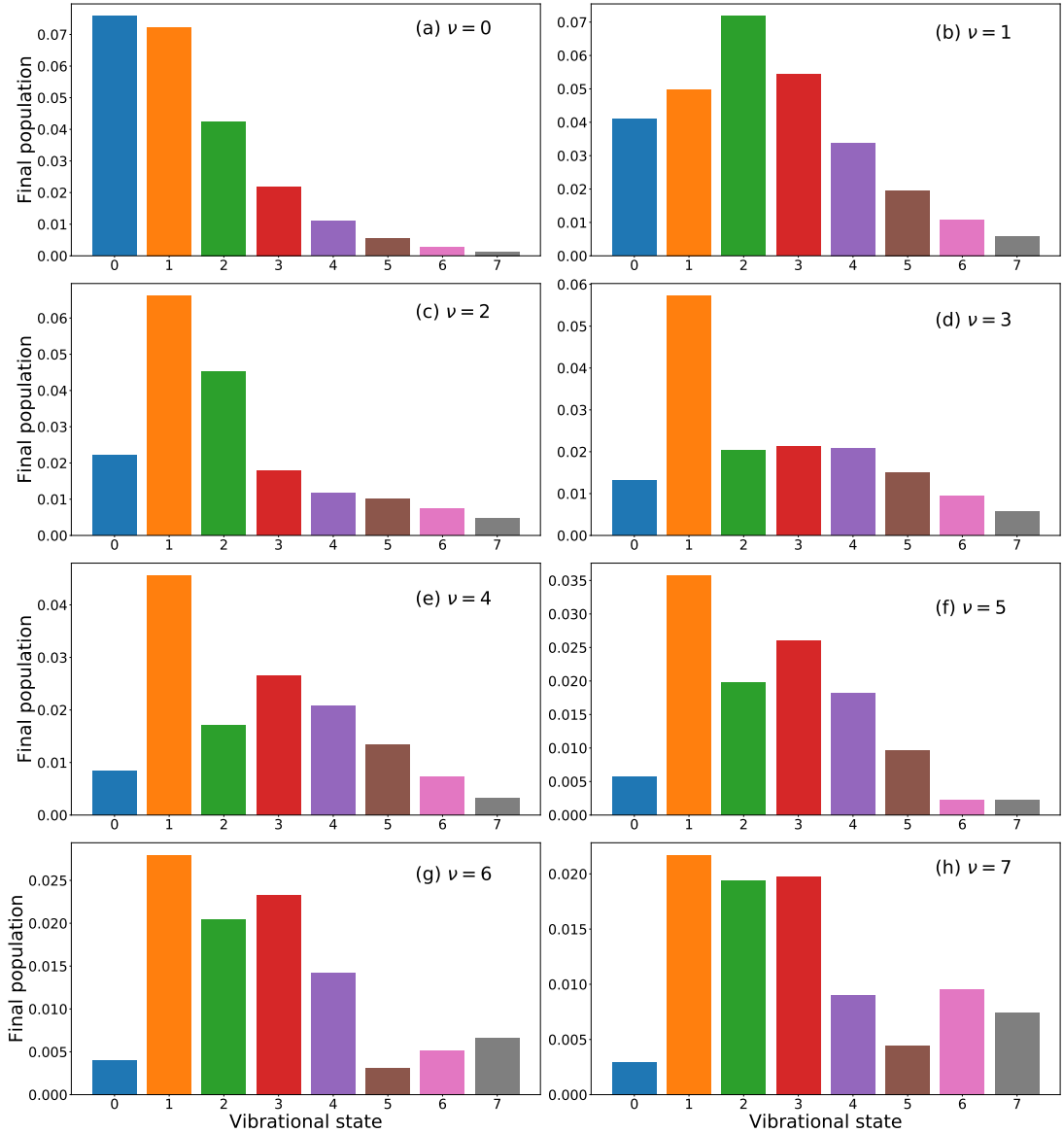


Figure 4.22: Final vibrational state populations of the H_2^+ after interaction with an 780 nm IR laser pulse (10 cycles, $2 \times 10^{14} \text{ W/cm}^2$). In each frame the initial state is a different vibrational state, and each bar presents the final population of each vibrational states. However in this figure all the vibrational states in each frame has been multiplied by a Franck-Condon factor, corresponding to the initial vibrational state.

The IR photon energy is nearly resonant with the energy gaps between vibrational states, causing vibrational excitation and eventually leading to dissociation, as we could see in Figure 4.21. Hence, the molecule is stretched, since higher vibrational states are associated with larger internuclear distances, and consequently the harmonic emission is more efficient. This is due to the fact that the ionisation rate is dependent on the internuclear distance, a phenomenon that has been called charge-resonant enhanced ionisation, CREI [124, 130, 252]. At the same time, as the molecule dissociates, the nuclei reach critical CREI internuclear distances that leads to ionisation and recombination on the rising part of the pulse. The falling part of the pulse has a negative chirp, causing a redshift in the harmonic peaks [253]. In addition, it has been theoretically predicted that the recombination step also changes at large internuclear distances, modifying dramatically the cut-off of the HHG spectrum [143–145].

Recently it has been observed that, when the molecule is dissociating, the IR field, with a photon energy of $E = 0.058$ Hartrees approximately, couples the $1s\sigma_g$ state with the $2p\sigma_u$ state via three-photon resonance at $R = 3.4$ au, or via one-photon resonance at $R = 5.2$ au [106, 109, 112]. These couplings lead to localisation of the electron on one of the two ions, creating a permanent dipole moment which breaks the spatial symmetry of homonuclear molecules. Therefore both odd and even harmonics can be produced in this case [254, 255]. Indeed, one can control the harmonic cut-off and the efficiency of the radiation emission by controlling the chirp of the incident laser pulse and the laser-coupling between the $1s\sigma_g$ and $2p\sigma_u$ states [256].

The high-harmonic spectra for H_2^+ starting from different vibrational states is shown in Figure 4.23 where the black thin vertical lines in each frame point the expected odd harmonics generated, and the red vertical lines denote the ionisation threshold, I_p (left line) and the cut-off limit, $I_p + 3.17U_p$ (right line). We observe that the HHG spectra depends dramatically on the initial configuration of the molecule, and hence on the evolution of the populations of other vibrational states during the interaction with the pulse, seen in Figure 4.21. For the $\nu = 0$ and $\nu = 1$ vibrational states the HHG yield is low, since the ionisation yield is low. For the $\nu = 2$ state the HHG plateau is more pronounced and for higher initial vibrational states the plateau and the cut-off are clearly visible, since higher initial vibrational state have higher ionisation yields. It is also interesting to note that, for all calculations the cut-off energy is lower than the classically predicted cut-off.

We must always bear in mind that in this case, HHG is occurring in the presence of vibrational excitation and dissociation. The lower cut-off energy observed is caused by nuclear motion, that modifies the states the electrons were originally ionised during the recombination step. Hence, this change in the state the electrons are recombining to produces a change in the harmonic intensity. The yield of the harmonics in the plateau are then proportional the modulus square of an autocorrelation function

$$C(t) = \int \chi^*(R, 0)\chi(R, t)dR \quad (4.29)$$

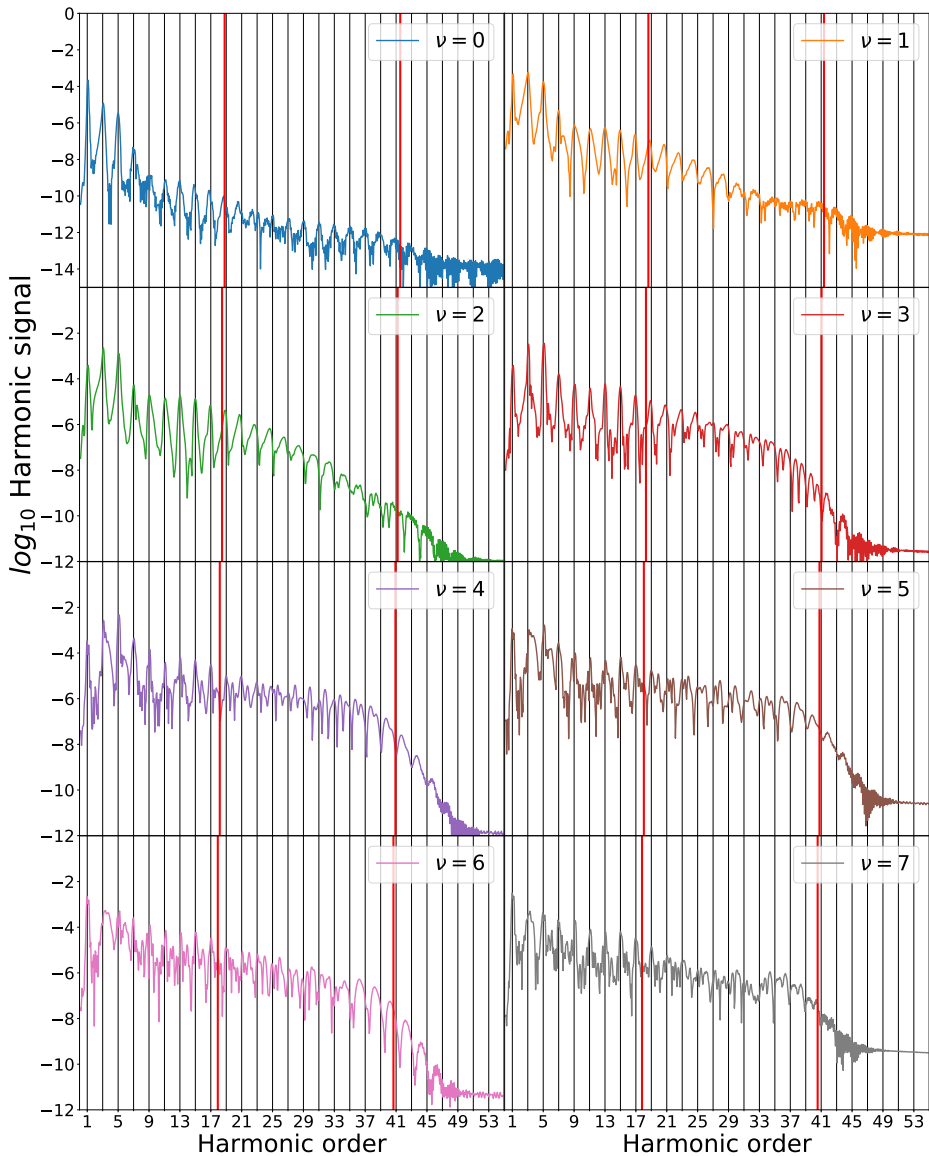


Figure 4.23: High-Harmonic spectra of H_2^+ driven by 780 nm IR pulse (10 cycles, $2 \times 10^{14} \text{ W/cm}^2$). Each frame corresponds to a different initial state set to one vibrational state from $\nu = 0, 7$. The black vertical grid lines marks the odd harmonics, and the red vertical lines represent the ionisation threshold I_p (left line) and the cut-off limit, $3.17U_p + I_p$ (right line).

where $C(t)$ is the autocorrelation function, $\chi(R, t)$ is the nuclear wavefunction, and t denotes the excursion time of the electrons. With light isotopes, the autocorrelation function decays faster than in the heavy isotope case, indicating that the nuclear wavepacket has been excited far from the ground state, and consequently suppressing the most energetic harmonics. This effect was first described by Lein [148, 257] and later observed experimentally [16].

In order to check if nuclear motion is behind the reduction of the cut-off energy, we have performed a series of fixed-nuclei calculations at different internuclear separations with the same laser pulse. The results are presented in Figure 4.24. For all internuclear separations

both the start and cut-off of the plateau are placed at the expected energies. In this case the nuclear autocorrelation function is equal to one and thus independent of time and so no modifications in these positions should be present. Also, the yield of the harmonics is lower than in the vibrating nuclei case, due to the enhanced ionisation at certain internuclear distances caused by CREI. Additionally the spectra for $R = 3$ and $R = 4$ show that even harmonics are produced, due to the fact that these internuclear distances are near the values of R at which the ground state and the first excited state are connect via one of three photon resonance.

Regarding the parity of the harmonics, we can see that the spectra for $\nu = 0$ and $\nu = 1$ do not posses even harmonics. However, from $\nu = 2$, we start to see even harmonics from approximately harmonic number 20 to harmonic number 35. For $\nu = 3$ and higher the even harmonics extend to the cut-off region. To study HHG in Figure 4.23 in more detail, we have performed a time-frequency analysis on our spectra. In a time-frequency analysis (also called the Gabor transform) we Fourier transform a particular temporal window of the dipole acceleration, $d(t)$, using as a window a Gaussian function

$$H(\omega, t) = \int_{-\infty}^{\infty} dt' e^{-(t-t')^2/T^2} e^{-i\omega t'} d(t'), \quad (4.30)$$

where the parameter T controls the width of the Gaussian. Indeed, the choice of the width is important for the analysis: the narrower the window the lower the time resolution obtained. We consider a Gaussian width of

$$T = 0.05 \frac{2\pi}{\omega_L} \quad (4.31)$$

were ω_L is the central frequency of the laser. This is equivalent to use a Gaussian window with full width half maximum (FWHM) of $3\omega_L$. With a scan across all frequencies of the spectrum we can gain insight into the time at which the harmonics are generated.

Using time-frequency analysis it is possible to resolve in time when different harmonics were generated. Indeed, it is possible to identify the contribution of the long and short electron's trajectories to the harmonic spectrum. In particular, harmonics produced by short trajectories have a positive slope in the density plot, while harmonics produced by long trajectories have negative slope. The results obtained from the analysis are shown in Figure 4.25. As in the atomic case, harmonics due to short trajectories have a larger efficiency than those corresponding to long trajectories. This is caused by the spreading of the recolliding electron wavefunction that is greater for long trajectories [74].

For the initial vibrational state $\nu = 0$, the harmonics have a low spectral density, indicating low ionisation and recombination. The spectral density increases for higher initial vibrational states. For $\nu = 1$, harmonic density are larger, and the harmonic density increasing for higher initial vibrational states. The initial vibrational states $\nu = 4$ and $\nu = 5$ illustrate the underlying mechanism that leads to the redshift of the harmonic spectra [253]. The rising part of the pulse causes nuclear excitation that prepares the molecule at larger internuclear distances,

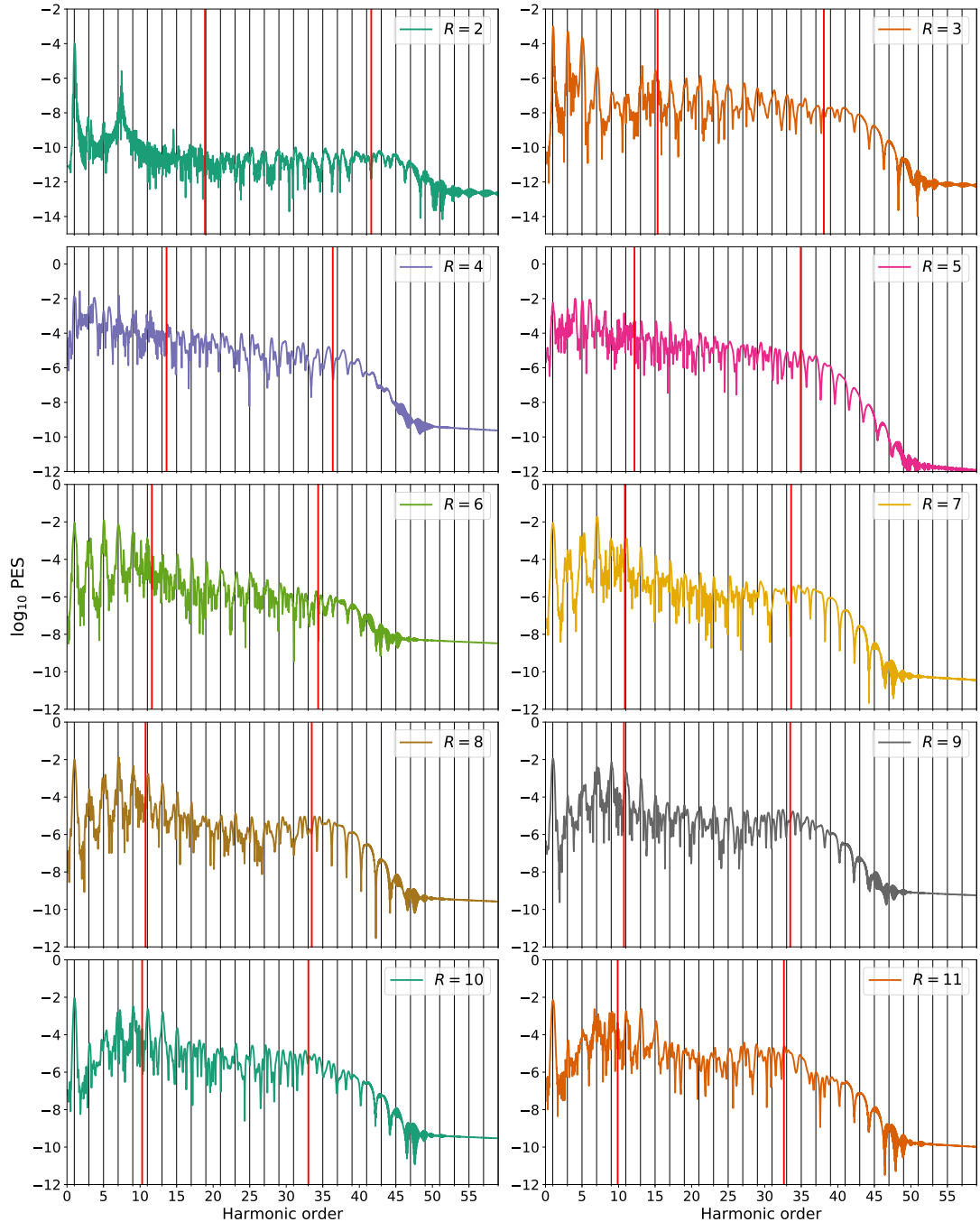


Figure 4.24: High-Harmonic spectra of fixed-nuclei H_2^+ driven by 780 nm IR pulse (10 cycles, $2 \times 10^{14} \text{ W/cm}^2$). Each frame shows the spectra at a particular internuclear distance, increasing R from the upper to the lower part of the figure. The black vertical lines represent the ionisation threshold I_p (left line) and the cut-off limit, $3.17I_p + I_p$ (right line).

and since ionisation rates depends on the internuclear distance of the molecule, is only at the trailing part that the ionisation occurs. If we consider higher initial vibrational states, $\nu > 5$, the critical internuclear distance associated with larger ionisation rates are reached sooner, and thus ionisation occurs at both the rising and trailing parts of the pulse, suppressing the redshift in the spectra.

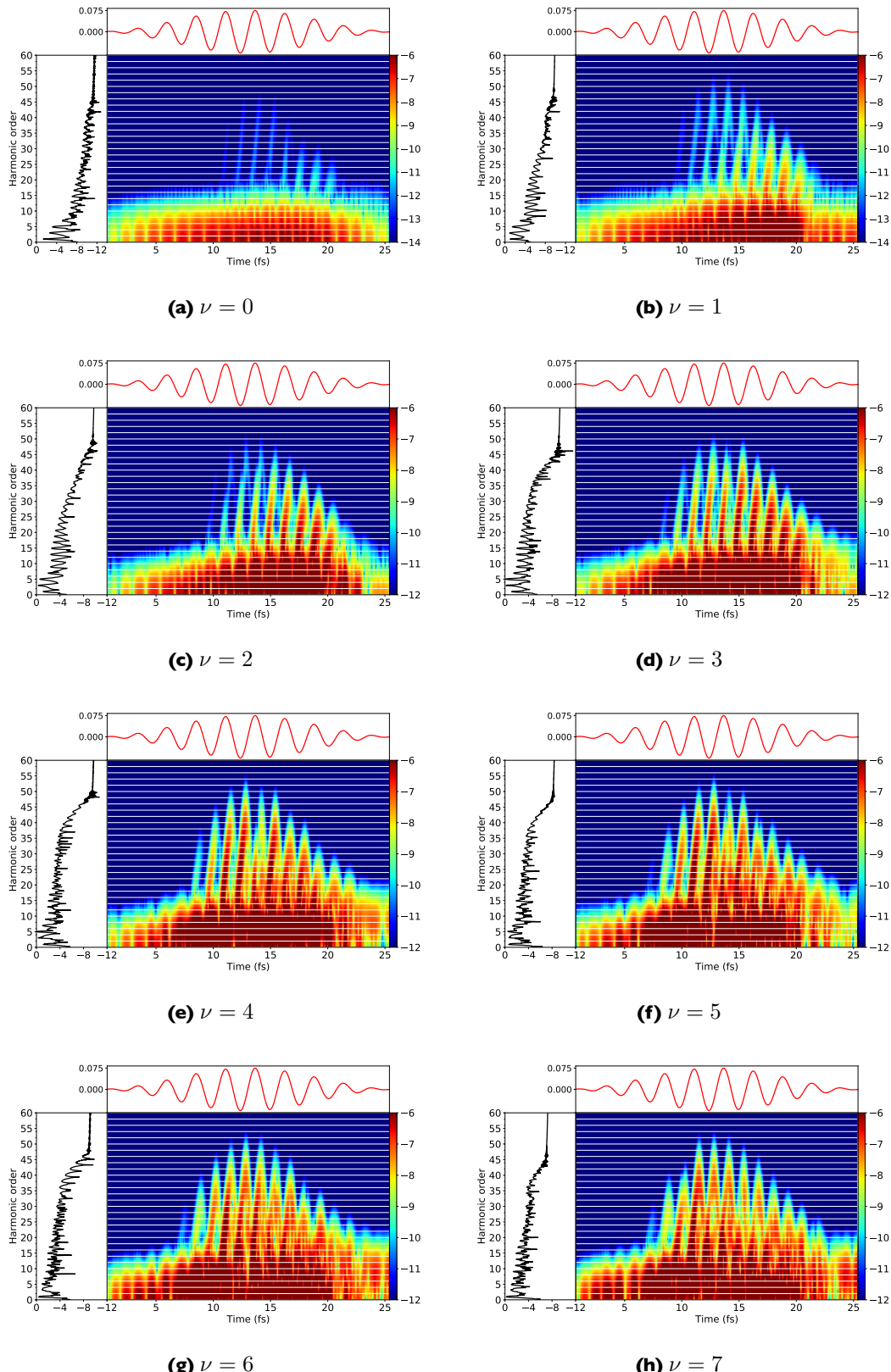


Figure 4.25: Density plots showing the time-frequency analysis on the HHG of H_2^+ interacting with a 10-cycle laser pulse, having a wavelength $\lambda = 780 \text{ nm}$ and a peak intensity of $I = 2 \times 10^{14} \text{ W/cm}^2$. In each frame the upper part presents the temporal profile of the electric field of the pulse, while the left side presents the corresponding HHG spectra. For clarity, the horizontal lines marks the even harmonic orders.

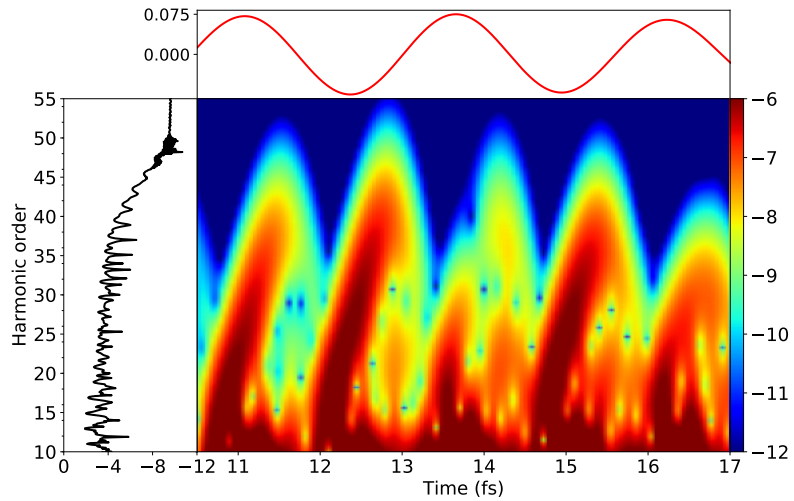


Figure 4.26: Zoom of the time-frequency analysis for the initial vibrational state $\nu = 4$ of the H_2^+ interacting with a 10-cycle laser pulse having a wavelength of $\lambda = 780$ nm and a peak intensity of $I = 2 \times 10^{14}$ W/cm 2 (shown in Figure 4.25e), between 10.5 and 17 fs. The upper frame corresponds to the electric field, while the left frame shows the corresponding to the high-harmonic generation spectra.

Moreover, it is possible from Figure 4.25 to determine when the even harmonics are created. For instance, consider the TFA for initial vibrational state $\nu = 5$, Figure 4.25f. We observe that in the middle of the pulse, around 5 fs, the maximum harmonic emitted is 56 (an even harmonic), in contrast to the maximum harmonic emitted, 53 (an odd harmonic), in the previous half-cycle. This indicates that during this half-cycle the molecule has reached the critical internuclear distance for three-photon resonance, $R = 5.4 a_0$.

Also, it is interesting to note that for initial vibrational states $\nu = 4$ and $\nu = 5$ there are half cycles in which the spectral density is lower than neighbour half-cycles. For instance, for $\nu = 4$, consider the harmonic density at 5.5 fs, during the 6th cycle of the pulse, in Figure 4.26. We speculate that this effect can be due to the interference between several vibrational states, because, if we look at the frames for these initial vibrational state in Figure 4.21, they present similar population of most of the vibrational states considered in the plot at the specific instant of the laser pulse. However, the study in detail of this effect requires further investigation and it is outside the scope of this thesis.

4.4 Summary

In this chapter we have presented results on the study of the role of vibrational states in the strong-field ionisation, dissociation and high harmonic generation of H_2^+ irradiated with intense laser pulses. In the first section of the chapter, we have tested the accuracy of the numerical implementation by solving the time-independent Schrödinger equation of our H_2^+ model, which uses a non-Born-Oppenheimer approach. Firstly, we have carried out a fixed-nuclei cal-

culation, where electronic states were obtained. We have then compared the two lowest potential energy curves, corresponding to the $1s\sigma_g$ ground state and the $2p\sigma_u$ first excited state with results obtained with a close-coupling method, where excellent agreement was found. Secondly, we have compared the vibrational energies, obtained with our non-Born-Oppenheimer approach, against two sets of results: in the latter calculation the eigenenergies are obtained from a finite-difference grid by diagonalising the Hamiltonian using PETSc and SLEPc packages. The former calculation obtains the eigenenergies from an accurate variational method, diagonalising the Hamiltonian using a Lanczos algorithm. The largest difference found between both sets of results is less than 1%. In the last part of the section, we have studied the dependence of the accuracy of the vibrational levels on the grid spacings for all coordinates, where it was found that setting ΔR to small values helps to achieve a faster convergence. This is due to nuclear motion, which occurs along the R coordinate, is closely related to the vibrational levels.

In Section 4.2 we have shown results from the interaction of H_2^+ with an intense ultrashort VUV pulse, starting from the $1s\sigma_g(\nu = 0)$ and the $1s\sigma_g(\nu = 2)$ vibrational states. The pulse parameters were set so that multiphoton ionisation would be the dominant mechanism. In addition, in each case the photon energy of the laser pulse was chosen to match the gap between the initial state and the $2p\sigma_u$ first excited state of the molecule. The time evolution of the wavefunction showed two nuclear wavepackets travelling along the R coordinate, whose spatial width can be related with the bandwidth of the incident pulse. If we assume nuclear wavepackets to be classical particles moving along potential energy curves, the resulting trajectories can be compared with the time evolution of the nuclear probability densities, where the spatial width of the nuclear wavepacket is taken into account by considering a range of initial positions. We found that, the trajectories within the $2p\sigma_u$ and $3s\sigma_g$ potential energy curves are in good agreement with the nuclear probability densities. For the case of starting from the $\nu = 2$ vibrational state, the snapshots of the evolution of the wavefunction showed that the vibrational structure of the molecule is imprinted in the dissociating nuclear wavepackets. Ionisation and dissociation yields are calculated from the division of the configuration space into regions and integrating the probability density for each of the regions. Doing so we have study the role of each vibrational state by comparing the yields obtained from calculations starting from one level of the ten lowest vibrational states. Also, we have compared the yield resulting from a calculation whose initial state is linear combination of vibrational states weighted with their correspondent Franck-Condon factors (we denote this calculation as FC) against the incoherent sum of the yields resulting from calculations that starts from one of the ten lowest vibrational states (denoted as IS). It is interesting to note that the dissociation yield for the case of the FC calculation starts later than the IS case, suggesting that the coherent combination of states prevents dissociation. The FC dissociation yield presents a hump at 9 fs, indicating a change in the dissociation rate long time after the end of the pulse due to a presence of a resonant state.

Finally, Section 4.3 is dedicated to the case of the H_2^+ irradiated with IR laser pulses. After

showing snapshots of the time evolution of the probability density of the wavefunction, we repeat the study on the role of the vibrational levels by comparing the ionisation and dissociation yields. In this case, ionisation rates showed a dependency of the ionisation rates on the initial vibrational level. Since vibrational states have a mean internuclear distance, the ionisation rates are dependent on the internuclear distance, an effect called charge-enhanced resonant ionisation (CREI). Moreover, the ionisation yields showed that for H_2^+ two ionisation bursts occur per half-cycle instead of one in the atomic case. We also showed the time evolution of the population of each individual vibrational state from calculation starting from one vibrational levels of the ten vibrational states. In those plots we clearly see Rabi oscillations whose amplitudes are smaller for higher initial vibrational state. The fact that starting from one particular vibrational state leads to a final combination of vibrational states is emphasised because its relevance in pump-probe studies.

The dependence on the vibrational states in the high harmonic spectra is discussed in the last part of this section. Starting from one particular vibrational level, we can see from the spectra that the amplitude in the harmonic signal is dependent on the initial vibrational level, due again to the CREI effect, since a higher ionisation rate leads to a higher harmonic signal. We also see, for higher vibrational levels, a reduction of the cut-off due to nuclear motion, that modifies the electronic states where the electrons are recombining and producing a change in the harmonic intensity. The fact that this effect is not present in the spectra obtained from fixed-nuclei calculations indicates that it is indeed caused by nuclear motion, and it can be described by an autocorrelation function between the initial and the time-dependent nuclear wavefunction. More interesting is the presence of even and odd harmonics in the spectra. In vibrating homonuclear molecules, the electron localisation, due to resonant coupling between electronic states, creates a permanent dipole that breaks the spatial symmetry. This symmetry breaking leads to the production of odd and also even harmonics, in contrast to the fixed nuclei case, which only odd harmonics are produced. In addition, the time-frequency analysis (TFA) reveals that for higher initial vibrational states harmonics are generated earlier during the pulse. Also, it is possible to determine when the even harmonics are generated by visual analysis of the TFA. For initial vibrational states $\nu = 4$ and $\nu = 5$ there are half cycles in which spectral density is reduced compared to neighbouring half cycles, suggesting a mechanism which inhibits harmonic production. However, further investigation is required to determine the origin of this effect.

5

Calculation of photoelectron spectrum: The POpSiCLE library

Photoelectron spectroscopy is a powerful tool used to obtain valuable information about matter irradiated by intense laser pulses. By measuring the energy and angular distributions of the photoproducts emitted during interaction with these laser pulses, we can obtain valuable information about the structure and dynamical response of the material.

Calculating photoelectron spectra is computationally demanding. A first approximation is to use an interaction volume large enough to hold the high-energy electrons produced during the interaction. The desired spectra will then be obtained by performing a Fourier transform of the unbound wavefunction at the end of the pulse. We call this the Fourier method, and it can be seen as a brute force method. The Fourier method approach for full-dimensional models involving more than two dimensions is incredibly expensive. First, due to high energy electrons moving large distances, extremely large boxes required. Secondly, performing the Fourier transform of a large multidimensional wavefunction is itself not a trivial task.

To reduce the computational demand a method analogous to how photoelectron spectra are experimentally recorded in laboratories has been proposed. Experimentally, photoelectrons are collected by detectors that are placed at a certain distance from the interaction volume. In the similar way, we can think of collecting the outgoing electron wavepackets as they pass certain points (detector points) in coordinate space, and energy analyse this information. In that case, the calculation size will be smaller since we can use absorbing boundaries to remove ionised wavepackets that have passed the detector points. We call this approach the sampling point method [258].

Another method to calculate photoelectron spectra is called the time-dependent surface flux method (t-SURFF) [259]. In this method we record the flux of ionised electrons that passes a surface of radius r_b . The spectra can then be obtained by calculating the projection of the outgoing electron wavepackets at this surface onto Volkov waves (the solutions of a free electron in the presence of a laser field), before the wavepackets are absorbed. In this case, the energy of outgoing electrons are obtained from a surface integral which is integrated over time, rather than a volume integral as is used by the Fourier method. This dramatically reduces the computational cost.

In the laser-matter community a large number of codes are used to solve the TDSE. Usually, each code implements its own approach to calculate the photoelectron spectra (in some cases there is no implementation available). This means that much effort goes into implementing the same approach many times. For that reason, we have developed a parallel library of routines for calculating the angular and energy resolved photoelectron spectra using three different approaches:

1. The Fourier transform of the spatial scattering solution into momentum space,
2. The sampling point method, and,
3. The time-dependent surface flux method (t-SURFF).

In this section we will introduce the three theoretical methods implemented in the library **P0pSiCLE**. In Section 5.1, we discuss how to obtain the spectral amplitudes of ionised electrons, and also the joint spectral amplitude for the photoelectron spectra and the kinetic energy release of the nuclei using the Fourier method. In Section 5.2 we describe the sampling point method, and how to easily extract the PES. Finally in Section 5.3 we review the time-dependent surface flux method (t-SURFF) for single ionisation and correlated electron-nuclear spectra. In Section 5.4 we present the numerical implementation of the library. Finally, in Section 5.5 we compare the interpolation routines introduced in Section 5.4 that are implemented in **P0pSiCLE**.

5.1 Fourier method

The simplest way to extract asymptotic information is by projecting the wavefunction onto field-free plane waves at the end of a calculation. We proceed as follows: consider coordinate space divided into two regions: an inner region which contains all the bound states of the system and an outer region which contains the scattering products of any interaction. Both regions are separated by a surface of radius r_b . Therefore, we can always write the wavefunction as

$$\Psi(\mathbf{r}, T) = \Psi_b(\mathbf{r}, T) + \Psi_s(\mathbf{r}, T) \quad (5.1)$$

where $\Psi_b(\mathbf{r}, t)$ is the bound part and $\Psi_s(\mathbf{r}, t)$ the scattering part of the wavefunction and T is a time large enough that the asymptotic part has time to cross the boundary surface r_b .

Therefore

$$\Psi_b(\mathbf{r}, T) \approx 0 \quad \text{for } |\mathbf{r}| \geq r_b \quad (5.2)$$

$$\Psi_s(\mathbf{r}, T) \equiv \int d\mathbf{k} e^{-iT\mathbf{k}^2/2} b(\mathbf{k}) \psi_k(\mathbf{r}) \approx 0 \quad \text{for } |\mathbf{r}| \leq r_b \quad (5.3)$$

where \mathbf{k} is the momentum vector, $b(\mathbf{k})$ are the spectral amplitudes that can be obtained by spectral decomposition of the wavefunction

$$b(\mathbf{k}) = \langle \psi_k | \Psi_s(T) \rangle e^{-iT\mathbf{k}^2/2} \quad (5.4)$$

and $\psi_k(\mathbf{r})$ are the scattering solutions of a time-independent Hamiltonian that governs the system after the interaction with the electromagnetic field. Hence, $\psi_k(\mathbf{r})$ obey the TDSE

$$H(T) |\psi_k\rangle = \frac{\mathbf{k}^2}{2} |\psi_k\rangle. \quad (5.5)$$

Photo-ionisation experiments implicitly assume that, at large distances from the interaction region (where the detectors are placed), and large times after the interaction, the scattering wavefunctions are described as free particles. In that case (at asymptotic distances and times) and neglecting the Coulomb potential, we can approximate the scattering solutions by plane waves of the form

$$\chi_k(\mathbf{r}) = \frac{1}{(\sqrt{2\pi})^3} e^{i\mathbf{k}\cdot\mathbf{r}}. \quad (5.6)$$

We can therefore decompose the spectral amplitudes using plane waves, i.e.

$$\begin{aligned} b(\mathbf{k}) e^{iT\frac{\mathbf{k}^2}{2}} &= \langle \chi_k | \Psi_s(T) \rangle = \int d\mathbf{r} \chi_k^*(\mathbf{r}) \Psi_s(\mathbf{r}, T) \\ &= \frac{1}{(\sqrt{2\pi})^3} \int d\mathbf{r} e^{-i\mathbf{k}\cdot\mathbf{r}} \Psi_s(\mathbf{r}, T). \end{aligned} \quad (5.7)$$

The result, Eq. (5.7), is merely the Fourier transform of the scattering part of the wavefunction [202, 208]. The only requirement imposed by the Fourier transform is that the canonical momentum of the wavefunction must be the same as the mechanical momentum. This means that, using the velocity gauge, the projection must be carried out after the passage of the laser pulse.

It is important to mention that the exact outgoing scattering solutions in the presence of the Coulomb potential, in the asymptotic limit, are given by [260]

$$\chi_k(\mathbf{r}) \sim \frac{1}{r} e^{i(kr - i\gamma \ln 2kr)} f_c(\theta) \quad (5.8)$$

where $\gamma = Z/k$ and Z the charge of the nucleus, $f_c(\theta)$ is known as the Coulomb scattering amplitude

$$f_c(\theta) = -\frac{\gamma}{2k \sin^2 \theta/2} e^{-i\gamma \ln(\sin^2 \theta/2) + 2i\sigma_0}, \quad (5.9)$$

and σ_0 is the Coulomb phase shift

$$\sigma_0 = \arg \Gamma(1 + i\gamma). \quad (5.10)$$

However, the scattering amplitudes obtained projecting against outgoing Coulomb waves,

$$b(\mathbf{k}) \sim \int d\mathbf{r} \frac{1}{r} e^{-i(kr - \gamma \ln 2kr)} f_c^*(\theta) \Psi_s(T), \quad (5.11)$$

do not correspond to the Fourier transform of the scattering part of the wavefunction. Therefore, Fourier transform algorithms can not be used, and instead less efficient numerical integrations are required to obtain the spectral amplitudes. In order to avoid that, we can always assume plane wave solutions if we consider far enough distances so the Coulomb potential is negligible.

We note that when performing a grid calculation then, if the edges of the grid act as hard walls, the wavefunction will perfectly reflect back when it reaches the edges. The momentum of the reflecting wavepackets will not change except for their direction. As long as the wavepacket do not interfere with the bound states of the box, a Fourier analysis will be unaffected by these reflections.

5.1.1 Joint electron-nuclear spectra for the hydrogen molecular ion

To obtain the spectral amplitude for both electrons and ions in the hydrogen molecular ion, we must take into account the nuclear motion as well. We can think again of, not two, but four regions and two boundary surfaces. In this case we have a boundary surface in the electronic coordinate, r_b , as described above together with another in the ionic coordinate which separates the bound molecule from the dissociated molecule, R_b (See Figure 5.1).

We distinguish two different channels in the break-up process of the H_2^+ molecule. Firstly, we have the dissociative ionisation (DI) channel



in which, after reacting with n photons of energy ω , the asymptotic state consists of two protons and an electron far away from each other. Secondly, we have the dissociation channel



in which the asymptotic state is formed by a hydrogen atom and a proton.

The joint electron-ion spectra is obtained from the dissociative ionisation channel. This can be obtained by generalising the result of Eq. (5.7) by projecting onto the scattering solutions

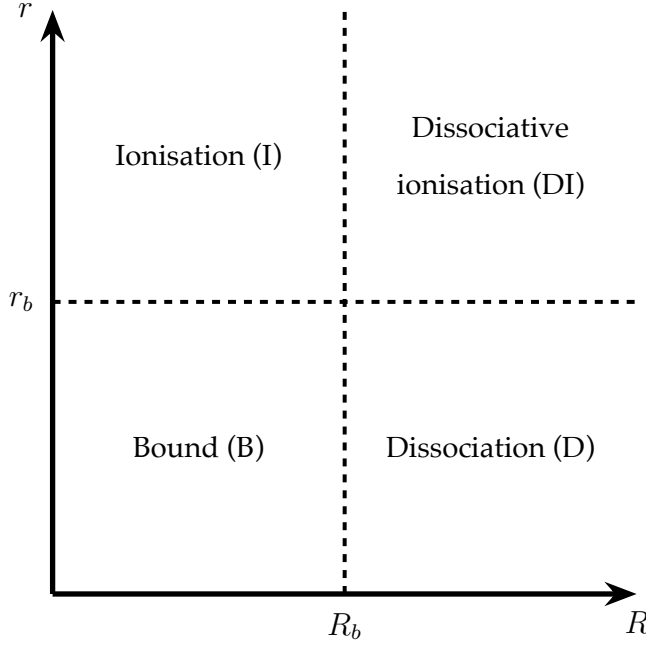


Figure 5.1: Diagram of the separation in different regions of the H_2^+ coordinate space interacting with an external laser pulse. The four regions are: Bound (B), Dissociation (D), Ionisation (I) and Dissociative ionisation (DI), and their boundaries are represented by dashed lines at $r = r_b$ and $R = R_b$.

for dissociative ionisation. We denote

$$|\chi_{k_R} \chi_{k_r}\rangle = |\chi_{k_R}\rangle \otimes |\chi_{k_r}\rangle \quad (5.14)$$

where \mathbf{k}_r and \mathbf{k}_R are respectively the momentum for electrons and ions and $\chi_{k_r}(\mathbf{r})$ and $\chi_{k_R}(\mathbf{R})$ are respectively electronic and nuclei plane waves where

$$\chi_{k_r}(\mathbf{r}) = \frac{1}{(\sqrt{2\pi})^3} e^{i \mathbf{k}_r \cdot \mathbf{r}} \quad (5.15)$$

and

$$\chi_{k_R}(\mathbf{R}) = \frac{1}{\sqrt{2\pi}} e^{i \mathbf{k}_R \cdot \mathbf{R}}. \quad (5.16)$$

The prefactor in Eq. (5.15) differs from that in Eq. (5.16) since the electronic solutions reside in a 3D space whereas the ionic solutions are in 1D since we only treat vibrational motion. Similarly to Eq. (5.7) we write the spectral amplitudes for dissociative ionisation as

$$\begin{aligned} b(\mathbf{k}_r, \mathbf{k}_R) e^{iT \frac{\mathbf{k}_r^2}{2}} e^{iT \frac{\mathbf{k}_R^2}{2}} &= \langle \chi_{k_R} \chi_{k_r} | \Psi_s(T) \rangle \\ &= \int \int d\mathbf{R} d\mathbf{r} \chi_{k_R}^*(\mathbf{R}) \chi_{k_r}^*(\mathbf{r}) \Psi_s(\mathbf{r}, \mathbf{R}, T) \\ &= \frac{1}{(2\pi)^2} \int \int d\mathbf{R} d\mathbf{r} e^{-i \mathbf{k}_r \cdot \mathbf{r}} e^{-i \mathbf{k}_R \cdot \mathbf{R}} \Psi_s(\mathbf{r}, \mathbf{R}, T). \end{aligned} \quad (5.17)$$

In this equation the integrals are taken over the dissociative ionisation region defined in Figure 5.1, i.e. $r > r_b$, $R > R_b$. For both the electronic spectrum and joint electron-ion spectrum we require a grid large enough to hold the wavefunction after the end of the pulse. This ex-

pensive requirement is even worse for electron-nuclear or multi-electron problems, where the size of the grid scales exponentially with the dimensionality of the problem. As a example, this approach was used by Taylor and coworkers to study non-sequential double ionisation of helium [225, 226, 261].

In the following we give the Fourier transform in Cartesian, cylindrical and spherical coordinates.

Joint electron-ion spectra in Cartesian coordinates

This form of the Fourier transform is required for calculations using RHYthMIC. In this case, we define

$$\mathbf{r} = x(\xi^x)\mathbf{i} + y(\xi^y)\mathbf{j} + z(\xi^z)\mathbf{k} \quad (5.18)$$

$$\mathbf{k}_R = k_x\mathbf{i} + k_y\mathbf{j} + k_z\mathbf{k} \quad (5.19)$$

and also

$$\mathbf{R} = R(\xi^R)\mathbf{l} \quad (5.20)$$

$$\mathbf{k}_R = k_R\mathbf{l} \quad (5.21)$$

where x, y, z and R are the scaled Cartesian coordinates introduced in Section 2.5.1. We express Eq. (5.17) in Cartesian coordinates

$$\begin{aligned} b(\mathbf{k}_r, \mathbf{k}_{bvR}) e^{iT \frac{\mathbf{k}_r^2}{2}} e^{iT \frac{\mathbf{k}_R^2}{2}} &= \frac{1}{4\pi^2} \int_0^{R_{\max}} d\xi^R R'(\xi^R) e^{-ik_R R(\xi^R)} \int_{-z_{\max}}^{z_{\max}} d\xi^z z'(\xi^z) e^{-ik_z z(\xi^z)} \\ &\times \int_{-y_{\max}}^{y_{\max}} d\xi^y y'(\xi^y) e^{-ik_y y(\xi^y)} \int_{-x_{\max}}^{x_{\max}} d\xi^x x'(\xi^x) e^{-ik_x x(\xi^x)} \\ &\times \Psi_s(x(\xi^x), y(\xi^y), z(\xi^z), R(\xi^R), T) \end{aligned} \quad (5.22)$$

where we have split Eq. (5.17) in four consecutive integrals.

Joint electron-ion spectra in cylindrical coordinates

This form of the Fourier transform is required for calculations involving THeREMIN. In this case we define

$$\mathbf{r} = \rho(\xi^\rho) \cos \varphi \mathbf{i} + \rho(\xi^\rho) \sin \varphi \mathbf{j} + z(\xi^z) \mathbf{k} \quad (5.23)$$

$$\mathbf{k}_R = k_\rho \cos \varphi_k \mathbf{i} + k_\rho \sin \varphi_k \mathbf{j} + k_z \mathbf{k} \quad (5.24)$$

and also define

$$\mathbf{R} = R(\xi^R)\mathbf{l} \quad (5.25)$$

$$\mathbf{k}_R = k_R\mathbf{l} \quad (5.26)$$

where ρ and z are the scaled cylindrical coordinates introduced in Section 2.5.2. In that case

$$\begin{aligned}\mathbf{k}_r \cdot \mathbf{r} &= k_\rho \rho(\xi^\rho) \cos \theta \cos \theta_k + k_\rho \rho(\xi^\rho) \sin \theta \sin \theta_k + k_z z(\xi^z) \\ &= k_\rho \rho(\xi^\rho) (\cos \theta \cos \theta_k + \sin \theta \sin \theta_k) + k_z z(\xi^z) \\ &= k_\rho \rho(\xi^\rho) \cos(\theta - \theta_k) + k_z z(\xi^z)\end{aligned}\quad (5.27)$$

If we substitute Eq. (5.27) into Eq. (5.7) we get

$$\begin{aligned}b(\mathbf{k}_R, \mathbf{k}_R) e^{iT\frac{\mathbf{k}_r^2}{2}} e^{iT\frac{\mathbf{k}_R^2}{2}} &= \frac{1}{(2\pi)^2} \int_0^{R_{\max}} d\xi^4 R'(\xi^R) e^{-ik_R R} \int_{-z_{\max}}^{z_{\max}} d\xi^z z'(\xi^z) e^{-ik_z z} \\ &\times \int_0^{\rho_{\max}} d\xi^\rho \rho(\xi^\rho) \rho'(\xi^\rho) \int_0^{2\pi} d\theta e^{-ik_\rho \rho(\xi^\rho) \cos(\theta - \theta_k)} \\ &\times \Psi_s(\rho(\xi^\rho), z(\xi^z), R(\xi^R), t).\end{aligned}\quad (5.28)$$

Letting $\Theta = \varphi - \varphi_k$ we can simplify the last integral to

$$\int_{-\varphi_k}^{2\pi - \varphi_k} d\Theta e^{-ik_\rho \rho(\xi^\rho) \cos \Theta} = \int_0^{2\pi} d\Theta e^{-ik_\rho \rho(\xi^\rho) \cos \Theta} = J_0(k_\rho \rho(\xi^\rho)) \quad (5.29)$$

which is just the zeroth order Bessel function [208]. Thus we can write

$$\begin{aligned}b(\mathbf{k}_r, \mathbf{k}_R) e^{iT\frac{\mathbf{k}_r^2}{2}} e^{iT\frac{\mathbf{k}_R^2}{2}} &= \frac{1}{(\sqrt{2\pi})^3} \int_0^{R_{\max}} d\xi^R R'(\xi^R) e^{-ik_R R(\xi^R)} \int_{-z_{\max}}^{z_{\max}} d\xi^z z'(\xi^z) e^{-ik_z z(\xi^z)} \\ &\times \int_0^{\rho_{\max}} d\xi^{rho} \rho(\xi^\rho) \rho'(\xi^\rho) \\ &\times \Psi_s(\rho(\xi^\rho), z(\xi^z), R(\xi^R), t) J_0(k_\rho \rho(\xi^\rho))\end{aligned}\quad (5.30)$$

In Eq. (5.30), the integral over the R and z coordinates is again a Fourier transform, while the integral over ρ is a Hankel transform [208] (also as the Fourier-Bessel transform). The Hankel transform is just the equivalent of a Fourier transform in polar coordinates.

5.2 The sampling point method

In the Fourier method we evaluate the PES by projecting the wavefunction onto scattering solutions. This involves the calculation of volume integrals which can become prohibitively expensive. In actual experiment, the PES is measured by collecting electrons that enter detectors placed at various points in space. We can think of calculating the PES using the same idea. In this case we record the wavefunction at particular points in space, and then Fourier-transform this collected wavefunction in time:

$$\Psi_s(\mathbf{r}_M, \omega) = \frac{1}{\sqrt{2\pi}} \int dt e^{i\omega t} \Psi(\mathbf{r}_M, t) \quad (5.31)$$

where \mathbf{r}_M is the measure point in which the wavefunction is collected.

We can show that Eq. (5.31) is related to $b(\mathbf{k})$, and so the PES can be calculated using $\Psi_s(\mathbf{r}_M, \omega)$ instead of the spectral amplitudes $b(\mathbf{k})$ [258]. In that case we can write

$$\Psi_s(\mathbf{r}_M, \omega) = \int d\Omega d\mathbf{k} k^2 \frac{1}{(\sqrt{2\pi})^3} e^{i\mathbf{k}\cdot\mathbf{r}_M} \int dt \frac{1}{\sqrt{2\pi}} e^{i(\omega-\omega_k)t} b(\mathbf{k}) \quad (5.32)$$

$$= \frac{1}{2\pi} \int d\Omega d\mathbf{k} k^2 e^{i\mathbf{k}\cdot\mathbf{r}_M} \delta(\omega - \omega_k) b(\mathbf{k}) \quad (5.33)$$

$$= \frac{1}{2\pi} \int d\Omega d\mathbf{k} k^2 e^{i\mathbf{k}\cdot\mathbf{r}_M} \delta(k - \sqrt{2\omega_k}) b(\mathbf{k}) \quad (5.34)$$

$$= 4\pi k^2 b(\sqrt{2\omega_k}) e^{iz_M \sqrt{2\omega_k}} \quad (5.35)$$

where $d\Omega = \sin \theta d\theta$ and $\omega_k = \frac{k^2}{2}$. We identify $E = \omega_k$, and the PES yield is simply given by

$$\frac{dP_M(E)}{dE} = \frac{1}{\sqrt{E}} |b(\mathbf{k})|^2 \propto \sqrt{E} |\Psi_s(\mathbf{r}_M, E)|. \quad (5.36)$$

We note that we have used $k = \sqrt{2\omega_k}$, which assumes that $k > 0$, hence we only consider outgoing wavepackets. We also assume that the momentum vector of these outgoing wavepackets are parallel to the radial vector, so $\mathbf{k} \cdot \mathbf{r}_M = k r_M$.

The average of the PES from all the measuring points across a sphere is the total PES

$$\frac{dP(E)}{dE} = \sum_M \frac{dP_M(E)}{dE} \gamma_M \quad (5.37)$$

In order to average between the points, the weighting factors γ_M are introduced. If we divide the surface covered by the measuring points on the unit sphere, with the surface S_M corresponding to a particular point \mathbf{r}_M , each weighting factor is just the solid angle covered by each point:

$$\gamma_M = \int d\Omega_M. \quad (5.38)$$

If we map each measuring point to their corresponding (θ, ϕ) pair, we get the photo-angular distribution (PAD):

$$|b_{\Omega_M}(\mathbf{k})| = |\Psi(\Omega_M, \omega)|. \quad (5.39)$$

The method was originally proposed by Pohl, Reinhard and Suraud [258] to study photo-fragmentation of clusters. The method is useful in situations where we want to know the shape of the PES, or the position of the peaks in the spectra, as in experiments with clusters and large systems [262–264], but not when we are interested in the actual values of the scattering amplitudes. The method gives a PES which is proportional to the spectral amplitudes by evaluating the energies that crosses the measuring points.

The sampling point method is a good approximation for short wavelengths and weak fields (and far from the bound states for long-range potentials). But for strong laser inter-

actions this is not the case any more. At very high field intensities we must consider Volkov solutions. To include those solutions in Eq. (5.32) a phase can be added to the wavefunction. The purpose of this phase is to cancel the phase introduced by the laser field. This approach was called ‘Phase augmented’ [265].

5.3 The surface flux method (t-SURFF)

Like the sampling point method, the surface flux method simplifies the calculation of the PES by avoiding the calculation of volume integrals. This means that large grids are not required to hold the ionised wavefunction. In the surface flux method the configuration space is divided into two regions, inner and outer, as described in Section 5.1. The flux of outgoing electrons passing through the surface between the two regions is recorded. One thing to consider is that the non-local interaction of the dipole and the external electric field modifies the energies of the system everywhere, therefore stationary solutions no longer apply in the outer region. In order to describe the evolution of the wavefunction once it has passed the surface we assume that the dynamics of the particle are only governed by the electromagnetic field, i.e. the dynamics are described by Volkov waves. This assumption allows to convert the volume integral in Eq. (5.7) into a time integral of a time-dependent flux passing through a surface. The fact that the outgoing wavepackets are only stored at certain points on the grid allows the use of absorbing boundaries at the edge of the boxes, reducing dramatically the size of the grid required.

The surface flux (t-SURFF) was developed by Tao and Scrinzi for one and two electron systems [259, 266], and it has been further applied to the strong field ionisation of H_2^+ [267, 268], and more complex systems with time-dependent configuration interaction singles (TD-CIS) [269]. To obtain the spectral amplitudes we use Eq. (5.7), but now we introduce a new operator

$$b(\mathbf{k}) e^{iT\mathbf{k}^2/2} = \langle \chi_k | \Psi_s(T) \rangle = \langle \chi_k | \theta(r_b) | \Psi_s(T) \rangle \quad (5.40)$$

where $\theta(r_b)$ is the Heaviside function and r_b is the radius of the surface which separates the inner and outer regions. We define the matrix element

$$\langle \chi_k | \theta(r_b) | \Psi_s \rangle \equiv \int_{|\mathbf{r}|>r_b} d\mathbf{r} \chi_k^*(\mathbf{r}) \Psi_s(\mathbf{r}, T). \quad (5.41)$$

The key of the method is to convert the volume integral in Eq. (5.41) into a time-dependent surface integral. Neglecting again the Coulomb potential, and assuming that the dynamics in this region is only governed by the electromagnetic field, the Volkov Hamiltonian in this region is

$$\mathcal{H}_V(t) = \frac{1}{2} [\mathbf{k} - \mathbf{A}(t)]^2 \quad (5.42)$$

whose solutions are Volkov waves

$$\chi_k(\mathbf{r}, t) = \frac{1}{(\sqrt{2\pi})^3} e^{i\mathbf{k}\mathbf{r}} e^{-i\Phi(\mathbf{k}, t)} \quad (5.43)$$

where $\Phi(\mathbf{k}, t)$ is the Volkov phase

$$\Phi(\mathbf{k}, t) = \frac{1}{2} \int_0^t dt' [\mathbf{k} - \mathbf{A}(t')]^2 \quad (5.44)$$

and $\mathbf{A}(t)$ is the vector potential of the electric field.

The transformation from volume integral to time dependent surface integral is obtained by calculating

$$\begin{aligned} \langle \chi_k | \theta(r_b) | \Psi_s \rangle &= \int_0^T dt \frac{d}{dt} \langle \chi_k | \theta(r_b) | \Psi_s(T) \rangle \\ &= i \int_0^T dt \langle \chi_k | \mathcal{H}_V(t) \theta(r_b) - \theta(r_b) \mathcal{H}(t) | \Psi_s(T) \rangle \\ &= i \int_0^T dt \langle \chi_k | \left[-\frac{1}{2} \nabla^2 - i \mathbf{A}(t) \cdot \nabla, \theta(r_b) \right] | \Psi_s(T) \rangle \end{aligned} \quad (5.45)$$

Thus the volume integral is reduced to a surface integral at $r = r_b$.

Most previous 3D implementations of the t-SURFF method have been in spherical coordinates. Consider the evaluation of Eq. (5.45) in spherical polar coordinates, and consider an elliptically polarised laser pulse lying in the x - z plane and propagating in the y -direction. In that case we can express the commutator as

$$\begin{aligned} \left[-\frac{1}{2} \nabla^2 - i \mathbf{A}(t) \nabla, \theta(r_b) \right] &= \\ &= -\frac{1}{2r^2} \frac{\partial}{\partial r} r^2 \delta(r - r_b) - \frac{1}{2} \delta(r - r_b) \frac{\partial}{\partial r} - \end{aligned} \quad (5.46)$$

$$\begin{aligned} &- i A_x(t) \sin \theta \cos \phi \delta(r - r_b) - i A_z(t) \cos \theta \delta(r - r_b) \\ &= -\frac{1}{r} \delta(r - r_b) + \overleftarrow{\frac{\partial}{\partial r}} \frac{1}{2} \delta(r - r_b) - \frac{1}{2} \delta(r - r_b) \frac{\partial}{\partial r} - \\ &- i A_x(t) \sin \theta \cos \phi \delta(r - r_b) - i A_z(t) \cos \theta \delta(r - r_b) \end{aligned} \quad (5.47)$$

where in the last equality, we have used the property $\delta_r = -\overleftarrow{\delta_r}$ (the derivative $\overleftarrow{\delta_r}$ is acting on the operator on its left) [201].

The Volkov states are also written in spherical coordinates, in this case the exponential $\exp(i \mathbf{k} \cdot \mathbf{r})$ is expressed as a multipole expansion,

$$e^{i \mathbf{k} \cdot \mathbf{r}} = 4\pi \sum_{lm} i^l j_l(\mathbf{k} \cdot \mathbf{r}) Y_{lm}(\theta_r, \phi_r) Y_{lm}^*(\theta_k, \phi_k) \quad (5.48)$$

where $j_l(\mathbf{k} \cdot \mathbf{r})$ are Bessel functions of the first kind and $Y_{l,m}(\theta, \phi)$ are spherical harmonics. We can think of our wavefunction expanded in a basis of spherical harmonics, i.e.

$$\Psi(r, \theta, \phi) = \sum_{lm} f_{lm}(r) Y_{lm}(\theta, \phi) \quad (5.49)$$

Using Eq. (5.48), Eq. (5.46) and Eq. (5.49) in Eq. (5.45) gives

$$\begin{aligned}
b(\mathbf{k})e^{-iT\mathbf{k}^2/2} &= \langle \chi_k | \theta(r_b) | \Psi_s \rangle \\
&= ir_b^2 \sqrt{\frac{2}{\pi}} \int_0^T dt \exp \left(\frac{i}{2} \int_0^t d\tau [\mathbf{k} + \mathbf{A}(\tau)]^2 \right) \\
&\quad \times \sum_{lm} \frac{(-i)^l}{2} [kj'_l(kr_b)f_{lm}(r_b) - j_l(kr_b)f'_{lm}(r_b)] Y_{lm}(\Omega_k) \\
&\quad - (-i)^{l+1} j_l(kr_b) \left(\sum_{l'm'} A_x(t) \langle Y_{lm}(\Omega_r) | \sin \theta \cos \phi | Y_{l'm'}(\Omega_r) \rangle f_{l'm'}(r_b) \right. \\
&\quad \left. + A_z(t) \langle Y_{lm}(\Omega_r) | \cos \theta | Y_{l'm'}(\Omega_r) \rangle f_{l'm'}(r_b) \right) Y_{lm}(\Omega_k)
\end{aligned} \tag{5.50}$$

where the vector \mathbf{k} represents (k, Ω_k) . We note that

$$\langle Y_{lm} | \sin \theta \cos \phi | Y_{l'm'} \rangle = \delta_{l\pm 1, l'} \delta_{m\pm 1, m'} \tag{5.51}$$

$$\langle Y_{lm} | \cos \theta | Y_{l'm'} \rangle = \delta_{l\pm 1, l'} \delta_{m, m'}. \tag{5.52}$$

The angle-resolved photoionisation spectrum will be given by

$$\frac{d^2 P(E, \Omega_E)}{dE d\Omega_E} = \frac{1}{k} \frac{d^2 P(k, \Omega_k)}{dk d\Omega_k} = |b(k, \Omega_k)|^2 \tag{5.53}$$

and if we integrate over the solid angle Ω_E we get

$$\frac{dP(E)}{dE} = \int d\Omega_k k^2 \frac{|b(k, \Omega_k)|^2}{k} = \int d\Omega_k k |b(k, \Omega_k)|^2 \tag{5.54}$$

The flexibility of the method allows us to choose if we want to calculate the time integral during or after the calculation. In our case we calculate the time integral afterwards. The numerical procedure will be explained in Section 5.4.3.

Joint electron-ion spectra using t-SURFF

As described in Section 5.1.1, joint electron-ion spectra requires two surfaces to divide electronic and nuclear wavepackets. In the surface flux method we can use the same idea in order to calculate the joint spectra.

In this work we only consider the nuclear vibration. As it was mentioned in Chapter 2, we treat all degrees of freedom of the molecule quantum mechanically. We remember that our molecular Hamiltonian has the form Equation (2.4):

$$\mathcal{H}(\mathbf{r}, \mathbf{R}, t) = T_e(\mathbf{r}) + T_N(\mathbf{R}) + V_{eN}(\mathbf{r}, \mathbf{R}) + V_N(\mathbf{R}). \tag{5.55}$$

We are interested in calculating the DI of the H_2^+ . In order to distinguish between the dis-

sociative channel, Eq. (5.12), and the dissociative ionisation channel, Eq. (5.13), we divide the coordinate space into different regions, delimited by the boundaries r_b and R_b , as in Figure 5.1. Introducing the Heaviside operators θ_e and θ_N

$$\theta_e = \begin{cases} 0 & \text{for } |r| < r_b \\ 1 & \text{for } |r| > r_b \end{cases} \quad (5.56)$$

$$\theta_N = \begin{cases} 0 & \text{for } |R| < R_b \\ 1 & \text{for } |R| > R_b \end{cases} \quad (5.57)$$

we are able to split the electron-ion wavefunction into a bound (B) part, an ionised (I) part, a dissociated (D) part and a dissociative ionised (DI) part

$$\Psi(t) = \underbrace{(1 - \theta_e)(1 - \theta_N)\Psi(t)}_{\Psi_B(t)} + \underbrace{\theta_e(1 - \theta_N)\Psi(t)}_{\Psi_I(t)} + \underbrace{(1 - \theta_e)\theta_N\Psi(t)}_{\Psi_D(t)} + \underbrace{\theta_e\theta_N\Psi(t)}_{\Psi_{DI}(t)} \quad (5.58)$$

Within the dissociative ionisation region we neglect the electron-nuclear potential and the Coulomb repulsion between the nuclei. Therefore, the DI Hamiltonian is only formed by the terms $\mathcal{H}_{DI} = T_e + T_N + U_L$. The corresponding TDSE

$$i \frac{d}{dt} |\Psi_{DI}\rangle = \mathcal{H}_{DI} |\Psi(t)\rangle \quad (5.59)$$

has a solution that can be separated into an electronic part and a nuclear part. The electronic solution, $\chi_{k_e}(\mathbf{r}, t)$ is a Volkov wave,

$$\chi_{k_e}(\mathbf{r}, t) = \frac{1}{(\sqrt{2\pi})^3} e^{i\mathbf{k}_e \cdot \mathbf{r}} e^{-i\Phi(\mathbf{k}_e, t)}, \quad (5.60)$$

whereas the nuclear one, $\chi_{k_N}(\mathbf{R}, t)$, is a plane wave,

$$\chi_{k_N}(\mathbf{R}, t) = \frac{1}{\sqrt{2\pi}} e^{i\mathbf{k}_N \cdot \mathbf{R}} e^{-i\mathbf{k}_N^2/2t}. \quad (5.61)$$

As in Section 5.1.1, we denote

$$|\chi_{k_e}(\mathbf{r}, t)\chi_{k_N}(\mathbf{R}, t)\rangle = \langle \chi_{k_e}(\mathbf{r}, t)| \otimes \langle \chi_{k_N}(\mathbf{R}, t)|. \quad (5.62)$$

At very long times T , the amplitude for the DI region is given by

$$b(\mathbf{k}_e, \mathbf{k}_N, T) = \langle \chi_{k_e}(\mathbf{r}, T)\chi_{k_N}(\mathbf{R}, T)| \theta_e(r_b) \theta_N(R_b) |\Psi(\mathbf{r}, \mathbf{R}, T)\rangle. \quad (5.63)$$

If we convert this volume integral into a time-dependent surface integral we obtain

$$\begin{aligned} b(\mathbf{k}_e, \mathbf{k}_N, T) &= \int_0^T dt \frac{d}{dt} \langle \chi_{k_e}(t)\chi_{k_N}(t)| \theta_e(r_b) \theta_N(R_b) |\Psi(\mathbf{r}, \mathbf{R}, t)\rangle \\ &= \int_0^T dt [B^e(\mathbf{k}_e, \mathbf{k}_N, t) + B^N(\mathbf{k}_e, \mathbf{k}_N, t)] \end{aligned} \quad (5.64)$$

In Eq. (5.64) the two terms represents the flux coming from the ionisation and the dissociation regions respectively into the DI region

$$B^e(\mathbf{k}_e, \mathbf{k}_N, t) = \langle \chi_{k_e}(t) \chi_{k_N}(t) | [T_e + U_L, \theta_e(r_b)] \theta_N(R_b) | \Psi(\mathbf{r}, \mathbf{R}, t) \rangle \quad (5.65)$$

$$B^N(\mathbf{k}_e, \mathbf{k}_N, t) = \langle \chi_{k_e}(t) \chi_{k_N}(t) | [T_N, \theta_N(R_b)] \theta_e(r_b) | \Psi(\mathbf{r}, \mathbf{R}, t) \rangle \quad (5.66)$$

These two terms must be summed coherently in order to get the DI amplitude. However, as Yue and Madsen [268] point out, we can neglect the term $B^e \approx 0$ if we choose R_b large enough.

Consider the flux that crosses the electron-ion boundary, Eq. (5.66), which is the only one that contributes to the total DI amplitude. We can rewrite this quantity as

$$B^N(\mathbf{k}_e, \mathbf{k}_N, t) = i \int_0^T dt \sum_n \langle \chi_{k_N} \chi_{k_e} | [T_N, \theta_N] \theta_e | \Psi(\mathbf{r}, \mathbf{R}, t) \rangle. \quad (5.67)$$

The term $\theta_e | \Psi(\mathbf{r}, \mathbf{R}, t) \rangle$ represents the wavefunction outside the electronic boundary. As beyond r_b we are using an absorbing boundary method to prevent reflection of the function against the edges of the box, we can not know the exact form of $\theta_e | \Psi(\mathbf{r}, \mathbf{R}, t) \rangle$. In that case we can expand this term in a time-independent basis of orthogonal functions, $\xi_n(\mathbf{R})$, and Volkov waves, $\chi_{k_N}(\mathbf{R})$, i.e

$$\theta_e | \Psi(\mathbf{r}, \mathbf{R}, t) \rangle = \int d^3 \mathbf{k}_e \sum_n \chi_{k_e}(\mathbf{r}, t) \xi_n(\mathbf{R}) \beta'(\mathbf{k}_e, n, t) \quad (5.68)$$

where

$$\beta'(\mathbf{k}_e, n, t) = \int d^3 \mathbf{k}_e q_\theta(\mathbf{k}, \mathbf{k}', t) \beta(\mathbf{k}'_e, n, t), \quad (5.69)$$

and

$$\beta(\mathbf{k}_e, n, t) = \int d\mathbf{r} \chi_{k_N}^*(\mathbf{r}, t) \theta_e \int d\mathbf{R} \xi^*(\mathbf{R}) \Psi(\mathbf{r}, \mathbf{R}, t) \quad (5.70)$$

can be obtained by orthogonal projection. In Eq. (5.69) $q_\theta(\mathbf{k}, \mathbf{k}', t)$ is a term introduced to ensure orthonormality of the plane waves

$$\int d^3 \mathbf{k}_e q_\theta(\mathbf{k}, \mathbf{k}', t) \langle \chi_{k'_e} | \theta_e | \chi_{k''_e} \rangle = \delta^3(\mathbf{k} - \mathbf{k}''). \quad (5.71)$$

The basis functions $\xi_n(\mathbf{R})$ are an orthogonal set of functions. As we are neglecting the Coulomb potential within the DI region, then, in the absence of an electric field, we can assume a plane wave once again and choose a sine basis set of the form

$$\xi_n(\mathbf{R}) = \sin \left(\frac{n\pi \mathbf{R}}{\mathbf{R}_{\max}} \right) \quad (5.72)$$

where \mathbf{R}_{\max} the maximum value of the internuclear coordinate.

Thus Eq. (5.70) can be written

$$\beta(\mathbf{k}_e, n, t) = \langle \xi_n | \langle \chi_{k_e} | \theta_e | \Psi(\mathbf{r}, \mathbf{R}, t) \rangle . \quad (5.73)$$

If we take the time derivative of Eq. (5.73) we obtain

$$\begin{aligned} \frac{d}{dt} \beta(\mathbf{k}_e, n, t) &= \frac{d}{dt} \langle \xi_n | \langle \chi_{k_e} | \theta_e | \Psi(\mathbf{r}, \mathbf{R}, t) \rangle \\ &\quad + \langle \xi_n | \frac{d}{dt} \langle \chi_{k_e} | \theta_e | \Psi(\mathbf{r}, \mathbf{R}, t) \rangle + \langle \xi_n | \langle \chi_{k_e} | \theta_e \frac{d}{dt} | \Psi(\mathbf{r}, \mathbf{R}, t) \rangle \\ &= -i \langle \xi_n | \mathcal{H}_N \sum_m |\xi_m\rangle \langle \xi_m | \langle \chi_{k_e} | \theta_e | \Psi(\mathbf{r}, \mathbf{R}, t) \rangle \\ &\quad + i \langle \xi_n | \langle \chi_{k_e} | [\mathcal{H}_v, \theta_e] | \Psi(\mathbf{r}, \mathbf{R}, t) \rangle \\ &= -i \sum_m \langle \xi_n | \mathcal{H}_N |\xi_m\rangle \beta(\mathbf{k}_e, m, t) + i \langle \chi_{k_e} | [\mathcal{H}_v, \theta_e] \langle \xi_n | \Psi(\mathbf{r}, \mathbf{R}, t) \rangle \end{aligned} \quad (5.74)$$

The second part of the last equality accounts for the flux through the electronic surface, and its commutator takes the same form given in Eq. (5.46). In spherical coordinates, the bracket $\langle \xi_n | \Psi(\mathbf{r}, \mathbf{R}, t) \rangle$ can be expanded in spherical harmonics as in Eq. (5.49), i.e.,

$$\langle \xi_n | \Psi(\mathbf{r}, \mathbf{R}, t) \rangle = \sum_{lm} f_{nlm}(r) Y_{lm}(\theta, \phi). \quad (5.75)$$

The inhomogeneous differential equation, Eq. (5.74), can be easily solved using a 4th-order Runge-Kutta method. We assume as initial condition that there is no ionisation at $t = 0$ and so the initial condition is

$$\beta(\mathbf{k}_e, n, 0) = 0. \quad (5.76)$$

Substituting $\beta(\mathbf{k}_e, n, t)$ into the time integral of Eq. (5.66) gives

$$B_N(\mathbf{k}_e, \mathbf{k}_N, t) = \sum_n \langle \chi_{k_N} | [\mathcal{H}_N, \theta_N] |\xi_n\rangle \beta(\mathbf{k}_e, n, t). \quad (5.77)$$

The commutator takes the simple form

$$[T_N, \theta_N] = -\frac{1}{2} \overleftarrow{\frac{\partial}{\partial R}} \delta(R - R_b) - \delta(R - R_b) \frac{\partial}{\partial R} \quad (5.78)$$

where $\overleftarrow{\frac{\partial}{\partial R}}$ acts on the operator on its left.

With this prescription we obtain the spectral amplitudes as

$$\begin{aligned} b(\mathbf{k}_e, \mathbf{k}_N, T) &= i \int_0^T dt B_N(\mathbf{k}_e, \mathbf{k}_N, t) \\ &= i \int_0^T dt \sum_n \langle \chi_{k_N} | [T_N, \theta_N] |\xi_n\rangle \beta(\mathbf{k}_e, n, t) \\ &= \frac{i}{\mu_N \sqrt{2\pi}} \int_0^T dt \sum_n e^{-ik_N R} [-ik_N \xi_n(R_b) - \xi'_n(R_b)] \beta(\mathbf{k}_e, n, t). \end{aligned} \quad (5.79)$$

5.4 Numerical implementation of the library

In this section we will discuss the numerical implementation of the methods described above in a numerical library called `P0pS iCLE`, which stands for PhOtoelectron SpeCtrum library for Laser-matter intEractions. `P0pS iCLE` implements these methods in a range of coordinates systems (Cartesian, cylindrical and spherical) in order to interface with a range of computer codes for solving the TDSE. It is written in FORTRAN 2003 and comes with a number of helper and post-processing scripts written in python. The library can be used for serial and parallel calculations. One of the main purposes of the library was to create a tool that can be used in massively parallel calculations. For efficient communication between nodes and efficient I/O, the library uses the MPI protocol and the HDF5 file format to store the spectral information. The library is available on the CCPForge repository (<https://ccpforge.cse.rl.ac.uk/gf/project/popsicle/>).

One additional requirement is a method to calculate FFTs. With suitable compilation flags, the user can choose either the Intel Math Kernel Library (MKL) [270] or the stand-alone Fastest Fourier Transform in the West (FFTW) [271, 272]. MKL is a proprietary and highly efficient library for computing FFTs. It is specially designed to have higher performance on Intel architectures. FFTW is another efficient library, written in C, to compute the FFT algorithm. It is available across different architectures and is one of the most popular implementation for FFT calculations in many scientific applications.

In this section we will describe the numerical implementation of the library. We have divided this section in three parts. In Section 5.4.1 we will discuss the implementation of the Fourier method. Section 5.4.2 will then describe how we interpolate the wavefunction information onto spherical surfaces for use in the t-SURFF and sampling point methods. In Section 5.4.3 the implementation of the t-SURFF methods will be described while the implementation of the sampling point method will be described in Section 5.4.4.

5.4.1 Implementation of the Fourier method

As discussed in Section 5.1, performing Fourier transforms on large multidimensional grids is a difficult task. In general, we can employ the Discrete Fourier Transform (DFT), which is simply the discretised version of the Fourier transform over particular points in configuration and frequency space. For an array x of values x_n with N values, the DFT can be written

$$F_k = \sum_{n=0}^{N-1} x_n \cdot e^{-i2\pi kn/N} \quad \text{for } k \in \mathbb{Z} \quad (5.80)$$

The DFT is a computationally expensive algorithm because it scales as $O(N^2)$. However, if our coordinates are equally spaced, the most efficient Fourier transform method is the Fast Fourier

Transform (FFT) algorithm [244, 273]¹. The FFT algorithm exploits the symmetry between the odd and even terms of a DFT, following a ‘divide and conquer’ strategy. This algorithm scales as $O(N \log N)$, which means that for an array of length $N = 10^6$ the calculation will last around 50 ms, whereas with the DFT it will take around 20 hours. The only constraint for us is that the points in configuration and frequency space must be equally spaced in order to exploit the before mentioned symmetry properties of DFT. Most implementations of the FFT are serial. This presents a problem when large grids are used as memory access problems can occur. Due to this limitation, our strategy is to implement a set of subroutines that redistributes the decomposition of the wavefunction itself. This allows us to overcome the memory problems while and not spoiling the efficiency of the underlying FFT algorithm.

To show how our parallel scheme works, consider the 2D example illustrated in Figure 5.2. In this case the wavefunction for the system, lying in the $x - y$ plane, is distributed across 16 processes, arranged as a 4×4 grid. Along the x axis, N_p points are stored per process so that the total number of x -points in the calculation is $N = 4N_p$. Along the y axis, M_p points are stored per process so that the total number of y -points in the calculation is $M = 4M_p$. The calculation begins with each process containing its own piece of the total grid. We will FFT the wavefunction for each coordinate in turn. Consider the FFT in the x coordinate. Each process will have to carry out an FFT M_p times (one for each y value), therefore each FFT requires the wavefunction information for all N points along the x -axis. However, each process only has N_p elements. We communicate this particular slice of the wavefunction to all the processes which participate in this direction with a `MPI_Alltoall` call. After the FFT completes each process, it obtains its own range of the corresponding k_x values (the momentum values in x) with another `MPI_Alltoall` call. Once the FFTs are calculated along the x coordinate, the process is repeated for the y coordinate. Before FFTing the wavefunction, a mask function is applied to the wavefunction to remove the bound states present on the wavefunction array. The library provide routines to create different types of masks. These masks will be discussed in Section 6.1 and Section 6.2.

For the case of THeREMIN, which solves the TDSE in cylindrical coordinates, we require the Fourier transform of the ρ coordinate, lying in the range $0 \leq \rho \leq \infty$. In this case, we require the Bessel transform of the wavefunction, i.e.

$$F(k_\rho) = \int_0^{\rho_{\max}} d\rho J_0(k_\rho \rho) f(\rho), \quad (5.81)$$

where $J_0(k_\rho \rho)$ is the zero-order Bessel function of first kind. Since ρ is also distributed across processes, we parallelise this as illustrated in Figure 5.3.

`POpSiCLE` provides two main routines for transforming a wavefunction from coordinate

¹The FFT is the most efficient algorithm used to calculate Fourier transforms, developed by J.W. Cooley and J.W. Tukey in 1965. However, it is known that the first person who work on this algorithm was C.F. Gauss in 1805. Gauss used it to calculate the orbits of celestial bodies [274].

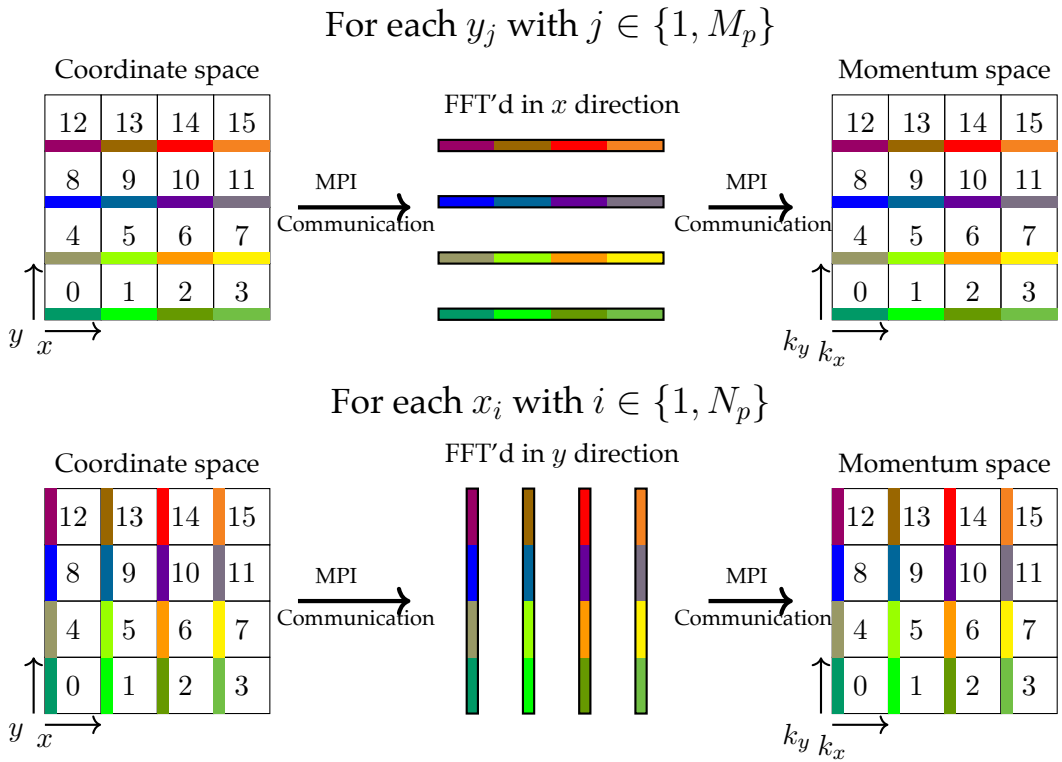


Figure 5.2: Schematic diagram showing how the FFT of a wavefunction parallelised on a 2D grid can be carried out. See text for a complete description.

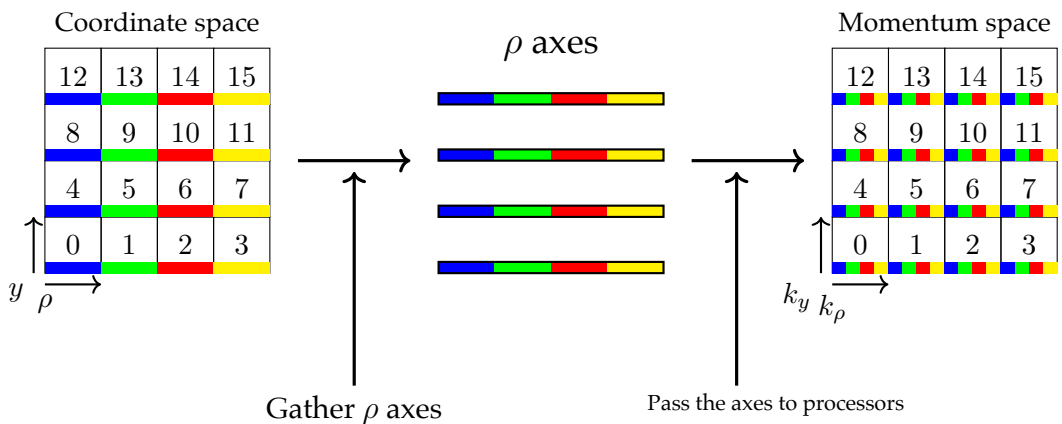


Figure 5.3: Schematic diagram showing how the Fourier-Bessel transform of a wavefunction parallelised on a 2D grid can be carried out. See text for a complete description.

space to momentum space

1. FourierTransform

To call the main routine, `FourierTransform`, the user must provide the rank and dimensions of the grid, (apart from the input and output array, of course). If the user wants to use the parallel version, he/she also needs to provide the dimensions of the wavefunction in total and per processor, the global MPI communicator and the position that each processor occupies on the total grid.

2. FourierBesselTransform

To call this routine for use with the ρ coordinate in cylindrical coordinates, the user must specify the same inputs for this coordinate as are used for `FourierTransform`.

The library also contain auxiliary subroutines that are not essential but useful in this type of calculation. There is a module dedicated to save data to HDF5 files. The full spectral amplitude and also different projections of the amplitude can be saved. The other pack of auxiliary subroutines are dedicated to the transformation of the amplitudes from cylindrical and Cartesian coordinates to spherical coordinates. To interpolate the original arrays onto regular spherical meshes, bi/tri-cubic interpolation is used: this will be described in Section 5.5.

5.4.2 Interpolation of the wavefunction onto spherical surfaces

For both the t-SURFF and the sampling point method, we need to know the values of the wavefunction (and its first derivative) at a series of points on a spherical shell at a given radius from the origin. In light of the spherical nature of the problem and the fact that the initial implementation of t-SURFF was in spherical coordinates, this is the most appropriate coordinate system to use. However, many codes, including those used in this thesis, are not written in spherical coordinates and so we require a method for interpolating the wavefunction information onto a spherical shell. Since we are only interested in these values on a defined shell at radius r_b , one way to proceed is to calculate these values during the execution of the TDSE solver, store these quantities to file and then post-process this data at a later time. We find this is more flexible because of the computational demand of calculating the time-integral in the t-SURFF method and the FFT's for the sampling point method is small compared to the effort required to solve the TDSE.

In order to interpolate the wavefunction at the required surface, the user can choose between two multi-dimensional interpolation algorithms.

1. Shepard's method

The Shepard interpolation is a method used to interpolate scattered data in two and three dimensions. We use the external package of routines SHEPPACK, written in FORTRAN 90, which contains the implementation of the modified Shepard algorithm [275]. Before interpolating, it performs a gridding operation through all points to locate them in an area or volume (depending if the interpolation is 2D or 3D). This method is computationally expensive, and it can cause the huge slow down in the TDSE/TDDFT solver.

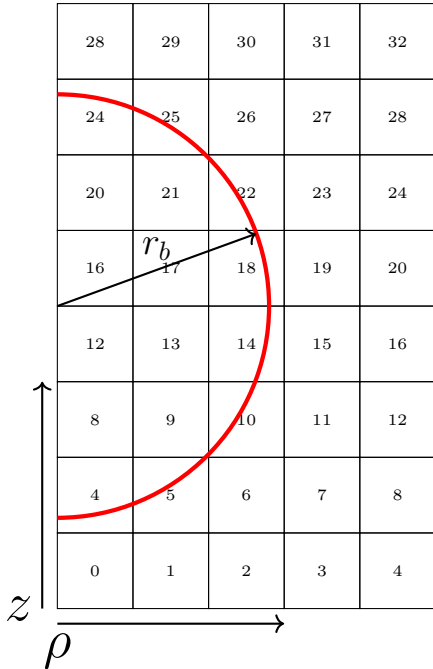


Figure 5.4: Scheme of a cylindrical grid decomposed over processor elements. In this case we can see that the surface only passes through some of these processors.

2. Bi/tri-cubic interpolation

For two-dimensional data we implement bicubic interpolation [244] while for three-dimensional data we use tricubic interpolation [276]. Both methods work by carrying out cubic interpolation on 2D and 3D regions of space using piecewise polynomials. The overall performance of the bi/ (tri)-cubic method is a couple of orders of magnitude faster than Shepard's method at the same level of error. For that reason bi/tri cubic interpolation is POpSiCLE's default interpolator. In Appendix B we show how the interpolation method works.

Our goal is to know the values of the wavefunction and its first radial derivative on the surface over a regular spherical mesh. The first derivative will be calculated by a finite difference rule. Therefore, we have to interpolate the wavefunction at several radial points in order to apply the finite difference rule. In addition, initial implementations of t-SURFF in spherical coordinates used spherical harmonics for describing the angular coordinates. We do the same and so the user must specify the maximum angular momentum quantum number to use. This value allows us to determine the number of (θ, ϕ) points that will be mapped over the spherical surface. Use of the interpolation routines requires three steps in the TDSE solver.

S1 Initialization

- `initialize_cylindrical_surface`
- `initialize_cartesian_surface`

These routines allocate and initialise the arrays to be used to interpolate the wavefunc-

tion from the working coordinates to spherical coordinates. It also creates the HDF5 surface file with its own internal folder structure. The user must provide the following as input parameters: the mesh points for the grid, the boundary radius, r_b , the maximum angular momenta of the stored wavefunction and information on how the grid is split between processors. In order to calculate derivatives of the wavefunction using finite-differences, the finite difference rule type is specified together with the radial grid spacing Δr .

After creating a grid in spherical coordinates for all required points on the surface, the initialisation routine locates the closest surface points in the original coordinate system by finding their corresponding array indices. These array indices serve as a mapping between the original and the spherical coordinate systems.

For example, in cylindrical coordinates, after having created a mesh of N_θ points in the θ coordinate (Gauss pivots) on the spherical surface, the subroutine calculates the coordinates of those points in cylindrical coordinates using

$$\begin{aligned}\rho_k &= r_b \sin \theta_k \\ z_k &= r_b \cos \theta_k\end{aligned}$$

for all $k = 1, \dots, N_\theta$. The positions i, j on the axes ρ and z are then located so that

$$\begin{aligned}\rho[i] &\leq \rho < \rho[i + 1] \\ z[j] &\leq z < z[j + 1].\end{aligned}$$

S2 Interpolation

- `get_cylindrical_surface`
- `get_cartesian_surface`

These subroutines, called each timestep during a simulation, take the wavefunction, time, electric field and vector potential as input parameters. The wavefunction is transformed to spherical coordinates and its first radial derivative is calculated on a spherical surface. Both quantities are then written to file.

Usually grid-based codes are parallelised by distributing the grid across cores. In this scenario, the surface will be contained on some processing cores. For example, a diagram of a parallelised grid in cylindrical coordinates is shown in Figure 5.4. The initialisation routine determines which processors contain the surface and which do not. Only cores containing a part of the spherical surface will carry out interpolation.

S3 Finalization

- `delete_surface_2D`
- `delete_surface_3D`

At the end of the simulation, this deallocates all allocated arrays and closes the output file.

The I/O routines create a single HDF5 file that is opened collectively by all the participating MPI processes. Each process writes its piece of the surface to this file. One of the advantages of using the HDF5 format is that each file can be split in a folder-like structure, allowing for the highly organised collection of data. Additionally, the HDF5 format gives efficient MPI-I/O performance.

For calculation of joint electron-ion spectra the procedure is similar to above. In this case we now need to deal with two surfaces: the electronic surface (at r_s) and an ionic surface (at R_s). In this case, since we only deal with vibrational motion (a 1D treatment) we do not need to perform an interpolation in the ionic coordinate. Three sets of routines are then provided to output the surface files. For THeREMIN, these routines are

- `initialize_correlated_cylindrical_surface`
- `get_correlated_cylindrical_surface`
- `delete_correlated_surface_2D`

while for RHYthMIC we use

- `initialize_correlated_cartesian_surface`
- `get_correlated_cartesian_surface`
- `delete_correlated_surface_3D`

5.4.3 Implementation of the t-SURFF method

Once we have obtained the surface file from a time-dependent calculation, we can calculate the spectral amplitudes with the t-SURFF method solving Eq. (5.50) and Eq. (5.79). This can be achieved using an external program, `tsurff_calculator`, that is distributed with the library. This program processes the surface file that is outputted from the TDSE/TDDFT solver. When executed, this program asks the user for various parameters that were used in the calculation, creates the required arrays, reads the relevant data from the file, calculates the surface integral, integrates this in time and outputs the resulting spectral information to disk. This output can then be visualised by another supplied python script, `popsicle_viewer`. For the calculation of the spherical Bessel functions we use a numerically accurate implementation available in reference [277].

The parameter requested by `tsurff_calculator` at runtime are

- the name of the surface file,
- the surface radius, given in atomic units,
- the grid spacing of the k coordinate in atomic units,

- the maximum value of the k coordinate in atomic units,
- the maximum angular momentum of the calculation,
- if we want to transform the wavefunction from length to velocity gauge, and
- the filename for the PES file, the filename for the file containing the spectral amplitudes integrated over angles, and the filename for the file containing the angularly resolved spectral amplitudes.

Once this information has been supplied the main calculation begins and proceeds in three stages

1. The surface information in spherical coordinates are decomposed in spherical harmonics. This decomposition is often called Spherical Harmonics Transform (SHT). For a brief overview of the decomposition procedure see Appendix A.
2. The amplitudes are then calculated according to the Eq. (5.50)
3. For calculation the time integral we use Simpson's rule.

When calculating joint electron-ion spectra using THeREMIN and RHYthMIC we use an external program called `tsurff_correlated_calculator`. In this case we read in the above parameters for the electronic surface. In addition, we now read in parameters for

- the ionic surface radius in atomic units,
- the grid spacing of the k coordinate for the ionic coordinate in atomic units, and
- the maximum value of the k coordinate for the ionic coordinate in atomic units.

This code then integrates the time integrals detailed in Eq. (5.79).

5.4.4 Implementation of the sampling point method

The raw data for the sampling point method can be obtained in the interpolation and data output phase of a t-SURFF calculation, as described in Section 5.4.2. In this case the set of (θ, ϕ) points on the surface at r_b represent the sampling points as described in Section 5.2. During a calculation, the wavefunction information at these sampling points are output to the surface file.

In order to calculate the PES, using Eq. (5.31), we use the utility routine `sampling_calculator`, that is distributed with the library. This program processes the surface file that is output from the TDSE/TDDFT solver. When executed, this program asks the user for various parameters that were used in the calculation, reads the relevant data from the file, calculates the Fourier transforms and outputs the resulting spectral information to disk. This output can then be visualised using the python script, `popsicle_viewer`.

In order to improve the resolution of the spectra, the utility routine can pad zeros at the end of the time domain. The grid spacing in frequency space, $\Delta\omega$, is given by

$$\Delta\omega = \frac{2\pi}{N_t \Delta t} \quad (5.82)$$

where N_t is the number of time-steps in the output file and Δt is the value of the time step. According to Eq. (5.82), a longer signal in time will result in smaller grid spacing in the frequency space. However, it is not possible to resolve higher frequencies by decreasing $\Delta\omega$ only padding with zeros at the end of the signal. To explain this, we can distinguish between two resolutions, the sampling resolution, $\Delta\omega_s$ and the FFT resolution. The sampling resolution is given by

$$\Delta\omega_s = \frac{2\pi}{T_{\text{int}}} = \frac{2\pi}{N_{\text{int}} dt} \quad (5.83)$$

where T_{int} is the time duration of the interaction, without any padding. The FFT resolution is given by Eq. (5.82). Then, the duration of the time domain signal is $T = N_t \Delta t$ is, so

$$T = T_{\text{int}} + T_{\text{pad}}, \quad (5.84)$$

where T_{pad} is the time with pad with zeros. Therefore, the highest frequency we can resolve depends on $\Delta\omega_s$, the FFT resolution, no matter how fine $\Delta\omega$ is.

5.5 Efficiency of the interpolation routines

In this section we compare the two interpolation methods (Shepard's method and bi/tri-cubic interpolation) implemented in **PoPSiCLE** and described in Section 5.4.2. In order to perform a realistic case similar to what will be done in an actual calculation, we interpolate the 3d state of the hydrogen atom (whose quantum numbers are $n = 3$, $l = 2$ and $m = 0$) at a given value of the surface radius. To measure these interpolation times we carry out serial calculations, in 2D and 3D.

Firstly, we test the 2D routines using **THeREMIN**, where the 3d eigenstate is represented in cylindrical coordinates. The grid parameters used in this calculation are set out in table 5.1. In this case the surface radius is at $r_b = 20 a_0$. In this surface we interpolate at 101 θ -points, where these θ points are chosen as Gauss-Legendre quadrature points. The timing obtained using bicubic interpolation and Shepard's method are presented in table 5.2. We can see that bicubic interpolation is 37 times faster than the Shepard's method. In addition, in order to test the accuracy of the methods, we also present the maximum error obtained when interpolating the function. The maximum error is obtained from the maximum difference between the trial function (the 3d eigenstate) and the interpolated function over all grid points. We observe that, at this radius, the bicubic interpolation has a maximum error four orders of magnitude lower than the Shepard method. The lower error, in addition to his better performance, makes bicubic interpolation clearly superior to Shepard's method in two dimensions.

Coordinate	Number of points	Grid spacing (Bohr)	Mesh extent (Bohr)
ρ	500	0.1	$0 \leq \rho \leq 50$
z	500	0.1	$-25 \leq z \leq 25$

Table 5.1: Grid parameters used for testing the interpolation routines in 2D (employing THeREMIN).

Interpolation method	Timing (seconds)	Max. error ($r = 20 a_0$)
Shepard's method	1.1022	5.56×10^{-9}
Bicubic interpolation	0.0296	3.78×10^{-13}

Table 5.2: Timings for 2D interpolation using both methods: Shepard's method and bicubic interpolation. The 3d state of the hydrogen atom on a surface at radius $r = 20 a_0$ is interpolated from a 2D grid in cylindrical coordinates, whose grid parameters are given in table 5.1, to spherical coordinates. The timings shown in this table have been averaged over 10 runs. The maximum error for each interpolation method is also shown.

Secondly, we test the 3D routines using RHYthMIC. As in the 2D case, we interpolate the 3d eigenstate of the hydrogen atom, in Cartesian coordinates (grid parameters for this calculation are given in table 5.3). We interpolate onto a surface at radius $r_b = 4.5 a_0$. In this case 101 θ -points and 201 ϕ -points (20301 points are used in total). In this case, the θ points are chosen as Gauss-Legendre quadrature points, while the ϕ -points are equally spaced within the range $[0, 2\pi]$. The results are present in table 5.4. We see that tricubic interpolation is 4.85 times faster than Shepard's method in this case. Again, the maximum error of the interpolation is presented to show the accuracy of the methods, in this case in 3D. To compare the accuracy between the methods in 2D and 3D, we also present the maximum error of the interpolation using 2D routines at the same radius, $r_b = 4.5 a_0$. In 3D both methods the maximum error have the same order of magnitude, which is considerable larger compared to the 2D case. In the 2D case, the errors at this radius, $r = 4.5 a_0$ are larger with respect to the interpolation at $r = 20 a_0$ due to the lower local density of original grid points at smaller radius. Since the interpolation of the surface values must be carried out once per time step in an actual calculation, the longer times needed by the Shepard's method add an excessive overhead that make its use unfeasible for production calculations. For this reason we prefer to use the bi-tricubic interpolation method.

It is worth to mention that these tests for interpolation are computationally more demanding than actual parallel calculations. In a serial run all the interpolation is carried out by only one processor, whereas in a parallel run the surface is split across processors, therefore a given processor only has to interpolate a fraction of the total points on the surface.

Coordinate	Number of points	Grid spacing (Bohr)	Mesh extent (Bohr)
x	121	0.1	$-6 \leq x \leq 6$
y	121	0.1	$-6 \leq y \leq 6$
z	121	0.1	$-6 \leq z \leq 6$

Table 5.3: Grid parameters used for testing the interpolation routines in 3D (employing RHYthMIC).

Interpolation method	Timing (seconds)	Max. error ($r = 4.5 a_0$)	Max. error in 2D
Shepard's method	740.1859	7.35×10^{-2}	9.38×10^{-6}
Tricubic interpolation	152.5022	7.34×10^{-2}	8.44×10^{-9}

Table 5.4: Timings for 3D interpolation using both methods: Shepard's method and tricubic interpolation. The 3d state of the hydrogen atom on a surface at radius $r = 4.5 a_0$ is interpolated from a 3D grid in Cartesian coordinates, whose grid parameters are given in table 5.3. The timings shown in this table have been averaged over 10 runs. The maximum error between the trial function and the interpolated one is given. In addition, we also present the maximum interpolation error at the same radius when using the 2D interpolating routines.

5.6 Summary

In this chapter we have discussed the calculation of the photoelectron spectrum for laser-matter interactions. The extraction of scattering amplitudes from solutions of the TDSE using grid methods is still a computational challenge. In addition, we have presented the implementation of a library for efficient calculation of the PES. The library, named **P0pSiCLE** (PhOtоЛeCtron SpeCtrum library for Laser-matter intEractions) is based on three different methods for calculating photoelectrons spectra: The Fourier method, the sampling-point method, and the t-SURFF method.

The Fourier method is the simplest approach to extract scattering amplitudes from the solutions of the time-dependent Schrödinger equation, but is also the most computationally demanding, because a volume integral is required to extract the scattering information. Moreover, another disadvantage is that, since the Fourier method obtains the photoelectrum by projecting onto field-free scattering solutions (plane waves), the resulting spectrum is overestimated due to the presence of the Coulomb potential. Two solutions were proposed. The first solution is to propagate the TDSE further in time, allowing the electron wavepacket to travel to a region where the contribution of the Coulomb potential is negligible. However, this solution implies an even larger computational effort. The second solution proposed is to truncate the Coulomb potential at a certain radius to ensure that we project the ejected wavepacket against the correct scattering states.

In the sampling-point method and the t-SURFF methods we avoid the calculation of a volume integral by recording over time the values of the wavefunction at a particular surface. In the case of the sampling-point method, it can be shown that the photoelectron spectra

can be obtained by performing a Fourier transform on the surface values over time. Since a Fourier transform is used, the method implicitly assumes the projection of the wavefunction onto field-free scattering solutions, which raise the same problem as in the Fourier method. Another disadvantage of the method is that, since no volume element is considered, the resulting spectrum reproduces the correct energies but not the correct amplitudes.

Finally, in the t-SURFF method a volume integral is converted into a surface integral over time. The method is the superior of the three methods presented for two reasons. The first reason is that the calculation of a surface integral instead of a volume integral reduces dramatically the computationally cost, due to only the record of the wavefunction values at the surface and its first radial derivative is required. The second reason is that, since the method allows the use of Volkov solutions as scattering solutions, more accurate PES can be obtained.

In the second part of the chapter, details about the numerical implementation of the library are given. In particular, in the implementation of the Fourier method we distinguish two cases, depending on the code employed: using **THeREMIN**, which implements the TDSE in cylindrical coordinates, the Hankel transform of first order must be used, while using **RHYthMIC**, which is implemented in Cartesian coordinates, the Fourier transform is required, allowing the use of the Fast Fourier Transform. We present a procedure to parallelise the execution of the transforms across multiple processors, allowing the extraction of scattering amplitudes from wavefunctions that can reach sizes of several gigabytes.

For the surface methods, the spherical nature of the scattering problem makes it appropriate to implement the t-SURFF method in spherical coordinates. However, a problem arises, since many codes, such as the codes used in this thesis, are implemented in other coordinate systems. For that reasons, in order to obtain the values of the wavefunction (and its first radial derivative) on the surface it is required to interpolate of the wavefunction onto a spherical shell. The library uses two methods for interpolating functions in more than one dimension: the Sheppard's method and the bi/tri-cubic interpolation. The former method is used for interpolating scattered data, while the latter method is based of interpolation using piecewise polynomials. Performing an interpolation once per time-step during the time evolution introduces an additional overhead to the propagation of the TDSE. As it was shown in the final section of the Chapter, bi-cubic interpolation method performs 37 times faster than Sheppard's method in 2D on a single processor, while the tri-cubic method is 4.85 times faster in 3D. The maximum error of bi-cubic interpolation is three orders of magnitude lower than the Shepard's method, and both methods have the same level of error in the 3D case. For these reasons, the bi/tri-cubic method is clearly superior than Shepard's method and was chosen as the default interpolation method of the library.

6

Photoelectron spectra of H_2^+ by intense laser pulses

One of the most popular experimental techniques currently used to gain insight into the processes occurring during laser-molecule interactions is time-of-flight spectroscopy. This technique makes use of technologies such as Velocity Map Imaging (VMI) [278, 279]), or more recently, the sophisticated Cold Target Recoil Ion Momentum Spectroscopy (COLTRIMS) method [280]. Using these techniques, it is possible to analyse the photo-fragments produced (electrons and ions) with unprecedented angular and energy resolution. Therefore, it is essential to provide a sensitive and powerful theoretical tool with which to study photoelectron spectra.

However, as we saw in Chapter 5, calculating the PES is extremely challenging, as electrons that are ionised during interaction with the laser pulse can gain high velocities and travel large distances in a short time. In this chapter we will calculate the PES for H_2^+ ionised by VUV and IR laser pulses using our developed library `P0pSiCLE`. The chapter is arranged as follows. In Section 6.1 we present a comparison between the three approaches for calculating PES in `P0pSiCLE` (Fourier transform method, sampling point method and t-SURFF) with a simple test case of ionisation of H_2^+ by a short XUV laser pulse. This comparison is made using both `THeREMIN` (2D calculations) and `RHYthMIC` (3D calculations). In addition, we show how the methods perform in terms of computational resources required. Finally, Section 6.3 we will present results for ionisation of H_2^+ by IR laser pulses using `THeREMIN`.

Pulse	ω_L	λ	T	No. cycles
	au	eV	nm	fs
1	1.37	37.22	33.30	0.111
2	1.98	53.76	23.05	0.076
3	2.58	70.30	17.63	0.058
4	3.19	86.84	14.27	0.047

Table 6.1: Laser pulse parameters for each of the 4 pulses employed in our calculations of photoelectron spectra in H_2^+ . All pulses have a duration of 1 fs, a peak intensity of $I = 10^{13} \text{ W/cm}^2$ and a temporal profile described by a \sin^2 function. In the table, ω_L represents the photon energy, λ the wavelength, and T the period.

6.1 Comparison between different PES approaches

In order to benchmark the different PES calculation methods implemented in `POpSiCLE` we will study the interaction of H_2^+ with linearly polarised laser VUV attosecond pulses. In this photoionisation regime it is possible to compare with the well-established results available in the literature. For instance, Bates et al. [116, 117] were the first to calculate photoionisation cross sections using two-centre electronic wavefunctions. Later Plummer and McCann [126–128] used a basis set Floquet technique to calculate photoionisation cross sections and ionisation rates. Also, Rescigno, McCurdy et al. [119, 121, 122] have used different grid techniques (discrete variable representation and finite elements) to calculate photoionisation cross sections of H_2^+ .

We consider 4 laser pulses, each having an intensity of $I = 10^{13} \text{ W/cm}^2$ and a duration of 1 fs. The pulse parameters are detailed in table 6.1. For these laser pulses we can neglect the nuclear motion since the pulse durations are so short. Therefore, it is reasonable to consider the nuclei fixed. In our benchmark calculations we consider the molecule in its $1s\sigma_g$ ground state at a fixed internuclear distance of $R = 2 a_0$.

We first consider calculation of the PES using `THeREMIN` by solving the TDSE in cylindrical coordinates. For the laser pulses considered multiphoton ionisation is the dominant ionisation mechanism and so we expect the ejected electron travels radially outwards, we therefore employ flat scaling for the ρ coordinate as described in Section 3.1.

The grid parameters employed in the 2D tests can be found in Table 6.2. Five sets of grid parameters are considered. These are detailed below:

- I The parameters in set (I) were employed to calculate the spectra with the Fourier method. As described in Section 5.1, in order to apply the Fourier method the size of our grid must be large enough to contain the whole wavefunction at the end of the time evolution. To allow ionised electron wavepackets to travel enough distance from the parent ion we propagate for 10 cycles after the end of the pulse. This ensures sufficient separation of the scattering and bound states of the molecule.

- II The parameters in set (II) are used for the surface methods (sampling point method and

Set	Method	Points per core		No. cores		Grid spacing		Surface radius	Mesh extent	
		ρ	z	ρ	z	ρ	z		ρ_{\max}	z_{\max}
I	Fourier	300	301	4	9	0.1	0.1	-	117.5	± 135.4
II	Surface	300	301	2	3	0.1	0.1	20	60	± 45.15
III	Surface	255	301	2	3	0.1	0.1	20	45	± 45.15
IV	Surface	245	291	3	5	0.1	0.1	50	71.12	± 72.7
V	Surface	301	271	4	9	0.1	0.1	80	117.5	± 121.9
VI	Surface	305	271	4	9	0.1	0.1	100	119.6	± 121.9

Table 6.2: Grid parameters employed for calculating the PES in 2D using THeREMIN. Six sets of grid parameters were considered. In set (I) the Fourier method is used, which requires a large grid extent. In sets (II), (III), (IV), (V) and (VI) the surface methods (sampling point and t-SURFF methods) were used, in which during the time evolution we record a single surface file. The surface radius and the mesh extent for each set is given in atomic units.

t-SURFF method). In order to compare the efficiency between the Fourier method and the surface methods, the number of grid points and the grid spacing in set (II) are similar to those used in set (I). Since we are only interested in the values of the wavefunction and its first derivative at the surface (for this calculation the surface radius is $r_b = 20 a_0$) the grid extent is smaller than that used for set (I).

- III The set (III) were also used for the surface methods, but this time the extent and the number of grid points in the ρ coordinate were reduced in order to maximise the efficiency of the calculation.
- IV The parameters in set (IV) and corresponds to a larger grid extent, and it was used in a surface calculation where the surface radius was placed at $r_b = 50 a_0$.
- V The parameters in set (V) corresponds to a larger grid extent than in set (IV). The number of grid points per processor and the number of processors used were also larger than in set (IV), and it was used in a surface calculation were the surface radius was placed at $r_b = 80 a_0$.
- VI Finally parameters in set (VI) are similar to those in set (V), but this time the surface radius was $r_b = 100 a_0$.

6.1.1 Fourier method results

In the following we first consider the results obtained using the Fourier method. The parameters of the calculation correspond to set (I), in Table 6.2. For the Fourier method no absorbing boundaries are used since we want to perform a Fourier transform on the scattering part of the wavefunction. In Figure 6.1 we show the wavefunction at the end of the time evolution for the four VUV pulses described in table 6.1. An animation for the case of ionisation by Pulse 2 in Table 6.2 (corresponding to frame (b) in Figure 6.1) is available in the supplied CD, labelled movie5.mp4 and movie6.mp4. We can clearly distinguish that the probability density is split in two parts: one localised near the origin which corresponds to the bound states of the

molecule, and the other part, far from the origin, which corresponds to the ionised electron wavepacket. The ejected electron density forms a spherical shell with a node along the ρ axis. As we will see later, this node is due to the symmetry of the $2p\sigma_u$ final state of the molecule.

In order to extract scattering amplitudes with the Fourier method we must remove the bound state contribution. Instead of projecting out all the bound eigenstates of the molecule, we just apply a Gaussian mask to the wavefunction to remove these states. This procedure is computationally efficient. The masking function is defined as

$$M(r) = \begin{cases} 0 & \text{if } 0 \leq r \leq r_0 \\ 1 - \exp \left[-\left(\frac{r-r_0}{\sigma} \right)^2 \right] & \text{if } r_0 \leq r \leq r_1 \\ 1 & \text{if } r_1 \leq r \leq r_{\max} \end{cases} \quad (6.1)$$

with

$$\sigma = \frac{r_1 - r_0}{\sqrt{-\ln 10^{-8}}}. \quad (6.2)$$

The function is illustrated in Figure 6.2, where in our work we have used $r_0 = 10 a_0$ and $r_1 = 25 a_0$. In case of cylindrical coordinates the masking radius is $r = \sqrt{\rho^2 + z^2}$.

Once the bound states of the molecule have been removed, we can Fourier transform the resulting wavefunction. In Figure 6.3 we show the momentum distribution of the ejected electrons for each of the pulses applied. For all the pulses considered, the intensity used ($I = 1 \times 10^{13} \text{ W/cm}^2$) is high enough to produce two-photon absorption. In Figure 6.4 we can clearly see the first two ATI peaks, where the first peak is placed at $\omega_p - I_p = 0.875$ Hartrees, and the second one is at $2\omega_p - I_p = 2.852$ Hartrees. The third ATI peak, that must be at $2\omega_p - I_p = 4.827$ Hartrees, is not present. Absorption of one photon produces a spherical distribution centred at the origin with radius the momentum of the electron $k_e = \sqrt{2E_e}$. The ejected electron energy E_e is given by $E_e = \omega_L - I_p$, where ω_L is the photon energy and I_p is the ionisation potential of the molecule. In particular, for fixed-nuclei H_2^+ at $R = 2$, $I_p = 1.1$ au. The bandwidth of frequencies of the ejected wavepacket is given by the bandwidth of the incident pulse. For envelope pulses described by the \sin^2 function we take the pulse bandwidth as $\Delta\omega = 4\pi/T_d$, being T_d the duration of the pulse.

As in Figure 6.3, we see a node along the k_ρ axis. In diatomic molecules l is not a good quantum number, however it helps us to illustrate the nodal structure arising in the angular distributions. The absorption of one photon changes the angular momenta of an ionised electron by one, i.e. $\Delta l = 1$. The electronic ground state of the molecule, $1s\sigma_g$, is essentially an s state ($l = 0$), therefore after absorption of one photon, the ejected electron will be in a p state ($l = 1$), resulting in a node at $\theta = 0$.

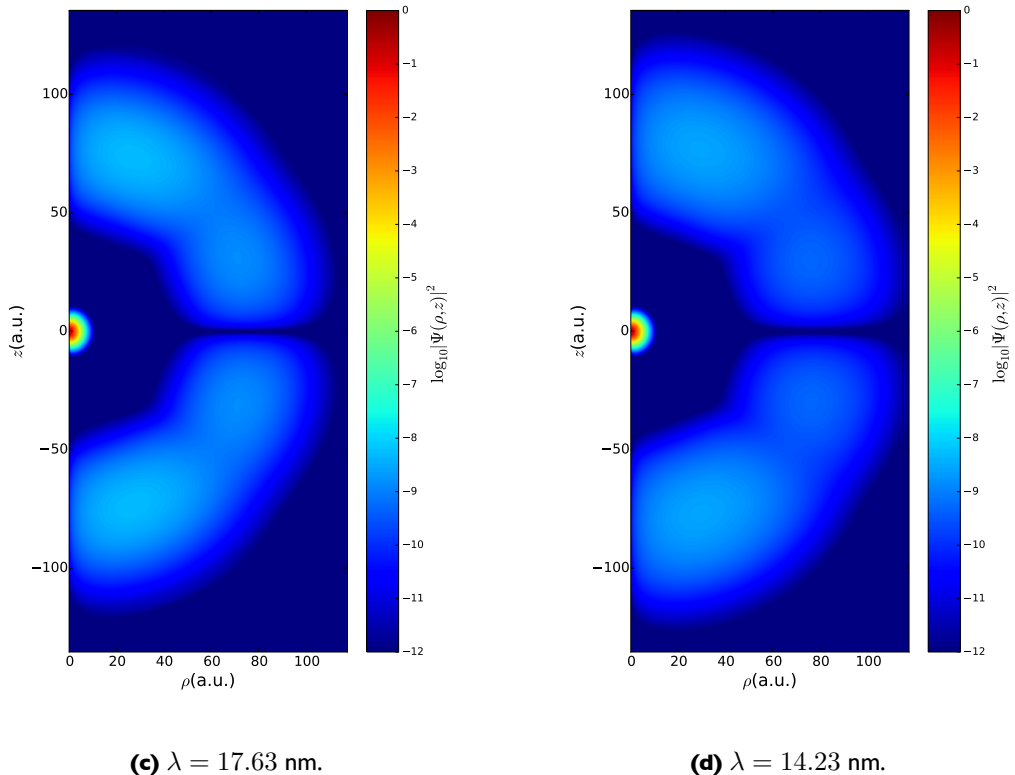
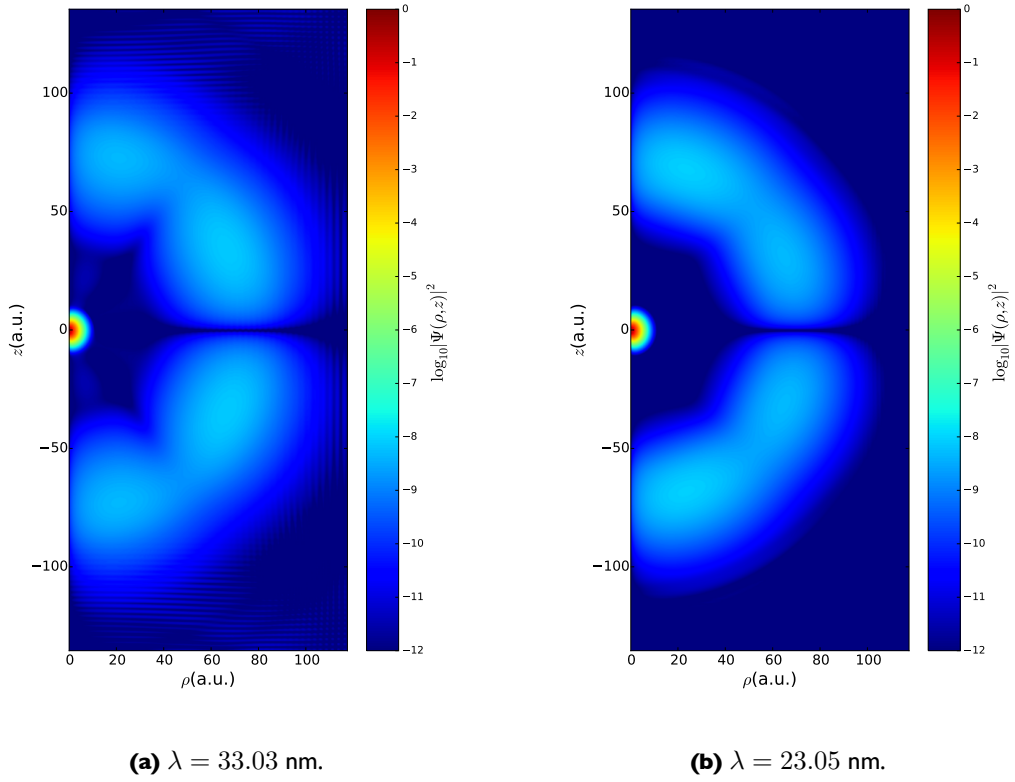


Figure 6.1: Snapshots of the wavefunction at the end of the evolution for H_2^+ by VUV pulses. The laser polarisation is parallel to the internuclear axis. The laser pulses parameters are shown in table 6.1, and corresponds to: (a) 9-cycle, $\lambda = 33.3 \text{ nm}$ (photon energy $\omega_L = 1.37 \text{ Ha}$), (b) 13-cycle, $\lambda = 23.05 \text{ nm}$ (photon energy $\omega_L = 1.98 \text{ Ha}$), (c) 17-cycle, $\lambda = 17.63 \text{ nm}$ (photon energy $\omega_L = 2.58 \text{ Ha}$) and (d) 21-cycle, $\lambda = 14.27 \text{ nm}$ (photon energy $\omega_L = 3.19 \text{ Ha}$). All laser pulses have a peak intensity of $8.4 \times 10^{12} \text{ W/cm}^2$ and a total duration of 1 fs.

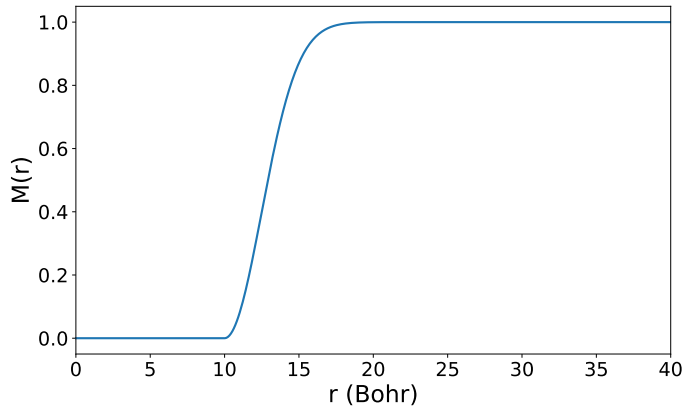


Figure 6.2: Masking function used to remove the eigenstates from the wavefunction, defined in Eq. (6.1). The function takes the value zero within the inner region and the value within the outer region. The value of the function changes smoothly from zero at r_0 to one at r_1 using a Gaussian function. In this case, the limits of the inner and outer region are $r_0 = 10 a_0$ and $r_1 = 25 a_0$.

In Figure 6.5 we show convergence of the PES obtained with the Fourier method depending on the time step used during the time evolution. The PES was extracted from the scattering amplitudes on the grid after propagation with time steps of $\Delta t = 0.05 \text{ au}$, $\Delta t = 0.03 \text{ au}$, $\Delta t = 0.02 \text{ au}$ and $\Delta t = 0.01 \text{ au}$ used in this Figure. We can see that convergence is achieved for $\Delta t = 0.02$. We have found that the time step used during the time evolution is critical for obtaining converged results.

An important issue that must be addressed is that with the Fourier method we project the scattering solutions onto field-free scattering states, i.e. plane waves. These scattering states assumes the particle feels no potential. This is not the case in our calculations, where we extract photoelectron spectra after the end of the pulse, when the Coulomb potential is still present. However, using the exact scattering states of a particle in a long range potential will not allow use of the Fourier transform to calculate the photoelectron spectra. In addition, analytical scattering states with a Coulomb-like asymptotic behaviour, $V(r) \approx 1/r$, are only known for a few simple cases. One possible solution to this problem would be to propagate the TDSE for longer after the interaction with the laser field to let the wavepacket travel further to a region where the contribution of the Coulomb potential is negligible enough, but this will increase the computational cost, spoiling the efficiency of the method. Another, more pragmatic, solution is to truncate the long range behaviour of the Coulomb potential at a certain radius

$$V(r) \rightarrow f(r)V(r) \quad (6.3)$$

where $f(r)$ is smooth function that takes the form

$$f(r) = \begin{cases} 1 & r > r_a \\ \frac{2}{(b-a)^3}(r-b)^2 \left(r - \frac{3a-b}{2}\right) & r_a \leq r \leq r_b \\ 0 & r > r_b. \end{cases} \quad (6.4)$$

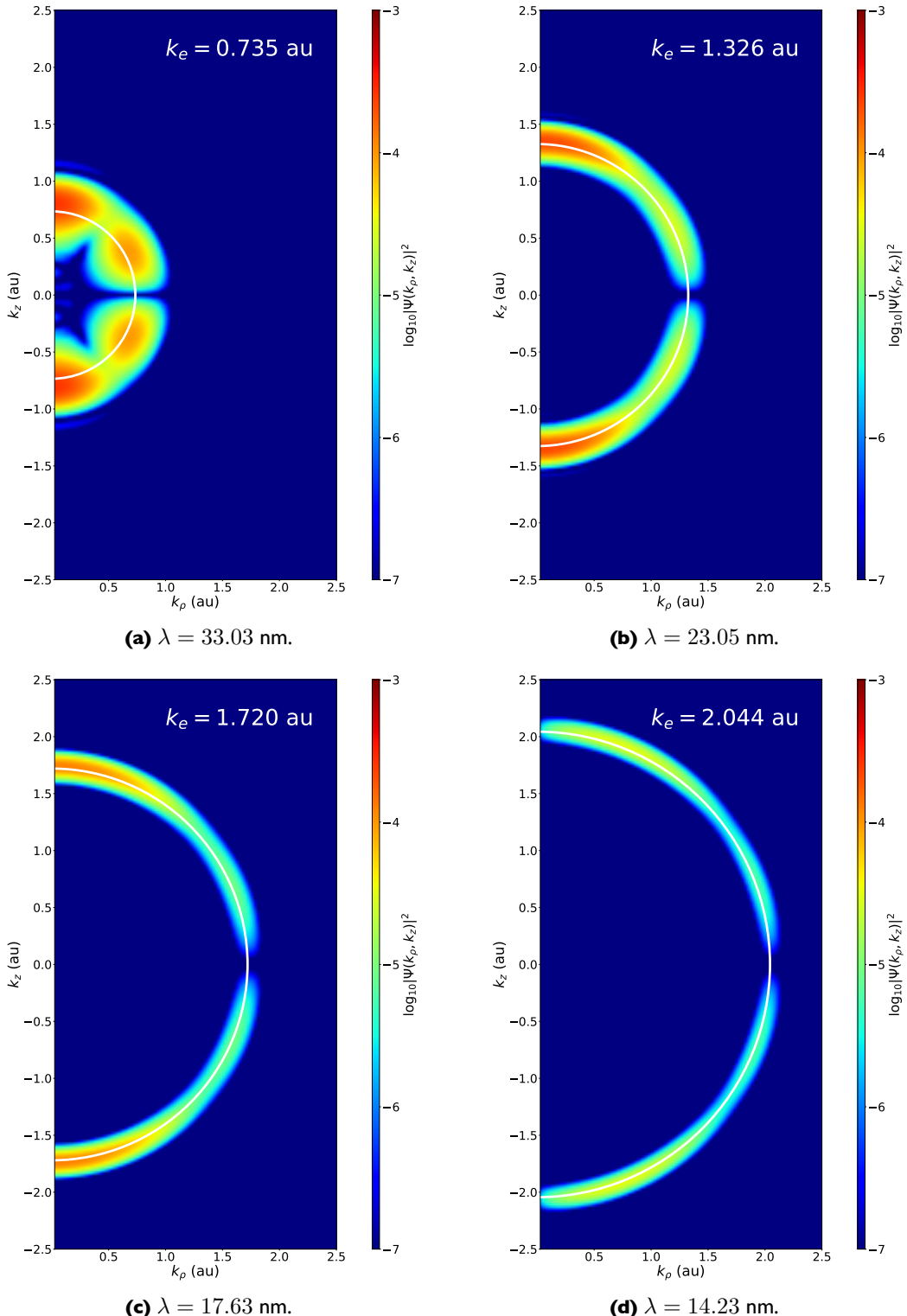


Figure 6.3: Momentum distribution of the ionised electrons for single-photon ionisation with laser polarisation parallel to the internuclear axis from the $1s\sigma_g$ state of the fixed-nuclei H_2^+ , calculated with the Fourier method. Pulse parameters for each calculation can be found in table 6.1, and corresponds to: (a) 9-cycle, $\lambda = 33.3 \text{ nm}$ (photon energy $\omega_L = 1.37 \text{ Ha}$), (b) 13-cycle, $\lambda = 23.05 \text{ nm}$ (photon energy $\omega_L = 1.98 \text{ Ha}$), (c) 17-cycle, $\lambda = 17.63 \text{ nm}$ (photon energy $\omega_L = 2.58 \text{ Ha}$) and (d) 21-cycle, $\lambda = 14.27 \text{ nm}$ (photon energy $\omega_L = 3.19 \text{ Ha}$). All laser pulses have a peak intensity of $8.4 \times 10^{12} \text{ W/cm}^2$ and a total duration of 1 fs. In each plot, a white semicircle with radius $k_e = \sqrt{k_\rho^2 + k_z^2}$, the electron momentum, is given.

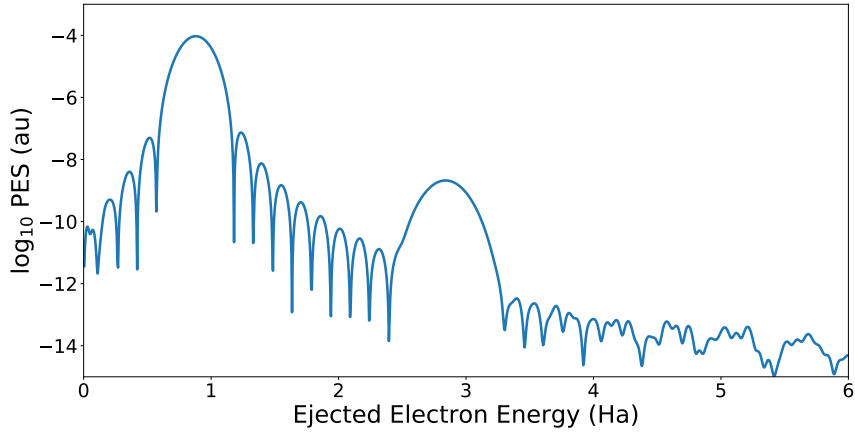


Figure 6.4: Photoelectron spectra in a logarithmic scale for photoionisation of H_2^+ after interaction with a 13 cycle laser pulse having wavelength $\lambda = 23.05 \text{ nm}$ and peak intensity $1.0 \times 10^{13} \text{ W/cm}^2$. The PES was calculated with the Fourier method, using the grid parameters of set (I) and propagating the wavefunction 10 cycles after the end of the pulse. The first two ATI peak are visible at 0.875 and 2.852 Hartrees respectively.

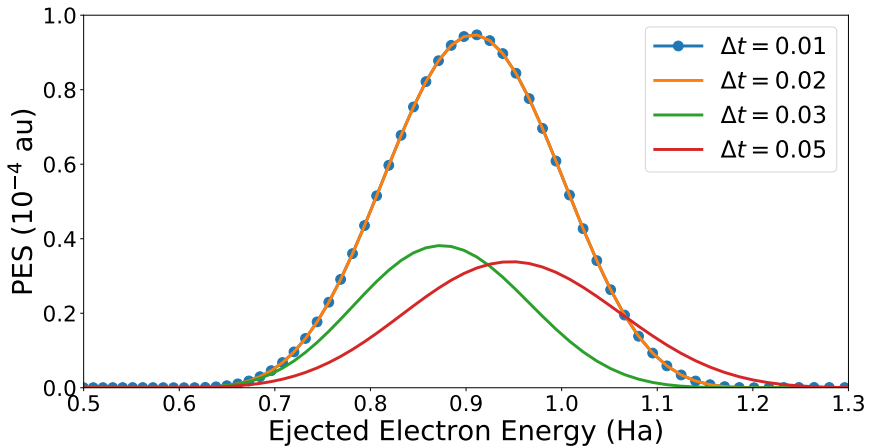


Figure 6.5: Comparison between photoelectron spectra calculated with the Fourier method for photoionisation of H_2^+ using different time steps for the TDSE evolution. The molecule was exposed to a 13 cycle laser pulse having wavelength $\lambda = 23.05 \text{ nm}$ and peak intensity $1.0 \times 10^{13} \text{ W/cm}^2$.

This truncation function is controlled by a third order polynomial that has continuous derivatives at r_a and r_b .

In Figure 6.6 we illustrate both methods to circumvent the problem: we plot the PES extracted from wavepackets that have been propagated for different durations after the pulse using the laser parameters of pulse 3 in table 6.1, where the Coulomb potential has not been truncated. We also plot the PES resulting from calculations where the potential has been truncated at different radius from the origin, $r = 20 a_0$ and $r = 40 a_0$. In this case the TDSE was propagated 10 cycles after the end of the pulse to obtain ionised wavepackets in the region where the Coulomb potential is zero. We see that the spectra calculated with the full

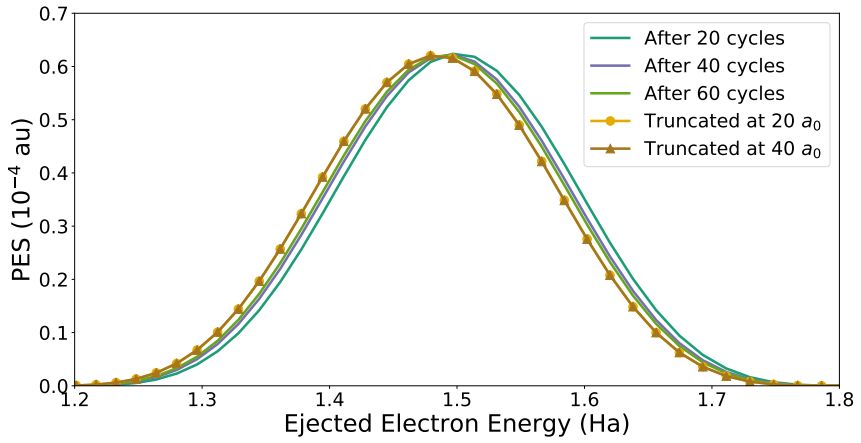


Figure 6.6: Photoelectron spectra for photoionisation of H_2^+ calculated using the Fourier method. The solid lines correspond to the PES extracted after propagating 20, 40, 45 and 60 optical cycles after the end of a 17 cycle laser pulse having wavelength $\lambda = 17.63 \text{ nm}$ and peak intensity $1.0 \times 10^{13} \text{ W/cm}^2$, from a calculation using the full Coulomb potential. The lines with dots and triangles correspond to the PES extracted from a calculation using the truncated Coulomb potential, where the TDSE was evolved 10 cycles after the end of the pulse. The Coulomb potential was truncated at radius $r = 20 a_0$ (dots) and $r = 40 a_0$ (triangles). The grid parameters for all the calculations were those of set (I).

potential are displaced slightly to higher energies: the photoelectron energies obtained by projection onto field-free scattering solutions are overestimated due to the presence of a long range potential. As we propagate the TDSE for longer after the interaction with the laser field, the wavepacket travels further to a region where the contribution of the Coulomb potential is smaller. By contrast, there is an agreement in energy and bandwidth between both PES extracted from wavepackets that have been propagated in truncated potentials, at $r = 20 a_0$ and $r = 40 a_0$. Also, absorption of one photon of energy $\omega_L = 2.58 \text{ Hartrees}$ will give the ionised electron a kinetic energy of $E_e = 1.48 \text{ Hartrees}$. We observe in Figure 6.6 the peaks of both PES obtained using the truncated potential are centred at this energy. Thus, we obtain the PES located at the correct energies. Hence, for these laser parameters it is enough to truncate the Coulomb potential at $r = 20 a_0$. We also note that, as the TDSE is propagated using the full potential for longer times after the pulse, the extracted PES converges with the PES calculated using the truncated Coulomb potential.

6.1.2 Sampling point and t-SURFF results

We now consider the calculation of the PES using the sampling point and t-SURFF methods. We remember that in both methods the PES can be calculated on the same surface during the time evolution (the wavefunction passing through this surface is stored in what we call the ‘surface’ file), as was discussed in Section 5.4.2. Therefore the same calculation can be used for obtaining results using both methods. Five sets of grid parameters are used in these calculation, as shown in table 6.2. In all cases the grids are smaller compared to the grid required for the Fourier method. This is because for both surface methods absorbing boundaries are used just beyond the measuring surface.

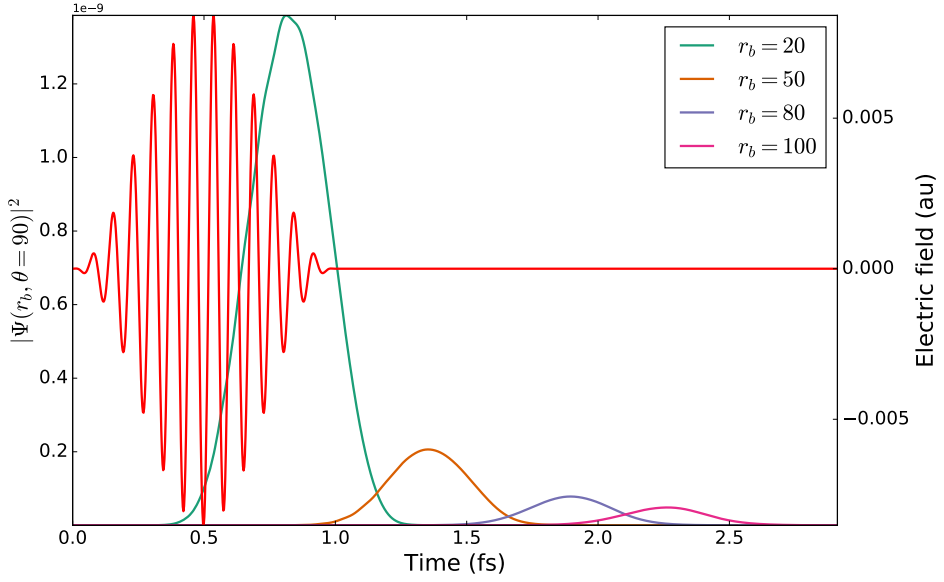


Figure 6.7: Electron probability density $|\Psi(r_b, \theta = \pi/2)|^2$ crossing surfaces with different surface radii ($r_b = 20, 50, 80, 100 a_0$) after photo-ionisation of H_2^+ by a 13 cycle laser having a wavelength $\lambda = 23 \text{ nm}$ and a peak intensity $1.0 \times 10^{13} \text{ W/cm}^2$. Also shown is the electric field of the laser pulse.

For these calculations we must propagate the TDSE after the pulse ends to allow the ionised wavepackets to completely pass through the surface. In Figure 6.7 we show the probability density of the ejected electron wavepacket as it crosses surfaces with different radii. We can see how the wavepacket takes longer to fully cross surfaces at larger distances from the molecule. We point out that for the surface at $r_b = 20 a_0$, the ionising wavepacket crosses the surface during interaction with the laser pulse: this distorts the wavepacket as it passes through the surface. The sampling point and the t-SURFF methods also suffer from a problem related with the long range nature of the Coulomb potential, similar to the problem described previously for the Fourier method. In the t-SURFF method, we neglect the Coulomb potential and assume that the solutions at the surface are Volkov waves, i.e solutions of the free particle in the presence of a laser field, whose analytical solutions are known. However, this is an approximation, since the Coulomb potential never vanishes due to this long range behaviour

$$V(r) \rightarrow 0 \quad \text{when} \quad r \rightarrow \infty, \quad (6.5)$$

thus the Coulomb tail has an influence at r_b . It is possible to solve the problem choosing a large surface radius r_b , so the influence of the potential will become negligible. However, the easiest solution which doesn't add additional computational effort is to truncate the Coulomb potential, as in Section 6.1.1, using Eq. (6.4).

In Figure 6.8 we present the PES obtained after interaction with a 13-cycle laser pulse,

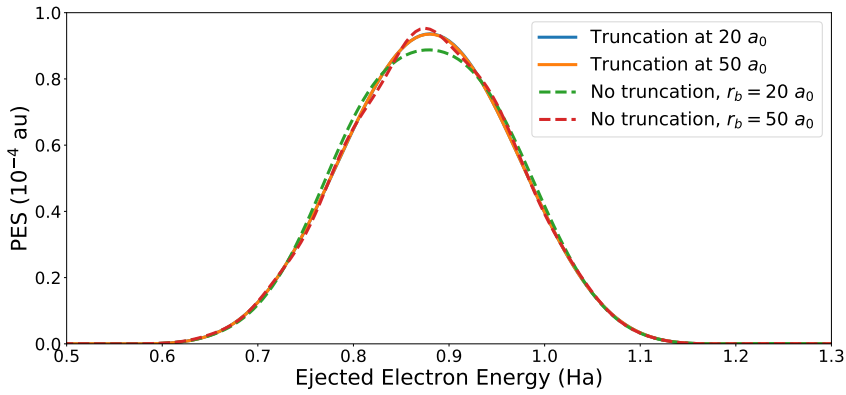


Figure 6.8: Photoelectron spectra of H_2^+ exposed to a 13-cycle laser pulse, having a wavelength of $\lambda = 23.05 \text{ nm}$ and a peak intensity of $I = 10^{13} \text{ W/cm}^2$. The solid lines correspond to the PES obtained using a truncated Coulomb potential, while the dashed lines correspond to the PES obtained using the full potential. The grid parameters used in the calculations with a surface radius at $r_b = 20 \text{ } a_0$ are those of set (III), while calculations with $r_b = 50 \text{ } a_0$ used those of set (IV). In the plot, the line corresponding to truncation at $r_b = 50 \text{ } a_0$ is completely superimposed to the line corresponding to truncation at $r_b = 20 \text{ } a_0$.

having a wavelength of $\lambda = 23.05 \text{ nm}$ and a peak intensity of $I = 10^{13} \text{ W/cm}^2$ (pulse 3 in table 6.1), using the t-SURFF method in a calculation with truncated and full Coulomb potentials. For each case, the PES is extracted at two surface radius, $r_b = 20 \text{ } a_0$ and $r = 50 \text{ } a_0$. The grid parameters employed correspond to those of set (III) when using the surface radius at $r_b = 20 \text{ } a_0$ and those of set (IV) for $r_b = 50 \text{ } a_0$. We observe that, although all the PES shows a single peak centred at the same energy, when using the full potential the spectra is distorted in shape, and the distortion is different for different radii. However, both PES calculated using a truncated Coulomb potential agree in both amplitude and shape.

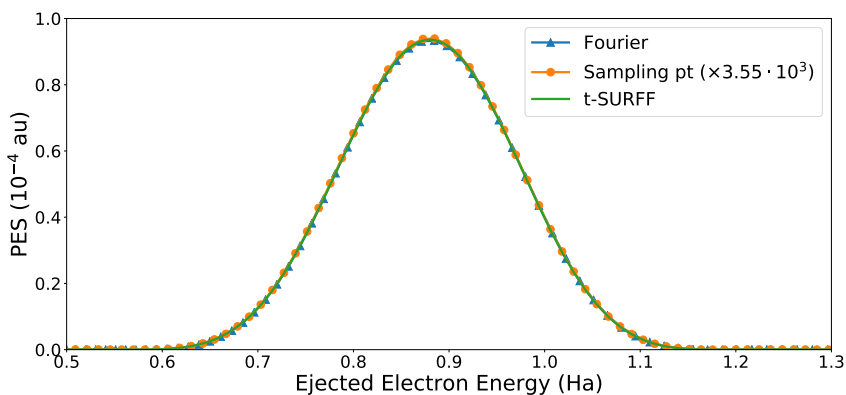


Figure 6.9: Photoelectron spectra for photoionisation of H_2^+ after interaction with a 13 cycle laser pulse having wavelength $\lambda = 23.05 \text{ nm}$ and peak intensity $1.0 \times 10^{13} \text{ W/cm}^2$. Results were calculated in THeREMIN by the three methods implemented in POpSiCLE: the Fourier method, the sampling point method and the t-SURFF method. For the sampling point and t-SURFF method we made use of the grid parameters of set (III), while for the Fourier method calculation we used grid parameters of set (I). For the surface calculations (sampling point and t-SURFF method), the surface radius was $r_b = 20 \text{ } a_0$. For the Fourier method we propagated the wavefunction 10 cycles after the end of the pulse. For all the methods the Coulomb potential is truncated at $r = 20 \text{ } a_0$.

We present results for the photoelectron spectra calculated using the sampling point method and the t-SURFF method in Figure 6.9, and compare these results with the results from the Fourier methods. It is important to mention that the Coulomb potential is truncated at $r_b = 20 a_0$ in Eq. (6.4), just at the surface radius for the sampling point and the t-SURFF method, for extracting the PES with all the methods. These results are obtained using laser pulse number 2 in table 6.1, and for the sampling point and t-SURFF methods we used the grid parameters of set (III), while for the Fourier method calculation we used the set (I) of grid parameters. For the given laser pulse, absorption of one photon will ionise an electron with a kinetic energy of $E_e = 0.87$ Hartrees ($k_e = 1.32$ au), therefore we should see a single peak at this energy. The position of the peak for the three methods is identical. The position and the shape of the peak produced with the sampling point method is in good agreement with the peak produced with the t-SURFF and the Fourier method. However, as expected, the spectral density is not correct with this method. The only methods that reproduces correctly the PES (magnitude, position and shape of the peak) are the Fourier and the t-SURFF methods.

In Figure 6.10 the PES calculated using the sampling point method using different propagation times after the end of the pulse are shown. The sampling point method involves Fourier transforming the wavefunction on the surface values over time. Therefore, in order to gain resolution we can just add more points in the spectra by padding with zeros the end of the time signal, as detailed in Section 5.4.4.

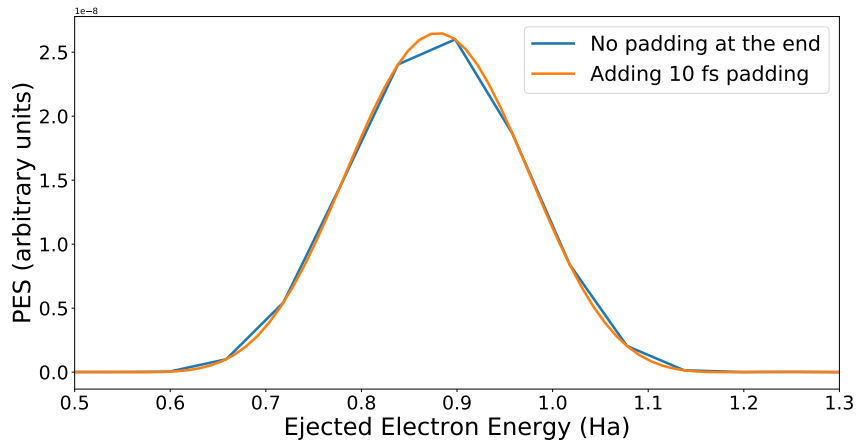
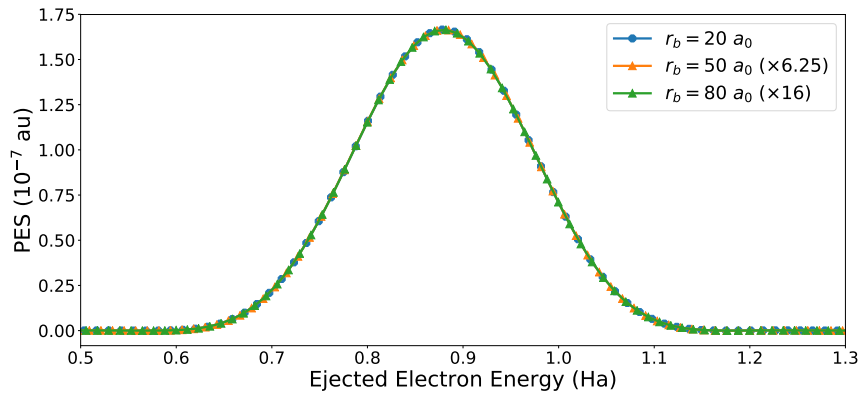


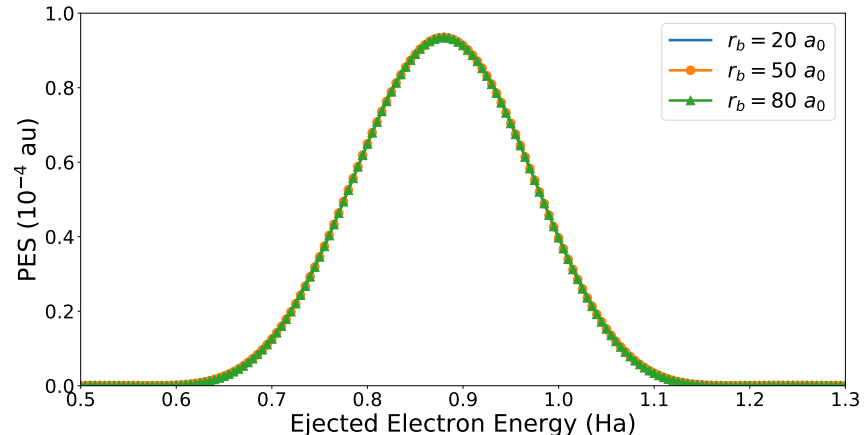
Figure 6.10: PES calculated with the sampling point method, using set of grid parameters number (III) with a surface radius $r_b = 20 a_0$, for different propagation times after the pulse. The blue line represents the PES calculated after propagation for 1.54 fs (20 laser cycles) more after the pulse, whereas the green line represents the PES calculated after propagation of, in addition to the 20 cycles, 10 fs more after the pulse. (11.54 fs added in total after the pulse). The last 10 fs were added padding with zeros at the end of the surface values over time.

We now compare how the photoelectron spectrum depends on the choice of surface radius for the sampling point and the t-SURFF methods. In the upper panel of Figure 6.11 we see that for the sampling point method the amplitude of the PES depends on the surface ra-

dius, whereas in the lower panel we can see that for the t-SURFF method the amplitude is independent on the surface radius chosen. The sampling point method does not give the correct amplitude of the spectra because it does not take into account the distance at which the surface values have been recorded. However, in order to reproduce the correct position in energies and the correct shape at radius r_1 and r_2 using the sampling point method we must scale the PES obtained at r_2 by $(r_2/r_1)^2$, which is the ratio of the volume elements between the two surfaces. For instance, in Figure 6.11, if we scale the PES for $r_b = 50 a_0$ by a factor $(50/20)^2 = 6.25$, we obtain agreement between the spectra at surface values $r_b = 50 a_0$ and $r_b = 20 a_0$. Again, if we scale the PES for $r_b = 80 a_0$ by a factor $(80/20)^2 = 16$ we observe agreement between the spectra obtained at different surface radii.



(a) Calculated with the sampling point method



(b) Calculated with the t-SURFF method

Figure 6.11: Photo-electron spectra of single-photon ionisation of H_2^+ after interaction with pulse 2 of table 6.1. (a): PES calculated with the sampling point method. (b): PES calculated with the t-SURFF method. In both plots the PES have been calculated placing the surface at radius $r_b = 20, 50, 80 a_0$, and the grid parameters used were those of sets (III), (IV) and (V) respectively. In (a), the results for $r_b = 50 a_0$ and $r_b = 80 a_0$ have been scaled by a factor given in the legend.

Figure 6.12 shows the angularly resolved photo-electron spectra obtained using the three methods. The probability densities are a function of the electron energy $E_e = k_e^2/2$ and the

polar angle θ . For the spectra obtained through the Fourier method, we transform the amplitudes obtained originally in cylindrical coordinates to spherical coordinates by interpolation onto a spherical grid. This operation is carried out using one of the interpolation routines described in Section 5.4.2. We see excellent agreement between the three approaches. The spectra corresponding to the sampling point result has been scaled by a factor of 2×10^3 in order to compare with the other approaches. We again observe the node at $\theta = 0$ which has already been discussed.

Most previous computational studies of photoionisation of H_2^+ were carried out using time-dependent perturbation theory [118, 119, 121, 281] or the Floquet method [126, 131, 132]. We will use an approach that will allow us to calculate the total and differential cross sections from the scattering amplitudes obtained from solving the TDSE. This approach was introduced by Palacios *et al.* [282] for atomic photoionisation of one and two-electron atoms, and later applied to photoionisation of H_2^+ [121]. The benefit of this approach is that it goes beyond perturbation theory and thus allows us to describe the situation when high intensity, short duration laser pulses are used to excite the system. A brief description of the approach is given in Appendix C.

In order to compare with results obtained using TDPT, we choose our set of parameters in the regime of long pulses and moderate intensities, because in that regime TDPT can still be used to extract cross-sections. We solve the TDSE for H_2^+ exposed to four different laser pulses, each with increasing photon energy, whose polarisation axis is collinear with the internuclear axis of the molecule. We keep the pulse duration constant, $T = 1$ fs, for each of the pulses and use the same intensity, $I = 10^{13} \text{W/cm}^2$. The different photon energies employed and their corresponding parameters can be found in table 6.1. We fixed the internuclear distance to $R = 2$ for all the calculations, and consider transitions from the $1s\sigma_g$ ground state. The photoelectron spectra and the total photoionisation cross sections are shown in Figure 6.13. The lower panel shows the radial energy distribution of the ejected electron corresponding to the four laser pulses detailed in table 6.1, while the upper frame presents the corresponding cross section calculated from the energy distributions. We compare our results with those of Hou *et al* [123]; these results agree with the results of Bates and Öpik [117], Plummer and McCann [126] and Rescigno and McCurdy [119]. We see very good agreement between our results and the LOPT results.

Finally we consider how the performance of the calculation of the TDSE depends on the choice of the method for calculating the photoelectron spectra. The resources required for the time evolution of the TDSE for the Fourier method and the surface flux method are shown in table 6.3. The set of data corresponding to Set (II) corresponds to a grid that has the same number of points per core as set (I). We can see that the computation time per time step is smaller for the surface flux method. Even if there is an extra overhead in carrying out the

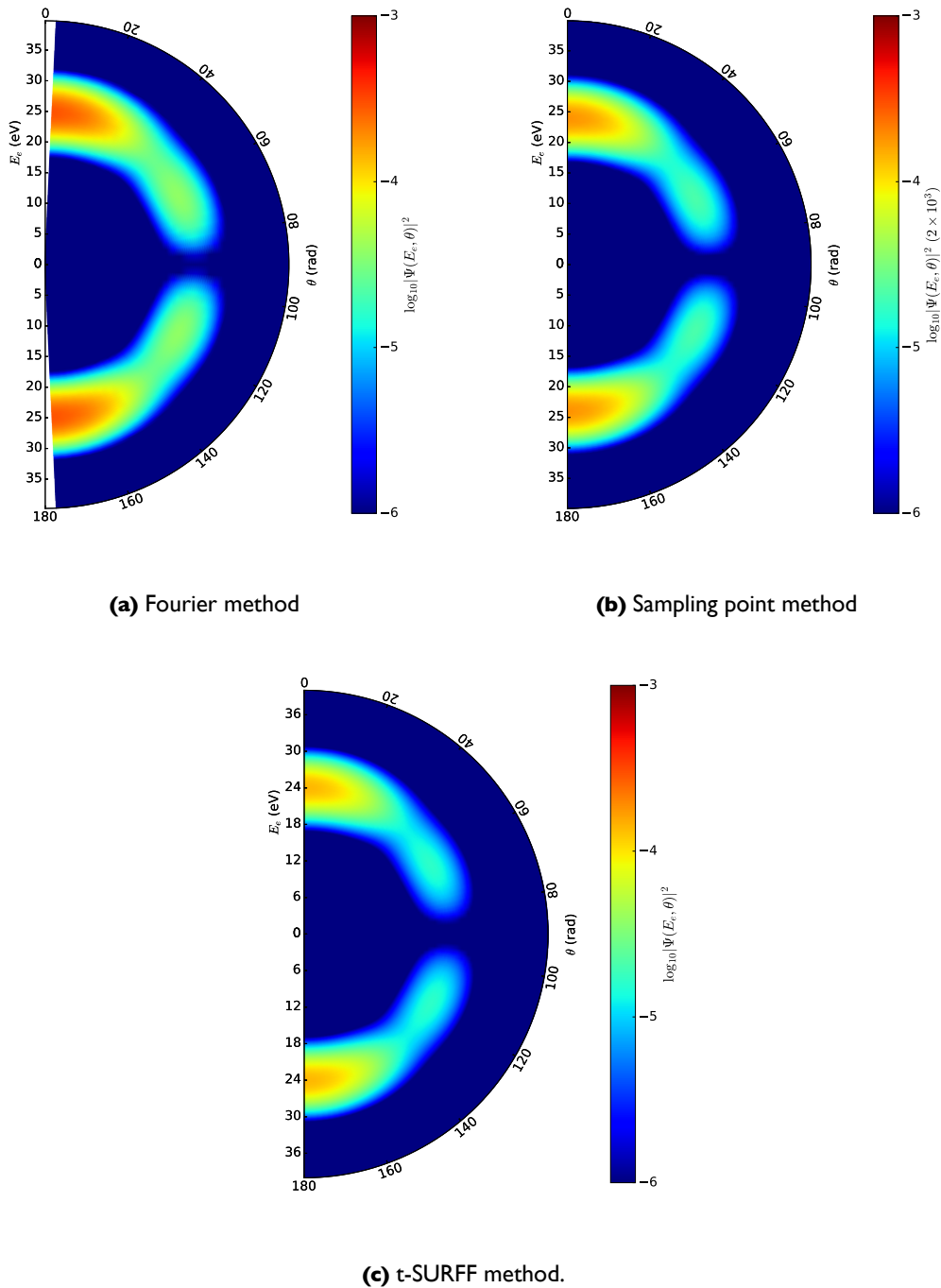


Figure 6.12: Polar plots showing the angularly resolved photoelectron distributions of fixed-nuclei H_2^+ after interaction with a 13 cycle laser pulse having wavelength $\lambda = 23.05$ nm and peak intensity 1.0×10^{13} W/cm². Results were calculated in 2D using THeREMIN using: (a) the Fourier method, (b) the sampling point method and (c) the t-SURFF method. The sampling point results have been scaled by a factor of 2×10^3 .

interpolation of the wavefunction onto the spherical surface, the overhead caused by the global communications is larger due to the larger grid used in the Fourier method. From the table we see that the total compute resource used for the Fourier method was 35 core hours, compared to the 3.8 hours for the surface flux method. Hence, the surface flux method requires 89 % less resource than the Fourier method. With the grid used in Set (II) we keep the same number of

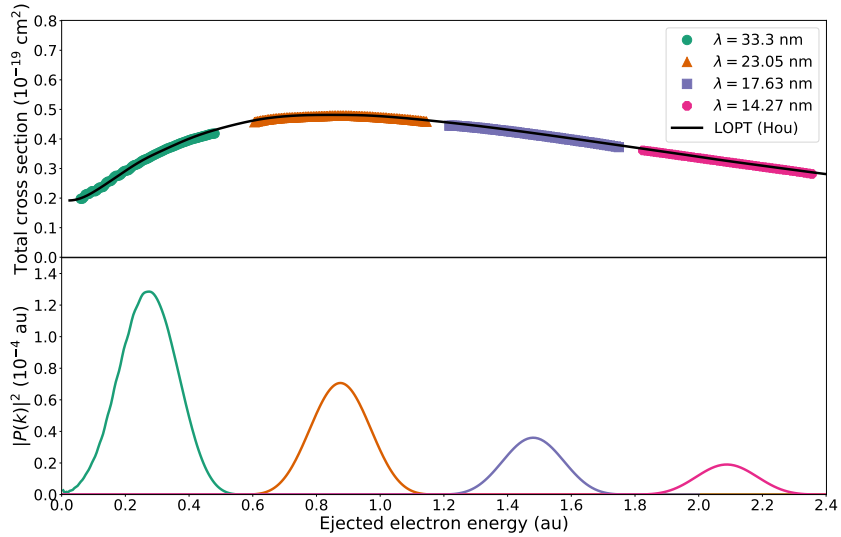


Figure 6.13: Total cross section for single-photon ionisation of H_2^+ from the Σ_g ground state in the presence of four linearly polarised laser pulses. All the pulses have a total duration of 1 fs, and an intensity of $I = 10^{13} \text{ W/cm}^2$. In the upper frame we compare with the results of Hou [123], obtained with LOPT.

Set	Method	No. cores (minutes)	Calculation time (seconds)	Time per time step (core hours)	Total resource
I	Fourier	36	58	0.97	35
II	Surface	6	38	0.62	3.8
III	Surface	6	28	0.46	2.8

Table 6.3: Timings for the calculation of the TDSE using THeREMIN (2D) for the Fourier method (upper part) and for the surface methods (middle and lower part). The grid parameters of each evolution are given in table 6.2.

grid points per core, although we can even reduce the size of the grid to have the same extent in both ρ and z directions, 45 Bohr. In set (III) the total resource spent was only of 2.8 core hours, using 92 % less resource than the Fourier method to produce the same spectra.

6.2 Comparison of PES approaches in 3D

We now detail our convergence tests for the calculation of PES in 3D using our RHYthMIC code, which solves the TDSE in Cartesian coordinates. In this case the Fourier method and the surface flux methods will be compared. While this code can consider arbitrary orientations between the laser and the molecule, we will compare our results to these calculated in Section 6.1. We consider the same pulse parameters as in the 2D case, corresponding to the pulse 2 in table 6.1.

In order to reduce the computational size of these calculations we have tested a larger grid spacing in $\Delta x = \Delta y = 0.4$ Bohr, keeping the same the grid spacing of the coordinate in

State	Fine 1	Coarse 1	Fine 2	Coarse 2
1	-1.10444	-1.10982	-1.10273	-1.10207
2	-0.66937	-0.67389	-0.66764	-0.66655
3	-0.42867	-0.42854	-0.42867	-0.42856
4	-0.42867	-0.42854	-0.42867	-0.42856
5	-0.36106	-0.36228	-0.36080	-0.36087

Table 6.4: Comparison of five lowest eigenvalues of the fixed-nuclei H_2^+ , using different grid spacings calculated in 3D using the RHYthMIC code. The grid spacings and finite-difference (FD) rules are: **Fine 1:** We use a fine grid with grid spacings $\Delta x = \Delta y = \Delta z = 0.2$ and a 5-point FD rule; **Fine 2:** We use again a fine grid of grid spacings $\Delta x = \Delta y = \Delta z = 0.2$ and a 9-point FD rule; **Coarse 1:** We use grid spacings $\Delta x = \Delta y = 0.4$ and $\Delta z = 0.2$, and a 5-point FD rule; **Coarse 2:** Again we use grid spacings $\Delta x = \Delta y = 0.4$ and $\Delta z = 0.2$, and a 9-point FD rule.

which lies the internuclear axis, $\Delta z = 0.2$. In combination with these grid spacings we also consider a 9-point rule finite difference (FD) operator in each coordinate to maintain accuracy at a similar level compared to a grid with smaller grid spacing. To test the accuracy of these grid spacings coarse grid, we check the five lowest eigenvalues for a fixed nuclei calculation of H_2^+ at $R = 2 a_0$ using different combinations of grid spacings and finite difference rules.

The eigenvalues calculated are given in table 6.4. We can see that the values obtained using a 9-point rule have no difference up to the third decimal figure.

The grid parameters employed in the 3D test can be found in table 6.5:

- I The parameters in set (I) were employed to calculate the spectra with the Fourier method. The grid spacing employed are those corresponding of grids coarse 1 and coarse 2 (see caption in Figure 6.4).
- II The parameters in set (II) are used for the surface methods (sampling point and t-SURFF methods). In order to compare the efficiency between the Fourier method and the surface methods, the number of grid points and the grid spacing are similar to those used in set (I). Since we are only interested in the values of the wavefunction and its first derivative at the surface, and for this calculation the surface radius is $r_b = 20 a_0$, a grid extent smaller than the extent used in set (I) is used.
- III The set (III) were also used for the surface methods, but this time the extent and the number of grid points were reduced in order to maximise the efficiency of the calculation.
- IV Set (IV) has the small grid spacings used in fine 1 and fine 2 to calculate the five lowest eigenenergies of the fixed-nuclei H_2^+ shown in table 6.4.

As in the 2D case, the grid size for the Fourier method is larger than in the surface methods in order to contain the full wavefunction at the end of the calculation. The time step used for

Set	Method	Points per core			No. cores			Grid spacing			Mesh extent		
		x	y	z	x	y	z	x	y	z	x _{max}	y _{max}	z _{max}
I	Fourier	71	71	75	7	7	13	0.4	0.4	0.2	±99.2	±99.2	±97.4
II	Surface	71	71	75	3	3	6	0.4	0.4	0.2	±42.4	±42.4	±44.9
III	Surface	67	67	59	3	3	7	0.4	0.4	0.2	±40.0	±40.0	±41.2
IV	Surface	81	81	59	5	5	7	0.2	0.2	0.2	±40.4	±40.4	±41.2

Table 6.5: Grid parameters employed for calculating the PES in 3D using RHYthMIC. Four calculations were considered. In set (I) the Fourier method is used, which requires a large grid extent. In sets (II), (III) and (IV) the surface methods (sampling point and t-SURFF methods) were used, in which during the time evolution we record a single surface file. The surface radius employed in these sets is $r_b = 20 a_0$. The mesh extent for each set is given in atomic units.

all the calculations is $\Delta t = 0.02$ au, again the same as in the previous 2D tests.

Similar to Figure 6.1, we can calculate probability density of the H_2^+ wavefunction at the end of the interaction. This density is presented in Figure 6.14. Since we have calculated the wavefunction in 3D we show 2D plots of the density. For a given instant of time, t , the 2D probability density is obtained integrating over one of the coordinates

$$P(x, y, t) = \int dz \psi^*(x, y, z, t)\psi(x, y, z, t) \quad (6.6)$$

where, for example, in Eq. (6.6) we obtain the probability density in the $x - y$ plane integrating over the z coordinate. As in Figure 6.1, we observe a central node perpendicular to the internuclear axis at $z = 0$, exactly as we see in the 2D case in Figure 6.1.

In order to obtain the spectral amplitudes using the Fourier method, we apply the mask in Eq. (6.1). In this case, the mask radius, r , is defined as $r = \sqrt{x^2 + y^2 + z^2}$. We use a mask with parameters $r_0 = 7 a_0$ and $r_1 = 15 a_0$. After applying the mask, the resulting probability density of the momentum distribution is calculated. Similar to Eq. (6.6) in momentum space, the 2D density are obtained from the 3D momentum probability density integrating over one of the coordinates

$$P(k_x, k_y, t) = \int dk_z \psi^*(k_x, k_y, k_z, t)\psi(k_x, k_y, k_z, t) \quad (6.7)$$

where, as in Eq. 6.6, for example we obtain the 2D momentum probability density in the $k_x - k_y$ plane integrating over the k_z coordinate. 2D representations of these are presented in Figure 6.15.

We compare again the PES obtained using the three methods for the coarse grid with parameters labelled III in table 6.5. As we can see in Figure 6.16, the position and shape of the peak obtained with the t-SURFF in good agreement with the sampling point method. The spectra produced with the Fourier method is shifted to higher energies due to the long range potential, as it was explained in the previous subsection, because in this case the Coulomb

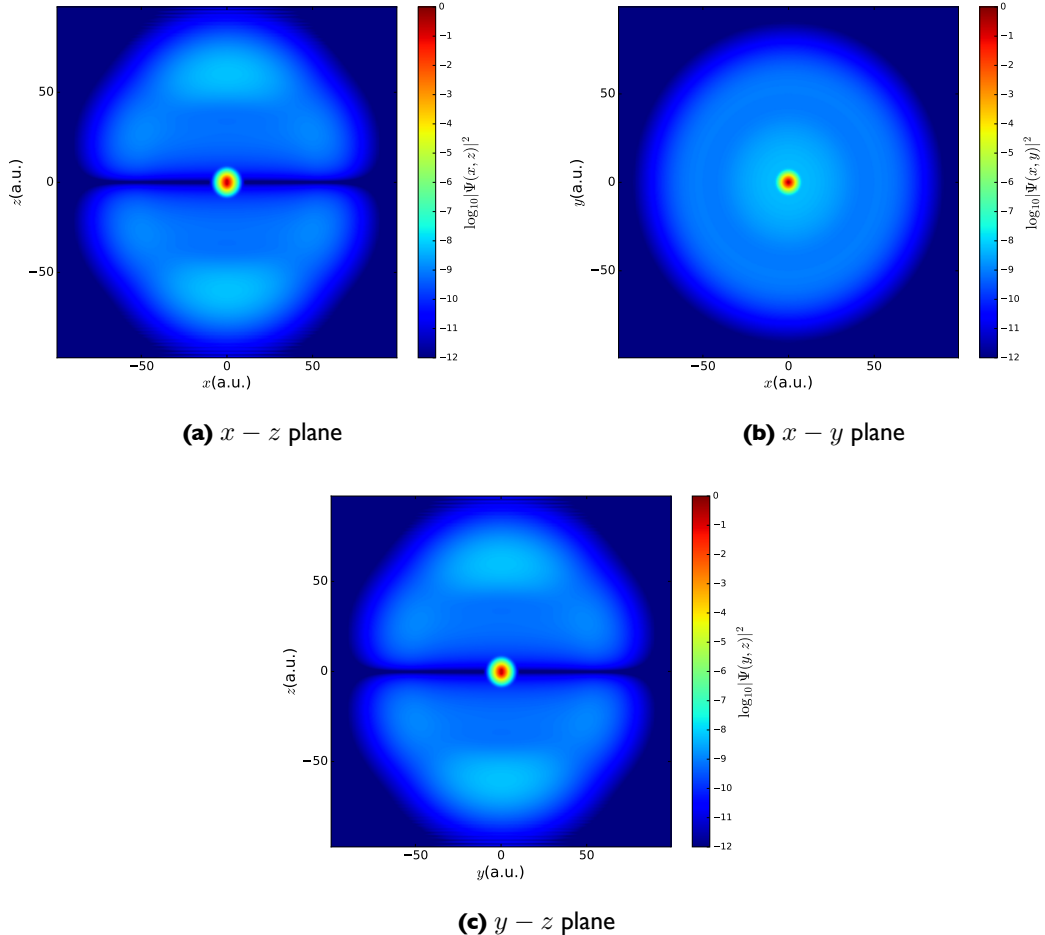


Figure 6.14: Snapshots of the wavefunction at the end of simulation after photoionisation by a 13-cycle laser pulse of $\lambda = 23$ nm of wavelength and an intensity of $I = 10^{13}$ W/cm². The three frames correspond to (a) $P(x, z)$ (b) $P(x, y)$ and (c) $P(y, z)$ which are been obtained by integrating the 3D density over one coordinate.

potential has not been truncated.

In the following we want to compare the PES obtained using a fine and a coarse grid, corresponding to the grid parameters of sets (III) and (IV) of table 6.5. For clarity, in Figure 6.17 we only compare results obtained with the surface method. In both set we have used a 5-point and 9-point rule FD derivative operators. The last set plotted in the figure corresponds to the result in 2D using cylindrical coordinates and the code `THeREMIN`, already shown in Section 6.1. We use the 2D results as a reference for the results in 3D, although we do not show the convergence results here.

Using the results in 2D as a reference, we can clearly see that the closest curve to the 2D PES corresponds to set (IV), which have a grid spacing of $\Delta x = \Delta y = \Delta z = 0.2$ Bohr. However, we can see that the PES calculated using set (IV) is not fully converged. We think that for this reason the PES corresponding to the same grid parameters but using a higher order FD rule, set (IV) with a 9-point rule, does still not converge to the 2D results and actually differs more

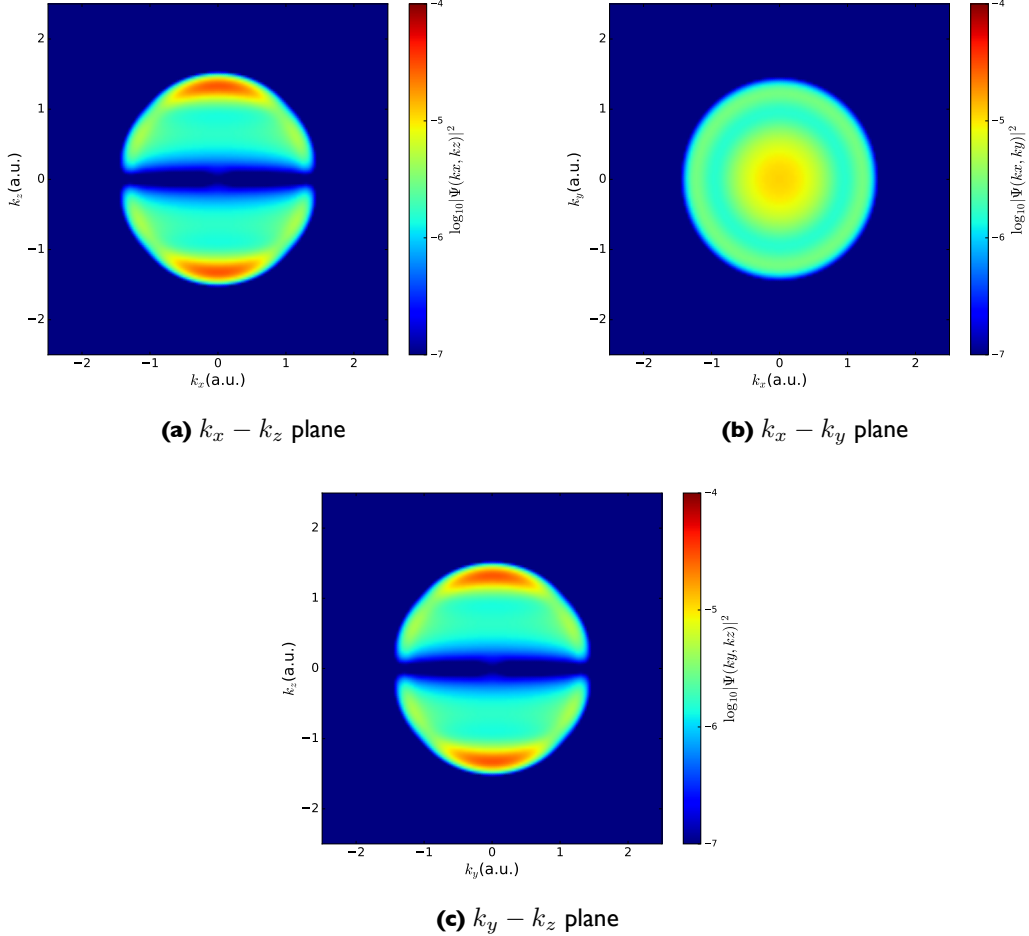


Figure 6.15: 2D photo-electron momentum distributions after ionisation of H_2^+ from the $1s\sigma_g$ ground state after interaction with a 13-cycle laser pulse of $\lambda = 23$ nm of wavelength and $I = 10^{13}$ W/cm 2 , obtained with the Fourier method using set (I). The frames correspond to (a) $P(k_x, k_z)$ (b) $P(k_x, k_y)$ and (c) $P(k_y, k_z)$ which have been obtained by integrating over one coordinate.

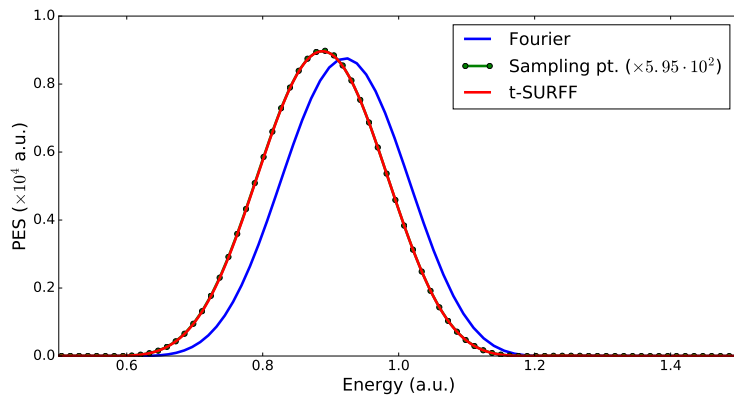


Figure 6.16: Photoelectron spectra for photoionisation of H_2^+ after interaction with a 13 cycle laser pulse having wavelength $\lambda = 23.05$ nm and peak intensity 1.0×10^{13} W/cm 2 . Results were calculated in RHYthMIC (3D) by the three methods implemented in PoPSiCLE: the Fourier method, the sampling point method and the t-SURFF method

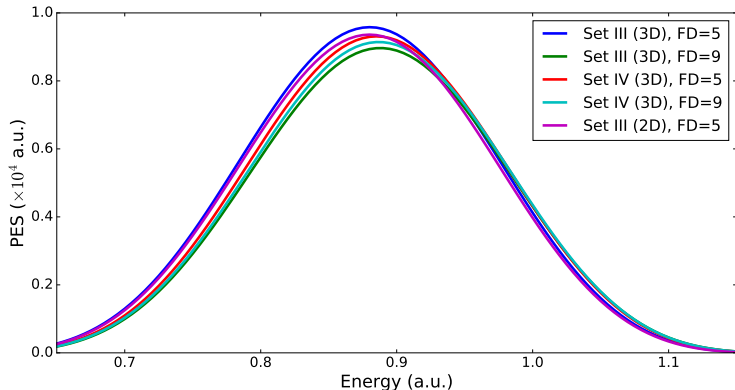


Figure 6.17: Photoelectron spectra for photoionisation of H_2^+ after interaction with a 13 cycle laser pulse having wavelength $\lambda = 23.05 \text{ nm}$ and peak intensity $1.0 \times 10^{13} \text{ W/cm}^2$. Results were calculated using the t-SURFF method in 3D with RHYthMIC, except for the line corresponding to set III, which was calculated in 2D with THeREMIN. FD denotes the order of the finite-difference rule employed.

Method	No. cores	Calculation time (minutes)	Time per time step (seconds)	Total resource (core hours)
Fourier	637	208	3.75	2208.27
Surface (I)	54	279	4.60	251.10
Surface (II)	63	197	3.25	206.85
Surface (III)	175	298	4.91	869.17

Table 6.6: Timings for the time-evolution of the TDSE using RHYthMIC (3D) for the Fourier method (upper part) and for the surface methods (middle and lower part). The grid parameters of each evolution are given in table 6.5.

than using a 5-point FD rule. As expected, the bigger difference with the PES of reference are the two spectra calculated with the coarse grid, set (III). With this set using a 5-point FD rule the PES of reference is overestimated, while using a 9-point FD rule is underestimated. We found that using a higher order FD rule it does not reduce the level of error in the calculation and actually underestimates our PES of reference. In this study we have not included a converged PES due to the size of the calculation using a grid spacing of $\Delta = 0.1$.

Finally, the performance of the different methods in 3D are shown in table 6.6. We can see that the computational cost of the Fourier method in 3D has increased dramatically with respect to the 2D case, from 35 core hours in 2D to 2208.27 core hours in 3D, an increase of resources of 6308 %, even though we have employed a larger grid spacing. For that reason more demanding and intensive calculations using the Fourier method are practically infeasible.

Regarding the Surface method, if we consider the same grid parameters as in the Fourier case, which corresponds to the grid Surface (I), the total resources decrease by one order of magnitude, 251.1 core hours, which corresponds to 88.62% less resource. If we use more points per processor (reducing the local computational workload), which corresponds to Surface (II),

Method	Points per core		No. cores		Grid spacing		Surface radius	Mesh extent		
	ρ	z	ρ	z	ρ	z		r_b	ρ_{\max}	z_{\max}
Surface	75	177	4	9	0.1	0.2	140	164.3	± 159.2	

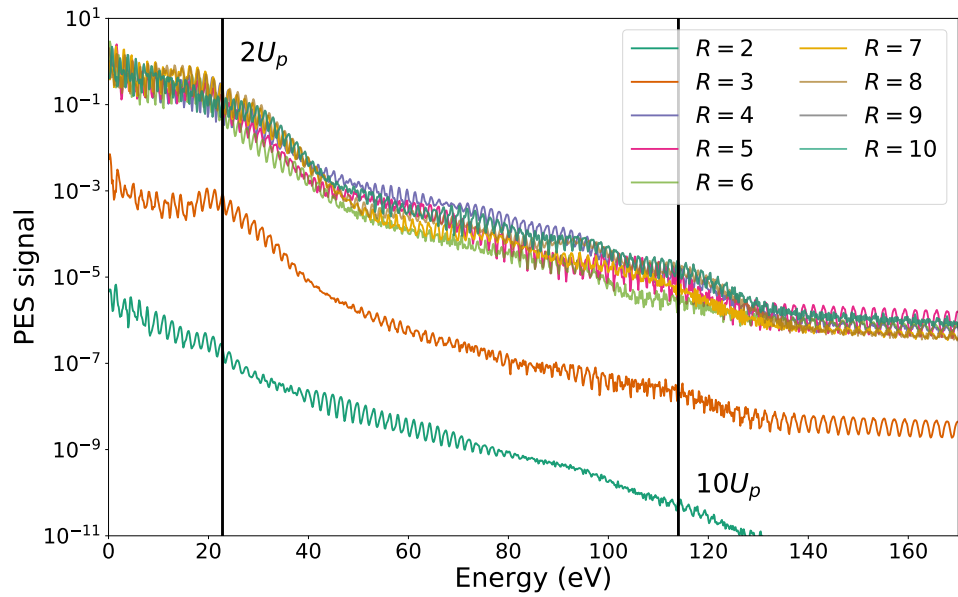
Table 6.7: Grid parameters employed for calculating the photoelectron spectra of H_2^+ after interacting with an intense, infrared 10-cycle laser pulse having $\lambda = 780$ nm and an intensity of $I = 2 \times 10^{14}$ W/cm². The PES is calculated in 2D using THeREMIN where we employ the t-SURFF method. The surface radius and the mesh extent for each set is given in atomic units.

we see an improvement in the computational cost, with the resources being 90.63% less than the Fourier method. If we finally consider the grid parameters in Surface (III), which uses a grid spacing of $\delta x = \delta y = \delta z = 0.2$ Bohr, comparable to the grid used in the 2D case, the total resources spent are 869,17 core hours. Even in this case, in which we employ a finer mesh, the computational gain is about 60.64% compared to the Fourier method.

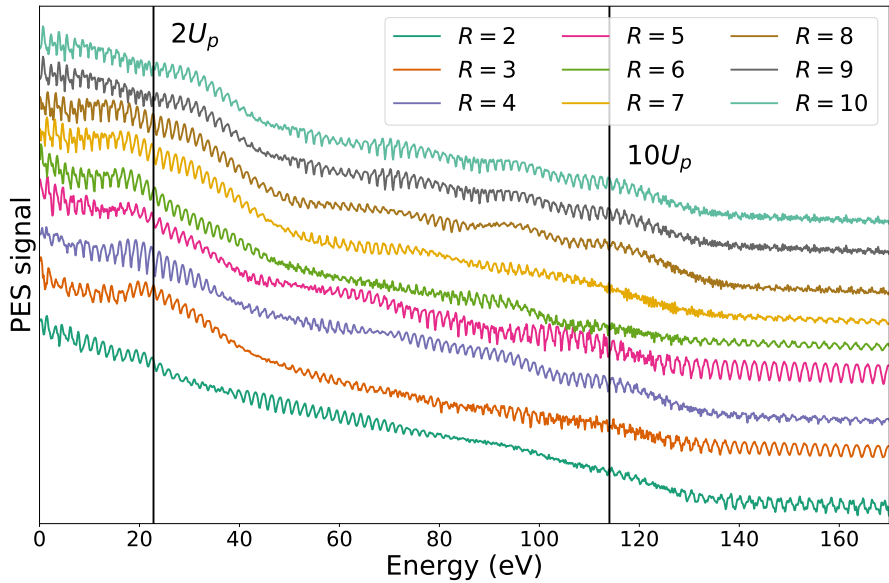
6.3 Photoelectron spectra in strong IR fields

In this section we calculate the photoelectron spectra of fixed-nuclei H_2^+ ionised by intense, infrared laser pulses. For these calculations we will only use the t-SURFF method, as it is the most accurate and computationally least expensive of the three methods considered. Consider H_2^+ interacting with a 10 cycle (26 fs of duration) linearly polarised laser pulse having wavelength $\lambda = 780$ nm and a peak intensity of $I = 2 \times 10^{14}$ W/cm². We consider the molecule aligned along the laser polarisation direction. These laser parameters are the same used in Section 4.2 when studying HHG. We calculate the PES at several fixed separations of the molecule ranging from $R = 2 a_0$ to $R = 10 a_0$, starting from the $1s\sigma_g$ ground state of the molecule. The grid parameters used for these calculations can be found in table 6.7. In these calculations we place the start of the Coulomb truncation region at $r_a = 130 a_0$ and the surface radius at $r_b = 140 a_0$. We interpolate onto a spherical surface with 101 θ -grid points. For integrating the surface flux Eq. 5.50 we include up to $l_{\max} = 25$ angular momenta in order to get converged results. We use an energy grid with a maximum energy of $E_{\max} = 8$ Ha, with an energy grid spacing of $\Delta E = 0.005$ Ha. To allow low energy electrons to cross the surface we propagate for 5 cycles after the end of the pulse. A time step of $\Delta t = 0.05$ au is used for the time evolution.

The results are presented in Figure 6.18, where for all calculations (presented in Figure 6.18a and for each internuclear distance separately in Figures 6.19, 6.20 and 6.21) we see a series of peaks at multiples of the laser frequency, a clear signature of above threshold ionisation (ATI) [66]. As we described in Section 1.2, the spectra present the characteristic low energy region, up to the cut-off at an energy $2U_p$ due to direct electrons, followed by a plateau region which extends up to an energy of $10U_p$ due to rescattered electrons. We also observe that, at

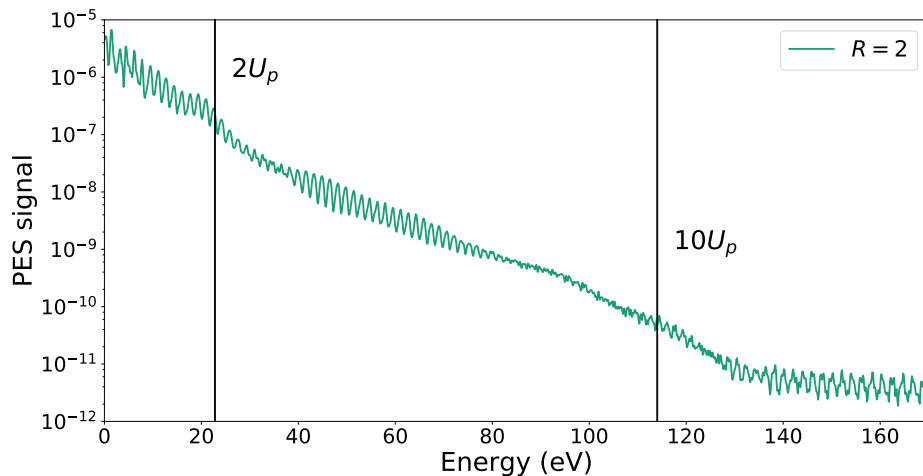


(a)

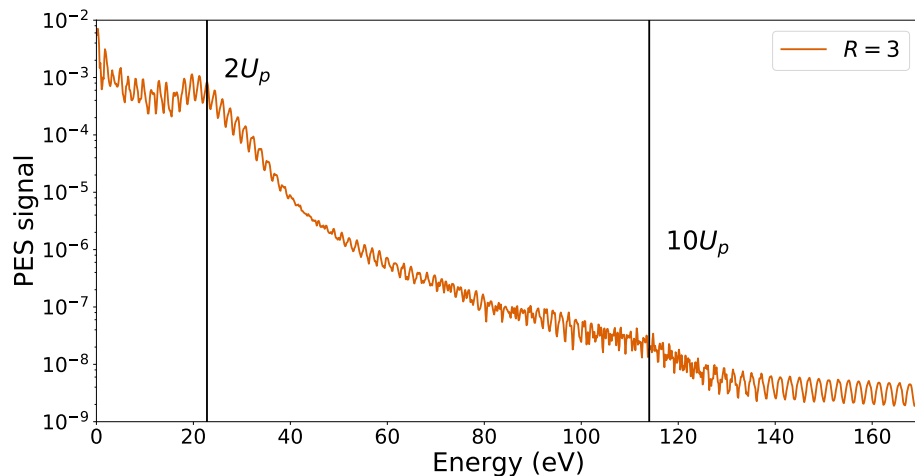


(b)

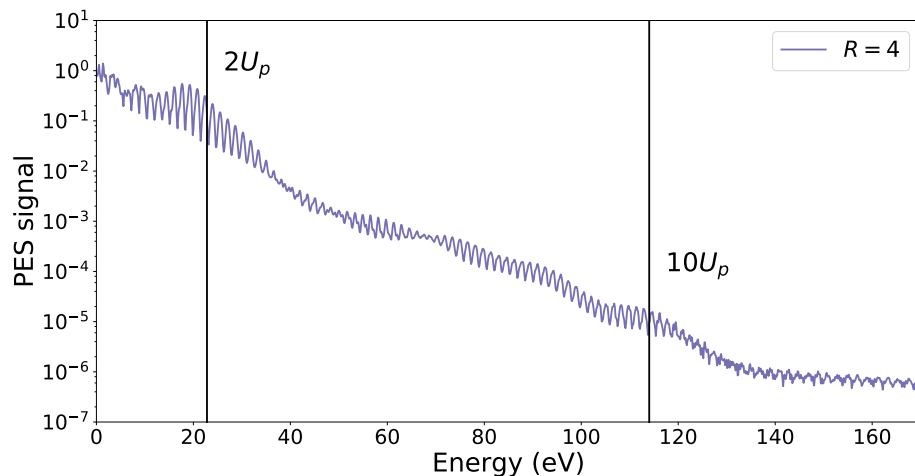
Figure 6.18: (a): Photoelectron spectra of photoionisation of fixed-nuclei H_2^+ with different internuclear distances, from $R = 2 a_0$ to $R = 10 a_0$, after interaction with a 10 cycle laser pulse having a wavelength of $\lambda = 780 \text{ nm}$ and a peak intensity of $I = 2 \times 10^{14} \text{ W/cm}^2$. In (b), we have sorted out vertically the PES for each internuclear distance in order to compare between them.



(a) $R = 2 a_0$

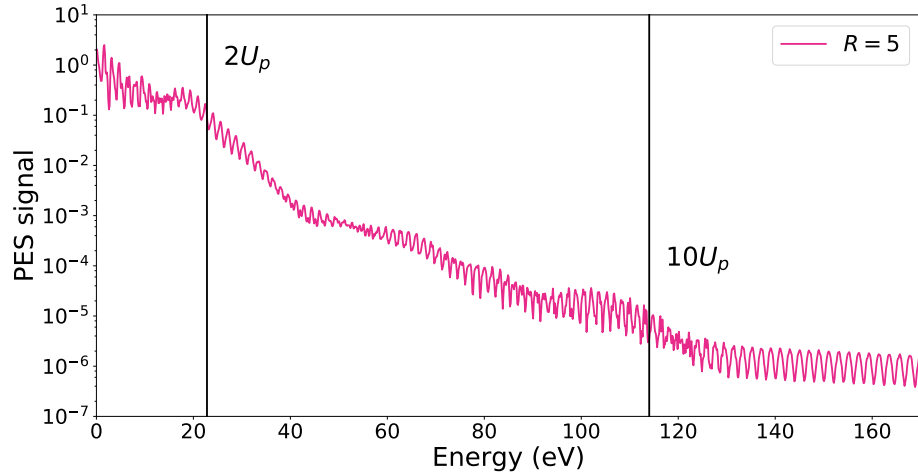


(b) $R = 3 a_0$

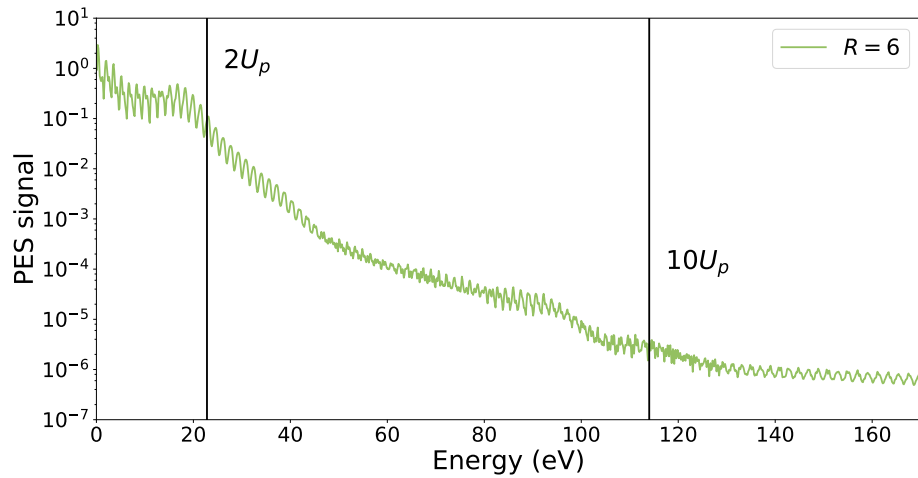


(c) $R = 4 a_0$

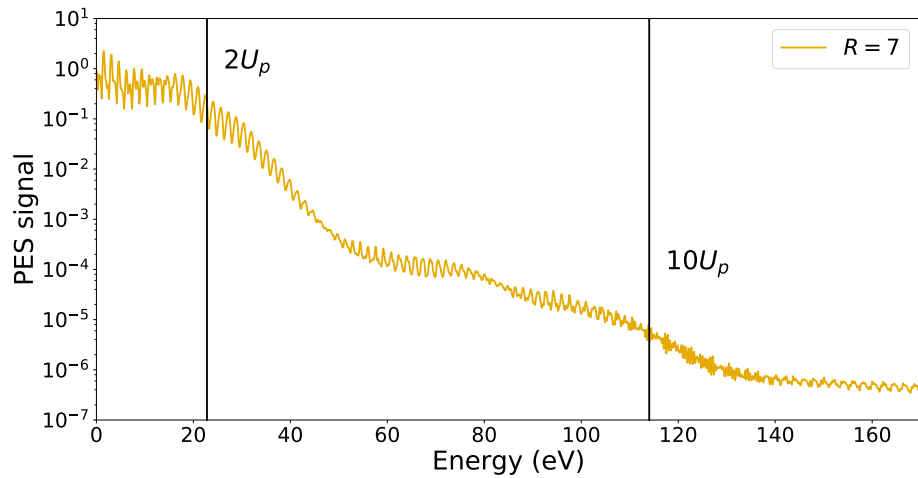
Figure 6.19: Photoelectron spectra for photoionisation of H_2^+ after interaction with a 10-cycle laser pulse having a wavelength of $\lambda = 780 \text{ nm}$ and a peak intensity of $I = 2 \times 10^{14} \text{ W/cm}^2$. On this figure we show the PES for internuclear distances of $R = 2 a_0$, $R = 3 a_0$ and $R = 4 a_0$. The solid black lines correspond to the $2U_p$ and $10U_p$ energy limits.



(a) $R = 5 a_0$

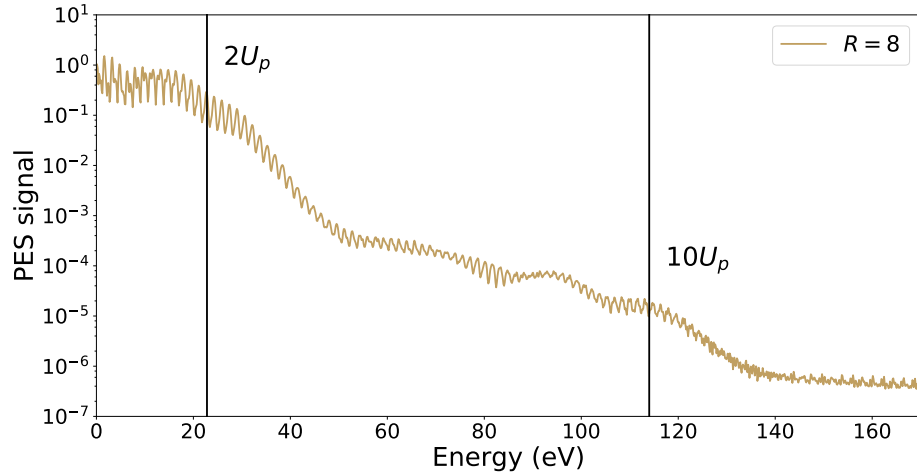


(b) $R = 6 a_0$

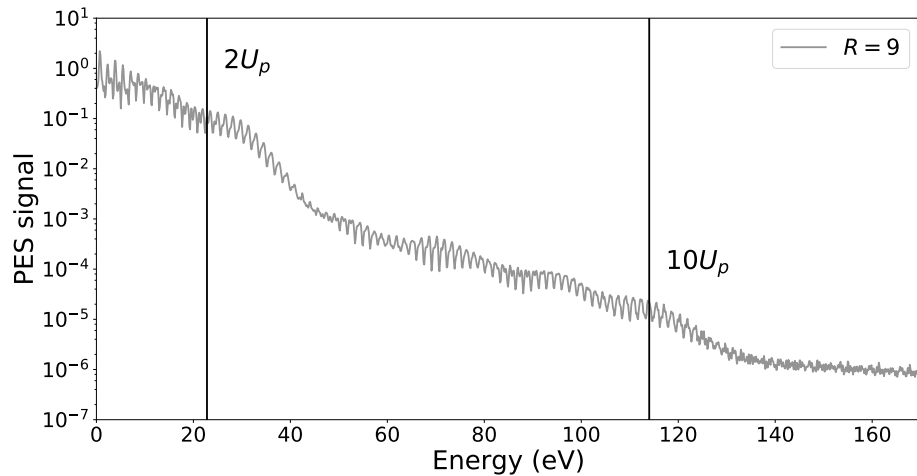


(c) $R = 7 a_0$

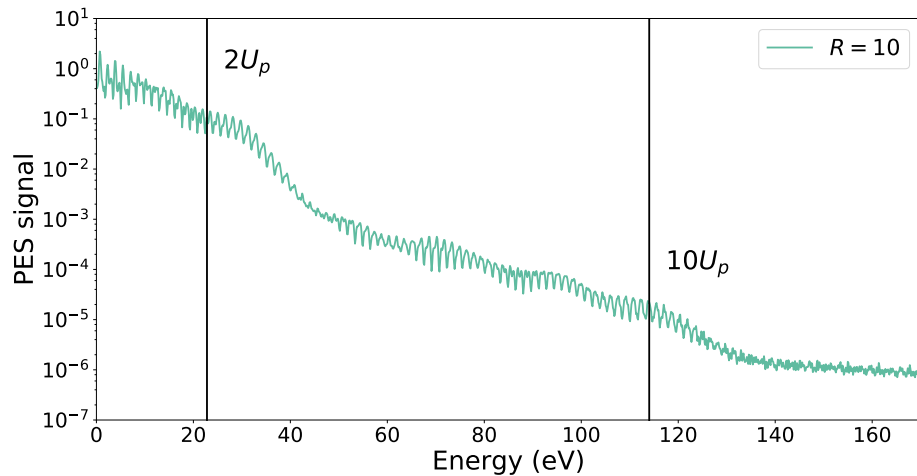
Figure 6.20: Photoelectron spectra for photoionisation of H_2^+ after interaction with a 10-cycle laser pulse having a wavelength of $\lambda = 780 \text{ nm}$ and a peak intensity of $I = 2 \times 10^{14} \text{ W/cm}^2$. On this figure we show the PES for internuclear distances of $R = 5 a_0$, $R = 6 a_0$ and $R = 7 a_0$. The solid black lines correspond to the $2U_p$ and $10U_p$ energy limits.



(a) $R = 8 a_0$



(b) $R = 9 a_0$



(c) $R = 10 a_0$

Figure 6.21: Photoelectron spectra for photoionisation of H_2^+ after interaction with a 10 cycle laser pulse having a wavelength of $\lambda = 780 \text{ nm}$ and a peak intensity of $I = 2 \times 10^{14} \text{ W/cm}^2$. On this figure we show the PES for internuclear distances of $R = 8 a_0$, $R = 9 a_0$ and $R = 10 a_0$. The solid black lines correspond to the $2U_p$ and $10U_p$ energy limits.

$R = 2 a_0$ (Figure 6.19a) and $R = 3 a_0$ (Figure 6.19b) the amplitude of the PES is respectively 6 and 2 orders of magnitude lower than for the rest of internuclear distances. These lower PES signals at $R = 2 a_0$ and $R = 3 a_0$ are due to high ionisation potentials at these internuclear distances which results in lower ionisation yields. Since the spectra for the other R values overlap, we spread these out vertically in Figure 6.18b.

In Figures 6.22, 6.23 and 6.24 we present angle-resolved photoelectron spectra for the different internuclear distances. The left hand plots present the full spectra up to an energy of 130 eV, whereas the right hand plots present the spectra for energies up to 40 eV. The white circles indicate the $2U_p$ and $10U_p$ cut-off's, which for these pulse characteristics are at energies 22.8 eV and 114.2 eV respectively. Note that different clamp values are used in each plot. In the low-energy region (up to $2U_p$) we observe a fan-like structure of radial stripes which are coming out from zero energy, and it clearly changes with the internuclear distance. This structure is related with the angular momentum of the final state and the minimum number of photons required to ionise the molecule [283, 284], i.e. changing the ionisation potential will change the number of photons required for ionisation. Therefore, as we increase the internuclear distance the ionisation potential I_p is lower, and more excess photons are absorbed from the field. Thus, when more excess photons are absorbed more radial stripes will be present in the fan-like structure.

Within the region up to $10U_p$, we can also observe rings whose centres are shifted along the polarisation axis (for instance, see Figure 6.23b). Those structures are due to rescattering [285], and their intensities are given by the electron-ion scattering differential cross-section [286]. We can isolate a single rescattering event by exposing the molecule to a 3-cycle (7.8 fs duration approximately) laser pulse with the same photon energy and intensity. The resulting PES is then shown in Figure 6.25 for $R = 2 a_0$. It is known that for few-cycle pulses the carrier envelope phase (CEP) plays a crucial role in ionisation [287]. In the left hand side we use a $\text{CEP} = 0$, which results in no rescattering, whereas in the right hand side we use a $\text{CEP} = -\pi/2$, which in this case results in only one rescattering event at the third cycle of the pulse.

One of the main characteristics of photoelectron spectra in diatomic molecules is the expected two-centre interference pattern. Two-centre interference phenomena have been studied in the context of high-harmonic generation diatomic molecules [146, 147, 288, 289], above-threshold ionisation [290, 291], and molecular imaging [292]. We point out that the two-centre interference minima in strong-field photoemission naturally arises within the SFA framework, as was firstly discussed by Becker and Faisal [293] using intense-field many-body S-matrix theory (IMST) for calculating ionisation rates for homonuclear molecules (N_2 and O_2). Later Hetzheim *et al.* [294] used standard SFA theory for studying interference effects in above-threshold ionisation (ATI) in diatomic molecules. Also, the Coulomb-Volkov distorted wave approximation has been employed by Ciappina *et al.* [295] for studying near-threshold ionisation. More

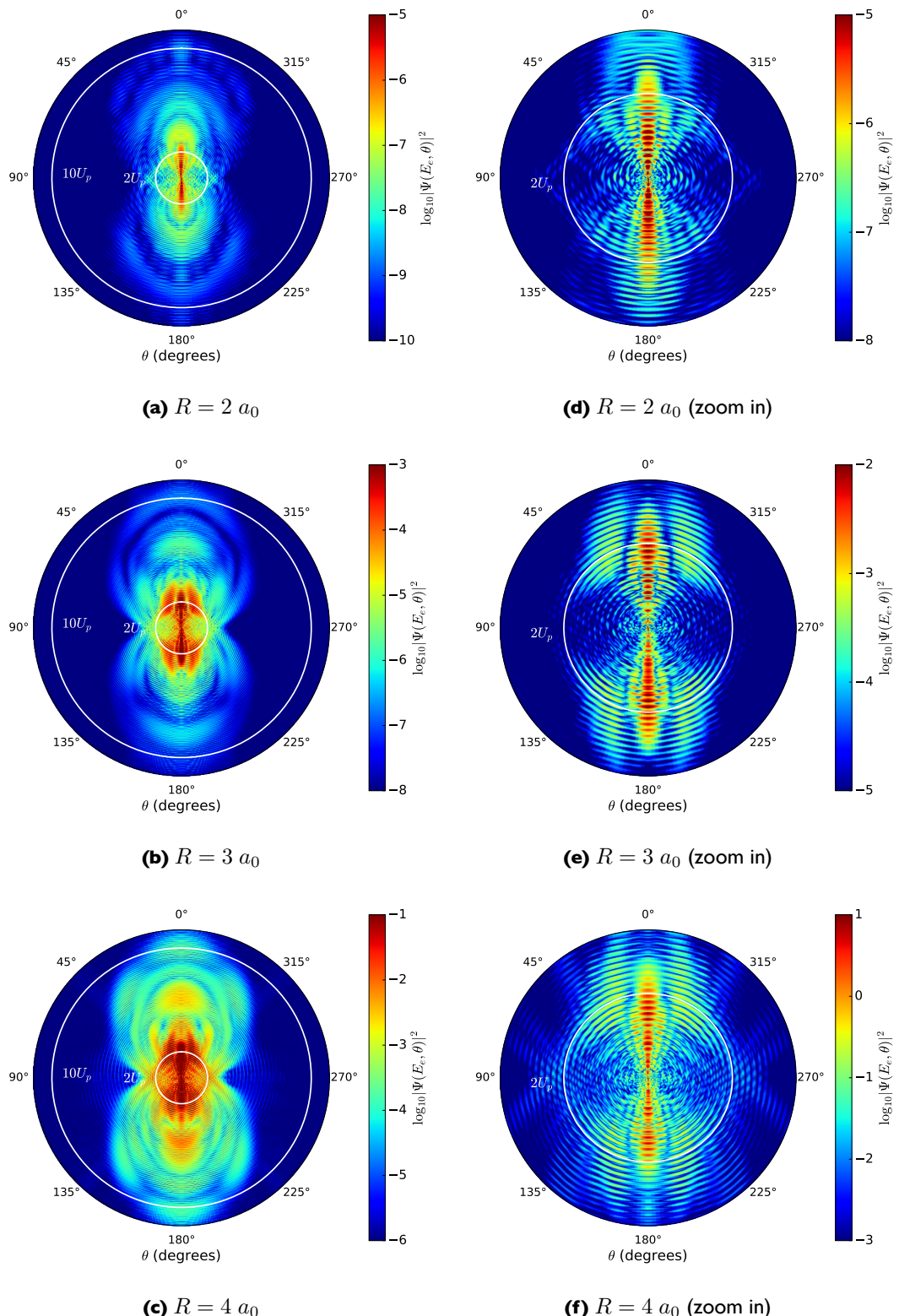


Figure 6.22: Angularly resolved photoelectron spectra for photoionisation of H_2^+ after interaction with a 10 cycle laser pulse having a wavelength of $\lambda = 780 \text{ nm}$ and a peak intensity of $I = 2 \times 10^{14} \text{ W/cm}^2$. On this figure we show PAD for internuclear distances of $R = 2 a_0$, $R = 3 a_0$ and $R = 4 a_0$. The left hand side shows a general view of the PAD up to $10U_p$, whereas in the right panels we show a zoom in up to $2U_p$ of the left hand side.

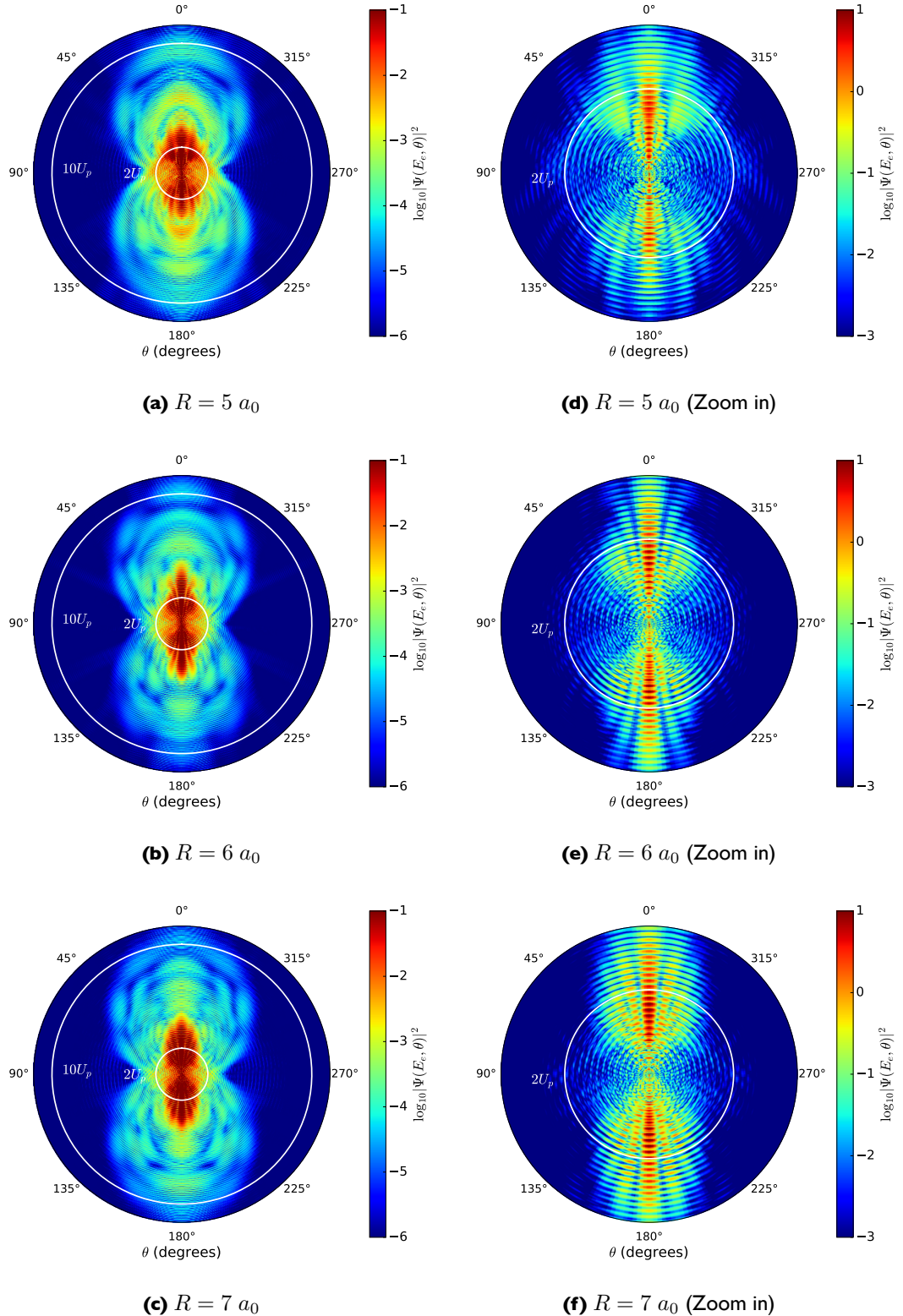


Figure 6.23: The same as in Figure 6.22. On this figure we show PAD for internuclear distances of $R = 5 a_0$, $R = 6 a_0$ and $R = 7 a_0$ Bohr. The left hand side shows a general view of the PAD up to $10U_p$, whereas in the right panels we show a zoom in up to $2U_p$ of the left hand side.

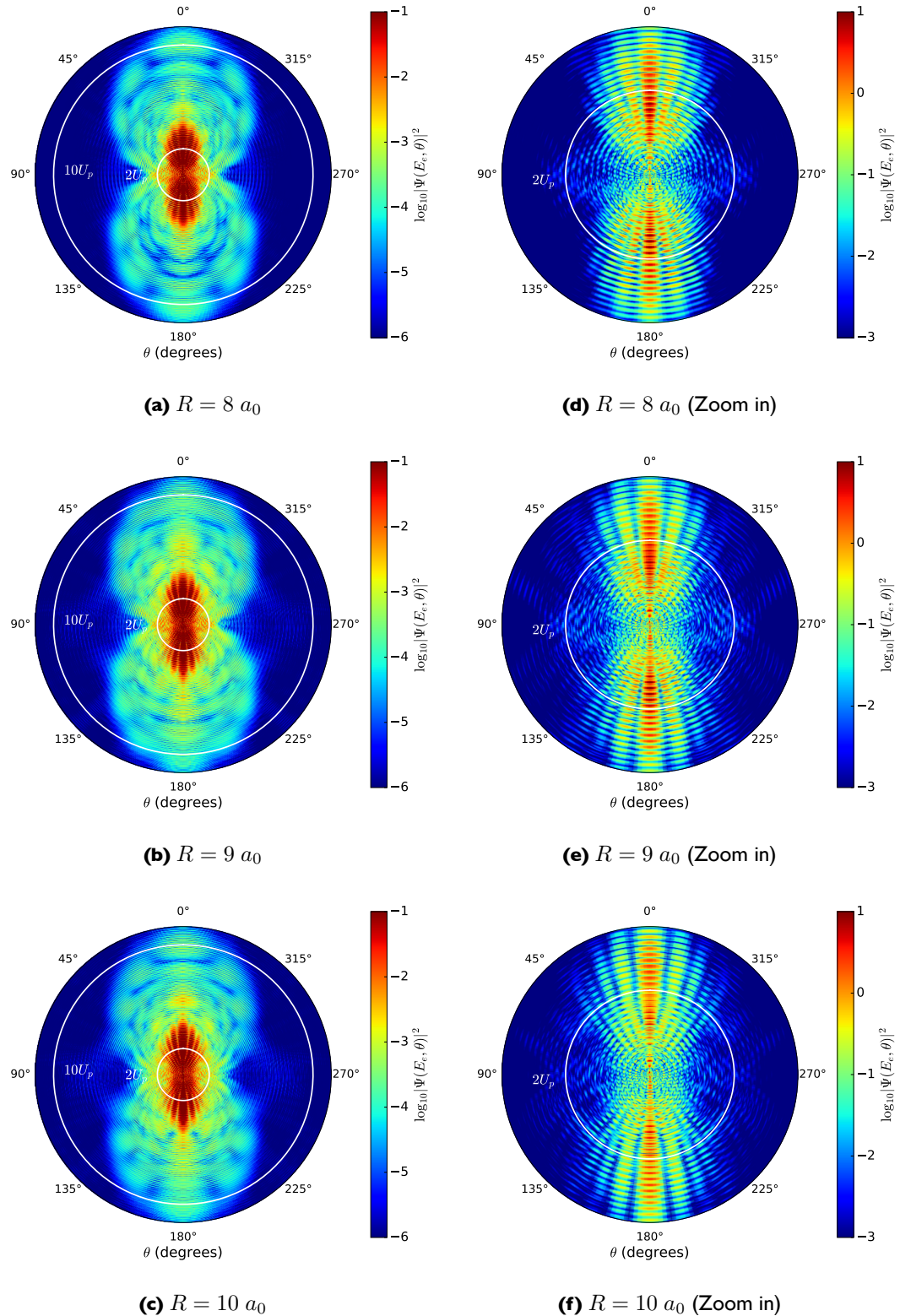


Figure 6.24: The same as in Figure 6.22 and Figure 6.23. On this figure we show PAD for internuclear distances of $R = 8 a_0$, $R = 9 a_0$ and $R = 10 a_0$ Bohr. The left hand side shows a region of the PAD up to 130 eV, whereas in the right panels we show a zoom in of the left hand side panels within a region of 40 eV.

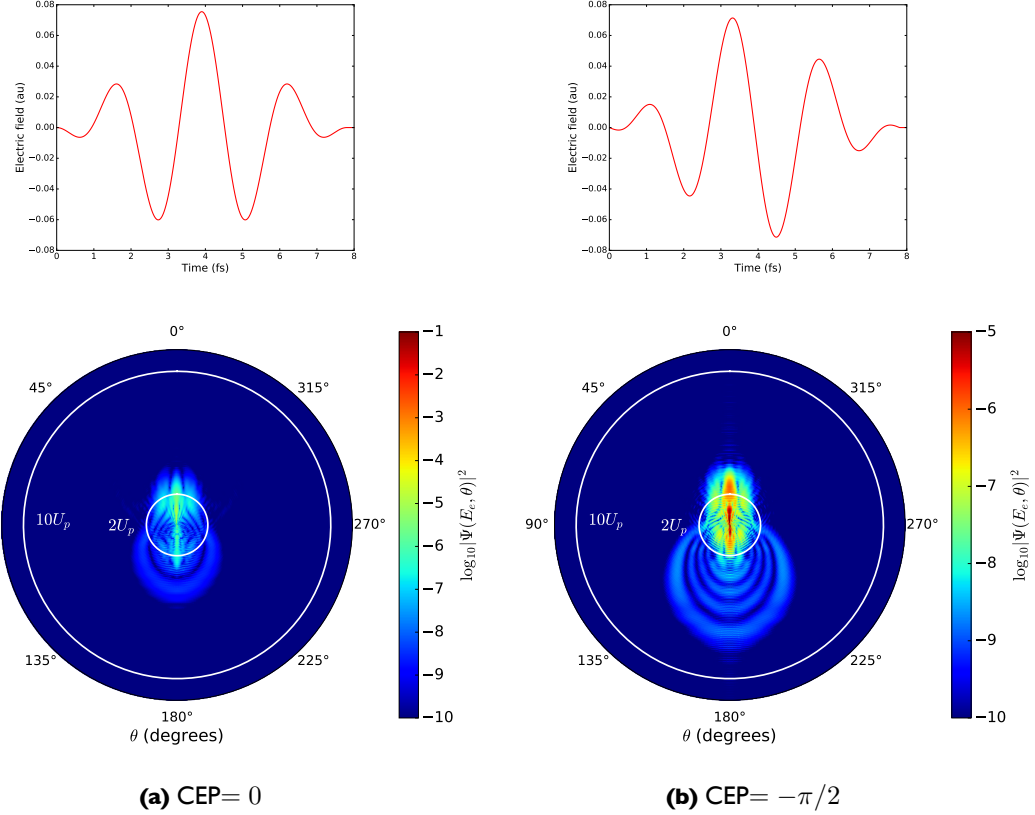


Figure 6.25: Angularly resolved PES for photoionisation of fixed-nuclei H_2^+ at $R = 2 a_0$, exposed to 3-cycle 780 nm laser pulse at $I = 2 \times 10^{14} \text{ W/cm}^2$. The lower panel on the left hand side corresponds to a pulse with $\text{CEP} = 0$, whereas the lower panel on the right hand side corresponds to a pulse with $\text{CEP} = -\pi/2$. In the upper panels the corresponding temporal profile of the electric field are shown.

recently Suárez *et al.* [296] have used a generalised SFA theory for calculating ATI spectra of diatomic molecules. The ionisation rate for a homonuclear diatomic molecule in a linearly polarised field with N_e equivalent electrons is [293]

$$\Gamma^+ = N_e \sum_{N=N_0}^{\infty} \int d\mathbf{k}_N \sigma_{\text{at}}^N(\mathbf{k}_N) \times 4 \begin{cases} \cos^2(\mathbf{k}_N \cdot \mathbf{R}/2) & \text{for bonding} \\ \sin^2(\mathbf{k}_N \cdot \mathbf{R}/2) & \text{for antibonding} \end{cases} \quad (6.8)$$

where \mathbf{k}_N is the electron momentum after absorption of N photons, $\sigma_{\text{at}}^N(\mathbf{k}_N)$ is the N -photon cross section of the atomic species, and \mathbf{R} is the internuclear axis vector. Thus Eq. 6.8 can be understood as an atomic ionisation rate with a trigonometric term that takes into account the interference due to electron emission from one of the two nuclei. In case of ionisation of electrons from molecular orbitals with bonding symmetry we have a sine term. For electrons with low momenta (small values of \mathbf{k}_N) this gives a destructive interference since

$$\sin(\mathbf{k}_N \cdot \mathbf{R}/2) \ll 1. \quad (6.9)$$

Alternatively, for ionisation from molecular orbitals with anti-bonding symmetry we have a

cosine term. Again, for low momenta electrons this gives a constructive interference since

$$\cos(\mathbf{k}_N \cdot \mathbf{R}/2) \approx 1. \quad (6.10)$$

By considering Eq.6.8 for bounding symmetry, the interference minima should appear when

$$\mathbf{k} \cdot \mathbf{R} = (2n + 1)\pi \quad \text{for } n = 0, 1, 2, \dots \quad (6.11)$$

where \mathbf{k} is the electron momentum and \mathbf{R} the internuclear axis. In spherical coordinates, we can write Eq. (6.11) as

$$kR \cos \theta = (2n + 1)\pi \quad \text{for } n = 0, 1, 2, \dots \quad (6.12)$$

where θ is the angle between the molecular axis and the electron momentum vector. If we only consider electrons travelling along the $z = 0$ axis, the formula reduces to

$$k_e \cdot R = (2n + 1)\pi \quad \text{for } n = 0, 1, 2, \dots \quad (6.13)$$

Thus, the minima should appear at energies

$$E = \frac{(2n + 1)^2 \pi^2}{2R^2} \quad \text{for } n = 0, 1, 2, \dots \quad (6.14)$$

In order to see the angular dependence of Eq. (6.13), the two-centre interference present in the angle-resolved PES of H_2^+ shown in Figure 6.26, where we only consider the molecule with their internuclear distance fixed to $R = 6 a_0$. We exposed again the molecule to a 10-cycle laser pulse as before, having a wavelength of $\lambda = 780 \text{ nm}$ and a peak intensity of $I = 2 \times 10^{14} \text{ W/cm}^2$. The grid parameters used in this calculation are the same as those given in table 6.7. The first three orders of the expected energy minima at this internuclear distance for electrons emitted at different directions are given in table 6.8. The white lines drawn over the plot in Figure 6.26 represent those energies in the case that the electron is emitted along the $z = 0$ axis. In this case, we see that the minima for $n = 0$ is not appreciable from the density plot. For $n = 1$, the minima is considerably shifted to higher energies with respect to the expected one, about 30 eV. Regarding the minima for $n = 2$, the minima is still shifted, but the shift in this case, around 11 eV, is smaller compared to the $n = 1$ case.

n	$\theta = 0^\circ$	$\theta = 30.30^\circ$	$\theta = 59.24^\circ$	$\theta = 90^\circ$
0	3.73	5.00	14.26	-
1	33.57	45.03	128.38	-
2	93.25	125.09	356.63	-

Table 6.8: Energies for the two-centre interference minima calculated from Eq. (6.14) for different electrons emission directions. θ corresponds to angle between the molecular axis and the electron momentum vector. The molecule has a fixed internuclear of $R = 6 \text{ Bohr}$.

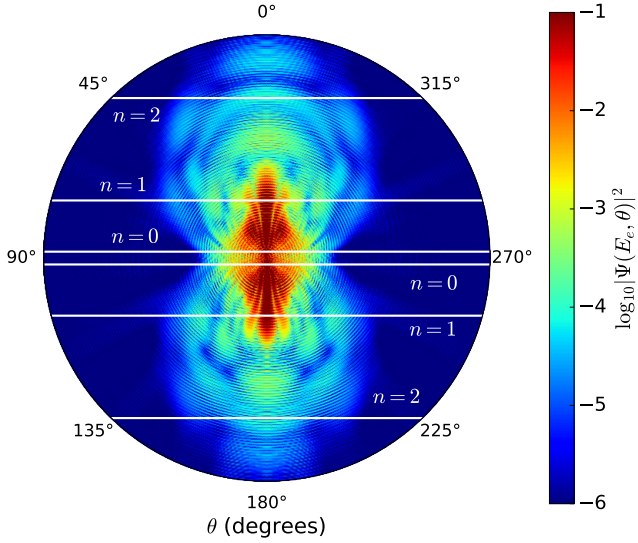


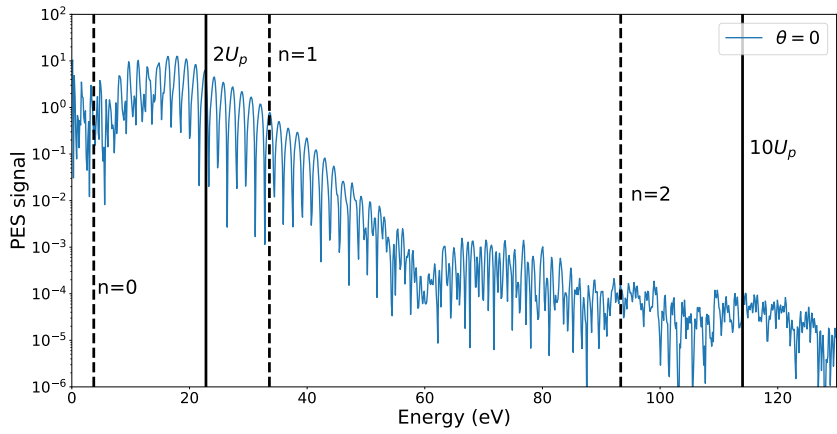
Figure 6.26: Angularly resolved PES for photoionisation of fixed-nuclei H_2^+ at $R = 6 \text{ } a_0$, exposed to 10-cycle 780 nm laser pulse at $I = 2 \times 10^{14} \text{ W/cm}^2$. The horizontal white lines represent the expected two-centre interference energy minima predicted by Eq. (6.14) for the case of $\theta = 0^\circ$, where the electrons are ejected along the molecular axis.

The origin of the disagreement between the predicted and the calculated interference energy minima is explained since Eq. 6.8 only considers direct ionisation of electrons, and does not take into account ionisation due to rescattering electrons. Indeed, the PES posses contributions coming from electrons that are ionised from one ion and rescatters off the other. These contributions are not proportional to the cosine term, therefore the interference structure is mostly suppressed in the plateau region [294].

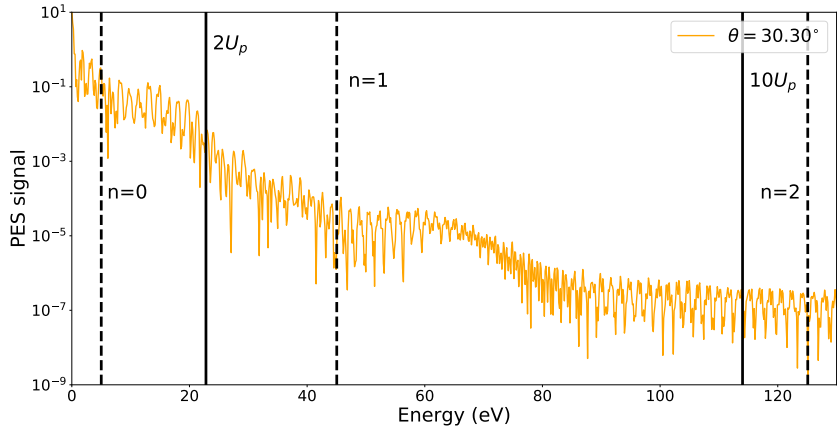
However, in the low-energy region the interference is clearly appreciable, since this region is due to direct electrons drifted by the electric field after tunnel ionisation from the molecule. In Figure 6.27 and 6.28 we extract from Figure 6.26 the PES for four different directions of electron emission: $\theta = 0^\circ$, $\theta = 30.30^\circ$, $\theta = 59.24^\circ$ and $\theta = 90^\circ$, where the angles correspond to a particular grid point of the θ coordinate. It is visible that the energy minimum for $n = 0$ for $\theta = 0^\circ$, $\theta = 30.30^\circ$ and $\theta = 59.24^\circ$ coincides with the expected minimum, a feature that it is hard to see in the density colour plots in Figure 6.26. In case of electrons ejected perpendicularly to the molecular axis, Eq. (6.14) does not predict any minimum energy, as we can see the Figure 6.28.

6.4 Summary

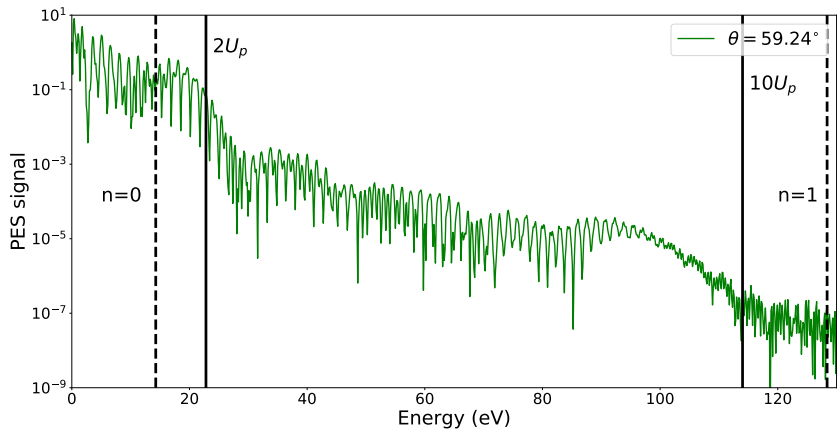
In this chapter, Sections 6.1 and 6.2 have been dedicated to the discussion of the performance of the different methods to calculate the photoelectron spectrum implemented in the library `POpSiCLE`. For these tests, we have exposed the hydrogen molecular ion to a ultra short VUV laser pulse of approximately 1 fs of duration. We have kept the peak laser intensity low enough



(a) $\theta = 0^\circ$



(b) $\theta = 30.30^\circ$



(c) $\theta = 59.20^\circ$

Figure 6.27: PES for a particular electron emission of H_2^+ after interaction with a 10-cycle laser pulse having a wavelength of $\lambda = 780 \text{ nm}$, and a peak intensity of $I = 2 \times 10^{14} \text{ W/cm}^2$. The plots corresponds to: (a) $\theta = 0^\circ$, (b) $\theta = 30.30^\circ$, (c) $\theta = 59.20^\circ$, where θ is the angle of electron emission with respect to the molecular axis. The solid lines indicate the $2U_p$ and the $10U_p$ thresholds respectively. The energy minima for each emission angle are represented by dashed lines, and can be found in table 6.8.

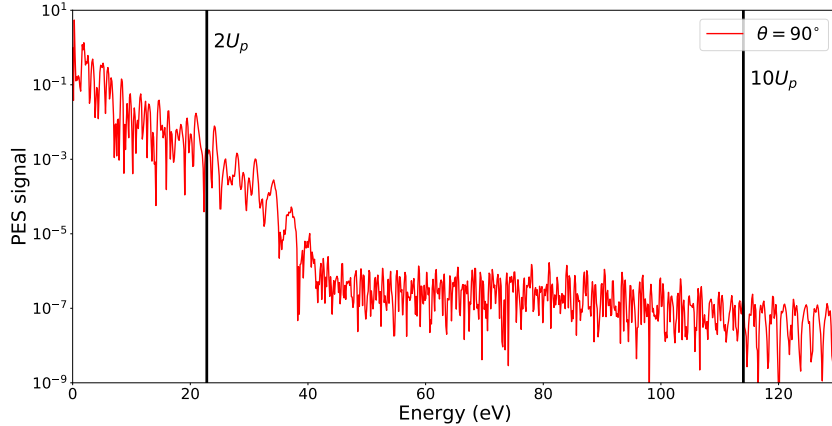


Figure 6.28: PES for a particular electron emission of H_2^+ after interaction with a 10-cycle laser pulse having a wavelength of $\lambda = 780 \text{ nm}$, and a peak intensity of $I = 2 \times 10^{14} \text{ W/cm}^2$. The plots corresponds to $\theta = 90^\circ$, where θ is the angle of electron emission with respect to the molecular axis. The solid lines indicate the $2U_p$ and the $10U_p$ thresholds respectively. The energy minima for this emission angle are represented by dashed lines, and can be found in table 6.8.

so we can compare our results with previous results available in the literature. In these calculations we have considered the molecule with their nuclei frozen, with an internuclear distance of $R = 2 a_0$, starting from the $1s\sigma_g$ ground state.

Firstly, in Section 6.1, we have presented results obtained in 2D using the THeREMIN code to propagate the TDSE. Projections of the probability density at the end of the time evolution have been shown. Using the Fourier method, scattering amplitudes were extracted from the wavefunction at the end of the calculation, where a masking function was used to remove the bound states of the molecule. Projections of the probability density in coordinate and momentum space were presented. In order to test the accuracy of the Fourier method, we have shown the dependence of the PES on the time step used for the time evolution. Also, the influence of the Coulomb potential in the resulting PES have been studied. As it was explained in the previous chapter, the Fourier method assumes that the scattering amplitudes can be obtained by projecting onto field-free scattering states, i.e. plane waves. Hence, the long range potential introduces an overestimation of the energies in the spectrum. For longer propagation times after the end of the pulse this overestimation is progressively reduced, because the ionised wavepacket is able to travel to regions where the Coulomb potential is negligible. However, truncating the Coulomb potential at a certain radius allows the PES to converge to the correct energies. For the surface methods, the sampling point and the t-SURFF methods, the PES obtained from wavefunction values at different surface radius were presented. It was shown that the sampling point method is not able to obtain the correct scattering amplitudes, although if the spectrum is multiplied by a factor that corresponds to the volume element in spherical coordinates, the correct amplitudes are reproduced. We found very good agreement between the different methods when the truncated Coulomb potential is introduced. After comparing the angularly resolved photoelectron spectra calculated using the three methods, the section ends by comparing the total cross sections obtained using the t-SURFF method with a total cross

sections calculated with low order perturbation theory, where good agreement was found. The computational cost of the PES calculation using the surface methods (sampling point and t-SURFF methods) is greatly reduced compared with the Fourier method, because the use of smaller grid sizes allow the reduction of core hours required from 89% to 92%, depending on the grid parameters.

Secondly, in Section 6.2, we have presented results obtained in 3D using the RHYthMIC code, which implements the solution of the TDSE in Cartesian coordinates. In order to reduce the computational cost of these three dimensional calculations, we have study the accuracy of the PES employing coarse grid spacings. We found agreement between the PES calculated with the sampling point and the t-SURFF methods, although we see that the PES obtained with the Fourier method is overestimated. We also found that increasing the order of the finite-difference derivative operators while keeping a coarse grid spacing does not reduce the level of error and even underestimates the PES. The computational cost of calculating the PES using the Fourier method in 3D is considerable larger than the 2D case, with an increase of resources of 6308%. Employing the surface methods can reduce from 60.64% to 90.63% the total core hours required for calculating the PES, depending of the grid parameters used.

Lastly, we have presented results of photoelectron spectrum for H_2^+ ionised by an IR laser pulse. In our calculations we have calculated the PES at several internuclear distances, ranging from $R = 2 a_0$ to $R = 10 a_0$. For all the internuclear distances considered, we can see the main features that corresponds to above-threshold ionisation in the resulting PES. We also see that the PES amplitude is significantly lower for $R = 2 a_0$ and $R = 3 a_0$, 6 and 2 orders of magnitude approximately, than the rest of internuclear distances. The difference in amplitude is due to the higher ionisation potential for smaller internuclear distances. In addition, we present angularly resolved PES for the range of internuclear distances considered, where we can observe a fan-like structure within the low-energy region (up to $2U_p$), which changes with the internuclear distance. This structure is due to the angular momentum of the final state, and it is related with the ionisation potential, which changes with the internuclear distance of the molecule. Also, we observe a series of rings centred along the polarisation axis. Those rings are due to rescattering. In order to study the origin of these rings, we have isolated a single rescattering event by exposing the molecule to a 3-cycle laser pulse. For a CEP=0, almost no rescattering occurs, while for CEP=− $\pi/2$ we obtain one rescattering event, which yields to a clean ring structure centred at only one of the ions. Two-centre interference is discuss in the angular resolved PES. We found that the interference minima are shifted, or even suppressed, in the plateau region, while they are present in the low-energy region. This suppression of the interference is due to several contributions to the spectra, coming from electrons that do not scatter from the same ion that they were ejected from.

Conclusions and future work

Conclusions

In this thesis we have studied the hydrogen molecular ion irradiated by intense, ultra short laser pulses, including both electron and ionic degrees of freedom quantum mechanically. In particular we have focused on the role of the vibrational states in ionisation, dissociation and high harmonic generation in H_2^+ , and in the efficient calculation of the photoelectron spectra from time-dependent numerical calculations.

In Chapter 1, an overview of the progress in laser technology over the last several decades was given. From the Q-Switched oscillator to the chirped-pulse amplification technique, advances in laser amplification made the development of intense, short laser pulses possible. Higher laser intensities led to the discovery of strong field physics processes: tunnel ionisation, over-the-barrier ionisation, multiphoton ionisation, above-threshold ionisation and high-harmonic generation. The understanding of these processes led to the production of attosecond laser pulses, which paved the way to the new field of attosecond science. The last section of the chapter was dedicated to a review of recent experiments which laid the foundations of ultrafast molecular science. Among these experiments we can cite charge migration in biomolecules, observation of ultrafast nuclear dynamics using HHG spectroscopy and attosecond molecular charge control in small molecules such as H_2^+ . In most studies that treat electronic ultrafast dynamics in large molecules, the nuclear dynamics are usually neglected, due to the complexity and the computational cost of such descriptions. Indeed the simultaneous description of electronic and ionic degrees of freedom is only possible for small molecules, such as H_2^+ and H_2 . Understanding electron-ion correlations in small molecules will serve as a platform to understand more complex behaviour in larger molecules.

In Chapter 2, we presented our theoretical treatment of the hydrogen molecular ion. The model treats electronic and ionic degrees of freedom quantum mechanically. To efficiently implement solutions of the TDSE, a Lagrangian formalism is introduced, which allows us to use generalised curvilinear coordinates. In Chapter 3, details of the numerical implementation of our H_2^+ model was given. This has resulted in the development of two computer codes: a code that implements the solution of the TDSE in cylindrical coordinates, named **THeREMIN** (vibraTing HydRogEn Molecular IoN), and another code that implements the solution of the TDSE in Cartesian coordinates, named **RHYthMIC** (vibRating HYdrogen Molecular Ion in Cartesians). Our model is based on finite-difference techniques to solve the time-dependent Schrödinger

equation that can be parallelised for massively parallel supercomputers. The benefit of using the generalised curvilinear coordinates introduced in Chapter 2 is that they allow for a high density of grid points in particular regions of space in order to improve the accuracy of the calculations. In the case of Cartesian coordinates, the Coulomb potential is obtained by solving the Poisson equation, since the coincidence of one of the grid points with an ion leads to a singularity on the grid when directly evaluating the potential. The parallelisation scheme employed to calculate the Laplacian operator over several processors, called boundary swapping, only involves communication between neighbouring processors, minimising the communication overhead. When increasing the number of processors, for THeREMIN code calculation time increased by 10% when increasing from 888 to 2590 the number of processors, while for RHYthMIC calculation time increased by only 5% when increasing from 1134 to 18522 processors.

Chapter 4 was dedicated to the study of the role of vibrational states in ionisation, dissociation and high-harmonic generation in H_2^+ . The accuracy of our model was tested, obtaining very good agreement with previous results available in the literature. Indeed the largest difference between vibrational energies calculated using our implementation with previously published results is less than 1%. A study based on a visual analysis of the wavefunction was carried out for the molecule exposed to an ultra-short VUV laser pulse. This pulse was chosen to lie in the multiphoton regime, and calculations starting from either the $1s\sigma_g(\nu = 0)$ or $1s\sigma_g(\nu = 2)$ vibrational states were performed. The analysis of the electron probability density during the simulations reveals two dissociating wavepackets, whose spatial width can be related to the bandwidth of the incident pulse. A classical calculation of the trajectories of the dissociating wavepacket on either $1s\sigma_g$ or $3s\sigma_g$ potential energy surfaces is in good agreement with our results. Also, the visual analysis showed that the vibrational structure of the molecule is imprinted to the dissociating nuclear wavepackets.

Further investigation on the interplay of the vibrational states was carried out by dividing configuration space into distinct regions and integrating the probability density in each region. Thus, ionisation and dissociation yields were obtained for calculations starting from different initial vibrational states. After comparing these yields, we also compared two yields defined as follows. The first yield was extracted from a calculation in which a linear combination of vibrational states multiplied by their correspondent Franck-Condon factors was chosen as the initial state: we called this the FC initial state. The second yield was obtained from the incoherent sum (denoted IS) of the yields obtained by starting particular vibrational states. We found that for the case of the FC initial state, dissociation starts later than in the IS suggesting that the coherent combination of vibrational states prevents dissociation. In addition, the dissociation yield corresponding to the FC initial state presents a hump, indicating an intermediate resonant state that it is not taken into account in the IS case.

We extend the study of vibrational states by considering the interaction of H_2^+ with a strong IR laser pulse, whose laser parameters as such that tunnelling ionisation is expected. In the

case of infrared fields the photon energy is similar to the energy gap between vibrational states, and so interaction of pulse leads to ionisation and vibrational excitation prior to dissociation of the molecule. Ionisation yields showed that, in contrast to the fixed nuclei case, more than one ionisation event occur per half-cycle, this phenomena has been called multiple ionisation bursts [249]. Also, higher vibrational states result in larger ionisation yields due to charge-enhanced resonant ionisation (CREI). This establishes an ionisation rate dependency on the internuclear distance. A particular characteristic of high harmonic spectra for small vibrating molecules, such as H_2^+ , is the production of not only odd but even harmonics. This is due to electron localisation induced by IR fields, which creates a permanent dipole. Thus, the breaking of the molecular symmetry yields the production of even harmonics. Another characteristic of the HHG spectra of H_2^+ is the reduction of the cut-off. This effect is due to a modification of the electronic states at which the ionised electrons recollide, and it is caused by nuclear motion. Indeed, the reduction can be described by a function resulting from the autocorrelation between the initial and the time-dependent nuclear wavefunction [257].

In Chapters 5 and 6 we introduced three methods for extracting the photoelectron spectra from solutions of the TDSE. The methods, namely the Fourier method, the sampling point method and the t-SURFF method were introduced. A library which efficiently implements the methods was developed, especially designed for massively parallel supercomputers. The Fourier method extracted the scattering amplitudes from the Fourier transform of the wavefunction: this is computationally the most expensive of the methods. The sampling point and the t-SURFF methods are based on recording the outgoing flux of ionised electrons over a surface during the time evolution. The main difference between these two methods is that the t-SURFF method gives the correct spectral magnitudes. Spherical coordinates are the most natural coordinate system to implement the sampling point and the t-SURFF methods. However, since many of the existing codes, including the codes developed in this thesis, implements the solution of the TDSE in other coordinate systems, our numerical implementation includes routines to interpolate wavefunction values onto a spherical shell in 2D and 3D. Thus, an efficient interpolation method is required, since the acquisition of the wavefunction over the surface is repeated multiple times during propagation. In contrast, the Fourier method only requires the Fourier transform of the wavefunction in configuration space at the end of the time evolution. However, this can be an arduous task since in typical calculations the wavefunction can be several gigabytes in size. For this reason the routines that implement the Fourier transform were parallelised.

In Chapter 6 we compared the results and performance of the photoelectron spectra obtained using the three methods when irradiating H_2^+ with VUV laser pulses. It was found that the accuracy of the t-SURFF method is greater, because the Fourier method overestimates the PES, due to the long range tail of the Coulomb potential, and the sampling point method does not give the correct scattering amplitudes because it does not take into account any volume element when integrating the flux. Although there are ways to overcome these problems for the Fourier method and the sampling point method, the t-SURFF method is still superior due

to its greater efficiency: it allows a computational reduction of approximately 92% in 2D, and 90.63% in 3D. We also presented angularly resolved PES for H_2^+ exposed to intense IR fields. In these spectra the main characteristics of ATI are clearly visible. In addition, signatures of two-centre interference are found, where minima of the spectral amplitude is found at certain energies. The minima in the spectra is caused by an interference between direct ionisation of electrons that are ejected from one of the two nuclei. Hence the interference is only visible in the low energy region, up to $2U_p$, and is suppressed in the plateau region, where the contribution from electrons that ionise from rescatter off the other ion wash out the interference.

Future Work

We now end this thesis by discussing how the work presented can be extended to study correlated electron-ion dynamics in the hydrogen molecular ion in more detail.

We have seen that including ionic degrees of freedom in the description of H_2^+ exposed to intense, ultra-short laser pulses is required for a realistic representation of ultrafast dynamics in H_2^+ . Processes such as vibrational excitation and dissociation by infrared fields, the production of even and odd harmonics or the reduction of the cut-off frequency in HHG can not be understood without nuclear motion. For instance, the nuclear motion can modify the high harmonic spectrum produced from H_2^+ , generating odd and even harmonics, or modifying the electronic states where the electrons can recombine. We now can investigate the effect of these processes on the spatio-temporal characteristics of the coherent radiation produced from HHG.

However, in order to study the results presented in Chapter 4 in more detail, an efficient tool is required to extract observables from the wavefunction. After showing the accuracy and performance of the `P0pSiCLE` library in the spectra presented in Chapter 6 for fixed nuclei calculations, we can consider the calculation of correlated electron-ion spectra using the current implementation of the library as an additional step in our investigation. In particular, joint electron-ion spectra are required for a deeper analysis of the mechanisms triggered by IR laser pulses, where the interplay of processes such vibrational excitation, ionisation and dissociation adds additional complexity to the problem. In principle, the developed library can be used to calculate the correlated photoelectron spectrum and kinetic energy release spectrum from pump-probe experiments in which the pump pulse prepares the molecule in a particular combination of vibrational states. In this case, experiments which include electronic and nuclear degrees of freedom would required a considerable computational effort, thus a numerical tool, such as `P0pSiCLE`, which allow us to reduce the size of the calculations is mandatory.

Differential (in proton and electron energy) ionisation cross sections have been theoretically obtained for H_2^+ [120] and H_2 [192] irradiated by laser fields whose polarisation axis is parallel to the molecular axis. Those studies showed that including the vibrational motion of the molecule it is possible to control the ratio between dissociative and non-dissociative

ionisation. However, all the available work that uses circularly or elliptically polarised fields has been performed within the fixed nuclei approximation. In this approximation, linearly polarised laser pulses oriented parallel to the molecular axis excite σ_u/σ_u states ($\Delta M = 0$), whereas perpendicular oriented pulses populate π_u states after one-photon absorption ($\Delta M = \pm 1$) and subsequently to σ_g, δ_g states after additional photon absorptions. Indeed, all those symmetries can be excited simultaneously if the molecule is irradiated by elliptically polarised laser pulses, since we can consider elliptically polarised light as a combination of parallel and perpendicular polarised fields. Photo-angular distributions (PAD) have recently been studied for linear [297] and elliptically polarised laser pulses [298, 299], where it has been shown that the rotational symmetry of PAD with respect to the molecular and the polarisation axis are strongly dependent of the interplay between intermediate resonant states. In principle, the RHYthMIC code in combination with the POpSiCLE library allows the study of angularly resolved correlated electron-ion spectra, first for arbitrary orientations between the laser polarisation axis and the molecular axis, and then for elliptically polarised laser fields.

In the past studies of orientation effects in the strong field ionisation of H_2^+ have been carried out, such as the dependence on the ellipticity of the incident pulse in HHG [300–303], and also in ATI [304, 305]. However, using the RHYthMIC code is it possible to use arbitrary orientations between the laser polarisation and the molecular axis. This allows us to include nuclear motion in order to extend our investigation of the role vibrational states have on ionisation, dissociation and high harmonic generation in these cases.

Appendices

A

Bessel functions and spherical harmonics

A.1 Bessel functions

The Bessel functions are the solutions of the differential equation

$$\left[z^2 \frac{d^2}{dz^2} + z \frac{d}{dz} + (z^2 - \nu^2) \right] y(z) = 0 \quad (\text{A.1})$$

where ν can be a real or a complex number. The possible solutions of this equation, depending on the parameters used, are the Bessel function of the first kind, $J_\nu(z)$, the Bessel functions of the second kind, $Y_\nu(z)$, the Hankel functions of the first kind, $H_\nu^{(1)}(z)$ and the Hankel functions of the second kind, $H_\nu^{(2)}(z)$.

The Bessel functions of first kind are non-singular at the origin, $z = 0$, and can be expanded in a series that takes the form

$$J_\nu(z) = \left(\frac{z}{2}\right)^2 \sum_{k=0}^{\infty} \frac{(-\frac{1}{4}z^2)^k}{k! \Gamma(\nu + k + 1)}. \quad (\text{A.2})$$

The Bessel functions of the second kind are singular at the origin, $z = 0$, and can be expressed as a function of Bessel functions of first kind with the formula

$$Y_\nu(z) = \frac{J_\nu(z) \cos(\nu\pi) - J_{-\nu}(z)}{\sin(\nu\pi)}. \quad (\text{A.3})$$

The Hankel functions are linear combinations of the Bessel functions of first and second kind, namely

$$H_\nu^{(1)} = J_\nu(z) + iY_\nu(z) \quad (\text{A.4})$$

and

$$H_\nu^{(2)} = J_\nu(z) - iY_\nu(z). \quad (\text{A.5})$$

The Bessel function of first kind for small arguments can be expressed as

$$\lim_{z \rightarrow 0} J_\nu(z) = \frac{(-\frac{1}{2}z)}{\Gamma(\nu + 1)} \quad (\text{A.6})$$

and in the asymptotic limit takes the form

$$\lim_{z \rightarrow \infty} J_\nu(z) = \sqrt{\frac{2}{\pi z}} \cos \left[z - \left(\nu + \frac{1}{2} \right) \frac{\pi}{2} \right]. \quad (\text{A.7})$$

Similarly, the Bessel function of second kind has the asymptotic form

$$\lim_{z \rightarrow \infty} Y_\nu(z) = \sqrt{\frac{2}{\pi z}} \sin \left[z - \left(\nu + \frac{1}{2} \right) \frac{\pi}{2} \right]. \quad (\text{A.8})$$

The Spherical Bessel function of first kind is defined as

$$j_l(z) = \sqrt{\frac{\pi}{2z}} J_{l+\frac{1}{2}} \quad (\text{A.9})$$

These functions provide solutions to the differential equation that has the form

$$\left[\frac{d^2}{dz^2} + \frac{1}{z} \frac{d}{dz} - \frac{(l + \frac{1}{2})^2}{z^2} + 1 \right] \phi(z) = 0. \quad (\text{A.10})$$

The Eq. (A.10) reduces to the radial time-independent Schrödinger equation in a centrifugal potential if we take $z = kr$ and $\phi(z) = z j_l(z)$

$$\left[\frac{d^2}{dz^2} - \frac{l(l+1)}{r^2} + k^2 \right] \phi(z) = 0 \quad (\text{A.11})$$

where $k^2 = 2E$.

The first few spherical functions are

$$j_0(z) = \frac{\sin z}{z}, \quad (\text{A.12})$$

$$j_1(z) = \frac{\sin z}{z^2} - \frac{\cos z}{z}, \quad (\text{A.13})$$

$$j_2(z) = \left(\frac{3}{z^3} - \frac{1}{z} \right) \sin z - \frac{3}{z^2} \cos z. \quad (\text{A.14})$$

For obtaining the higher-order spherical Bessel functions we can make use of the recurrence relations

$$j_{l-1}(z) + j_{l+1}(z) = \frac{2l+1}{z} j_l(z), \quad (\text{A.15})$$

$$l j_{l-1}(z) - (l+1) j_{l+1}(z) = (2l+1) j_l'(z) \quad (\text{A.16})$$

where $j_l'(z)$ is the first derivative of $j_l(z)$ with respect to z . We can also obtain the spherical Bessel functions using the Rayleigh formula

$$j_l(z) = z^n \left(-\frac{1}{z} \frac{d}{dz} \right)^n \frac{\sin z}{z}. \quad (\text{A.17})$$

The spherical Bessel functions obey the orthogonality relation

$$\int_0^a j_l \left(\alpha_{lp} \frac{\rho}{a} \right) j_l \left(\alpha_{lq} \frac{\rho}{a} \right) \rho^2 d\rho = \frac{a^3}{2} [j_{l+1}(\alpha_{lp})]^2 \delta_{pq} \quad (\text{A.18})$$

where α_{lp} and α_{lq} are roots of $j_l(z)$.

A.2 Spherical harmonics

The spherical harmonics are the functions which satisfy the spherical harmonic differential equation, that has the form [208]

$$-\left[\frac{1}{\sin \theta} \frac{\partial}{\partial \theta} \left(\sin \theta \frac{\partial}{\partial \theta} \right) + \frac{1}{\sin^2 \theta} \frac{\partial^2}{\partial \phi^2} \right] Y_{lm}(\theta, \phi) = l(l+1) Y_{lm}(\theta, \phi). \quad (\text{A.19})$$

which can be also expressed as

$$\hat{\mathbf{L}}^2 Y_{lm}(\theta, \phi) = l(l+1) Y_{lm}(\theta, \phi), \quad (\text{A.20})$$

$$\hat{L}_z Y_{lm}(\theta, \phi) = m Y_{lm}(\theta, \phi). \quad (\text{A.21})$$

They can be expressed as

$$Y_{lm}(\theta, \phi) = (-1)^m \sqrt{\frac{2l+1}{4\pi} \frac{(l-m)!}{(l+m)!}} P_l^m(\cos \theta) e^{im\phi} \quad (\text{A.22})$$

where $P_l^m(\cos \theta)$ are the associated Legendre polynomials and $(-1)^m$ is the Condon-Shortley phase. It is common to include the normalisation factor inside the polynomial as

$$\tilde{P}_l^m(\cos \theta) = (-1)^m \sqrt{\frac{2l+1}{4\pi} \frac{(l-m)!}{(l+m)!}} P_l^m(\cos \theta). \quad (\text{A.23})$$

The spherical harmonics defined in Eq. (A.22) have a normalisation that fulfils the orthonormality relation

$$\int_0^{2\pi} d\phi \int_0^\pi \sin \theta d\theta Y_{l'm'}^*(\theta, \phi) Y_{lm}(\theta, \phi) = \delta_{l,l'} \delta_{m,m'} \quad (\text{A.24})$$

A useful property of the spherical harmonics is

$$Y_{l-m}(\theta, \phi) = (-1)^m Y_{lm}^*(\theta, \phi). \quad (\text{A.25})$$

and the first few spherical harmonics are

$$Y_{00}(\theta, \phi) = \frac{1}{\sqrt{4\pi}}, \quad (\text{A.26})$$

$$Y_{10}(\theta, \phi) = \sqrt{\frac{3}{4\pi}} \cos \theta, \quad (\text{A.27})$$

$$Y_{11}(\theta, \phi) = \sqrt{\frac{3}{8\pi}} \sin \theta e^{i\phi}, \quad (\text{A.28})$$

$$Y_{20}(\theta, \phi) = \frac{1}{2} \sqrt{\frac{5}{4\pi}} (3 \cos^2 \theta - 1), \quad (\text{A.29})$$

$$Y_{21}(\theta, \phi) = \sqrt{\frac{15}{8\pi}} \sin \theta \cos \theta e^{i\phi}, \quad (\text{A.30})$$

$$Y_{22}(\theta, \phi) = \frac{1}{4} \sqrt{\frac{15}{2\pi}} \sin^2 \theta e^{i2\phi}. \quad (\text{A.31})$$

A.2.1 Spherical harmonics decomposition

Consider a function continuous over a sphere $f(\theta, \phi)$ [244]

$$f(\theta, \phi) = \sum_{lm} h_{lm} Y_{lm}(\theta, \phi). \quad (\text{A.32})$$

In order to obtain the coefficients h_{lm} we invert the expression in Eq. (A.32) as

$$h_{lm} = \int \int \sin \theta d\theta d\phi f(\theta, \phi) Y_{lm}^*(\theta, \phi). \quad (\text{A.33})$$

If we substitute Eq. (A.22) and Eq. (A.23) onto Eq. (A.33), we get

$$h_{lm} = \int \sin \theta d\theta d\phi f(\theta, \phi) \tilde{P}_{l,m}(\cos \theta) e^{-im\phi}, \quad (\text{A.34})$$

or, if we discretise the integral over the angles we can write

$$h_{lm} = \sum_i \sum_j w_i w_j f(\theta_i, \phi_j) \tilde{P}_{lm}(\cos \theta_i) e^{-im\phi_j} \Delta\theta \Delta\phi \quad (\text{A.35})$$

where w_i are the quadrature weights for the θ coordinate and w_i the weights for the ϕ coordinate.

The most efficient way to calculate the sum in Eq. (A.35) is first to FFT the function $f(\theta, \phi)$ over ϕ [244]

$$g(\theta_i) = \sum_j f(\theta_i, \phi_j) e^{-im\phi_j} \Delta\phi. \quad (\text{A.36})$$

where the weights over the ϕ coordinate just take the from $w_j = \Delta\phi$.

After the FFT, we use a Gaussian-Legendre quadrature to sum the resulting $g(\theta_i)$ over θ . Fi-

nally, we get the coefficients h_{lm} [244]

$$h_{lm} = \sum_j g(\theta_i) \tilde{P}_{lm}(\cos \theta_i) w_i \quad (\text{A.37})$$

where w_i and θ_i are the weights and pivots respectively for the Gaussian quadrature. The Gauss-Legendre quadrature for a polynomial of order d is exact for a function with degree N with $d = 2N - 1$, and since our integrands are polynomials of degree $2l_{\max}$, so if we want to decompose a wavefunction up to l_{\max} , the quadrature must have at least $N_\theta \geq l_{\max}$ points in θ axis. For this reason, the number of points in θ depends on the maximum angular momentum of the decomposition. Moreover, the number of points in ϕ axis will depend on l_{\max} as well. The maximum value of the magnetic angular momenta is given by $m_{\max} = 2l_{\max} + 1$, and because the number of points of a Fourier Transform pair must be the same, the number of ϕ points is $N_\phi = 2l_{\max} + 1$.

In the library, the user chooses l_{\max} as an input parameter. The number of points in θ and ϕ axes are set according to l_{\max} . We use the pivots of a Gauss-Legendre quadrature to set the points in θ , whereas the FFT requires an equidistant grid in the ϕ axis. In the case of laser polarisation parallel to the internuclear axis, there is no azimuthal dependence so m does not change. We set $N_\phi = 1$ and we skip the FFT of the decomposition.

B

Multi-dimensional cubic interpolation

In this appendix we briefly summarise the cubic interpolation method for two dimensions [244], namely bicubic interpolation. Tricubic interpolation (the case for 3D, which is also used in `POpSiCLE`) is analogous to bicubic interpolation. The reader is referred to [276] for a complete discussion in 3D. The bicubic interpolation is just a cubic interpolation in which we assume that on a rectangle (see figure B.1) our interpolating function is a piecewise function depending of coordinates x_1 and x_2 , of the form

$$f(x_1, x_2) = \sum_{i=0}^3 \sum_{j=0}^3 a_{ij} x_1^i x_2^j. \quad (\text{B.1})$$

We can obtain the 16 coefficients a_{ij} by imposing constraints that will ensure continuity and smoothness on the piecewise function. These constraints must be provided by the user, and they are the four tabulated values of the function at the corner points and together with

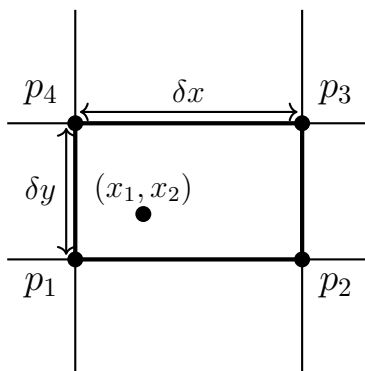


Figure B.1: Unit rectangle on a 2D regular mesh. We must know at the four corners, in the figure labelled p_1 , p_2 , p_3 and p_4 , the values of the function, and its first and cross-derivatives.

its derivatives $\{\frac{\partial}{\partial x}, \frac{\partial}{\partial y}, \frac{\partial^2}{\partial x \partial y}\}$. We display the coefficients a_{ij} as a vector

$$\alpha_{1+i+4j} = a_{ij} \quad \text{for all } i, j \in \{0, 1, 2, 3\} \quad (\text{B.2})$$

If we label the corner of the square $\{p_1, p_2, p_3, p_4\}$ we also display the constraints in a column vector $\boldsymbol{\alpha}$ as

$$\alpha_i = \begin{cases} f(p_i) & \text{if } 1 \leq i \leq 4 \\ \frac{\partial f}{\partial x}(p_{i-4}) & \text{if } 5 \leq i \leq 8 \\ \frac{\partial f}{\partial y}(p_{i-8}) & \text{if } 9 \leq i \leq 12 \\ \frac{\partial^2 f}{\partial xy}(p_{i-12}) & \text{if } 13 \leq i \leq 16 \end{cases} \quad (\text{B.3})$$

The vectors $\boldsymbol{\alpha}$ and \mathbf{b} are related by

$$\mathbf{b} = \mathbf{B}\boldsymbol{\alpha} \quad (\text{B.4})$$

which is nothing more than Eq. (B.1) expressed in matrix notation. The coefficients of \mathbf{B} are just integer numbers that can be worked out exactly from taking the derivatives of Eq. (B.1) (this can be calculated with basic arithmetic: easy but tedious to get). Therefore, the equation we must solve is

$$\boldsymbol{\alpha} = \mathbf{B}^{-1}\mathbf{b}. \quad (\text{B.5})$$

Once we have determined our coefficients, we can substitute the 16 a_{ij} 's into the cubic function (B.1) to know the value of a point that lies within the square mesh.

In principle it is possible to specify any values for the derivatives. This is left to the user, but as it is obvious, the more accurate the derivatives are, the more accurate the interpolation is. Our derivatives are calculated at the corner points using a finite-difference (FD) method. We calculate the FD stencil rule at each point using the algorithm described in [222, 223, 306]. This algorithm can calculate the coefficients of a FD rule for any arbitrarily spaced grid. Calculating the stencil specifically at every point help us to improve the accuracy of the derivatives in the case of scaled coordinate meshes (in many of these scalings the grid spacing is not constant). This operation causes no appreciable computational overhead.

C

Calculation of the cross section

In Time Dependent Perturbation Theory (TDPT) the cross section formula for single-photon ionisation in velocity gauge is [307]

$$\frac{d\sigma}{d\Omega} = \frac{4\pi^2 k}{mc\omega_{fi}} |\langle \Psi_f | \epsilon \cdot \mathbf{k} | \Psi_i \rangle|^2 \quad (\text{C.1})$$

On the other hand, the first term in the expansion of the transition amplitude between an initial state and a (final) scattering state (in velocity gauge) is given by [307]

$$b^{(1)}(\mathbf{k}) = -\frac{iA_0}{mc} \langle \Psi_f | \epsilon \cdot \mathbf{k} | \Psi_i \rangle F_V^{(1)}(\omega_L, \omega_{fi}, T) \quad (\text{C.2})$$

where $\langle \Psi_f | \epsilon \cdot \mathbf{k} | \Psi_i \rangle$ is the dipole matrix element between state i and f , m is the mass of the electron and c the speed of light, A_0 is the amplitude of the vector potential of the field, defined as

$$A(t) = A_0 F_v(t). \quad (\text{C.3})$$

$F_V(t)$ is the temporal dependence of the laser pulse. In this case we describe the envelope with a sine squared function:

$$F_V(t) = \sin^2\left(\frac{\pi t}{T}\right) \sin(\omega_L t). \quad (\text{C.4})$$

The function $F_V^{(1)}(\omega_L, \omega_{fi}, T)$ is merely the Fourier transform of the temporal dependence of the vector potential $A(t)$, Eq.(C.3), which can be expressed as

$$F_V^{(1)}(\omega_L, \omega_{fi}, T) = \int_0^T dt e^{i(\omega_f - \omega_i)t} F_V(t) \quad (\text{C.5})$$

where T is the duration of the laser pulse, ω_L the photon energy of the field, ω_{fi} the energy difference between the final and the initial state. The bandwidth of $F_V^{(1)}(\omega_L, \omega_{fi}, T)$ is $\Delta\omega = 4\pi/T$.

Making use of the rotating wave approximation we can write the Fourier transform of the field as [282]

$$F_{RW}^{(1)}(\omega_L, \omega_{fi}, T) = \frac{e^{-i\omega_L T} (e^{i(\omega - \omega_{fi})T} - 1) \pi^2}{[T^2(\omega - \omega_{fi})^2 - 4\pi^2] (\omega - \omega_{fi})}. \quad (\text{C.6})$$

In the case of a \sin^2 envelope, Eq. (C.6) takes analytic form of

$$|F_{RW}^{(1)}(\omega_L, \omega_{fi}, T)|^2 = \frac{4\pi^2 \sin^2 [(\omega_L - \omega_{fi}) T/2]}{\left[T^2(\omega_L - \omega_{fi})^2 - 4\pi^2\right]^2 (\omega_L - \omega_{fi})^2}. \quad (\text{C.7})$$

Substituting the dipole matrix element in Eq. (C.1) into substitute we finally obtain [122, 282]

$$\begin{aligned} \frac{d\sigma}{d\Omega} &= \frac{4\pi^2 mc}{\omega_{fi}} \frac{|b(\mathbf{k})|^2}{A_0^2 |F_V^{(1)}(\omega_L, \omega_{fi}, T)|^2} \\ &= \frac{4\pi^2 mc}{\omega_{fi}} \frac{|b^{(1)}(\mathbf{k})|^2}{A_0^2 |F_{RW}^{(1)}(\omega_L, \omega_{fi}, T)|^2}. \end{aligned} \quad (\text{C.8})$$

We can derive the cross section analogously in the length gauge. We start again with the formula (C.1) but this time in length gauge we have

$$\frac{d\sigma}{d\Omega} = \frac{4\pi^2 k \omega_{fi}}{mc} |\langle \Psi_f | \boldsymbol{\epsilon} \cdot \mathbf{r} | \Psi_i \rangle|^2. \quad (\text{C.9})$$

The transition amplitude is given by

$$b^{(1)}(\mathbf{k}) = -iE_0 \langle \Psi_f | \boldsymbol{\epsilon} \cdot \mathbf{r} | \Psi_i \rangle F_L^{(1)}(\omega_L, \omega_{fi}, T) \quad (\text{C.10})$$

where $F_L^{(1)}(\omega_L, \omega_{fi}, T)$ represents the Fourier transform of the electric field. Making use of the relation between the electric field and the vector potential

$$E(t) = -\frac{dA(t)}{dt} = -A_0 \frac{dF_V(t)}{dt} = -\frac{E_0}{\omega_L} \frac{dF_V(t)}{dt}. \quad (\text{C.11})$$

We can insert Eq. (C.11) in $F_L^{(1)}(\omega_L, \omega_{fi}, T)$ to get

$$F_L^{(1)}(\omega_L, \omega_{fi}, T) = \int_0^T dt e^{i\omega_{fi}t} F_L(t) \quad (\text{C.12})$$

$$F_L^{(1)}(\omega_L, \omega_{fi}, T) = \int_0^T dt e^{i\omega_{fi}t} \left(-\frac{1}{\omega} \frac{dF_V(t)}{dt} \right) \quad (\text{C.13})$$

$$F_L^{(1)}(\omega_L, \omega_{fi}, T) = -\frac{i\omega_{fi}}{\omega_L} F_V^{(1)}(\omega_L, \omega_{fi}, T) \quad (\text{C.14})$$

where in the last equality we have used the property of the Fourier transforms related with

derivative of a function. We can rewrite Eq. (C.10) as

$$b^{(1)}(\mathbf{k}) = \frac{\omega_{fi}}{\omega_L} E_0 \langle \Psi_f | \boldsymbol{\epsilon} \cdot \mathbf{r} | \Psi_i \rangle F_V^{(1)}(\omega_L, \omega_{fi}, T) \quad (\text{C.15})$$

so finally the expression for the cross section in length gauge is given by

$$\frac{d\sigma}{d\Omega} = \frac{4\pi^2 mc \omega_L}{\omega_{fi}} \frac{|b(\mathbf{k})|^2}{A_0^2 |F_V^{(1)}(\omega_L, \omega_{fi}, T)|^2}. \quad (\text{C.16})$$

We note that because Eq. (C.2) can be factorised we can extract the cross section for single-photon ionisation within the bandwidth of a single laser pulse. The range of frequencies for which $F_V^{(1)}(\omega_L, \omega_{fi}, T)$ is not zero is defined as the bandwidth of the pulse. Moreover, in reference [282] it is shown that it is possible to obtain similar expressions for two-photon interactions where the equations in TDPT are not factorizable.

Bibliography

- [1] A. Töpler. "Optische Studien nach der Methode der Schlierenbeobachtung". *Annalen der Physik* 207.6 (1867), p. 180.
- [2] J. D. B. Stillman and E. Muybridge. *The horse in motion as shown by instantaneous photography, with a study on animal mechanics founded on anatomy and the revelations of the camera, in which is demonstrated the theory of quadrupedal locomotion*. J. R. Osgood and company, Boston, 1882.
- [3] H. E. Edgerton and K. J. Germeshausen. "The mercury arc as an actinic stroboscopic light source". *Review of Scientific Instruments* 3.10 (1932), p. 535.
- [4] H. E. Edgerton, J. K. Germeshausen, and H. E. Grier. "High Speed Photographic Methods of Measurement". *Journal of Applied Physics* 8.1 (1937), p. 2.
- [5] *Iconic photos. Harold "Doc" Edgerton: Milk Drop Coronet - 1957.* <http://edgerton-digital-collections.org/galleries/iconic#hee-nc-57001>. (Accessed on 06/15/2017).
- [6] *Iconic photos. Harold "Doc" Edgerton: Cutting the Card Quickly - 1964.* <http://edgerton-digital-collections.org/galleries/iconic#hee-nc-64003>. (Accessed on 06/15/2017).
- [7] *Iconic photos. Harold "Doc" Edgerton: Bullet through apple - 1964.* <http://edgerton-digital-collections.org/galleries/iconic#hee-nc-64002>.
- [8] E. Muybridge. *The Horse in motion. "Sallie Gardner," owned by Leland Stanford; running at a 1:40 gait over the Palo Alto track, 19th June 1878.* <http://www.loc.gov/pictures/resource/cph.3a45870/>. (Accessed on 06/13/2017).
- [9] A. H. Zewail. "Femtochemistry: Atomic-Scale Dynamics of the Chemical Bond". *The Journal of Physical Chemistry A* 104.24 (2000), p. 5660.
- [10] N. F. Scherer, C. Sipes, R. B. Bernstein, and A. H. Zewail. "Real \square time clocking of bimolecular reactions: Application to H+CO₂". *The Journal of Chemical Physics* 92.9 (1990), p. 5239.
- [11] M. Dantus, M. J. Rosker, and A. H. Zewail. "Real \square time femtosecond probing of "transition states" in chemical reactions". *The Journal of Chemical Physics* 87.4 (1987), p. 2395.
- [12] H. Niikura et al. "Sub-laser-cycle electron pulses for probing molecular dynamics". *Nature* 417.6892 (2002), p. 917.
- [13] M. Meckel et al. "Laser-Induced Electron Tunneling and Diffraction". *Science* 320.5882 (2008), p. 1478.
- [14] C. I. Blaga et al. "Imaging ultrafast molecular dynamics with laser-induced electron diffraction". *Nature* 483.7388 (2012), p. 194.
- [15] J. Itatani et al. "Tomographic imaging of molecular orbitals". *Nature* 432.7019 (2004), p. 867.
- [16] S. Baker et al. "Probing Proton Dynamics in Molecules on an Attosecond Time Scale". *Science* 312.5772 (2006), p. 424.

- [17] F. Silva et al. "Spatiotemporal isolation of attosecond soft X-ray pulses in the water window". 6 (2015), 6611 EP.
- [18] J. Vura-Weis et al. "Crossover from Single-Step Tunneling to Multistep Hopping for Molecular Triplet Energy Transfer". *Science* 328.5985 (2010), p. 1547.
- [19] H. B. Gray and J. Halpern. "Distant charge transport". *Proceedings of the National Academy of Sciences of the United States of America* 102.10 (2005), p. 3533.
- [20] M. Smyth and J. Kohanoff. "Excess Electron Localization in Solvated DNA Bases". *Phys. Rev. Lett.* 106 (23 2011), p. 238108.
- [21] C. H. Townes. *How the laser happened. Adventures of a scientist*. Oxford University Press, 1999.
- [22] Center for History of Physics. American Institute of Physics. *Bright idea: the first lasers*. url: <https://www.aip.org/history/exhibits/laser/> (visited on 07/20/2016).
- [23] A. L. Schawlow and C. H. Townes. "Infrared and Optical Masers". *Phys. Rev.* 112.6 (1958), p. 1940.
- [24] N. G. Basov and A. M. Prokhorov. "Application of molecular beams for radiospectroscopic study of molecular rotational spectra". *JETP* 27.4 (10 1954), p. 431.
- [25] N. G. Basov and A. M. Prokhorov. "On the possible methods for obtaining active molecules for a molecular generator". *JETP* 28.2 (1955), p. 249.
- [26] T. H. Maiman. "Stimulated Optical Radiation in Ruby". *Nature* 187.4736 (1960), p. 493.
- [27] M. D. Perry and G. Mourou. "Terawatt to Petawatt Subpicosecond Lasers". *Science* 264.5161 (1994), p. 917.
- [28] G. Mourou, J. A. Wheeler, and T. Tajima. "Extreme light - An intense pursuit of fundamental high energy physics". *Europhysics News* 46.5–6 (2015), p. 31.
- [29] P. B. Corkum and F. Krausz. "Attosecond science". *Nat Phys* 3.6 (2007), p. 381.
- [30] B. E. A. Saleh and M. C. Teich. *Fundamentals of Photonics*. 2nd ed. John Wiley & Sons, 2007.
- [31] A. E. Siegman. *Lasers*. 1st ed. University Science Books, 1986.
- [32] M. Protopapas, C. H. Keitel, and P. L. Knight. "Atomic physics with super-high intensity lasers". *Reports on Progress in Physics* 60.4 (1997), p. 389.
- [33] G. A. Mourou, T. Tajima, and S. V. Bulanov. "Optics in the relativistic regime". *Rev. Mod. Phys.* 78.2 (2006), p. 309.
- [34] D. Strickland and G. Mourou. "Compression of amplified chirped optical pulses". *Optics Communications* 56.3 (1985), p. 219.
- [35] Wikipedia. *Chirped pulse amplification — Wikipedia, The Free Encyclopedia*. [Online; accessed 30-January-2017]. 2016.
- [36] M. Perry. "Multilayer Dielectric Gratings: Increasing the Power of Light". *Science & technology review / Lawrence Livermore National Laboratory* (1995).
- [37] V. Pervak et al. "Chirped-pulse amplification of laser pulses with dispersive mirrors". *Opt. Express* 17.21 (2009), p. 19204.
- [38] G. Mourou and T. Tajima. "More Intense, Shorter Pulses". *Science* 331.6013 (2011), p. 41.
- [39] W. Ackermann et al. "Operation of a free-electron laser from the extreme ultraviolet to the water window". *Nat Photon* 1.6 (2007), p. 336.
- [40] D. A. G. Deacon et al. "First Operation of a Free-Electron Laser". *Phys. Rev. Lett.* 38.16 (1977), p. 892.

- [41] L. R. Elias et al. "Observation of Stimulated Emission of Radiation by Relativistic Electrons in a Spatially Periodic Transverse Magnetic Field". *Phys. Rev. Lett.* 36.13 (1976), p. 717.
- [42] C. Pellegrini. "The history of X-ray free-electron lasers". *The European Physical Journal H* 37.5 (2012), p. 659.
- [43] P. Emma et al. "First lasing and operation of an angstrom-wavelength free-electron laser". *Nat Photon* 4.9 (2010), p. 641.
- [44] M. Göppert-Mayer. "Über Elementarakte mit zwei Quantensprüngen". *Annalen der Physik* 401.3 (1931), p. 273.
- [45] E. K. Damon and R. G. Tomlinson. "Observation of Ionization of Gases by a Ruby Laser". *Appl. Opt.* 2.5 (1963), p. 546.
- [46] K. Burnett, V. C. Reed, and P. L. Knight. "Atoms in ultra-intense laser fields". *Journal of Physics B: Atomic, Molecular and Optical Physics* 26.4 (1993), p. 561.
- [47] P. Agostini and L. F. DiMauro. "Chapter 3 - Atomic and Molecular Ionization Dynamics in Strong Laser Fields: From Optical to X-rays". *Advances in Atomic, Molecular, and Optical Physics*. Ed. by E. A. Paul Berman and C. Lin. Vol. 61. *Advances In Atomic, Molecular, and Optical Physics*. Academic Press, 2012, p. 117.
- [48] L. V. Keldysh. "Ionization in the field of a strong electromagnetic wave". *Soviet Physics JETP* 20 (1965), p. 1307.
- [49] M. Büttiker and R. Landauer. "Traversal Time for Tunneling". *Phys. Rev. Lett.* 49.23 (1982), p. 1739.
- [50] J. Parker and C. R. Stroud. "Generalization of the Keldysh theory of above-threshold ionization for the case of femtosecond pulses". *Phys. Rev. A* 40.10 (1989), p. 5651.
- [51] M. V. Fedorov, M. Y. Ivanov, and P. B. Lerner. "Interaction of atoms with supershort laser pulses and the generation of the supercontinuum". *Journal of Physics B: Atomic, Molecular and Optical Physics* 23.15 (1990), p. 2505.
- [52] K. Burnett, P. L. Knight, B. R. M. Piraux, and V. C. Reed. "Suppression of ionization in strong laser fields". *Phys. Rev. Lett.* 66.3 (1991), p. 301.
- [53] V. C. Reed, P. L. Knight, and K. Burnett. "Suppression of ionization in superintense fields without dichotomy". *Phys. Rev. Lett.* 67.11 (1991), p. 1415.
- [54] M. P. de Boer et al. "Adiabatic stabilization against photoionization: An experimental study". *Phys. Rev. A* 50.5 (1994), p. 4085.
- [55] G. S. Voronov and N. B. Delone. "Many-Photon Ionization of the Xenon Atom by Ruby Laser Radiation". *Soviet Physics JETP* 23.1 (1966), p. 54.
- [56] F. Fabre, G. Petite, P. Agostini, and M. Clement. "Multiphoton above-threshold ionisation of xenon at 0.53 and 1.06 μ m". *Journal of Physics B: Atomic and Molecular Physics* 15.9 (1982), p. 1353.
- [57] J. Morellec, D. Normand, and G. Petite. "Resonance shifts in the multiphoton ionization of cesium atoms". *Phys. Rev. A* 14.1 (1976), p. 300.
- [58] Petite, G., Morellec, J., and Normand, D. "Resonant multiphoton ionization of caesium atoms". *J. Phys. France* 40.2 (1979), p. 115.
- [59] E. Karule. "Two-photon ionisation of atomic hydrogen simultaneously with one-photon ionisation". *Journal of Physics B: Atomic and Molecular Physics* 11.3 (1978), p. 441.
- [60] P. Agostini et al. "Free-Free Transitions Following Six-Photon Ionization of Xenon Atoms". *Phys. Rev. Lett.* 42.17 (1979), p. 1127.

- [61] Y. Gontier, M. Poirier, and M. Trahin. "Multiphoton absorptions above the ionisation threshold". *Journal of Physics B: Atomic and Molecular Physics* 13.7 (1980), p. 1381.
- [62] F. H. M. Faisal. "Multiple absorption of laser photons by atoms". *Journal of Physics B: Atomic and Molecular Physics* 6.4 (1973), p. L89.
- [63] H. R. Reiss. "Effect of an intense electromagnetic field on a weakly bound system". *Phys. Rev. A* 22.5 (1980), p. 1786.
- [64] H. R. Reiss. "Inherent contradictions in the tunneling-multiphoton dichotomy". *Phys. Rev. A* 75.3 (2007), p. 031404.
- [65] K. J. Schafer, B. Yang, L. F. DiMauro, and K. C. Kulander. "Above threshold ionization beyond the high harmonic cutoff". *Phys. Rev. Lett.* 70.11 (1993), p. 1599.
- [66] P. Agostini and L. F. DiMauro. "Atoms in high intensity mid-infrared pulses". *Contemporary Physics* 49.3 (2008), p. 179.
- [67] P. B. Corkum. "Plasma perspective on strong field multiphoton ionization". *Phys. Rev. Lett.* 71.13 (1993), p. 1994.
- [68] Y. Mairesse et al. "Attosecond Synchronization of High-Harmonic Soft X-rays". *Science* 302.5650 (2003), p. 1540.
- [69] J. M. Dahlström, A. L'Huillier, and J. Mauritsson. "Quantum mechanical approach to probing the birth of attosecond pulses using a two-colour field". *Journal of Physics B: Atomic, Molecular and Optical Physics* 44.9 (2011), p. 095602.
- [70] A. McPherson et al. "Studies of multiphoton production of vacuum-ultraviolet radiation in the rare gases". *J. Opt. Soc. Am. B* 4.4 (1987), p. 595.
- [71] X. F. Li et al. "Multiple-harmonic generation in rare gases at high laser intensity". *Phys. Rev. A* 39.11 (1989), p. 5751.
- [72] J. J. Macklin, J. D. Kmetec, and C. L. Gordon. "High-order harmonic generation using intense femtosecond pulses". *Phys. Rev. Lett.* 70.6 (1993), p. 766.
- [73] J. Tate et al. "Scaling of Wave-Packet Dynamics in an Intense Midinfrared Field". *Phys. Rev. Lett.* 98.1 (2007), p. 013901.
- [74] J. A. Pérez-Hernández, J. Ramos, L. Roso, and L. Plaja. "Harmonic generation beyond the Strong-Field Approximation: Phase and temporal description". *Laser Physics* 20.5 (2010), p. 1044.
- [75] G. Farkas and C. Tóth. "Proposal for attosecond light pulse generation using laser induced multiple-harmonic conversion processes in rare gases". *Physics Letters A* 168.5 (1992), p. 447.
- [76] P. Antoine et al. "Theory of high-order harmonic generation by an elliptically polarized laser field". *Phys. Rev. A* 53.3 (1996), p. 1725.
- [77] I. P. Christov, M. M. Murnane, and H. C. Kapteyn. "High-Harmonic Generation of Attosecond Pulses in the "Single-Cycle" Regime". *Phys. Rev. Lett.* 78 (7 1997), p. 1251.
- [78] P. M. Paul et al. "Observation of a Train of Attosecond Pulses from High Harmonic Generation". *Science* 292.5522 (2001), p. 1689.
- [79] M. Hentschel et al. "Attosecond metrology". *Nature* 414.6863 (2001), p. 509.
- [80] Y. Mairesse et al. "Optimization of Attosecond Pulse Generation". *Phys. Rev. Lett.* 93 (16 2004), p. 163901.
- [81] K. Varjú et al. "Frequency chirp of harmonic and attosecond pulses". *Journal of Modern Optics* 52.2-3 (2005), p. 379.

- [82] A. L'Huillier, K. J. Schafer, and K. C. Kulander. "Higher-order harmonic generation in xenon at 1064 nm: The role of phase matching". *Phys. Rev. Lett.* 66.17 (1991), p. 2200.
- [83] P. Salières, A. L'Huillier, and M. Lewenstein. "Coherence Control of High-Order Harmonics". *Phys. Rev. Lett.* 74.19 (1995), p. 3776.
- [84] T. Popmintchev et al. "Phase matching of high harmonic generation in the soft and hard X-ray regions of the spectrum". *Proceedings of the National Academy of Sciences* 106.26 (2009), p. 10516.
- [85] T. Popmintchev et al. "Bright Coherent Ultrahigh Harmonics in the keV X-ray Regime from Mid-Infrared Femtosecond Lasers". *Science* 336.6086 (2012), p. 1287.
- [86] P. B. Corkum, N. H. Burnett, and M. Y. Ivanov. "Subfemtosecond pulses". *Opt. Lett.* 19.22 (1994), p. 1870.
- [87] I. J. Sola et al. "Controlling attosecond electron dynamics by phase-stabilized polarization gating". *Nat Phys* 2.5 (2006), p. 319.
- [88] G. Sansone et al. "Isolated Single-Cycle Attosecond Pulses". *Science* 314.5798 (2006), p. 443.
- [89] H. Vincenti and F. Quéré. "Attosecond Lighthouses: How To Use Spatiotemporally Coupled Light Fields To Generate Isolated Attosecond Pulses". *Phys. Rev. Lett.* 108 (11 2012), p. 113904.
- [90] A. Borot et al. "Attosecond control of collective electron motion in plasmas". *Nat Phys* 8.5 (2012), p. 416.
- [91] J. A. Wheeler et al. "Attosecond lighthouses from plasma mirrors". *Nat Photon* 6.12 (2012), p. 829.
- [92] M. Born and R. Oppenheimer. "Zur Quantentheorie der Moleküle". *Annalen der Physik* 389.20 (1927), p. 457.
- [93] B. Bransden and C. Joachain. *Physics of Atoms and Molecules*. 2nd ed. Pearson, 2003.
- [94] A. Stolow. "Femtosecond time-resolved photoelectron spectroscopy of polyatomic molecules". *Annual Review of Physical Chemistry* 54.1 (2003). PMID: 12524428, p. 89.
- [95] H. Kono et al. "Quantum mechanical study of electronic and nuclear dynamics of molecules in intense laser fields". *Chemical Physics* 304.1 (2004). Towards Multidimensional Quantum Reaction Dynamics, p. 203.
- [96] L. S. Cederbaum. "Born–Oppenheimer approximation and beyond for time-dependent electronic processes". *The Journal of Chemical Physics* 128.12 (2008), p. 124101.
- [97] A. Abedi, N. T. Maitra, and E. K. U. Gross. "Exact Factorization of the Time-Dependent Electron-Nuclear Wave Function". *Phys. Rev. Lett.* 105 (12 2010), p. 123002.
- [98] J. Breidbach and L. S. Cederbaum. "Universal Attosecond Response to the Removal of an Electron". *Phys. Rev. Lett.* 94.3 (2005), p. 033901.
- [99] L. Cederbaum and J. Zobeley. "Ultrafast charge migration by electron correlation". *Chemical Physics Letters* 307.3–4 (1999), p. 205.
- [100] H. Hennig, J. Breidbach, and L. S. Cederbaum. "Electron Correlation as the Driving Force for Charge Transfer: Charge Migration Following Ionization in N-Methyl Acetamide". *The Journal of Physical Chemistry A* 109.3 (2005). PMID: 16833360, p. 409.
- [101] A. I. Kuleff and L. S. Cederbaum. "Charge migration in different conformers of glycine: The role of nuclear geometry". *Chemical Physics* 338.2–3 (2007). Molecular Wave Packet Dynamics(in honour of Jörn Manz), p. 320.
- [102] F. Remacle and R. D. Levine. "An electronic time scale in chemistry". *Proceedings of the National Academy of Sciences* 103.18 (2006), p. 6793.

- [103] J. P. Marangos et al. "Dynamic imaging of molecules using high order harmonic generation". *Phys. Chem. Chem. Phys.* 10 (1 2008), p. 35.
- [104] J. P. Marangos. "Development of high harmonic generation spectroscopy of organic molecules and biomolecules". *Journal of Physics B: Atomic, Molecular and Optical Physics* 49.13 (2016), p. 132001.
- [105] S. Baker et al. "Dynamic Two-Center Interference in High-Order Harmonic Generation from Molecules with Attosecond Nuclear Motion". *Phys. Rev. Lett.* 101 (5 2008), p. 053901.
- [106] M. F. Kling et al. "Control of Electron Localization in Molecular Dissociation". *Science* 312.5771 (2006), p. 246.
- [107] M. F. Kling and M. J. Vrakking. "Attosecond Electron Dynamics". *Annual Review of Physical Chemistry* 59.1 (2008). PMID: 18031218, p. 463.
- [108] F. Lépine, G. Sansone, and M. J. Vrakking. "Molecular applications of attosecond laser pulses". *Chemical Physics Letters* 578 (2013), p. 1.
- [109] B. Fischer et al. "Steering the Electron in H_2^+ by Nuclear Wave Packet Dynamics". *Phys. Rev. Lett.* 105.22 (2010), p. 223001.
- [110] S. Gräfe and M. Y. Ivanov. "Effective Fields in Laser-Driven Electron Recollision and Charge Localization". *Phys. Rev. Lett.* 99 (16 2007), p. 163603.
- [111] X. M. Tong and C. D. Lin. "Dynamics of Light-Field Control of Molecular Dissociation at the Few-Cycle Limit". *Phys. Rev. Lett.* 98 (12 2007), p. 123002.
- [112] G. Sansone et al. "Electron localization following attosecond molecular photoionization". *Nature* 465.7299 (2010), p. 763.
- [113] J. H. Posthumus. "The dynamics of small molecules in intense laser fields". *Reports on Progress in Physics* 67.5 (2004), p. 623.
- [114] C. Calvert, W. Bryan, W. Newell, and I. Williams. "Time-resolved studies of ultrafast wavepacket dynamics in hydrogen molecules". *Physics Reports* 491.1 (2010), p. 1.
- [115] D. R. Bates, K. Ledsham, and A. L. Stewart. "Wave Functions of the Hydrogen Molecular Ion". *Philosophical Transactions of the Royal Society of London A: Mathematical, Physical and Engineering Sciences* 246.911 (1953), p. 215.
- [116] D. R. Bates, U. Öpik, and G. Poots. "Properties of the Hydrogen Molecular Ion II: Photo-Ionization from the $1s\sigma g$, $2s\sigma g$ and $3s\sigma g$ States". *Proceedings of the Physical Society. Section A* 66.12 (1953), p. 1113.
- [117] D. R. Bates and U. Öpik. "Undulations in the photoionization cross section curves of molecules". *Journal of Physics B: Atomic and Molecular Physics* 1.4 (1968), p. 543.
- [118] A. Apalategui, A. Saenz, and P. Lambopoulos. "Effect of vibration and internuclear axis orientation on multiphoton ionization of H_2^+ ". *Journal of Physics B: Atomic, Molecular and Optical Physics* 33.14 (2000), p. 2791.
- [119] T. N. Rescigno, D. A. Horner, F. L. Yip, and C. W. McCurdy. "Hybrid approach to molecular continuum processes combining Gaussian basis functions and the discrete variable representation". *Phys. Rev. A* 72.5 (2005), p. 052709.
- [120] A. Palacios, S. Barmaki, H. Bachau, and F. Martín. "Two-photon ionization of H_2^+ by short laser pulses". *Phys. Rev. A* 71.6 (2005), p. 063405.
- [121] L. Tao, C. W. McCurdy, and T. N. Rescigno. "Grid-based methods for diatomic quantum scattering problems: A finite-element discrete-variable representation in prolate spheroidal coordinates". *Phys. Rev. A* 79.1 (2009), p. 012719.

- [122] L. Tao, C. W. McCurdy, and T. N. Rescigno. "Grid-based methods for diatomic quantum scattering problems. II. Time-dependent treatment of single- and two-photon ionization of H_2^+ ". *Phys. Rev. A* 80.1 (2009), p. 013402.
- [123] X.-F. Hou, L.-Y. Peng, Q.-C. Ning, and Q. Gong. "Attosecond streaking of molecules in the low-energy region studied by a wavefunction splitting scheme". *Journal of Physics B: Atomic, Molecular and Optical Physics* 45.7 (2012), p. 074019.
- [124] T. Zuo and A. D. Bandrauk. "Charge-resonance-enhanced ionization of diatomic molecular ions by intense lasers". *Phys. Rev. A* 52.4 (1995), R2511.
- [125] A. D. Bandrauk and J. Ruel. "Charge-resonance-enhanced ionization of molecular ions in intense laser pulses: Geometric and orientation effects". *Phys. Rev. A* 59.3 (1999), p. 2153.
- [126] M. Plummer and J. F. McCann. "Complex-basis-function Floquet calculations of multiphoton ionization rates in hydrogen systems". *Journal of Physics B: Atomic, Molecular and Optical Physics* 28.18 (1995), p. 4073.
- [127] M. Plummer and J. F. McCann. "Field-ionization rates of the hydrogen molecular ion". *Journal of Physics B: Atomic, Molecular and Optical Physics* 29.20 (1996), p. 4625.
- [128] M. Plummer and J. F. McCann. "Orientation dependence of field ionization of the hydrogen molecular ion". *Journal of Physics B: Atomic, Molecular and Optical Physics* 30.11 (1997), p. L401.
- [129] L. B. Madsen and M. Plummer. " H_2^+ in intense laser fields: mechanisms for enhanced ionization in the multiphoton regime". *Journal of Physics B: Atomic, Molecular and Optical Physics* 31.1 (1998), p. 87.
- [130] G. N. Gibson, M. Li, C. Guo, and J. Neira. "Strong-Field Dissociation and Ionization of H_2^+ Using Ultrashort Laser Pulses". *Phys. Rev. Lett.* 79.11 (1997), p. 2022.
- [131] L. B. Madsen and M. Plummer. " H_2^+ in intense laser fields: mechanisms for enhanced ionization in the multiphoton regime". *Journal of Physics B: Atomic, Molecular and Optical Physics* 31.1 (1998), p. 87.
- [132] L. B. Madsen, M. Plummer, and J. F. McCann. "Multiphoton ionization of H_2^+ by intense light: A comparison of Floquet and wave-packet results". *Phys. Rev. A* 58.1 (1998), p. 456.
- [133] A. S. Kheifets. "Single-center model for double photoionization of the H_2 molecule". *Phys. Rev. A* 71 (2 2005), p. 022704.
- [134] A. S. Kheifets and I. Bray. "Double photoionization of He and H_2 at unequal energy sharing". *Phys. Rev. A* 72 (2 2005), p. 022703.
- [135] J. Colgan, M. S. Pindzola, and F. Robicheaux. "Triple Differential Cross Sections for the Double Photoionization of H_2 ". *Phys. Rev. Lett.* 98 (15 2007), p. 153001.
- [136] T.-G. Lee, M. S. Pindzola, and F. Robicheaux. "Double ionization of H 2 by intense attosecond laser pulses". *Journal of Physics B: Atomic, Molecular and Optical Physics* 43.16 (2010), p. 165601.
- [137] W. Vanroose, F. Martín, T. N. Rescigno, and C. W. McCurdy. "Complete Photo-Induced Breakup of the H_2 Molecule as a Probe of Molecular Electron Correlation". *Science* 310.5755 (2005), p. 1787.
- [138] L. Tao, C. W. McCurdy, and T. N. Rescigno. "Grid-based methods for diatomic quantum scattering problems. III. Double photoionization of molecular hydrogen in prolate spheroidal coordinates". *Phys. Rev. A* 82 (2 2010), p. 023423.
- [139] X. Guan, K. Bartschat, and B. I. Schneider. "Breakup of the aligned H_2 molecule by xuv laser pulses: A time-dependent treatment in prolate spheroidal coordinates". *Phys. Rev. A* 83 (4 2011), p. 043403.

- [140] J. Colgan, M. S. Pindzola, and F. Robicheaux. "Two-photon double ionization of the hydrogen molecule". *Journal of Physics B: Atomic, Molecular and Optical Physics* 41.12 (2008), p. 121002.
- [141] F. Morales et al. "Two-photon double ionization of H₂ at 30 eV using exterior complex scaling". *Journal of Physics B: Atomic, Molecular and Optical Physics* 42.13 (2009), p. 134013.
- [142] X. Guan, K. Bartschat, and B. I. Schneider. "Two-photon double ionization of H₂ in intense femtosecond laser pulses". *Phys. Rev. A* 82 (4 2010), p. 041404.
- [143] P. Moreno, L. Plaja, and L. Roso. "High-Order Harmonic Generation by Electron-Proton Recombination". *Europhysics Letters* 28.9 (1994), p. 629.
- [144] P. Moreno, L. Plaja, and L. Roso. "Ultrahigh harmonic generation from diatomic molecular ions in highly excited vibrational states". *Phys. Rev. A* 55.3 (1997), R1593.
- [145] R. Numico, P. Moreno, L. Plaja, and L. Roso. "High-order harmonic generation after photodissociation". *Journal of Physics B: Atomic, Molecular and Optical Physics* 31.18 (1998), p. 4163.
- [146] M. Lein et al. "Interference effects in high-order harmonic generation with molecules". *Phys. Rev. A* 66.2 (2002), p. 023805.
- [147] M. Lein et al. "Role of the Intramolecular Phase in High-Harmonic Generation". *Phys. Rev. Lett.* 88.18 (2002), p. 183903.
- [148] C. C. Chirilă and M. Lein. "High-order harmonic generation in vibrating molecules". *Journal of Modern Optics* 53.1-2 (2006), p. 113.
- [149] A. Scrinzi. "Infinite-range exterior complex scaling as a perfect absorber in time-dependent problems". *Phys. Rev. A* 81.5 (2010), p. 053845.
- [150] B. I. Schneider et al. "Recent Advances in Computational Methods for the Solution of the Time-Dependent Schrödinger Equation for the Interaction of Short, Intense Radiation with One and Two Electron Systems". *Quantum Dynamic Imaging: Theoretical and Numerical Methods*. Ed. by A. D. Bandrauk and M. Ivanov. New York, NY: Springer New York, 2011, p. 149.
- [151] M. Weinmüller, M. Weinmüller, J. Rohland, and A. Scrinzi. "Perfect absorption in Schrödinger-like problems using non-equidistant complex grids". *ArXiv e-prints* (2015).
- [152] D. Dundas, J. F. McCann, J. S. Parker, and K. T. Taylor. "Ionization dynamics of laser-driven H₂⁺". *Journal of Physics B: Atomic, Molecular and Optical Physics* 33.17 (2000), p. 3261.
- [153] D. Dundas. "Efficient grid treatment of the ionization dynamics of laser-driven H₂⁺". *Phys. Rev. A* 65.2 (2002), p. 023408.
- [154] D. Dundas, K. J. Meharg, J. F. McCann, and K. T. Taylor. "Dissociative ionization of molecules in intense laser fields". *The European Physical Journal D - Atomic, Molecular, Optical and Plasma Physics* 26.1 (2003), p. 51.
- [155] T. Niederhausen, U. Thumm, and F. Martín. "Laser-controlled vibrational heating and cooling of oriented H₂⁺ molecules". *Journal of Physics B: Atomic, Molecular and Optical Physics* 45.10 (2012), p. 105602.
- [156] L. Belshaw et al. "Observation of Ultrafast Charge Migration in an Amino Acid". *The Journal of Physical Chemistry Letters* 3.24 (2012). PMID: 26291106, p. 3751.
- [157] F. Calegari et al. "Ultrafast electron dynamics in phenylalanine initiated by attosecond pulses". *Science* 346.6207 (2014), p. 336.
- [158] S. Lünnemann, A. I. Kuleff, and L. S. Cederbaum. "Ultrafast charge migration in 2-phenylethyl-N,N-dimethylamine". *Chemical Physics Letters* 450.4 (2008), p. 232.

- [159] G. te Velde et al. "Chemistry with ADF". *Journal of Computational Chemistry* 22.9 (2001), p. 931.
- [160] M. J. Frisch et al. *Gaussian □ 09 Revision E.01*. Gaussian Inc. Wallingford CT 2009.
- [161] A. Castro et al. "octopus: a tool for the application of time-dependent density functional theory". *physica status solidi (b)* 243.11 (2006), p. 2465.
- [162] R. Weinkauf et al. "Highly Efficient Charge Transfer in Peptide Cations in the Gas Phase: Threshold Effects and Mechanism". *The Journal of Physical Chemistry* 100.47 (1996), p. 18567.
- [163] U. Saalmann and R. Schmidt. "Non-adiabatic quantum molecular dynamics: basic formalism and case study". *Zeitschrift für Physik D Atoms, Molecules and Clusters* 38.2 (1996), p. 153.
- [164] U. Saalmann and R. Schmidt. "Excitation and Relaxation in Atom-Cluster Collisions". *Phys. Rev. Lett.* 80.15 (1998), p. 3213.
- [165] T. Kunert and R. Schmidt. "Non-adiabatic quantum molecular dynamics: General formalism and case study H₂⁺ in strong laser fields". *The European Physical Journal D - Atomic, Molecular, Optical and Plasma Physics* 25.1 (2003), p. 15.
- [166] E. Runge and E. K. U. Gross. "Density-Functional Theory for Time-Dependent Systems". *Phys. Rev. Lett.* 52.12 (1984), p. 997.
- [167] M. Uhlmann, T. Kunert, F. Grossmann, and R. Schmidt. "Mixed classical-quantum approach to excitation, ionization, and fragmentation of H₂⁺ in intense laser fields". *Phys. Rev. A* 67.1 (2003), p. 013413.
- [168] A. Castro et al. "Excited states dynamics in time-dependent density functional theory". *The European Physical Journal D - Atomic, Molecular, Optical and Plasma Physics* 28.2 (2004), p. 211.
- [169] F. Calvayrac, P.-G. Reinhard, E. Suraud, and C. Ullrich. "Nonlinear electron dynamics in metal clusters". *Physics Reports* 337.6 (2000), p. 493.
- [170] D. Dundas. "Accurate and efficient non-adiabatic quantum molecular dynamics approach for laser-matter interactions". *Journal of Physics B: Atomic, Molecular and Optical Physics* 37.14 (2004), p. 2883.
- [171] D. Dundas. "Multielectron effects in high harmonic generation in N₂ and benzene: Simulation using a non-adiabatic quantum molecular dynamics approach for laser-molecule interactions". *The Journal of Chemical Physics* 136.19 (2012).
- [172] A. Wardlow and D. Dundas. "High-order-harmonic generation in benzene with linearly and circularly polarized laser pulses". *Phys. Rev. A* 93.2 (2016), p. 023428.
- [173] D. Dundas, P. Mulholland, A. Wardlow, and A. de la Calle. "Probing the role of excited states in ionization of acetylene". *Phys. Chem. Chem. Phys.* (2017), pp. -.
- [174] J. Breidbach and L. S. Cederbaum. "Migration of holes: Numerical algorithms and implementation". *The Journal of Chemical Physics* 126.3 (2007), p. 034101.
- [175] J. Breidbach and L. S. Cederbaum. "Migration of holes: Formalism, mechanisms, and illustrative applications". *The Journal of Chemical Physics* 118.9 (2003), p. 3983.
- [176] D. Toffoli, M. Stener, G. Fronzoni, and P. Decleva. "Convergence of the multicenter B-spline DFT approach for the continuum". *Chemical Physics* 276.1 (2002), p. 25.
- [177] J. Caillat et al. "Correlated multielectron systems in strong laser fields: A multiconfiguration time-dependent Hartree-Fock approach". *Phys. Rev. A* 71 (1 2005), p. 012712.

- [178] T. Kato and H. Kono. "Time-dependent multiconfiguration theory for electronic dynamics of molecules in intense laser fields: A description in terms of numerical orbital functions". *The Journal of Chemical Physics* 128.18 (2008), p. 184102.
- [179] T. Kato and K. Yamanouchi. "Time-dependent multiconfiguration theory for describing molecular dynamics in diatomic-like molecules". *The Journal of Chemical Physics* 131.16 (2009), p. 164118.
- [180] O. E. Alon, A. I. Streltsov, and L. S. Cederbaum. "Many-body theory for systems with particle conversion: Extending the multiconfigurational time-dependent Hartree method". *Phys. Rev. A* 79 (2 2009), p. 022503.
- [181] M. Nest. "The multi-configuration electron–nuclear dynamics method". *Chemical Physics Letters* 472.4 (2009), p. 171.
- [182] D. J. Haxton, K. V. Lawler, and C. W. McCurdy. "Multiconfiguration time-dependent Hartree-Fock treatment of electronic and nuclear dynamics in diatomic molecules". *Phys. Rev. A* 83 (6 2011), p. 063416.
- [183] D. J. Haxton and C. W. McCurdy. "Ultrafast population transfer to excited valence levels of a molecule driven by x-ray pulses". *Phys. Rev. A* 90 (5 2014), p. 053426.
- [184] D. J. Haxton and C. W. McCurdy. "Two methods for restricted configuration spaces within the multiconfiguration time-dependent Hartree-Fock method". *Phys. Rev. A* 91 (1 2015), p. 012509.
- [185] I. Sánchez and F. Martín. "Origin of Unidentified Structures in Resonant Dissociative Photoionization of H_2 ". *Phys. Rev. Lett.* 79 (9 1997), p. 1654.
- [186] I. Sánchez and F. Martín. "Resonant dissociative photoionization of H_2 and D_2 ". *Phys. Rev. A* 57 (2 1998), p. 1006.
- [187] J. L. Sanz-Vicario, H. Bachau, and F. Martín. "Time-dependent theoretical description of molecular autoionization produced by femtosecond xuv laser pulses". *Phys. Rev. A* 73 (3 2006), p. 033410.
- [188] A. Palacios, H. Bachau, and F. Martín. "Step-ladder Rabi oscillations in molecules exposed to intense ultrashort vuv pulses". *Phys. Rev. A* 74 (3 2006), p. 031402.
- [189] J. Sanz-Vicario et al. "Ab initio time-dependent method to study the hydrogen molecule exposed to intense ultrashort laser pulses". *Journal of Electron Spectroscopy and Related Phenomena* 161.1 (2007). Many particle spectroscopy of atoms, molecules, clusters and surfaces, p. 182.
- [190] A. Palacios, J. L. Sanz-Vicario, and F. Martín. "Theoretical methods for attosecond electron and nuclear dynamics: applications to the H_2 molecule". *Journal of Physics B: Atomic, Molecular and Optical Physics* 48.24 (2015), p. 242001.
- [191] F. Martín et al. "Single Photon-Induced Symmetry Breaking of H_2 Dissociation". *Science* 315.5812 (2007), p. 629.
- [192] A. Palacios, H. Bachau, and F. Martín. "Enhancement and Control of H_2 Dissociative Ionization by Femtosecond VUV Laser Pulses". *Phys. Rev. Lett.* 96.14 (2006), p. 143001.
- [193] A. Palacios, A. González-Castrillo, and F. Martín. "Molecular interferometer to decode attosecond electron–nuclear dynamics". *Proceedings of the National Academy of Sciences* 111.11 (2014), p. 3973.
- [194] L. A. A. Nikolopoulos, J. S. Parker, and K. T. Taylor. "Combined R -matrix eigenstate basis set and finite-difference propagation method for the time-dependent Schrödinger equation: The one-electron case". *Phys. Rev. A* 78 (6 2008), p. 063420.
- [195] L. Moore et al. "The RMT method for many-electron atomic systems in intense short-pulse laser light". *Journal of Modern Optics* 58.13 (2011), p. 1132.

- [196] M. A. Lysaght et al. "Ab Initio Methods for Few- and Many-Electron Atomic Systems in Intense Short-Pulse Laser Light". *Quantum Dynamic Imaging: Theoretical and Numerical Methods*. Ed. by A. D. Bandrauk and M. Ivanov. New York, NY: Springer New York, 2011, p. 107.
- [197] C. Ó Broin and L. A. A. Nikolopoulos. "R-matrix-incorporating-time method for H 2 + in short and intense laser fields". *Phys. Rev. A* 92.6 (2015), p. 063428.
- [198] C. Ó. Broin and L. A. A. Nikolopoulos. "R-matrix-incorporating-time theory of one-electron atomic and molecular systems in intense laser fields". *Journal of Physics B: Atomic, Molecular and Optical Physics* 50.3 (2017), p. 033001.
- [199] J. Wragg, J. S. Parker, and H. W. van der Hart. "Double ionization in R-matrix theory using a two-electron outer region". *Phys. Rev. A* 92 (2 2015), p. 022504.
- [200] J. Wragg and H. W. van der Hart. "Spin and spatial dynamics in electron-impact scattering off S-wave He using R-matrix-with-time-dependence theory". *Phys. Rev. A* 94 (3 2016), p. 032706.
- [201] P. M. Dirac. *The Principles of Quantum Mechanics*. 4th ed. Oxford University Press, 1958.
- [202] J. Sakurai and J. Napolitano. *Modern Quantum Mechanics*. 2nd ed. Pearson Education, 2011.
- [203] P. W. Milonni. *The quantum vacuum. An introduction to Quantum Electrodynamics*. Academic Press, 1994.
- [204] P. A. M. Dirac. "The Quantum Theory of the Emission and Absorption of Radiation". *Proceedings of the Royal Society of London A: Mathematical, Physical and Engineering Sciences* 114.767 (1927), p. 243.
- [205] M. H. Mittleman. *Introduction to the theory of laser-matter interactions*. 2nd ed. Plenum Press, 1993.
- [206] T. N. Todorov. "Time-dependent tight binding". *Journal of Physics: Condensed Matter* 13.45 (2001), p. 10125.
- [207] L. I. Schiff. *Quantum Mechanics*. 3rd ed. McGraw-Hill International Editions, 1968.
- [208] G. B. Arfken and H. Weber. *Mathematical methods for Physicists*. 6th ed. Elsevier Academic Press, 2005.
- [209] H. Kono, A. Kita, Y. Ohtsuki, and Y. Fujimura. "An Efficient Quantum Mechanical Method for the Electronic Dynamics of the Three-Dimensional Hydrogen Atom Interacting with a Linearly Polarized Strong Laser Pulse". *Journal of Computational Physics* 130.1 (1997), p. 148.
- [210] N. A. Modine, G. Zumbach, and E. Kaxiras. "Adaptive-coordinate real-space electronic-structure calculations for atoms, molecules, and solids". *Phys. Rev. B* 55.16 (1997), p. 10289.
- [211] I. Kawata and H. Kono. "Dual transformation for wave packet dynamics: Application to Coulomb systems". *The Journal of Chemical Physics* 111.21 (1999), p. 9498.
- [212] J. M. Pérez-Jordá. "Variational plane-wave calculations in adaptive coordinates". *Phys. Rev. B* 58.3 (1998), p. 1230.
- [213] I. Kawata, H. Kono, and Y. Fujimura. "Adiabatic and diabatic responses of H₂+ to an intense femtosecond laser pulse: Dynamics of the electronic and nuclear wave packet". *The Journal of Chemical Physics* 110.23 (1999), p. 11152.
- [214] J. D. Jackson. *Classical Electrodynamics*. 3rd ed. John Wiley & Sons, 1999.
- [215] H. R. Reiss. *Lectures on Ultrafast Intense Laser Science 1*. Ed. by K. Yamanouchi. Springer-Verlag Berlin Heidelberg, 2011.

- [216] F. Krausz and M. Ivanov. "Attosecond physics". *Rev. Mod. Phys.* 81.1 (2009), p. 163.
- [217] J. V. de Aldana. "Interaction of atoms with intense laser fields: Theoretical study and numerical models". PhD thesis. Universidad de Salamanca, 2001.
- [218] K. J. Cairns. "The helium atom and the hydrogen molecule in intense laser fields". PhD thesis. Queen's University Belfast, 2004.
- [219] W. C. Henneberger. "Perturbation Method for Atoms in Intense Light Beams". *Phys. Rev. Lett.* 21.12 (1968), p. 838.
- [220] F. Morales, M. Richter, S. Patchkovskii, and O. Smirnova. "Imaging the Kramers–Henneberger atom". *Proceedings of the National Academy of Sciences* 108.41 (2011), p. 16906.
- [221] M. Richter et al. "The role of the Kramers–Henneberger atom in the higher-order Kerr effect". *New Journal of Physics* 15.8 (2013), p. 083012.
- [222] B. Fornberg. "Generation of Finite Difference Formulas on Arbitrarily Spaced Grids". *Mathematics of Computation* 51.184 (1988), p. 699.
- [223] B. Fornberg. "Classroom Note: Calculation of Weights in Finite Difference Formulas". *SIAM Review* 40.3 (1998), p. 685.
- [224] K. Hirose, T. Ono, Y. Fujimoto, and S. Tsukamoto. *First-Principles Calculations in Real-Space Formalism*. 15. Imperial College Press, 2005. Chap. 2.
- [225] J. S. Parker et al. "Double-electron above threshold ionization of helium". *Journal of Physics B: Atomic, Molecular and Optical Physics* 34.3 (2001), p. L69.
- [226] J. S. Parker et al. "High-Energy Cutoff in the Spectrum of Strong-Field Nonsequential Double Ionization". *Phys. Rev. Lett.* 96.13 (2006), p. 133001.
- [227] U. Giovannini, A. H. Larsen, and A. Rubio. "Modeling electron dynamics coupled to continuum states in finite volumes with absorbing boundaries". *The European Physical Journal B* 88.3 (2015), p. 1.
- [228] E. S. Smyth, J. S. Parker, and K. Taylor. "Numerical integration of the time-dependent Schrödinger equation for laser-driven helium". *Computer Physics Communications* 114.1 (1998), p. 1.
- [229] R. Santra. "Why complex absorbing potentials work: A discrete-variable-representation perspective". *Phys. Rev. A* 74.3 (2006), p. 034701.
- [230] C. W. McCurdy, M. Baertschy, and T. N. Rescigno. "Solving the three-body Coulomb breakup problem using exterior complex scaling". *Journal of Physics B: Atomic, Molecular and Optical Physics* 37.17 (2004), R137.
- [231] A. Picón et al. "Two-center interferences in photoionization of a dissociating H₂⁺ molecule". *Phys. Rev. A* 83.1 (2011), p. 013414.
- [232] C. Lanczos. "An iteration method for the solution of the eigenvalue problem of linear differential and integral operators". *J. Res. Natl. Bur. Stand.* 45.4 (1950), p. 255.
- [233] K. Wu, A. Canning, H. Simon, and L.-W. Wang. "Thick-Restart Lanczos Method for Electronic Structure Calculations". *Journal of Computational Physics* 154.1 (1999), p. 156.
- [234] K. Wu and H. Simon. "Thick-Restart Lanczos Method for Large Symmetric Eigenvalue Problems". *SIAM J. Matrix Anal. Appl.* 22.2 (2000), p. 602.
- [235] Hilico, L., Billy, N., Grémaud, B., and Delande, D. "Ab initio calculation of the J = 0 and J = 1 states of the H+2, D+2 molecular ions". *Eur. Phys. J. D* 12.3 (2000), p. 449.
- [236] S. Balay et al. *PETSc Web page*. <http://www.mcs.anl.gov/petsc>. 2016.
- [237] S. Balay et al. *PETSc Users Manual*. Tech. rep. ANL-95/11 - Revision 3.7. Argonne National Laboratory, 2016.

- [238] S. Balay, W. D. Gropp, L. C. McInnes, and B. F. Smith. "Efficient Management of Parallelism in Object Oriented Numerical Software Libraries". *Modern Software Tools in Scientific Computing*. Ed. by E. Arge, A. M. Bruaset, and H. P. Langtangen. Birkhäuser Press, 1997, p. 163.
- [239] V. Hernandez, J. E. Roman, and V. Vidal. "SLEPc: Scalable Library for Eigenvalue Problem Computations". *Lect. Notes Comput. Sci.* 2565 (2003), p. 377.
- [240] V. Hernandez, J. E. Roman, and V. Vidal. "SLEPc: A scalable and flexible toolkit for the solution of eigenvalue problems". *ACM Trans. Math. Software* 31.3 (2005), p. 351.
- [241] J. E. Roman, C. Campos, E. Romero, and A. Tomas. *SLEPc Users Manual*. Tech. rep. DSIC-II/24/02 - Revision 3.7. D. Sistemes Informàtics i Computació, Universitat Politècnica de València, 2016.
- [242] T. Ericsson and A. Ruhe. "The spectral transformation Lanczos method for the numerical solution of large sparse generalized symmetric eigenvalue problems". *Mathematics of Computation* 35.152 (1980), p. 1251.
- [243] H. Goldstein, C. Poole, and J. Safko. *Classical Mechanics*. Addison Wesley, 2002.
- [244] W. Press, S. Teukolsky, W. T. Vetterling, and B. P. Flannery. *Numerical Recipes: The Art of Scientific Computing*. 3rd ed. Cambridge University Press, 2007.
- [245] R. E. F. Silva et al. "Energy- and angle-resolved ionization of H_2^+ interacting with xuv subfemtosecond laser pulses". *Phys. Rev. A* 92.1 (2015), p. 013426.
- [246] J. Franck and E. G. Dymond. "Elementary processes of photochemical reactions". *Trans. Faraday Soc.* 21.February (1926), p. 536.
- [247] E. Condon. "A Theory of Intensity Distribution in Band Systems". *Phys. Rev.* 28.6 (1926), p. 1182.
- [248] D. Wunderlich and U. Fantz. "Franck–Condon factors for molecule–ion reactions of and its isotopomers". *Atomic Data and Nuclear Data Tables* 97.2 (2011), p. 152.
- [249] N. Takemoto and A. Becker. "Multiple Ionization Bursts in Laser-Driven Hydrogen Molecular Ion". *Phys. Rev. Lett.* 105.20 (2010), p. 203004.
- [250] N. Takemoto and A. Becker. "Time-resolved view on charge-resonance-enhanced ionization". *Phys. Rev. A* 84.2 (2011), p. 023401.
- [251] N. Takemoto and A. Becker. "Visualization and interpretation of attosecond electron dynamics in laser-driven hydrogen molecular ion using Bohmian trajectories". *The Journal of Chemical Physics* 134.7 (2011), p. 074309.
- [252] T. Seideman, M. Y. Ivanov, and P. B. Corkum. "Role of Electron Localization in Intense-Field Molecular Ionization". *Phys. Rev. Lett.* 75.15 (1995), p. 2819.
- [253] X.-B. Bian and A. D. Bandrauk. "Probing Nuclear Motion by Frequency Modulation of Molecular High-Order Harmonic Generation". *Phys. Rev. Lett.* 113.19 (2014), p. 193901.
- [254] F. Morales et al. "High harmonic spectroscopy of electron localization in the hydrogen molecular ion". *Journal of Physics B: Atomic, Molecular and Optical Physics* 47.20 (2014), p. 204015.
- [255] R. E. F. Silva et al. "Even harmonic generation in isotropic media of dissociating homonuclear molecules". *Scientific Reports* 6 (2016), p. 32653.
- [256] M. Lara-Astiaso et al. "Enhancing High-Order Harmonic Generation in Light Molecules by Using Chirped Pulses". *Phys. Rev. Lett.* 117.9 (2016), p. 093003.
- [257] M. Lein. "Attosecond Probing of Vibrational Dynamics with High-Harmonic Generation". *Phys. Rev. Lett.* 94.5 (2005), p. 053004.

- [258] A. Pohl, P.-G. Reinhard, and E. Suraud. "Towards Single-Particle Spectroscopy of Small Metal Clusters". *Phys. Rev. Lett.* 84.22 (2000), p. 5090.
- [259] L. Tao and A. Scrinzi. "Photo-electron momentum spectra from minimal volumes: the time-dependent surface flux method". *New Journal of Physics* 14.1 (2012), p. 013021.
- [260] P. G. Burke. *R-Matrix Theory of Atomic Collisions*. 1st ed. 61. Springer-Verlag Berlin Heidelberg, 2011.
- [261] K. Taylor et al. "Multiphoton double ionization of atoms and molecules by {FEL} {XUV} light". *Journal of Electron Spectroscopy and Related Phenomena* 144–147 (2005). Proceeding of the Fourteenth International Conference on Vacuum Ultraviolet Radiation Physics, p. 1191.
- [262] P. Wopperer et al. "Orientation averaged angular distributions of photo-electrons from free Na clusters". *Physics Letters A* 375.1 (2010), p. 39.
- [263] P. Wopperer et al. "Angular distributions of photoelectrons from free Na clusters". *Phys. Rev. A* 82.6 (2010), p. 063416.
- [264] P. Wopperer, P. M. Dinh, E. Suraud, and P.-G. Reinhard. "Frequency dependence of photoelectron angular distributions in small Na clusters". *Phys. Rev. A* 85.1 (2012), p. 015402.
- [265] P. M. Dinh, P. Romaniello, P.-G. Reinhard, and E. Suraud. "Calculation of photoelectron spectra: A mean-field-based scheme". *Phys. Rev. A* 87.3 (2013), p. 032514.
- [266] A. Scrinzi. "t -SURFF: fully differential two-electron photo-emission spectra". *New Journal of Physics* 14.8 (2012), p. 085008.
- [267] L. Yue and L. B. Madsen. "Dissociative ionization of H_2^+ using intense femtosecond XUV laser pulses". *Phys. Rev. A* 90.6 (2014), p. 063408.
- [268] L. Yue and L. B. Madsen. "Dissociation and dissociative ionization of H_2^+ using the time-dependent surface flux method". *Phys. Rev. A* 88.6 (2013), p. 063420.
- [269] A. Karamatskou, S. Pabst, Y.-J. Chen, and R. Santra. "Calculation of photoelectron spectra within the time-dependent configuration-interaction singles scheme". *Phys. Rev. A* 89.3 (2014), p. 033415.
- [270] Intel(R) Math Kernel Library. url: <https://software.intel.com/en-us/intel-mkl> (visited on 07/19/2016).
- [271] M. Frigo and S. G. Johnson. "The Design and Implementation of FFTW3". *Proceedings of the IEEE* 93.2 (2005). Special issue on "Program Generation, Optimization, and Platform Adaptation", p. 216.
- [272] M. Frigo. *FFTW webpage*. url: <http://www.fftw.org> (visited on 01/28/2017).
- [273] J. W. Cooley and J. W. Tukey. "An algorithm for the calculation of complex Fourier series". *Math. Comp.* 19 (1965), p. 297.
- [274] M. Heideman, D. Johnson, and C. Burrus. "Gauss and the history of the fast fourier transform". *ASSP Magazine, IEEE* 1.4 (1984), p. 14.
- [275] W. I. Thacker et al. "Algorithm 905: SHEPPACK: Modified Shepard Algorithm for Interpolation of Scattered Multivariate Data". *ACM Trans. Math. Softw.* 37.3 (2010), 34:1.
- [276] F. Lekien and J. Marsden. "Tricubic interpolation in three dimensions". *International Journal for Numerical Methods in Engineering* 63.3 (2005), p. 455.
- [277] A. Barnett. "COULFG: Coulomb and Bessel functions and their derivatives, for real arguments, by Steed's method". *Computer Physics Communications* 27.2 (1982), p. 147.

- [278] D. W. Chandler and P. L. Houston. "Two-dimensional imaging of state-selected photodissociation products detected by multiphoton ionization". *The Journal of Chemical Physics* 87.2 (1987), p. 1445.
- [279] C. Bordas, F. Paulig, H. Helm, and D. L. Huestis. "Photoelectron imaging spectrometry: Principle and inversion method". *Review of Scientific Instruments* 67.6 (1996), p. 2257.
- [280] R. Dörner et al. "Cold Target Recoil Ion Momentum Spectroscopy: a 'momentum microscope' to view atomic collision dynamics". *Physics Reports* 330.2–3 (2000), p. 95.
- [281] H. Bachau. "Multiphoton ionization of one-electron diatomic molecules: the discretization approach for the two-centre problem". *Journal of Physics B: Atomic, Molecular and Optical Physics* 35.3 (2002), p. 509.
- [282] A. Palacios, C. W. McCurdy, and T. N. Rescigno. "Extracting amplitudes for single and double ionization from a time-dependent wave packet". *Phys. Rev. A* 76.4 (2007), p. 043420.
- [283] Z. Chen et al. "Analysis of two-dimensional photoelectron momentum spectra and the effect of the long-range Coulomb potential in single ionization of atoms by intense lasers". *Phys. Rev. A* 74.5 (2006), p. 053405.
- [284] T. Morishita, Z. Chen, S. Watanabe, and C. D. Lin. "Two-dimensional electron momentum spectra of argon ionized by short intense lasers: Comparison of theory with experiment". *Phys. Rev. A* 75.2 (2007), p. 023407.
- [285] T. Morishita, A.-T. Le, Z. Chen, and C. D. Lin. "Accurate Retrieval of Structural Information from Laser-Induced Photoelectron and High-Order Harmonic Spectra by Few-Cycle Laser Pulses". *Phys. Rev. Lett.* 100.1 (2008), p. 013903.
- [286] Z. Chen, A.-T. Le, T. Morishita, and C. D. Lin. "Quantitative rescattering theory for laser-induced high-energy plateau photoelectron spectra". *Phys. Rev. A* 79.3 (2009), p. 033409.
- [287] D. B. Milošević, G. G. Paulus, D. Bauer, and W. Becker. "Above-threshold ionization by few-cycle pulses". *Journal of Physics B: Atomic, Molecular and Optical Physics* 39.14 (2006), R203.
- [288] B. Shan et al. "High-order harmonic cutoff extension of the O₂ molecule due to ionization suppression". *Phys. Rev. A* 66.6 (2002), p. 061401.
- [289] C. Altucci et al. "Dependence upon the molecular and atomic ground state of higher-order harmonic generation in the few-optical-cycle regime". *Phys. Rev. A* 71.1 (2005), p. 013409.
- [290] F. Grasbon et al. "Signatures of symmetry-induced quantum-interference effects observed in above-threshold-ionization spectra of molecules". *Phys. Rev. A* 63.4 (2001), p. 041402.
- [291] A. Jarón-Becker, A. Becker, and F. H. M. Faisal. "Ionization of N₂, O₂, and linear carbon clusters in a strong laser pulse". *Phys. Rev. A* 69.2 (2004), p. 023410.
- [292] M. Spanner, O. Smirnova, P. B. Corkum, and M. Y. Ivanov. "Reading diffraction images in strong field ionization of diatomic molecules". *Journal of Physics B: Atomic, Molecular and Optical Physics* 37.12 (2004), p. L243.
- [293] J. Muth-Böhm, A. Becker, and F. H. M. Faisal. "Suppressed Molecular Ionization for a Class of Diatomics in Intense Femtosecond Laser Fields". *Phys. Rev. Lett.* 85.11 (2000), p. 2280.
- [294] H. Hetzheim, C. Figueira de Morisson Faria, and W. Becker. "Interference effects in above-threshold ionization from diatomic molecules: Determining the internuclear separation". *Phys. Rev. A* 76.2 (2007), p. 023418.

- [295] M. Ciappina and W. Cravero. "Two center and Coulomb effects in near-threshold ionization of H₂ by short laser pulses". *Journal of Modern Optics* 56.1 (2009), p. 11.
- [296] N. Suárez et al. "Above-threshold ionization and laser-induced electron diffraction in diatomic molecules". *Phys. Rev. A* 94.4 (2016), p. 043423.
- [297] X. Guan, E. B. Secor, K. Bartschat, and B. I. Schneider. "Double-slit interference effect in electron emission from H₂⁺ exposed to x-ray radiation". *Phys. Rev. A* 85.4 (2012), p. 043419.
- [298] X. Guan, R. C. DuToit, and K. Bartschat. "Photoionization of the H₂⁺ ion by ultrashort elliptically polarized laser pulses". *Phys. Rev. A* 87.5 (2013), p. 053410.
- [299] K.-J. Yuan and A. D. Bandrauk. "Molecular above-threshold-ionization angular distributions with intense circularly polarized attosecond XUV laser pulses". *Phys. Rev. A* 85.5 (2012), p. 053419.
- [300] D. A. Telnov and S.-I. Chu. "Ab initio". *Phys. Rev. A* 76 (4 2007), p. 043412.
- [301] D. A. Telnov, J. Heslar, and S.-I. Chu. "Effect of nuclear vibration on high-order-harmonic generation of aligned H₂⁺ molecules". *Phys. Rev. A* 90 (6 2014), p. 063412.
- [302] K. N. Avanaki, D. A. Telnov, H. Z. Jooya, and S.-I. Chu. "Generation of below-threshold even harmonics by a stretched H₂⁺ molecular ion in intense linearly and circularly polarized laser fields". *Phys. Rev. A* 92 (6 2015), p. 063811.
- [303] K. N. Avanaki, D. A. Telnov, and S.-I. Chu. "Exploration of the origin of anomalous dependence for near-threshold harmonics in H₂⁺ on the ellipticity of driving laser fields". *Journal of Physics B: Atomic, Molecular and Optical Physics* 49.11 (2016), p. 114002.
- [304] M. Murakami and S.-I. Chu. "Photoelectron momentum distributions of the hydrogen molecular ion driven by multicycle near-infrared laser pulses". *Phys. Rev. A* 94 (4 2016), p. 043425.
- [305] B. Fetić and D. B. Milošević. "Numerical solution of the time-dependent Schrödinger equation for H₂⁺ ion with application to high-harmonic generation and above-threshold ionization". *Phys. Rev. E* 95 (5 2017), p. 053309.
- [306] B. Fornberg. *A Practical Guide to Pseudospectral Methods*. Cambridge University Press, 1995.
- [307] A. Messiah. *Quantum Mechanics*. Dover Books on Physics. Dover Publications, 2014.